Crystal structure of
Pseudomonas aeruginosa condensing enzyme PqsBC

Fajar Prasetya

4236173

School of Pharmacy

The University of Nottingham

2018

Abstract

Pseudomonas aeruginosa is an opportunistic bacterium that can infect immunocompromised people, and is especially prevalent in patients with cystic fibrosis. Treatment of *P. aeruginosa* is complicated due to resistance to many classes of antibiotics. This is partly due to biofilm formation, which is not simply a diffusion barrier, but also has a distinct mechanism for resisting the action of antibiotics. *P. aeruginosa* quinolone signal (PQS) has an important role in quorum sensing, which is involved in biofilm formation. PqsBC is a condensing enzyme in the biosynthesis of the PQS. The crystal structures of $PqsBC^{C129A}$ and $PqsBC^{C129A}$-Fe^{3+} were collected to 2.04 Å and to 2.3 Å, respectively. The crystal structure showed that PqsB and PqsC have a pseudo 2-fold symmetry that mimics the FabH homodimer as well as the presence of a catalytic diad instead of the typical catalytic triad in PqsBC, seen in other FabH family enzymes. The $PqsC^{C129A}$ active site volume is twice the volume as those of FabH enzymes or PqsD, with a calculated volume of 761$Å^3$, compared to 389$Å^3$ for PqsD and 367$Å^3$ for FabH.The $PqsBC^{C129A}$-Fe^{3+} crystal structure shows that Fe^{3+} binds to nitrogen atoms from PqsB His282 and PqsC His2 along with oxygen atoms from PqsB Glu48 and Glu280. Therefore, there are four bonds involved in the interaction between Fe^{3+} and $PqsBC^{C129A}$. These bond lengths are very similar to those observed in the structures of Azurin and FutA1 complexed with iron. These crystal structures of PqsBC provide a unique insight into substrate recognition and establish a scaffold for structure guided drug design of novel antimicrobial agents.

Acknowledgement

Foremost, I would like to express my sincere gratitude to my supervisors Prof. Jonas Emsley and Dr Ingrid Dreveny for the continuous support throughout my PhD study and research, for the patience, motivation, enthusiasm, and immense knowledge. Their guidance helped me in all the time of research and writing of this thesis.

Besides my supervisors, my sincere thank also goes to all colleagues in the crystallography and protein lab: Dr Chan Li for helping me start my initial experiments, Dr Simon Caulton as my good friend who has been always constantly support and timely help inside and outside lab, Dr Muhammad Saleem, Dr Selva Kumar, Dr Kim Hyojung, Dr Danilo Belviso, Dr Monika Pathak, Dr Susan Wong, and Bubacarr Kaira for their guidance and assistance during my PhD.

I am grateful to all my fellow lab mates in crystallography group Peni Indrayudha, Emma Gunnell, Stephanie Ward, and Mohamed Halawa for working together and all the fun that we have had in the last four years. Also, I would like to thank our project collaborator in Institute of Molecular Microbiology and Biotechnology, University of Münster, especially Steffen Lorenz Drees for helping me to fully understand the biochemistry of PqsBC.

Very special thanks to my mom, dad, and my sisters. Without their constant support encouragement and prayers, this would not have been possible.

Finally, I am incredibly grateful to Niken Sulistyowati as my wife also our angels Aisyah Batrisya Qaireen and Muhammad Yusuf Ibrahim for keeping me alive over the last 4 years. Without them I would not have been able to complete the PhD, and for that I am forever indebted.

Table of Contents

Abstract ii

Acknowledgement iii

Table of Contents v

List of Figures ix

List of Tables xviii

Abbreviations xix

1 Chapter 1: Introduction 1

1.1 Introduction 2

1.2 *Pseudomonas aeruginosa* 4

1.3 Quorum Sensing in Pseudomonas aeruginosa 6

1.3.1 Quorum sensing an overview 6

1.3.2 The four interconnected QS in *P. aeruginosa* 8

1.3.3 PQS: a signal molecule providing a regulatory link between the Las and Rhl systems 10

1.4 *Pseudomonas aeruginosa* virulence factors related to QS 11

1.4.1 *P. aeruginosa* adherence to mucosal surfaces 13

1.4.1.1 Type IV pili 14

1.4.1.2 Flagellum 14

1.4.1.3 Alginate capsule 15

1.4.2 Pyoverdine and pyochelin 15

1.4.3 Pyocyanin 16

1.4.4 Biofilms 17

1.5 AHL- and AQ-dependent QS 18

1.6 PqsA, PqsB, PqsC, PqsD, and PqsE and PQS biosynthesis 19

1.7 PQS in quorum sensing and iron uptake 21

1.8 Inhibition of PQS as resistance-free antimicrobial specific *P. aeruginosa* 23

1.9 Clinical significance of PqsBC 24

1.10 Protein X-ray crystallography 25

1.11 Aims of this PhD project 26

2 Chapter 2: Protein crystal structure determination 28

2.1 Structural biology of macromolecules 29

2.2 Protein crystallography project outline 29

2.3 Protein sample preparation 31
2.3.1 Recombinant DNA technology 31
2.3.2 Protein expression 31
2.3.3 Protein purification 32
2.4 Crystallisation of proteins 32
2.4.1 Crystal formation 33
2.4.2 Crystallisation methodology 34
2.4.3 Vapour-diffusion method 35
2.5 Introduction of X-ray diffraction 37
2.6 Theory of X-ray diffraction 39
2.6.1 Electrons as an oscillation induction of the electrons 40
2.6.2 Scattering by a single electron 43
2.6.3 Scattering by a single atom 45
2.6.4 Scattering by number of atoms in a unit cell 46
2.6.5 Diffraction by a crystal 48
2.6.6 Bragg's Law 49
2.6.7 The reciprocal lattice and Ewald sphere construction 51
2.6.8 Data collection 53
2.7 Processing the data 53
2.7.1 Indexing, parameter refinement, and integration 54
2.7.2 Scaling and merging 57
2.7.3 Truncation 58
2.8 Phasing methods 58
2.8.1 Multiple isomorphous replacement 59
2.8.2 Multiple anomalous dispersion 61
2.8.3 Molecular replacement 61
2.9 Model building, structure refinement and validation 65
2.9.1 Model building 66
2.9.2 Model refinement 66
2.9.3 Validation of the model 69
3 Chapter 3: Materials and Methods 71
3.1 Materials used 72
3.1.1 PqsBC enzyme 72
3.1.2 Subtrates (ligands) 72
3.1.3 Bacterial strains used 73

3.1.4 Lysogeny Broth (LB) medium 73
3.2 PCR 73
3.3 Expression and purification of His-TEV protease 74
3.4 Expression and purification of PqsBC 76
3.5 Crystallisation and structure determination of PqsBC 79
3.6 SDS-Polyacrylamide gel electrophoresis (PAGE) 80
3.7 Analysing protein concentration 82
4 Chapter 4: Expression, purification, and crystallisation of PqsBC 83
4.1 Introduction 84
4.2 Expression and purification of PqsBC 85
4.3 Crystallisation of PqsBC 88
4.4 Optimisation of PqsBC crystallisation 90
5 Chapter 5: Crystal structure of PqsBC^{C129A}-Fe^{3+} 92
5.1 Co-crystallisation of PqsBC with additives 93
5.2 Crystallisation of PqsBC^{C129A}-Fe^{3+} 93
5.3 Data collection the PqsBC^{C129A}-Fe^{3+} crystal form 94
5.4 PqsBC^{C129A}-Fe^{3+} crystal structure refinement and validation 95
5.5 PqsBC^{C129A}-Fe^{3+} crystal structure shows iron binding to PqsB and PqsC 100
5.6 PqsBC^{C129A}-Fe^{3+} and PqsBC^{C129A} crystal structure alignment 101
5.7 PqsBC^{C129A}-Fe^{3+} crystal interfaces and packing analysis 104
5.8 Packing analysis of PqsBC^{C129A}-Fe^{3+} and PqsBC^{C129A} 113
5.9 Analysis of Fe^{3+} bond length in PqsBC^{C129A}-Fe^{3+} structure 118
5.10 Ligands in PqsBC^{C129A}-Fe^{3+} structure 120
6 Chapter 6: Structure determination and characterisation of PqsBC^{C129A} 124
6.1 Data collection of PqsBC^{C129A} crystal 125
6.2 PqsBC^{C129A} crystal structure refinement and validation 126
6.3 Structure comparisons of PqsBC^{C129A} 130
6.4 PqsBC^{C129A} crystal structure shows the similarity to FabH-like enzyme 130
6.5 PqsBC^{C129A} crystal structure is a heterodimer 131
6.6 PqsC^{129A} structure reveals a catalytic diad 135
6.7 Active site volume comparison of PqsBC^{C129A} with FabH and PqsD 136
6.8 Active site pocket of PqsBC^{C129A} is formed by PqsB and PqsC 138
6.9 Central cavity of PqsBC^{C129A} 138
6.10 Alignment of the PqsC with PqsD and FabH *E.coli* enzymes 144
6.11 PqsBC^{C129A}, PqsD, and FabH *E.coli* crystal structure superposition 145

7 Chapter 7: Comparison of PqsBC with FabH 150
7.1 PqsBC, a condensing enzyme in the biosynthesis of PQS 151
7.2 FabH (β-ketoacyl-ACP-synthase III) crystal structures 151
7.3 PqsBC as a heterodimer FabH with catalytic diad 159
7.4 Active site volume comparison of PqsBC^{C129A} with FabH 167
7.5 Active site pocket residues comparison of PqsBC^{C129A} with FabH 169
7.6 Substrates processing by PqsBC 174
8 Chapter 8: Oligomerisation of PqsBC 177
8.1 Mutagenesis stabilising tetramer PqsBC^{L229C} 178
8.2 Four of PqsC interfaces on PqsBC^{C129A} crystal structure 188
9 Chapter 9: Conclusion and future work 195
9.1 Conclusion and future work 196
10 References 201

List of Figures

Figure 1.1. *P. aeruginosa.* Imaged using scanning electron microscope (Kenneth Todar, 2012). 5
Figure 1.2. Quorum sensing networks in *Pseudomonas aeruginosa*, arrows indicate a stimulatory effect. PQS is connected to the AHL QS system as *las* system controls PQS synthesis. Subsequently, it is affecting the *rhl* system as a link between *las* and *rhl* systems (adapted from (Papenfort and Bassler, 2016b).....10
Figure 1.3. Virulence factors of *P. aeruginosa* related to QS that are employed during infections.....12
Figure 1.4. Structures of N-acyl homoserine lactones (AHLs) used as signals by *P. aeruginosa*. *N*-3-oxo-dodecanoyl-*L*-homoserine lactone N-(3-oxododecanoyl)-HSL and N-butyryl-HSL (C4-HSL).....18
Figure 1.5. The Biosynthetic pathway of PQS by PqsABCDEH operon. In the initial step, the acyl moiety of an activated carboxylic acid is transferred to a strictly conserved active-site cysteine residue. Subsequently, a β-ketoalkanoic acid (malonyl-ACP in the case of FabH, malonyl-CoA or malonyl-ACP in PqsD, 2-ABA in PqsBC) is decarboxylated. Intermediates and products of the alkyl quinolone biosynthetic pathway: Ant-CoA − anthranilate-coenzyme A, 2-ABA-CoA − 2-aminobenzoylacetyl-CoA, 2-ABA – 2-aminobenzoylacetate, HHQ –2-heptyl-4-hydroxyquinoline, PQS – *Pseudomonas* quinolone signal.....21
Figure 2.1. A flow chart of classical protein crystallography.....30
Figure 2.2. Crystallisation two-dimensional solubility diagram. Illustrating the change of protein concentration against precipitating concentration. Crystal formation or nucleation begins in nucleation zone and return to growth zone to grow in size.....34
Figure 2.3. Hanging drop and sitting drop are included as the vapour-diffusion method. As theoretically lead water gradually moves through the vapour phase, out of the drop and into reservoir lead to reduce the volume of the drop, and it will increase the concentration of protein inside the drop to a point where protein molecules start to precipitate out of solution. Subsequently, protein molecules are starting concentrate, they interact with one another rather than interact with the water molecules.....36
Figure 2.4. Young's double slit experiment used diffracted light from a single source passed into two more slits to be used as coherent sources. Yellow dots on optical screen represent the diffraction of light by slits.....38
Figure 2.5. Model of X-rays are allowed to pass through the slit, hence there is no diffraction pattern will be observed.....38
Figure 2.6. The interaction of the oscillating electric field vector in the anatomy of electromagnetic wave (Rupp, 2010). **H** is magnetic field vector, **E** is electric field vector, $\mathbf{S_0}$ is propagation vector, π is phase in radians with 1 rad = $180/\pi$ degrees. The vector $\mathbf{S}_0$ in the direction of wave propagation has magnitude $1/\lambda = n$. 42

Figure 2.7. X-ray coherent (Thomson) scattering by a free electron (Kasai-Kakudo and Kakudo, 2005). **Ao** is an amplitude of the wave motion of the incident X-ray, plane **P** is an amplitude of the scattered spherical wave at point in XY plane, **RF** is a distance from the electron.....43
Figure 2.8. Propagation of a spherical wave with amplitude **Ae** in direction **A** (Kasai-Kakudo and Kakudo, 2005). 44
Figure 2.9. The three dimensions of unit cell are described as vectors a, b, c, with the angles α, β, γ. 47
Figure 2.10. Bragg's law, it is a result of reflected waves **n** as integer (1, 2, 3 etc), from different layers that are perfectly in phase with each other and produce a bright point on a piece of photographic film.....50
Figure 2.11. Ewald sphere, representation of the conditions necessary for an observed reflection. Shows the complicated rotations required to resolve all possible reflections in the unit cell when performing single crystal diffraction. Miller indices, group of three numbers that indicates the orientation of a plane or set of parallel planes of atoms in a crystal. If each atom in the crystal is represented by a point and these points are connected by lines, the resulting lattice may be divided into a number of identical blocks, or unit cells; the intersecting edges of one of the unit cells defines a set of crystallographic axes, and the Miller indices are determined by the intersection of the plane with these axes. 52
Figure 2.12. Flow diagram for automated molecular replacement (cite from http://www.phaser.cimr.cam.ac.uk/index.php/File:Phaser_MR_auto2.png). Showing seven discrete steps that are 1) Anisotropy correction, 2) translational non-crystallographic symmetry (tNCS) correction, 3) rotation function, 4) translation function, 5) packing analysis, 6) refinement and phasing, 7) log-likelihood gain calculation.....64
Figure 3.1. example of SDS-PAGE result showing cleaved PqsBC^{C129S} on 15% SDS-PAGE gel. 81
Figure 4.1. Purification of PqsBC^{C129A} (**A)** Nickel column chromatogram. Curve of UV absorbance and the concentration of buffer B are shown. (**B**). SDS-PAGE of Nickel column fractions 9-16 shows that the protein is relatively pure. 86
Figure 4.2. Purification of PqsBC^{C129A} by Superdex 200 16/60 column (**A)** Gel filtration chromatogram showing a small peak at elution volume 50-60 ml (in yellow circle) which is an oligomer of PqsBC (explanation on chapter 8), and the heterodimer PqsBC^{C129A} peak at 80-90 ml elution volume (61 kDa). (**B**) SDS-PAGE of pooled gel filtration fractions 19-23 shows that the protein is relatively pure.....87
Figure 4.3. The initial hit of PqsBC^{C129A} crystals from a solution containing 0.2 M sodium chloride, 0.1 M Tris pH 8.5, 25% w/v polyethylene glycol 3,350. 90
Figure 4.4. The optimisation of PqsBC^{C129A} crystals produced in a precipitant solution of 0.2 M sodium chloride, 0.1 M Tris pH 8.3, 25% w/v polyethylene glycol 3350. 91
Figure 5.1. PqsBC^{C129A} crystals on 96 well within solution of 0.2 M Sodium chloride, 0.1 M Tris pH 8.5, 25% w/v Polyethylene glycol 3,350 that added 0.01 M iron (III) chloride hexahydrate. 94

Figure 5.2. Cartoon diagram of refined PqsBC^{C129A}-Fe^{3+} crystal structure. PqsC^{C129A} (green), PqsB (cyan) and Fe^{3+} are shown (red sphere).....97
Figure 5.3. Ramachandran plot of PqsBC^{C129A}-Fe^{3+} crystal structure showing residues in the most favoured regions (pink) 97.44% and additional allowed regions (yellow) 2.56% regions, generated using Coot (Emsley and Cowtan, 2004). The squares denote non-glycine residues, whereas glycine residues are denoted by triangles. 99
Figure 5.4. Cartoon diagram of refined PqsBC^{C129A}-Fe^{3+} crystal structure with space group $P4_12_12$. PqsC^{C129A} (green), PqsB (cyan) and Fe^{3+} (red sphere). Residues that involved on binding to Fe^{3+} shown by stick diagram. 100
Figure 5.5. Stick diagram of the binding site of PqsB and PqsC, a 2.3 Å electron density map is shown (grey), and the anomalous map is shown (red), rendered with Pymol showing the PqsC residue His2 as a stick in green, the PqsB residues Glu48, Glu280, and His282 as sticks in orange. 101
Figure 5.6. Cartoon diagram of structure superposition of PqsBC^{C129A}-Fe^{3+} (blue) and PqsBC^{C129A}(yellow) crystal structures. RMSD value is 1.021 aligned and calculated with PyMOL.....102
Figure 5.7. Cartoon diagram of PqsBC^{C129A}-Fe^{3+} (**A**) and PqsBC^{C129A} (**B**) quaternary crystal structures-conformation comparison. PqsC^{C129A} (green), PqsB (cyan) and Fe^{3+} (red sphere). Residues are involved on binding to Fe^{3+} shown by stick diagram. 103
Figure 5.8. Sphere (A) rendered with JyMOL and Cartoon (B) rendered with PyMOL diagram of SC1-BC interface. **A)** PqsB (blue), PqsC^{C129A} (cyan), interface area (red and green). **B)** PqsB (blue) and PqsC^{C129A} (cyan).....106
Figure 5.9. Part of PqsBC residues involved in stabilising the surface contact 1 (SC1-BC) through hydrogen interactions. **A**. Cartoon and stick diagram of SC1-BC residues that build the interface between PqsB (blue) and PqsC (cyan). **B**. Different angle of SC1-BC interface. **C**. Salt bridges on SC1-BC (dash in red), PqsB Asp116[O] – PqsC Arg137[NH]. 108
Figure 5.10. The surface contact 1 (SC1-BC) within PqsB and PqsC^{C129A}. The Molecules were rotated 90^o along X axis to show the contact surface of each monomer. The electrostatic surface representation clearly shows the charge distribution on the contact surface. The blue colour represents the positive charge and red represents the negative charge. This also clearly, show the surface is equally through hydrophobic and hydrophilic interactions.....109
Figure 5.11. Sphere (A) rendered with JyMOL and Cartoon (B) rendered with PyMOL diagram of SC2-BC interface. **A)** PqsC^{C129A} (blue), PqsC^{C129A} (cyan), interface area (red and green). **B)** PqsC^{C129A} (blue), PqsC^{C129A} (cyan), interface area is shown in stick diagram. 110
Figure 5.12. Sphere (**A**) and (**B**) rendered with JyMOL, Stick and cartoon diagram (**B**) rendered with PyMOL diagram of SC3-FeBC interface. (**A**) Interface of Fe^{3+} (red, green) with PqsB (cyan). (**B**) Interface of Fe^{3+} (red, green) with PqsC^{C129A} (cyan). (**C**) Interface that is formed by Fe^{3+} (red sphere) that binds to two nitrogen atoms of His282 (PqsB) and His2 (PqsC) along with two oxygen atoms on Glu48

(PqsB) and Glu280 (PqsB), PqsB stick and cartoon diagram in cyan and PqsC stick and cartoon diagram in green. 112
Figure 5.13. Cartoon diagram of PqsBC^{C129A}-Fe^{3+} (PqsB in cyan, PqsC in green, iron in red) symmetry generated within 4 Å**,** tetragonal crystal form (space group $P4_12_12$). 114
Figure 5.14. Surface representation of PqsBC^{C129A}-Fe^{3+} (PqsB in cyan, PqsC in green) crystallographic packing symmetry generated within 12 Å**,** tetragonal crystal form (space group $P4_12_12$). The Molecules were rotated 90^o along X axis to show the different views. 115
Figure 5.15. Cartoon and surface representation of PqsBC^{C129A} (PqsB in cyan, PqsC in green) crystallographic packing symmetry generated within 4 Å, orthorhombic crystal form (space group $P2_12_12_1$).....116
Figure 5.16. Cartoon diagram of (**A**) PqsBC^{C129A}-Fe^{3+} crystal structure with residues formed interface in stick diagram and (**B**) PqsBC^{C129A} heterodimer is shown with PqsB (green) and PqsC (cyan) covered with a transparent molecular surface illustrating the interface, interfaces reveals a large 2204.1 Å^2 surface area. 117
Figure 5.17. Sticks diagram of Fe^{3+} Interface that is formed by Fe^{3+} (red) that binds to **A**. Two nitrogen atoms of His282 (PqsB) and His2 (PqsC) along with two oxygen atoms on Glu48 (PqsB) and Glu280 (PqsB). **B**. One sulphur atom as one disulphide bond on Cys112 (2.4 Å), two nitrogen atoms of His117 (2.1 Å) and His46 (2.1 Å) along with one oxygen atoms on Glu121 (1.9 Å). **C**. Four oxygen atoms of Tyr55 (2.0 Å), Tyr185 (2.0 Å), Tyr241 (2.0 Å), Tyr242 (2.0 Å), one nitrogen atom of His54 (2.6 Å).....119
Figure 5.18. Ligplot (Wallace et al., 1995) show interactions between 3-(N-morpholino) propane-sulfonic acid (MOPS) to Asn244, Val245, and Trp279 of PqsC^{C129A}. **B.** Stick diagram of MOPS (cyan) covered by a 2.3 Å electron density map is shown (grey), rendered with Pymol showing MOPS are surrounded by PqsC^{C129A} residues Asn244, Val245, and Trp279 as sticks in green.....121
Figure 5.19. Stick diagram of four phosphate molecules (red) that inside the active site cleft covered by a 2.3 Å electron density map is shown (grey), rendered with Pymol showing phosphates molecules that interact to by PqsC residues Ser32, Arg168, Thr169, and His269 as sticks in green. 122
Figure 5.20. A. Ligplot (Wallace et al., 1995) show interactions between one of phospate ions inside PqsBC active site cleft to His269 of PqsC^{C129A}. **B**. Stick diagram of a phosphate molecule (red) covered by a 2.3 Å electron density map is shown (grey), rendered with Pymol showing the interaction one of PqsBC^{C129A} enzyme catalytic residue His269 with one of phosphate molecules that are lining up within active site pocket. With the bond length is 3.10 ÅChapter 6: Structure determination and characterisation of PqsBC^{C129A} 123
Figure 6.1. Refined PqsBC^{C129A} crystal structure with space group $P2_12_12_1$. PqsC^{C129A} (green) and PqsB (cyan). 127
Figure 6.2. Ramachandran plot of PqsBC^{C129A} crystal structure showing residues in the most favoured regions (red) 90.9%, additional allowed regions (yellow) 8.6%, generously allowed regions 0.5% (pale yellow), processed using PROCHECK

(Laskowski et al., 1993). The squares denote non-glycine residues, whereas glycine residues are denoted by triangles. 129
Figure 6.3. A, Cartoon diagram of the PqsBC^{C129A} structure as a heterodimer is shown with PqsB (blue) and PqsC (green), Cys/Ala129 and His269 in cyan are catalytic dyad. B. Cartoon diagram of PqsD which is a homodimer in magenta. 132
Figure 6.4. Cartoon diagram of the PqsBC^{C129A} structure as a heterodimer are shown with N-termini (black) and C-termini (yellow), PqsB in blue and PqsC in green. 133
Figure 6.5. Cartoon diagram of a superposition of PqsB (green) and PqsC^{C129A} (cyan). 133
Figure 6.6. Cartoon diagram of a superposition of PqsB (green) and PqsC^{C129A} (cyan), in the N-terminal subdomain. 134
Figure 6.7. Cartoon diagram of C-terminal subdomains of PqsB (155-279) in green and PqsC (188-348) in cyan, showing PqsB has a shorter sequence. 134
Figure 6.8. Stick diagrams of the catalytic site of PqsBC^{C129A} catalytic dyad, a 2.3 Å 2Fo-Fc electron density map is shown (grey) calculated using FFT, rendered with Pymol showing PqsC residues Ala129, Ala130, His 269, Gln270, Val 299, Met300 as sticks in green. 135
Figure 6.9. Stick diagrams of a superposition of PqsBC^{C129A} catalytic dyad (green) and PqsD catalytic triad (cyan). 136
Figure 6.10. Cartoon diagrams of active site volume calculated by using 3Vee (Voss and Gerstein, 2010). Calculated volume of PqsC^{C129A} active site approximately twice the volume of related FabH enzymes which may be a requirement to accommodate the aromatic substrate 2-ABA instead malonyl-ACP in case of FabH, malonyl-CoA or malonyl-ACP in PqsD. 137
Figure 6.11. Graphical representation of the PqsBC active site cleft created by using corel draw. Residues conserved with CoA binding sites of FabH/PqsD enzymes are W35 and R168. 138
Figure 6.12. Graphical representation of PqsBC^{C129A} central cavity with volume is 5034 Å^3, calculated by using 3Vee (Voss and Gerstein, 2010). 140
Figure 6.13. Cartoon diagram of PqsBC^{C129A} central cavity with volume is 5043 Å^3, **A.** Central cavity volume shown in mesh. **B.** Central cavity shown in surface. Both diagram rendered using UCSF Chimera (Pettersen et al., 2004). Central cavity volume calculated by using 3Vee (Voss and Gerstein, 2010). PqsB (cyan) and PqsC (green). 141
Figure 6.14. Sphere (A) rendered with JyMOL and Cartoon (B) rendered with PyMOL diagram of interface area between two PqsC is 902.5 Å^2. **A)** PqsC^{C129A} (blue), PqsC^{C129A} (cyan), interface area (red and green). **B)** PqsC^{C129A} (blue), PqsC^{C129A} (cyan), interface area is shown in stick diagram. 142
Figure 6.15. Alignment of the PqsC amino acid sequence with related enzymes showing the assignments of the PqsC^{C129A} structure at the top (***blue***). The catalytic residues are marked by *red triangles*. The sequences shown are PqsD (*P. aeruginosa*) and FabH (*E. coli*). 144

Figure 6.16. Cartoon diagram of the $PqsC^{C129A}$ structure is shown (*green*) superposed onto PqsD (*cyan*). Residues from PqsC shown as *sticks* in *blue* are Ala-129, His-269, Val-299, and Pro-242 (*orange*). PqsD residues Ala-112, His-257, and Asn-287 are shown as sticks (*cyan*). Showing the comparison of the $PqsC^{C129A}$ and PqsD crystal structures (PDB code 3h78), show that there are significant structural differences in the region of the active site cleft. 146
Figure 6.17. Schematic diagram of PqsBC (*cyan, green*) with the flap (PqsC residues 207–227) in *red* shown in the same orientation as the PqsD homodimer below (*green, cyan*). 147
Figure 6.18. Superposition of the PqsBC structure (*cyan, green*) with the PqsD homodimer (*grey*) illustrated as Cα-backbone representations with two views shown. 148
Figure 6.19. Superposition of β-strands for PqsB (*cyan*) and PqsD (*gray*) are shown as schematics. 149
Figure 7.1. Cartoon diagram of FabH *Escherichia coli* (magenta, cyan) (PDB code, 1hn9) as homodimeric subunit composition with the catalytic triad that is composed of Cys112, His244, and Asn274 (Qiu et al., 1999). 153
Figure 7.2. Cartoon diagram of FabH *Mycobacterium tuberculosis* (grey, magenta) (PDB code: 1hzp) as homodimeric subunit composition with the catalytic triad that is composed of Cys112, His244, and Asn274 (Scarsdale et al., 2001). 154
Figure 7.3. Cartoon diagram of FabH *Staphylococcus aureus* (red, green) a(PDB code: 1zow) as homodimeric subunit composition with the catalytic triad that is composed of Cys112, His238, and Asn268 (Qiu et al., 2005). 155
Figure 7.4. Cartoon diagram of FabH *Thermus thermophilus* (green, cyan) as homodimer (PDB code: 1ub7) (Inagaki et al., 2007). 156
Figure 7.5. Cartoon diagram of FabH *Escherichia coli* (cyan) catalytic triad that is composed of Cys112, His244, and Asn274 (Qiu et al., 1999). 156
Figure 7.6. Cartoon Proposed mechanism of the FabH reactions. **A**, schematic diagram of the acetylation reaction mechanism. Dotted lines indicate hydrogen bonds ; thick arrows indicate attack or electron transfer directions. His244 extracts a proton from Cys112, which may then attack the carbonyl of acetyl-CoA. The tetrahedral intermediate is stabilized by backbone nitrogen of Gly306 and Cys112. His244 may donate a proton at the end of acetylation to form a neutral CoA. **B**, FabH surface charge distribution viewed toward the active site cavity. The figure was calculated with the acetyl-CoA complex structure after removing the bound CoA. Red indicates negative potential, and blue indicates positive potential. The CoA molecule is shown to occupy the active site, with white for carbon atoms, blue for nitrogen, red for oxygens, yellow for phosphors, and green for the sulfur. **C**, the carboxylic acid moiety probably binds His244, whereas the carbonyl group interacts with Asn274. The decarboxylation produces a carbanion, which resonates with an enol intermediate that is stabilized by Asn274. The nucleophilic attack from the carbanion to the enzyme-bound acetyl group leads to a tetrahedral intermediate and finally yields the product acetoacetyl-ACP (Qiu et al., 1999). 158

Figure 7.7. Cartoon diagram of PqsBC^{C129A} (blue, green) as a heterodimeric subunit composition with the active site residues Ala/Cys129 along with His269 which lack of the canonical active-site asparagine (here Val299) in stick diagram (blue). 160
Figure 7.8. FabH mechanism the thiol of Cys112 is activated by the α-helix dipole effect. The acetyl-CoA forms a tetrahedral intermediate during loading onto the Cys. Decarboxylation of malonyl-ACP is assisted by the electron pushing of Phe205, and the charge formed on the thioester carbonyl is stabilized by Nε of His244 and Nδ of Asn274. A carbanion then forms on C2 of the substrate, and the nucleophile attacks the C1 of the acetate on the Cys. A tetrahedral intermediate is stabilized by the oxyanion hole formed by the backbone amides of Cys112 and Gly306. Breakdown of the intermediate releases product, acetoacetyl-ACP, from the enzyme (Heath and Rock, 2002). 162
Figure 7.9. The Biosynthetic pathway of PQS by PqsABCDEH operon. In the initial step, the acyl moiety of an activated carboxylic acid is transferred to a strictly conserved active-site cysteine residue. Subsequently, a β-ketoalkanoic acid (malonyl-ACP in the case of FabH, malonyl-CoA or malonyl-ACP in PqsD, 2-ABA in PqsBC) is decarboxylated. Intermediates and products of the alkyl quinolone biosynthetic pathway: Ant-CoA − anthranilate-coenzyme A, 2-ABA-CoA − 2-aminobenzoylacetyl-CoA, 2-ABA – 2-aminobenzoylacetate, HHQ –2-heptyl-4-hydroxyquinoline, PQS – *Pseudomonas* quinolone signal.....163
Figure 7.10. PqsBC^{C129A}-2ABA (1:1) crystals on 24-well sitting drop within solution of 0.2 M Sodium chloride, 0.1 M Tris pH 8.5, 25% w/v Polyethylene glycol 3,350. 165
Figure 7.11. PqsBC^{C129A}-Fe^{3+}-2ABA (1:1) crystals on 24-well sitting drop within solution of 0.2 M Sodium chloride, 0.1 M Tris pH 8.5, 25% w/v Polyethylene glycol 3,350 that added 0.1 M iron (III) chloride hexahydrate. 165
Figure 7.12. Part of PqsBC^{C129A} showing the possibility 2-ABA electron density site, showing catalytic diad residues which are His269 and Cys129. Yellow oval circle showing the 2-ABA possibility site (opened on WinCoot displays maps and models). 166
Figure 7.13. Alignment of cartoon and line diagram of Cys112 (*cyan* stick diagram) on FabH *Escherichia coli* and Cys/Ala129 (*green* stick diagram) on PqsBC^{C129A} and α-helix dipole effect cysteine which is positioned at the amino terminal end helix Cα, where the microenvironment of the pH is affected by the α-helix dipole effect to reduce the pKa of the Cys112 by 1.6 pH units (Kortemme and Creighton, 1995, Heath and Rock, 2002). 167
Figure 7.14. Cartoon diagrams of active site volume calculated by using 3Vee (Voss and Gerstein, 2010). Calculated volume of PqsC^{C129A} active site approximately twice the volume of related FabH enzymes which may be a requirement to accommodate the aromatic substrate 2-ABA instead malonyl-ACP in case of FabH.....168
Figure 7.15. Line and surface diagram of FabH *E. coli* active site pocket (*cyan*) (PDB code, 1hn9), stick diagram of catalytic triad residues (*cyan*) Cys112, His244, and Asn274, with Phe87 (*magenta*) residue from another monomer. **A.** a whole FabH *E. coli* active site pocket (*cyan*) with different angle. **B**. active site pocket of FabH *E.*

coli shows in green mesh rendered by using 3Vee (Voss and Gerstein, 2010). **C**. focus on Phe87 (*magenta*) residue from another monomer which involved on active site pocket construction. 170
Figure 7.16. Line and surface diagram of FabH *Staphylococcus aureus* active site pocket (*green*) (PDB code: 1zow), stick diagram of catalytic triad residues (*green*) Cys112, His244, and Asn274, with Phe87 (*cyan*) residue from another monomer. **A**. a whole FabH *Escherichia coli* active site pocket (*green*) with different angle. **B**. active site pocket of FabH *S. aureus* shows in green mesh rendered by using 3Vee (Voss and Gerstein, 2010). **C**. focus on Phe87 (*cyan*) residue from another monomer which involved on active site pocket construction. 171
Figure 7.17. Line and surface diagram of FabH *Mycobacterium tuberculosis* active site pocket (*magenta*) (PDB code: 1hzp), stick diagram of catalytic triad residues (*magenta*) Cys112, His244, and Asn274, with Gln86, Thr87, Ile196 (*grey*) residues from another monomer. A) a whole FabH *Escherichia coli* active site pocket (*magenta*) with different angle. B) focus on Gln86, Thr87, Ile196 (*grey*) residue from another monomer which involved on active site pocket construction. 172
Figure 7.18. Line and surface diagram of $PqsBC^{C129A}$ active site pocket (*green, magenta*), stick diagram of catalytic diad residues (*cyan*) Ala/Cys129, His269. A) angle that shows PqsB (*magenta*) and PqsC (*green*) sharing the active site pocket construction. B) opening of active site pocket which is located on PqsC. 173
Figure 7.19. Line, surface and mesh diagrams of PqsBC active site pocket (PqsB in *magenta*, PqsC in *green*, Ala/Cys129 and His269 in *cyan* stick diagram). The figure shows two branching-channel of PqsBC active site pocket as well as the possibilities direction way in and way out (*yellow arrow*). Mesh diagram of active site pocket rendered using MetaPocket (Huang, 2009). 175
Figure 7.20. Line and surface diagram of PqsBC active site pocket (PqsB in *magenta*, PqsC in *green*, Ala/Cys129 and His269 in *cyan* stick diagram). The first/smaller (**1**) channel seems may a place for the initial step, the acyl moiety of an activated carboxylic acid is transferred to a strictly conserved active-site cysteine residue. Subsequently, the second/bigger (**2**) channel is the place for β-ketoalkanoic acid, 2-ABA in PqsBC is decarboxylated due to it will need bigger space for aromatic substrate 2-ABA. 176
Figure 8.1. (**A**)**.** Cartoon diagram of $PqsBC^{C129A}$ (**A**), surface diagram (**B**), and schematic (**C**) crystal structure as heterotetrameric conformation. $PqsC^{C129A}$ (green) and PqsB (cyan). It can be seen that four of PqsC assembling on the centre that also forming four interfaces between them. 180
Figure 8.2. Sphere (**A**) rendered with JyMOL and Cartoon (**B**) rendered with PyMOL. Diagram of two of pqsC interface. **A)** Sphere diagram of PqsC (blue), PqsC (cyan), interface area (red and green). **B)** Cartoon diagram **of** PqsC (blue) and PqsC (cyan) rotate 180^0, residues that involved making interface are in sticks. 181
Figure 8.3. A. Cartoon diagram of two Leu229 (green and cyan stick) interaction within two subunit PqsC **B.** Ligplot (Wallace et al., 1995) show interactions between two Leu229 within different subunit $PqsBC^{C129A}$. 183

Figure 8.4. Model of cartoon diagram of two Cys229 (yellow and blue sticks) interaction within two subunit PqsBC^{L229C} to form disulphide bond. 184
Figure 8.5. Purification of PqsBC^{L229C} (**A)** Nickel column chromatogram. Curve of UV absorbance and the concentration of buffer B contains 500 mM imidazole which gradiently increase are shown. (**B**). SDS-PAGE of pooled Nickel column fractions 60-75 shows that the protein is relatively pure. 185
Figure 8.6. Purification of PqsBC^{L229C} (**A)** Gel filtration chromatogram showing another peak at retention time 59.2 minutes or elution volume 51.79 ml (490 kDa), beside the normal peak that used to appear at retention time 102.3 minutes or 80.81 ml elution volume (61 kDa) for a normal heterodimer PqsBC. (**B**) SDS-PAGE of Gel filtration fractions number 7 and 8 from the first peak and number 19 from the second peak. The yellow oval circle indicates the PqsBC^{L229C} oligomer that is too big to pass through 15% SDS-PAGE gel. Bands from fraction no 7 and 8 only visible in the presence of a reducing agent on (**C**). 186
Figure 8.7. ICC-1 interface, sphere (**A**) rendered with JyMOL and cartoon (**B**) rendered with PyMOL. Diagram of two of pqsC interface. **A)** Sphere diagram of PqsC (blue), PqsC (cyan), interface area (red and green). **B)** Cartoon diagram **of** PqsC (blue) and PqsC (cyan) rotate 180^0, residues that involved making interface are in sticks. 189
Figure 8.8. ICC-2 interface, sphere (**A**) rendered with JyMOL and cartoon (**B**) rendered with PyMOL. Diagram of two of pqsC interface. **A)** Sphere diagram of PqsC (blue), PqsC (cyan), interface area (red and green). **B)** Cartoon diagram **of** PqsC (blue) and PqsC (cyan), residues that involved making interface are in yellow sticks. 191
Figure 8.9. ICC-3 interface, sphere (**A**) rendered with JyMOL and cartoon (**B**) rendered with PyMOL. Diagram of two of pqsC interface. **A)** Sphere diagram of PqsC (blue), PqsC (cyan), interface area (red and green). **B)** Cartoon diagram **of** PqsC (blue) and PqsC (cyan), residues that involved making interface are in yellow sticks. 193
Figure 9.1. Cartoons and sticks diagram of the PqsBC^{C129A}-Fe^{3+} structure shows part of PqsB (cyan) and pqsC^{C129A} (green) that binding with iron which is seen may affect cysteine role as a nucleophile in the initial acylation step, a 2.3 Å electron density map is shown (grey). 200

List of tables

Table 3.1. The ligands of PqsBC enzymes used in this research.....72
Table 3.2. PCR protocol.....74
Table 3.3. Constituents used for making four of 15% SDS-PAGE gels.....81
Table 5.1. Data collection of $PqsBC^{C129A}$-Fe^{3+}.....95
Table 5.2. Refinement statistics of $PqsBC^{C129A}$-Fe^{3+}.....98
Table 5.3. PISA interfaces list. Interfaces in $PqsBC^{C129A}$-Fe^{3+} crystal.....104
Table 5.4. Hydrogen bonds and salt bridges of interfacial contact 1 (SC1-BC) 107
Table 5.5. Hydrogen bonds of surface contact 2 (SC2-CC) 111
Table 6.1. Data collection of $PqsBC^{C129A}$.....125
Table 6.2. Refinement statistics of $PqsBC^{C129A}$.....128
Table 6.3. Conservation mapping of $PqsBC^{C129A}$ crystal structure.....131
Table 6.4. Hydrogen bonds and salt bridges of surface contact between two PqsC. 143
Table 8.1. Hydrogen bonds and salt bridges of PqsC interface.....182
Table 8.2. Cloning of $PqsBC^{L229C}$ *Eschericia coli* expression constructs. 184
Table 8.3. Hydrogen bonds and salt bridges of PqsC ICC-1 interface.....190
Table 8.4. Hydrogen bonds and salt bridges of PqsC ICC-2 interface.....192
Table 8.5. Hydrogen bonds and salt bridges of PqsC ICC-3 interface.....194

Abbreviations

QS: quorum sensing

2-AA: 2-aminoacetophenone

2-ABA: 2-aminobenzoylacetate

2-ABA-CoA: 2-aminobenzoylacetyl-CoA

AQ: 2-alkyl-4(1H)-quinolone

BA: benzoylacetate

CV: column volume

DHQ: 2,4-dihydroxyquinoline

HHQ: 2-heptyl-4(1H)-quinolone

PQS: Pseudomonas quinolone signal

TEV: tobacco etch virus

PDB: Protein Data Bank

ACP: acyl carrier protein.

Chapter 1: Introduction

1.1 Introduction

Pseudomonas aeruginosa is an opportunistic bacteria that infects immunocompromised people, and which is especially prevalent in patients with cystic fibrosis. In order to initiate and coordinate an infection in the host, this aerobic bacterium uses quorum sensing (QS) to communicate (Whiteley et al., 1999).

Quorum sensing (QS) was first identified in the early 1970s in two luminous marine bacterial species, *Vibrio fischeri* and *Vibrio harveyi* that are present in the light organ of the Hawaiian squid *Euprymna scolopes*. Although, at that time it was not described as QS, only the observation of the phenomenon of light emission that begin during the middle of the logarithmic growth phase of *V. fischeri* and *V. harveyi* (Nealson et al., 1970, Nealson and Hastings, 1979). In 1994, Fuqua et al. introduced the term QS, which is found in various microbial organisms such as *V. fischeri*, *V. harveyi*, *Agrobacterium tumefaciens*, *P. aeruginosa* and *Erwinia carotovora* (Fuqua et al., 1994).

QS is the regulation of gene expression as a response to fluctuation in cell density. QS communication circuits are employed by both Gram-positive and Gram-negative bacteria for regulating a range of physiological activities (Miller and Bassler, 2001). The behaviour of bacterial cell communication depends on population density and is based on the synthesis of and response to small molecules known as autoinducers (Sifri, 2008). Meanwhile, autoinduction describes a system of

environmental sensing that enables bacteria to monitor their population density (Fuqua et al., 1994).

A recent article by Lee and Zhang (2015) described four interconnected QS systems in *P. aeruginosa* (*las*, *rhl*, *pqs* and *iqs*), which are responisble for the biosynthesis of the three classes of autoinducers: acylated homoserine lactones (AHLs), 4-hydroxy-2-alkylquinolines (HAQs), and integrated QS signal (IQS; 2-(2-hydroxyphenyl)-thiazole-4- carbaldehyde). The *las* and *rhl* systems utilise AHLs, the *pqs* system utilises HAQs and the *iqs* system ultilises IQS.

PqsBC is an enzyme which involve in *pqs* system. PqsBC catalyses the condensation of octanoyl-coenzyme A and 2-aminobenzoylacetate (2-ABA) to form the signal molecule 2-heptyl-4(1*H*)-quinolone (HHQ) (Drees et al., 2016, Dulcey et al., 2013). HHQ is a precursor of *pqs* system autoinducer which is PQS. HHQ itself was discovered to function as an autoinducer molecule per se (Diggle et al., 2007).

Bacterial cell of *P. aeruginosa* both take up and release HHQ, which is later converted to PQS (Deziel et al., 2004). Subsequently, HHQ is observed also as an intercellular signal as it is secreted by *P. aeruginosa* and the concentration of HHQ decreases whilst PQS production but increases whilst growth phase (Deziel et al., 2004). Whereas, PQS is an extracellular messenger that involves in QS systems in *P. aeruginosa* (Deziel et al., 2004).

HHQ and PQS are obtained in CF patients which is in the lung (Machan et al., 1992, Guina et al., 2003). Moreover, PqsR and *pqsH* mutants show decreasing virulence in the mouse infection (Gallagher and Manoil, 2001, Deziel et al., 2005, Venturi, 2006). Furthermore, role of PQS in pathogenesis is significant as it influences some virulence elements (Pesci et al., 1999, Calfee et al., 2001, Diggle et al., 2003, Deziel et al., 2004, Deziel et al., 2005, Venturi, 2006). Therefore, these signals are excellent target for solving antibiotic resistance and as target of drug development of anti-virulence.

1.2 *Pseudomonas aeruginosa*

Pseudomonas aeruginosa is a rod-shaped strict aerobe mostly found in soil and water and sometimes in plants and animals (Todar, 2012). It was discovered in 1882 by Carle Gessard, a chemist and bacteriologist. This ubiquitous γ-proteobacterium is very opportunistic, and may cause infections that often lead to hospitalisation and can often be life-threatening (Silhavy, 2010). As an opportunistic pathogenic bacterium, *P. aeruginosa* is able to cause urinary tract infections, respiratory system infections, bacteraemia, and a variety of systemic infections, particularly when the host's immune system is weak (Todar, 2012). In 2000, the PAO1 strain was the first to have its genome completely sequenced. At 6.3 million base pairs in size, it is larger than most prokaryotes and is close to the size of lower eukaryote genomes (Stover et al., 2000, Rehm, 2008).

The *Pseudomonas* genus covers one of the most diverse and ecologically significant groups of bacteria. Members of the genus are found in huge numbers in a wide range of environmental niches, such as terrestrial and marine environments, as well as in association with plants and animals (Rehm, 2008). *P. aeruginosa* is different from other members of the *Pseudomonas* genus because of its potential pathogenicity for human beings and other mammals. *P. aeruginosa* engages in infection in immunocompromised patients, like patients suffering from AIDS, cancer, burn wounds and cystic fibrosis (CF) (Rehm, 2008, Willenbrock et al., 2006, Willenbrock and Ussery, 2007, Lyczak et al., 2000). The versatility of *P. aeruginosa* is shown by its capability to grow at a wide range of temperatures and for tolerating conditions of low oxygen (Van Delden and Iglewski, 1998, Van Delden, 2004).

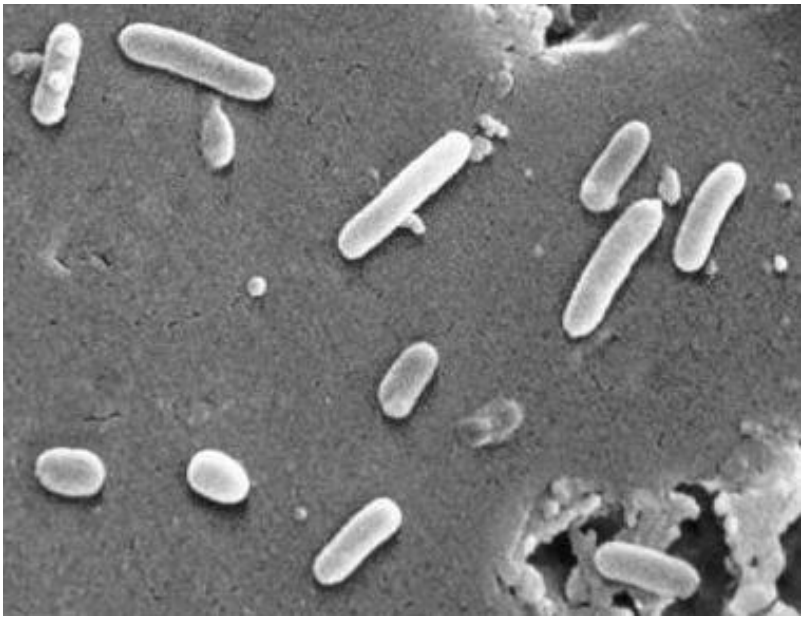


Figure 1.1. *P. aeruginosa.* Imaged using scanning electron microscope (Kenneth Todar, 2012).

Respiration is the main energy producing system of *P. aeruginosa* by utilising a proton-motive force for ATP synthesis (Arai, 2011). Alternatively, *P. aeruginosa* is able to grow under anaerobic conditions when nitrite or nitrate is present, by using nitrogen oxides as terminal electron acceptors (Zumft, 1997). *P. aeruginosa* moves in aqueous environments by using three types of motility: type IV pilus-mediated twitching (Bradley, 1980), type IV pilus-mediated swarming (Rashid and Kornberg, 2000), and flagellum-mediated swimming (Rashid and Kornberg, 2000).

1.3 Quorum Sensing in Pseudomonas aeruginosa

1.3.1 Quorum sensing an overview

Quorum sensing (QS) was first identified in the early 1970s in two luminous marine bacterial species, *Vibrio fischeri* and *Vibrio harveyi* that are present in the light organ of the Hawaiian squid *Euprymna scolopes*. Although, at that time it was not described as QS, only the observation of the phenomenon of light emission that begin during the middle of the logarithmic growth phase of *V. fischeri* and *V. harveyi* (Nealson et al., 1970, Nealson and Hastings, 1979). In 1994, Fuqua et al. introduced the term QS, which is found in various microbial organisms such as *V. fischeri*, *V. harveyi*, *Agrobacterium tumefaciens*, *P. aeruginosa* and *Erwinia carotovora* (Fuqua et al., 1994). QS is an extension of the concept from *luxI-luxR* system in *V. fischeri* that is observed in the light organ of *E. scolopes*. *P. aeruginosa* possesses two sets homologs of LuxI/LuxR circuits, which are LasI/LasR and RhlI/RhlR circuits (Gambello and Iglewski, 1991, Ochsner et al., 1994).

QS is the process whereby bacteria regulate and coordinate global gene expression for the benefit of the whole bacterial population, it is mediated by low molecular weight signals called autoinducers (Miller and Bassler, 2001). The behaviour of bacterial cell communication depends on population density and is caused by synthesis of and response to autoinducers (Sifri, 2008). Autoinduction describes a system of environmental sensing that enables bacteria to monitor their population density (Fuqua et al., 1994). QS communication circuits are employed by both Gram-positive and Gram-negative bacteria for regulating a range of physiological activities (Miller and Bassler, 2001).

In a low population density of bacteria, the autoinducer concentration is not sufficient to activate global gene expression. However, at a high population density of bacteria the autoinducer passes the limit of the threshold to saturate or activate the receptor (Nealson et al., 1970, Waters and Bassler, 2005). Furthermore, when the autoinducer reaches a sufficient concentration, transcription of genes involved in virulence factor production, biofilm formation, sporulation, antibiotic production and motility will initiate. This subsequently improves the bacterial defence against prokaryote and eukaryote defence mechanisms, and enhances its ability to access environmental niches (Venturi, 2006).

1.3.2 The four interconnected QS in *P. aeruginosa*

A recent article by Lee and Zhang (2015) described four interconnected QS systems in *P. aeruginosa* (*las*, *rhl*, *pqs* and *iqs*), which are responisble for the biosynthesis of the three classes of autoinducers: acylated homoserine lactones (AHLs), 4-hydroxy-2-alkylquinolines (HAQs), and integrated QS signal (IQS; 2-(2-hydroxyphenyl)-thiazole-4- carbaldehyde). The *las* and *rhl* systems utilise AHLs, the *pqs* system utilises HAQs and the *iqs* system ultilises IQS.

Each of the four QS systems (*las*, *rhl*, *pqs*, *iqs*) possesses a specific autoinducer synthase: LasI, RhlI, PqsABCDH and AmbBCDE, respectively (**Figure 1.2**) (Pesci et al., 1997, Calfee et al., 2001, Fuqua et al., 2001, Miller and Bassler, 2001, Lee and Zhang, 2015, Papenfort and Bassler, 2016a). LasI catalyses the production of N-(3-oxododecanoyl)-HSL (OdDHL), RhlI catalyses the production of N-butyryl-HSL (C4-HSL), PqsABCDH catalyses the production of 2-heptyl-3-hydroxy-4-quinolone (PQS) and AmbBCDE catalyses the production of IQS (Pesci et al., 1997, Calfee et al., 2001, Fuqua et al., 2001, Miller and Bassler, 2001, Lee and Zhang, 2015, Papenfort and Bassler, 2016a). These four autoinducers are recognised by the receptors LasR, RhlR and PqsR that act as transcription regulators in *las*, *rhl*, and *pqs* QS systems. However, currently the cytoplasmic transcription factor is currently unidentified (Pesci et al., 1997, Calfee et al., 2001, Fuqua et al., 2001, Miller and Bassler, 2001, Lee and Zhang, 2015, Papenfort and Bassler, 2016a).

All four systems are highly intertwined. To ensure proper functioning of the QS systems, they are all orchestrated with higher-level regulation. The *las* system regulates both *rhl* and *pqs* systems under rich-medium growth conditions, which interconnects the *las, rhl, and pqs* systems. In addition, the *rhl* system is controlled by both the *las* and *pqs* systems, although some virulence factors of QS dependent are triggered by RhlR- *N*-butyryl-homoserine lactone (C4-HSL) (Latifi et al., 1995, Whiteley et al., 1999, Winzer et al., 2000, Schuster et al., 2004). The *iqs* system is the most recently identified and lesser understood system, and is involved in cell-to-cell communication in response to stress and phosphate limitation (Lee et al., 2013). During phosphate depletion the *iqs* system may supercede the *las* system and subsequently activate QS networks and virulence gene expression (Jensen et al., 2006, Dekimpe and Deziel, 2009, Lee et al., 2013). Also, IQS biosynthesis is also tightly controlled by LasR and LasI in rich medium environments, since interference of *lasR* or *lasI* genes leads to abolishment of IQS production through reduced expression of *ambBCDE* (Lee et al., 2013).

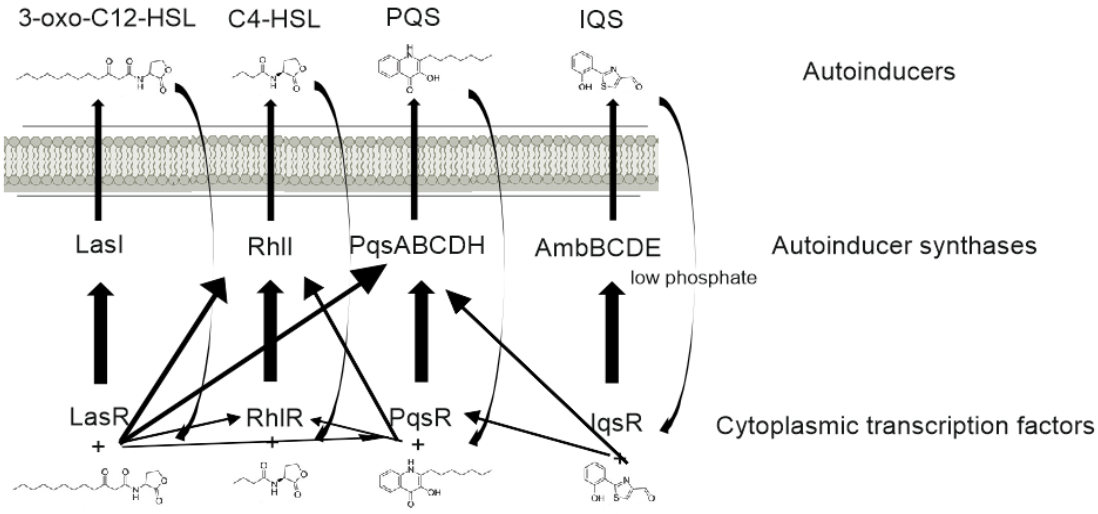


Figure 1.2. Quorum sensing networks in *Pseudomonas aeruginosa*, arrows indicate a stimulatory effect. PQS is connected to the AHL QS system as *las* system controls PQS synthesis. Subsequently, it is affecting the *rhl* system as a link between *las* and *rhl* systems (adapted from (Papenfort and Bassler, 2016b).

1.3.3 PQS: a signal molecule providing a regulatory link between the Las and Rhl systems

Pseudomonas quinolone signal (2-heptyl-3-hydroxy-4-quinolone, PQS) is a signalling molecule. It is synthesised by *P. aeruginosa*. PQS is classified in alkyl-4 quinolone (AQ) family. This compound family was described in 1940s, regarding to its antibacterial activities (Edwin E. Hays, 1945). Bioactivity and synthesis of PQS were also regulated by *las* and *rhl* QS systems (Pesci et al., 1999). Anthranilic acid is a precursor of chorismate which is a substrate of anthranilate by using anthranilate synthase (Cao et al., 2001, Deziel et al., 2004). Whereby, *phnAB* operon encodes the

anthranilate synthase (Cao et al., 2001, Gallagher et al., 2002, Deziel et al., 2004, Venturi, 2006). Subsequently, PqsABCDE enzymes converts anthranilate to HHQ, which is precursor of PQS (Coleman et al., 2008, Zhang et al., 2008, Dulcey et al., 2013, Drees and Fetzner, 2015). As can be seen in **Figure 1.2**, PQS is connected to the AHL QS system as *las* system controls PQS synthesis. Subsequently, it is affect the *rhl* system as a link between *las* and *rhl* systems (Venturi, 2006).

1.4 *Pseudomonas aeruginosa* virulence factors related to QS

QS in *P. aeruginosa* controls the secretion of virulence factors and biofilm formation (Brint and Ohman, 1995, Pearson et al., 1997, Van Delden and Iglewski, 1998, Van Delden, 2004, Ng and Bassler, 2009, Williams and Camara, 2009). *P. aeruginosa* is able to produce a range of virulence factors, such as proteases, flagella, type IV pili, pyocyanin, siderophores (pyoverdine and pyochelin), exotoxin A, exopolysaccharides (biofilm formation), etc. The majority of extracellular virulence factors are regulated by QS signals (**Figure 1.3**) (Brint and Ohman, 1995, Pearson et al., 1997).

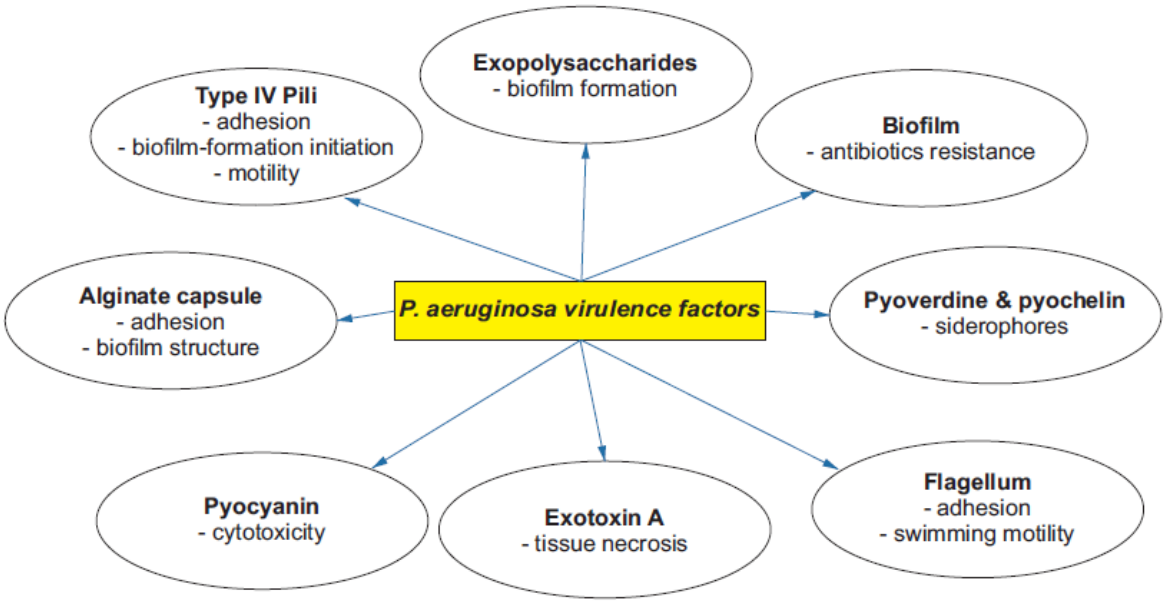


Figure 1.3. Virulence factors of *P. aeruginosa* related to QS that are employed during infections

Virulence is a degree of the ability to generate disease in a host organism or pathogenicity of the microbe. Virulence factors have an important role in colonisation, tissue invasion and bacterial survival. There are two types of *P. aeruginosa* virulence factors: those involved in acute infection and those involved in chronic infection.

The acute type virulence factors are either secreted or on the surface of *P. aeruginosa* and include: pili that enable adherence on epithelium; exoenzyme S and other adhesins that allow adherence to epithelial cells; phospholipase C, which is a thermolabile haemolysin; and exotoxin A, which is responsible for host tissue necrosis. At least four proteases produced by *P. aeruginosa* cause tissue necrosis and bleeding.

Exoenzyme S is the cause of cytoskeletal-organisation disruption, the destruction of immunoglobulin A and G, cause depolymerisation of actin filaments and assist in resistance to macrophages.

The chronic type virulence factors include siderophores (pyochelin and pyoverdine) that enable bacteria to multiply in the absence of ferrous ions. Isolated strains from cystic fibrosis patients possess an alginate pseudocapsule that protects the bacterium from phagocytosis, antibiotics and dehydration. Subsequently, it also improves the adherence to epithelial cells, forming a biofilm (Ben Haj Khalifa et al., 2011). In short, virulence factors produced by *P. aeruginosa* are type IV pili, flagella, lipopolysaccharides, proteases, siderophores, exopolysaccharides and type III secretion (Kiil et al., 2008). In addition, *P. aeruginosa* virulence factors can induce integrated stress reactions and unfolded proteins in airway epithelial cells (van 't Wout et al., 2015).

1.4.1 *P. aeruginosa* adherence to mucosal surfaces

Attachment or adherence of bacteria requires two factors: a receptor and a ligand (Kenneth Todar, 2012). In terms of bacterial adherence, the receptor is defined as peptides or specific carbohydrates on the cell surface of eukaryotic cells (Kenneth Todar, 2012). The bacterial ligand, which also known as adhesin is a macromolecular compound of the bacterial cell surface that interacts with the host cell receptor (Kenneth Todar, 2012). *P. aeruginosa* employs a range of bacterial ligands or adhesin

to attach to both abiotic or biotic surfaces, such as pili (Woods et al., 1980, Doig et al., 1988), flagella (Arora et al., 1998, Lillehoj et al., 2002), the alginate capsule (Doig et al., 1987), or outer membrane proteins (Carnoy et al., 1994).

1.4.1.1 Type IV pili

P. aeruginosa has retractable type IV pili, in which one subunit commonly contains methylated phenylalanine around its amino terminus. These N-methylphenylalanine pili have a role in adhesion to various cell types and are important in attachment to specific tissues, biofilm-formation initiation and non-opsonic phagocytosis (Alhazmi, 2015, Barken et al., 2008, Mahenthiralingam and Speert, 1995, Punsalang and Sawyer, 1973). Pili of *P. aeruginosa* interact with host epithelial cell membranes that contain glycosphingolipid (ganglio-N-tetraosylceramide/asialo-GM1) (Comolli et al., 1999). In addition to adhesion, type IV pili of *P. aeruginosa* have a role in twitching motility (Bradley, 1980).

1.4.1.2 Flagellum

P. aeruginosa possesses an unsheathed polar flagellum of approximately 4.5 µm, which enables movement through a liquid environment of low viscosity, known as swimming motility (Kohler et al., 2000). The absence of the flagellum in a *P. aeruginosa* isogenic mutant in a burned mouse model exhibits no virulence, hence the flagellum itself is therefore associated with virulence (Montie et al., 1982).

1.4.1.3 Alginate capsule

A mucoid exopolysaccharide capsule is synthesised by *P. aeruginosa*, and is composed of alginate, an an acetylated random co-polymer of β 1-4 linked D-mannuronic acid (poly-M) and L-guluronic acid (Gacesa and Wusteman, 1990). In the lungs of cystic fibrosis patients, overproduction of alginate was observed, which indicates the alginate capsule is responsible for adherence within the cystic fibrosis lung, and also believed to be involved in host defence resistance by decreasing phagocytosis sensitivity (Pier et al., 2001). Cystic fibrosis patients that carried non-mucoid *P. aeruginosa* exhibited significantly better lung function compared the patients carried mucoid *P. aeruginosa* (Parad et al., 1999).

1.4.2 Pyoverdine and pyochelin

Similar to most organisms, *P. aeruginosa* requires iron to maintain cellular processes, such as amino acid and nucleoside synthesis, and respiration (Cornelis and Dingemans, 2013). Four different iron uptake methods are employed by *P. aeruginosa:* production of extracellular Fe^{3+}-chelating siderophores (pyoverdine and pyochelin), uptake of xenosiderophores, heme uptake from the host hemoproteins, and Fe^{3+} to Fe^{2+} reduction through the FeO system. The strategy of iron uptake is dependent on acute or chronic infection (Cornelis and Dingemans, 2013).

Siderophores are low-molecular weight, high affinity iron chelators that characteristically chelate Fe^{3+}, and are taken up by specific receptors, determined by

the trans-periplasmic protein TonB (Braun and Killmann, 1999, Schalk et al., 2012, Cornelis and Dingemans, 2013). *P. aeruginosa* produces two siderophores: pyoverdine and pyocheline, which are different in both structure and their affinity for iron. Pyoverdines are high affinity siderophores employed in acute infection and *P. aeruginosa* pyoverdine is comprises a chromophore covalently linked with a peptide chain (Meyer, 2000, Ravel and Cornelis, 2003, Cornelis and Dingemans, 2013). *P. aeruginosa* pyochelin, however, is a low affinity siderophore consisting of a 354 Da small molecule (Cox et al., 1981, Brandel et al., 2012, Cornelis and Dingemans, 2013).

1.4.3 Pyocyanin

P. aeruginosa produces a secondary metabolite, known as pyocyanin (PCN), and is found in high quantities in the sputum of patients with *P. aeruginosa* cystic fibrosis (Lau et al., 2004). Regulation of pyocyanin (PCN) is achieved by QS and allows bacteria to regulate virulence gene expression (Fuqua et al., 2001). These low molecular weight signal molecules, N-butyryl-1-homoserine lactone (PAI-2) and N-(3-oxododecanoyl)-L-homoserine lactone (PAI-1), are generated by the *rhlI* and *lasI* gene products, respectively (Lau et al., 2004).

In vitro experiments show that the *P. aeruginosa* persistence in the CF patients' lung and cellular damage is associated with pyocyanin (Lau et al., 2004). Several studies have demonstrated that pyocyanin is able to cause damage to human cells, including disruption of calcium homeostasis (Denning et al., 1998), epidermal

cell growth (Sorensen and Klinger, 1987), and affect ciliary function. Pyocyanin also induces neutrophil apoptosis in pyocyanin concentrations, related physiologically from the sputum of CF patients (Usher et al., 2002).

1.4.4 Biofilms

Biofilms of *P. aeruginosa* are a community enveloped in an environment of extracellular polymeric substances (EPS) (Rodney, 2002, Karatan and Watnick, 2009, Rasamiravaka et al., 2015). There are five stages of *P. aeruginosa* biofilm formation; (1) translocation to a surface and reversible cell attachment, (2) irreversible attachment, (Coleman et al.) formation of a microcolony, (4) biofilm maturation and differentiation and (5) single cell dispersal from the biofilm (McDougald et al., 2008). Also, a number of factors are also required for biofilm formation such as adherence to mucosal surfaces, aggregation of cells via proteins, cell motility, polysaccharides and extracellular DNA (Ghannoum and O'Toole, 2004, Kjelleberg and Givskov, 2007).

Biofilms are also known as a city of microbes and EPS comprises 85% of the total biofilm biomass (Watnick and Kolter, 2000, Nikolaev and Plakunov, 2007). In addition, EPS itself consists of extracellular DNA (eDNA), polypeptides, and exopolysaccharides that act as architecture and structural scaffolding for the biofilm (Sutherland, 2001, Branda et al., 2005, Flemming and Wingender, 2010). *P. aeruginosa* that has developed a biofilm is more resistant to antibiotics or

antimicrobials than free-living bacteria. Biofilm formation is regulated by the bacteria, and is controlled by QS (McDougald et al., 2008).

1.5 AHL- and AQ-dependent QS

P. aeruginosa produces two molecules of AHL, which are *N*-3-oxo-dodecanoyl-*L*-homoserine lactone (3O-C_{12}-HSL) and *N*-butyryl-*L*-homoserine lactone (C_4-HSL) **(Figure 1.4),** which directly or indirectly control the expression of multiple virulence factors, secondary metabolites, swarming motility and biofilm development (Wagner and Iglewski, 2008, Williams and Camara, 2009).

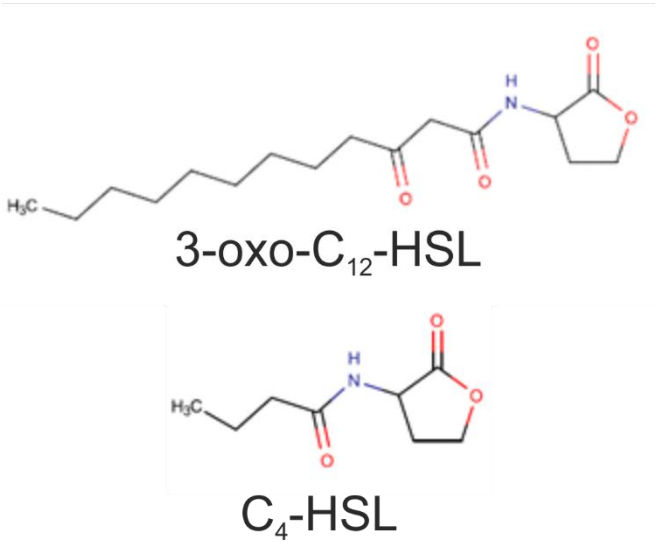


Figure 1.4. Structures of N-acyl homoserine lactones (AHLs) used as signals by *P. aeruginosa*. *N*-3-oxo-dodecanoyl-*L*-homoserine lactone N-(3-oxododecanoyl)-HSL and N-butyryl-HSL (C4-HSL).

In addition to AHL-based QS systems, *P. aeruginosa* also utilises the signal, 2-heptyl-3-hydroxy quinolone, known as *Pseudomonas* quinolone signal (PQS). Separation and characterisation of PQS was first achieved in 1999; it was discovered that extracts of used culture medium from wild type *P. aeruginosa* PAO1 that was added to strain PAO-R1 or *lasR*$^{-}$ mutant of *P. aeruginosa* induced *lasB'-lacZ* (Pesci et al., 1999). This kind of induction could not be imitated by the addition of N-(3-oxododecanoyl)-HSL and N-butyryl-HSL (C4-HSL), which means there was an unidentified third autoinducer present in used culture media extract of strain PAO1 (Pesci et al., 1999).

1.6 PqsA, PqsB, PqsC, PqsD, and PqsE and PQS biosynthesis

The alkyl quinolones in *P. aeruginosa* are derived via the condensation of anthranilate and β-keto fatty acid (Cornforth and James, 1956). Anthranilate is converted into the intermediate precursor of PQS, HHQ by the proteins PqsA, PqsB, PqsC, and PqsD (Calfee et al., 2001, Coleman et al., 2008, Zhang et al., 2008, Dulcey et al., 2013, Drees and Fetzner, 2015). HHQ can then be passed between cells and converted intracellularly into PQS through the action of PqsH (Gallagher et al., 2002). Quinolone synthesis in *P. aeruginosa* requires multiple genes, which were initially identified by screening transposon mutant libraries for clones displaying reduced pyocyanin production, and were denoted as *pqsABCDE, pqsR (MfvR), pqsH and pqsL*. The *pqsABCDE* genes are arranged in an operon, and adjacent to these are the anthranilate synthase genes *phnAB* and *pqsR* (Gallagher et al., 2002). Two other genes,

pqsH and *pqsL* are also involved in alkyl-quinolone synthesis, but both are located separately elsewhere on the chromosome.

The autoinducer synthase of PQS consists of *phnAB, pqsH* and *pqsABCD* (Gallagher et al., 2002). Anthranilate is produced using a tryptophan pathway intermediate, by specific alkyl-quinolone anthranilate synthase, which is encoded by *phnAB*. PqsA is involved in the activation of anthranilate, whereas PqsB and PqsC are similar to β-keto-acyl-acyl carrier protein synthases, which are involved in fatty acid metabolism and thus in the elongation of the acyl side chains of the quinolones (Diggle et al., 2003, Deziel et al., 2004). A recent study by Dulcey et al in 2013, suggests that there are two circuits for HAQ biosynthesis that also involves the enzymes of PqsABCD. First, synthesis of 2-aminobenzoylacetate (2-ABA) is achieved by condensation of malonyl-CoA together with anthraniloyl-CoA, mediated by PqsD. Moreover, HHQ, which is the precursor of PQS, is produced by a complex of PqsC and PqsB, by decarboxylative coupling of 2-aminobenzoylacetate (2-ABA) and an octanoate group (**Figure 1.5**) (Dulcey et al., 2013, Drees and Fetzner, 2015, Drees et al., 2016). A recent study by Drees and Fetzner (2015) suggested that PqsE has a role in HHQ synthesis. PqsE acts as a thioesterase, hydrolysing the intermediate biosynthetic 2-aminobenzoylacetyl-coenzyme A to form 2-aminobenzoylacetate, the precursor of HHQ and 2-aminoacetophenone (Drees and Fetzner, 2015, Drees et al., 2016).

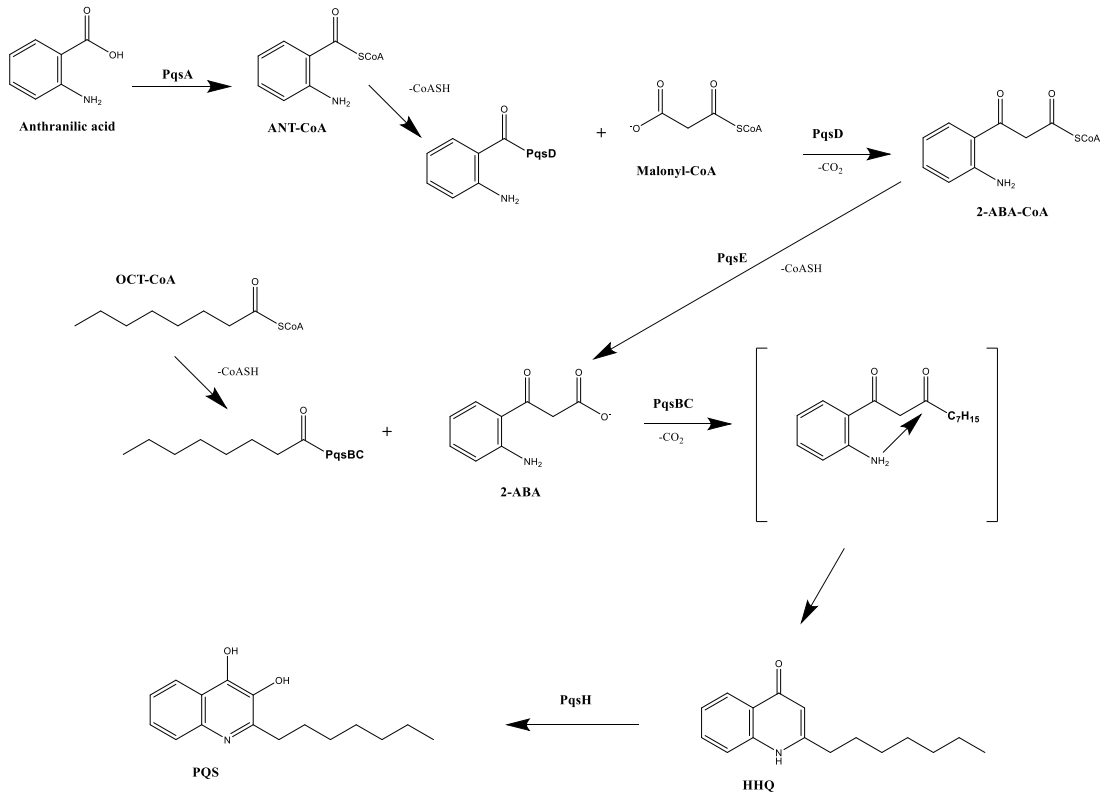


Figure 1.5. The Biosynthetic pathway of PQS by PqsABCDEH operon. In the initial step, the acyl moiety of an activated carboxylic acid is transferred to a strictly conserved active-site cysteine residue. Subsequently, a β-ketoalkanoic acid (malonyl-ACP in the case of FabH, malonyl-CoA or malonyl-ACP in PqsD, 2-ABA in PqsBC) is decarboxylated. Intermediates and products of the alkyl quinolone biosynthetic pathway: Ant-CoA − anthranilate-coenzyme A, 2-ABA-CoA − 2-aminobenzoylacetyl-CoA, 2-ABA – 2-aminobenzoylacetate, HHQ –2-heptyl-4-hydroxyquinoline, PQS – *Pseudomonas* quinolone signal.

1.7 PQS in quorum sensing and iron uptake

P. aeruginosa requires iron to maintain cellular processes, such as amino acid and nucleoside synthesis, and respiration (Cornelis and Dingemans, 2013). Iron

insufficiency in *P. aeruginosa* causes an increase in expression of genes related to iron uptake, such as siderophores of ferric uptake (pyoverdine and pyochelin), haem also *feo* as ferrous iron transporters, exoenzymes that could cleave iron-bound host proteins (alkaline protease, *lasB* elastase) and other redox enzymes and toxins (exotoxin A)(Ochsner et al., 2002). Furthermore, the iron depletion causes inhibition of oxygen transfer from the environment to medium of *P. aeruginosa* cultures, thus protecting bacteria from oxidative stress (Kim et al., 2003).

As previously explained, *P aeruginosa* has multiple pathways to increase iron uptake, including the use of siderophores, uptake of xenosiderophores, uptake of heme, and the FeO system. Interestingly, PQS also demonstrates the ability to chelate iron, which was shown by the depletion of iron in the growth medium after the PQS was added (Bredenbruch et al., 2006). To confirm, PQS was dissolved in methanol-Fe(III)sulfate solution resulting a red-pink colour, which indicates complex formation (Bredenbruch et al., 2006). As the result of the PQS iron-chelating activity, the transcriptional profile of *P. aeruginosa* PAO1 shows increased transcription of genes involved with iron uptake (Bredenbruch et al., 2006, Diggle et al., 2007).

Furthermore, PQS also enhances production of siderophores but not HHQ in each strain, by using *pqsA*, *pqsE*, and *pqsR* mutants as the induction of pyoverdine synthesis in the parent (Diggle et al., 2007). This suggests that PQS may induce the production of siderophores using three different signalling pathways, which are (i) iron deprivation, in which PQS's iron chelation induces production of siderophores, (ii) the

pqsE/pqsR pathway in which PQS promotes gene expression, such as *lecA* and others required for pyocyanin production, and (iii) the *pqsR* pathway in which PQS promotes the expression of genes such as *pqsA* (Diggle et al., 2007).

1.8 Inhibition of PQS as resistance-free antimicrobial specific *P. aeruginosa*

QS in *P. aeruginosa* is integral in the construction of biofilms, colonisation of the host, adaptation in differing environments, defence from other competitors, and the production of large number of virulence factors, such as elastase, rhamnolipids, and pyocyanin. These virulence factors are responsible for tissue damage and disruption of tight junctions. *P. aeruginosa* usually infects patients with immune system deficiencies (Li and Tian, 2012, Schaadt et al., 2013).

Treatment of *P. aeruginosa* is complicated due to resistance to many classes of antibiotics (Obritsch et al., 2004). Thien-Fah et al, (2003) found that *P. aeruginosa* was resistant to most antibiotics due to biofilm formation and that this was not simply a diffusion barrier, but also had a distinct mechanism for resisting the action of antibiotics (Mah et al., 2003).

Burnt-mouse, murine acute pneumonia, and rat chronic lung infection models infected with *P. aeruginosa* show that inactivation of QS genes results in reduced virulence compared to the wild type (Tang et al., 1996). Furthermore, the signal molecules AHLs and HAQs were directly measured in the sputum of CF patients

chronically colonised with *P. aeruginosa* (Middleton et al., 2002). In the cystic fibrosis lung, *P. aeruginosa* grows primarily as biofilms (Hoiby et al., 1977, Lam et al., 1980, Singh et al., 2000), which provides protection from the host defence system and from the action of antibiotics (Koch and Hoiby, 1993).

PQS has an important role in *P. aeruginosa* QS, which are reported to involve in biofilm formation (Diggle et al., 2003), provide a link between the *las* and *rhl* systems (Venturi, 2006), and could also take over the dependency of LasR in activating the *rhl* QS system expression and production of subsequent virulence factors (Diggle et al., 2003). Therefore, inhibition on PQS biosynthesis is one of the solutions to overcome antimicrobial resistance.

1.9 Clinical significance of PqsBC

Evidence suggests that *P. aeruginosa* is the most common Gram-negative bacteria found in hospital-acquired infections, representing a major cause of pneumonia, urinary tract, surgical wound, burn wound and bloodstream infections (Van Delden and Iglewski, 1998). *P. aeruginosa* also participates in infection of immunocompromised individuals, such as patients suffering from AIDS, cancer, burn wounds and cystic fibrosis (CF) (Lyczak et al., 2000).

Meanwhile, surveillance by Obritsch, et al (2004) indicates that in several hospitals *P. aeruginosa* are frequently found to be resistant to imipenem, aztreonam,

ceftazidime, ciprofloxacin, tobramycin, and imipenem (Obritsch et al., 2004). The phenomenon of *P. aeruginosa* antibiotic resistance is due to it is ability to form a biofilm (Rodney, 2002, Karatan and Watnick, 2009, Rasamiravaka et al., 2015).

Biofilm formation are one of the virulence factors of *P. aeruginosa* that is controlled by QS and regulated by PQS. PqsBC catalyses the condensation of octanoyl-coenzyme A and 2-ABA to form HHQ, the precursor of PQS. As mentioned previously, PQS has an important roles in *P. aeruginosa* QS, as it is involved in biofilm formation (Diggle et al., 2003), links the *las* and *rhl* systems (Venturi, 2006), and affects LasR regulation of the *rhl* QS system (Diggle et al., 2003). The heterodimeric PqsBC complex is essential for the formation of HHQ, the precursor of PQS. Therefore, inhibition of PQS biosynthesis through PqsBC is a possible solution to overcome antimicrobial resistance.

1.10 Protein X-ray crystallography

Structural biology includes a range of techniques that identify the 3D structure of biological macromolecules. Having an understanding of the 3D structure of a target protein can greatly assist rational drug design for therapeutics. PqsBC is an essential enzyme in *P. aeruginosa* QS because of its role in PQS biosynthesis (Drees et al., 2016), and using X-ray crystallography to study its 3D structure will allow the design of novel therapeutics through rational drug design.

X-ray crystallography is a tool to determine the 3D structure of biological macromolecules, including proteins and nucleic acids (such as DNA, RNA). The double helix structure of DNA was determined through experimental data obtained through X-ray fibre diffraction. X-ray diffraction analysis allows the visualisation of protein structure at the atomic level, or closer enough in atomic stage when leaded to pure protein crystals. More than 80 years crystallography has been used to solve crystal structures (Mcpherson, 2009).

In 1958, Kendrew et al. published their historic study of myoglobin, which was the first protein structure solved (Kendrew et al., 1958). Afterwards, in 1960, Dickerson et al. published another study of myoglobin, which was another historic protein structure solved (Dickerson et al., 1961). The knowledge of accurate molecular structures is a prerequisite for rational drug design and for structure-based functional studies to aid the development of effective therapeutic agents and drugs. Crystallography can reliably provide the answer of many structure related questions, from global folds to atomic details of bonding (Rupp, 2010).

1.11 Aims of this PhD project

The nature of *P. aeruginosa* and its high level of antibiotic resistance means there is an urgency to understand structural, physical and chemical properties of the PqsABCDEH enzymes. This project will focus on PqsBC, as PqsBC is the enzyme that catalyses condensation of 2-aminobenzoylacetate (2-ABA) and octanoyl-

coenzyme A to form HHQ (Drees et al., 2016). HHQ itself was discovered to function as an autoinducer molecule per se (Diggle et al., 2007). Moreover, HHQ is the precursor of PQS which is an extracellular messenger that involves in QS systems in *P. aeruginosa*. Therefore, solving on crystal structures of PqsBC provide a unique insight into substrate recognition and establish a scaffold for structure guided drug design of novel antimicrobial agents especially related with antibiotic resistance.

The objectives of this project are:

- Determine the crystal structure of the PqsBC enzyme and ligand complexes.
- Understand the PqsBC enzyme mechanism.

Chapter 2: Protein crystal structure determination

2.1 Structural biology of macromolecules

Structural biology is a multidisciplinary research area drawing from biochemistry, biophysics, and molecular biology that focuses on macromolecules such as proteins and nucleic acids. It includes the investigation of conformation and structural configuration and how this relates to function. It includes the study of macromolecules in their singular state, or in complex with other macromolecules or small molecules (Banaszak, 2000a). Individual proteins are too small to observe through the light microscope. Therefore, the majority of structural biologists employ macromolecular crystallography as a method to determine the 3D structures of proteins. Whereas, cells' functions that are employed by macromolecules within the crystal which are mostly the proteins in certain conformations and configurations which are three-dimensional shape, especially the assembled subunits.

2.2 Protein crystallography project outline

An outline of protein crystallography given in **Figure 2.1.** Protein crystallography begins with obtaining pure protein, which can be attained through native purification or by using recombinant methods. It starts with construct design, construction of primers for cloning and is following with expression and purification of the protein. Subsequently, pure protein is subject to crystallisation in order to reveal the 3D protein structure. Obtaining this protein structure allows structural drug design to produce agonists or antagonists for the enzyme.

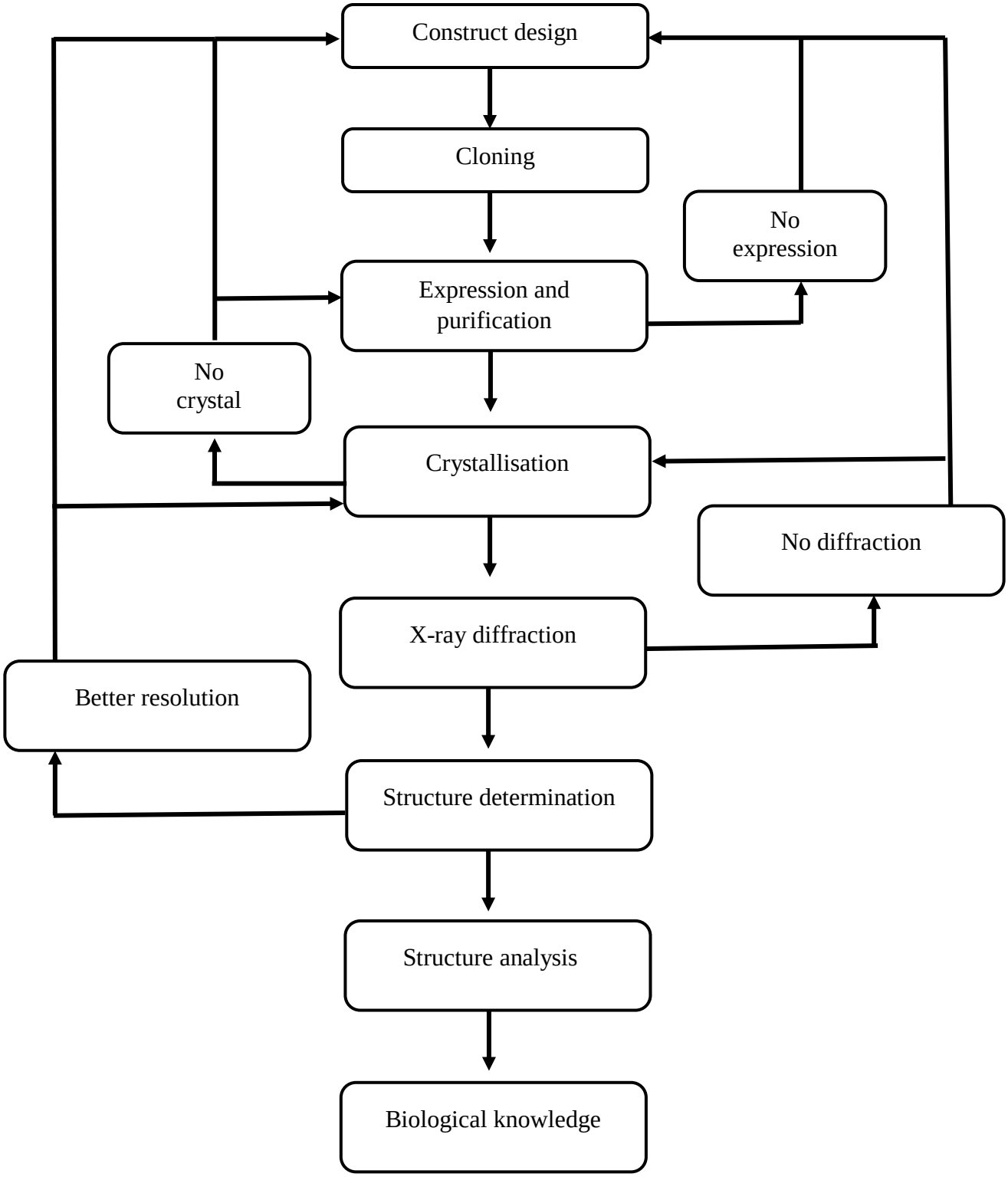


Figure 2.1. A flow chart of classical protein crystallography.

2.3 Protein sample preparation

Generally, the protein sample for crystallisation must be have a purity 95 to 98%, as the appearance of any impurity may impede the crystallisation process. In addition, purified protein should be homogenous and stable.

2.3.1 Recombinant DNA technology

Molecular cloning, which is also called recombinant DNA technology, is a methodology to assemble DNA with genetic information from two different organisms to generate a desired genetic sequence (Glick and Patten, 2017). Furthermore, molecular cloning consists of ligation of a target DNA fragment to a DNA vector and transformation of this DNA construct into a host cell (Glick and Patten, 2017). If the DNA fragment is inserted into an expression vector, then the organism and vector can be used to express a protein of interest.

2.3.2 Protein expression

Protein expression is an experimental procedure used to over-express proteins so that they can be used for downstream purposes. It may indicate the way of proteins are synthesised, modified, and organised in cell organism. The organism used in an expression system should preferably be easy to culture, fast growing, and able to produce large yields of protein. The most frequently used expression tool for the manufacture of recombinant protein is bacterial expression, even though yeast, insect,

mammalian and cell-free systems are available. Protein expression through *Escherichia. coli,* for instance, is comparably simple to conduct, economical to culture, and the needed time to synthesise a recombinant protein is relatively small (Doyle, 2008). After protein expression is conducted, then purification of protein may be performed.

2.3.3 Protein purification

In protein crystallisation requires large quantities of highly pure protein. Therefore, after expression, protein purification is performed to extract one or more proteins from a heterogenous mixture, such as lysates obtained from tissues or cells of an organism. In crystallography, protein purification also holds a vital role in the characterisation of function, structure, and interactions of the protein interest. In general, purification of proteins in active conformations are purified, which can often be identified by characteristics such as size, solubility, specific binding affinity, and charge (Berg et al., 2002). Techniques for protein purification include salting out, dialysis, gel-filtration chromatography, ion-exchange chromatography, affinity chromatography (Berg et al., 2002).

2.4 Crystallisation of proteins

The word 'crystal' originates from the Greek word '*krustallos',* meaning 'clear ice'. The crystal itself is a substantially homogeneous solid (Lima-de-Faria, 1990). Crystallisation is a process controlled by thermodynamic and kinetic factors

where molecules arrange into repeated units that interact in all three-directions in a periodic manner (McPherson et al.). Crystallisation itself comprises two prominent phases, which are nucleation and crystal growth. Nucleation is a process where diffuse molecules in a solution begin to assemble nanometer-sized clusters.

2.4.1 Crystal formation

The classical view of crystal nuclei formation and growth is explained by two-dimensional phase diagram in **Figure 2.2.** The undersaturated zone is located under the solubility curve, in which crystallisation will never occur. Crystal formation or nucleation occurs in the nucleation zone, which is above the solubility curve in the supersaturated zone. Subsequently, the crystal grows within growth zone.

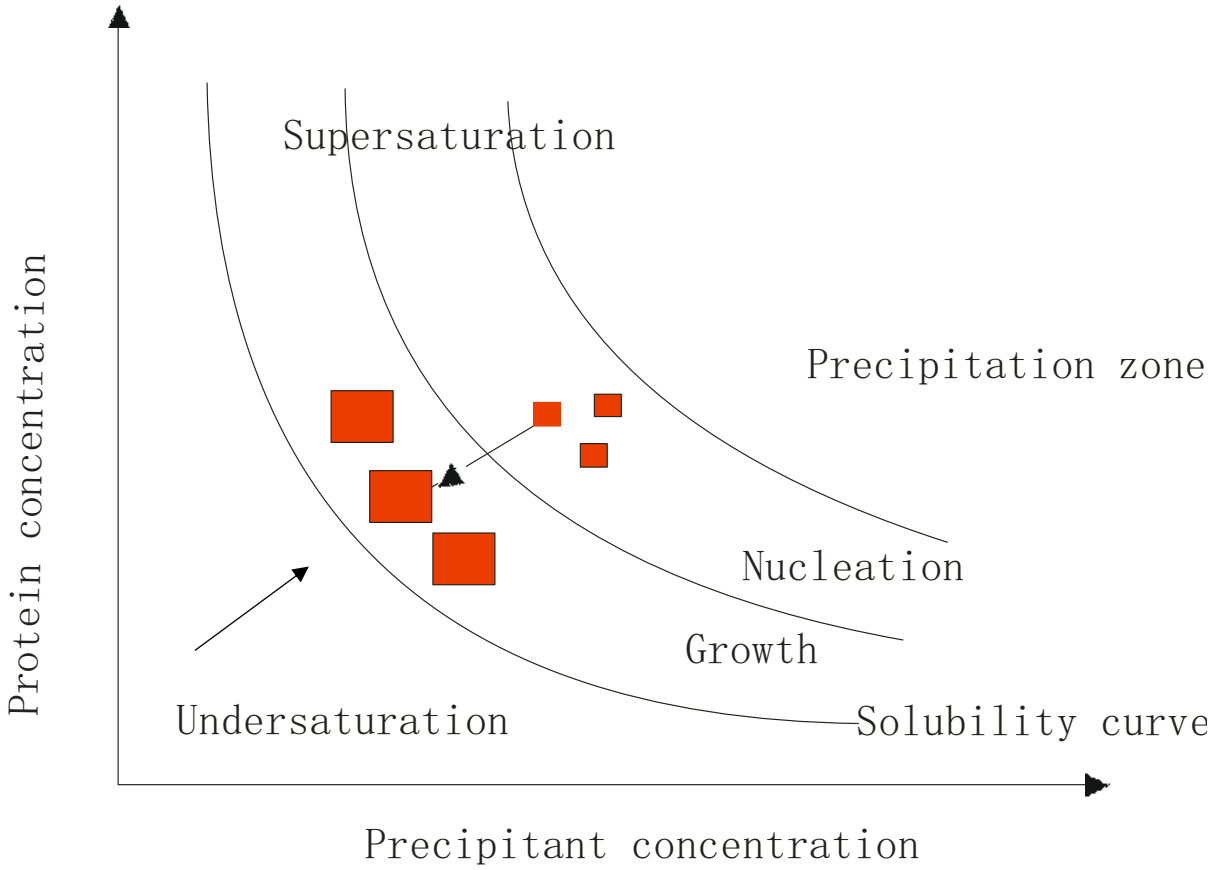


Figure 2.2. Crystallisation two-dimensional solubility diagram. Illustrating the change of protein concentration against precipitating concentration. Crystal formation or nucleation begins in nucleation zone and return to growth zone to grow in size.

2.4.2 Crystallisation methodology

Crystallisation techniques employ chemical and physical means to promote saturation of a protein solution through manipulation of the solution environment. Several methods are used to promote protein crystallisation through controlled

increase of protein concentration. There are three prominent crystallisation methods: batch methods, liquid-diffusion methods and vapour-diffusion methods. The batch crystallisation method is the simplest crystallisation technique, where a concentrated solution of precipitant is added to a concentrated solution of protein within a closed well and then left undisturbed to generate a final saturated solution. Dialysis employs diffusion and equilibration of precipitant molecules by a semipermeable membrane in order to slowly increase the concentration to the point where the protein in solution crystallises (Chirgadze, 2001).

2.4.3 Vapour-diffusion method

The vapour-diffusion includes hanging-drop and sitting-drop methods, and are the most frequently applied techniques for protein crystallisation (Luft et al., 2014). The vapour-diffusion method employs water diffusion and evaporation between solutions with different concentrations of protein and precipitant in order to obtained a solution of supersaturated protein (Chirgadze, 2001). Generally, the solution of protein is mixed in a 1:1 ratio with a precipitant solution, which is at the desired concentration for vapour equilibration (Chirgadze, 2001). The drop is either hanging from a cover slip or sitting on the plate, and the well is sealed (**Figure 2.3.**). Water gradually moves through the vapour phase, out of the drop and into reservoir, leading to a reduction in drop volume. Subsequently, this process will increase the concentration of protein inside the drop to a point where protein molecules start to precipitate out of solution. Consequently, protein molecules start to interact with one another rather than with the water molecules. For crystallisation, this precipitation

should be controlled to form an ordered lattice, rather than forming an amorphous precipitate.

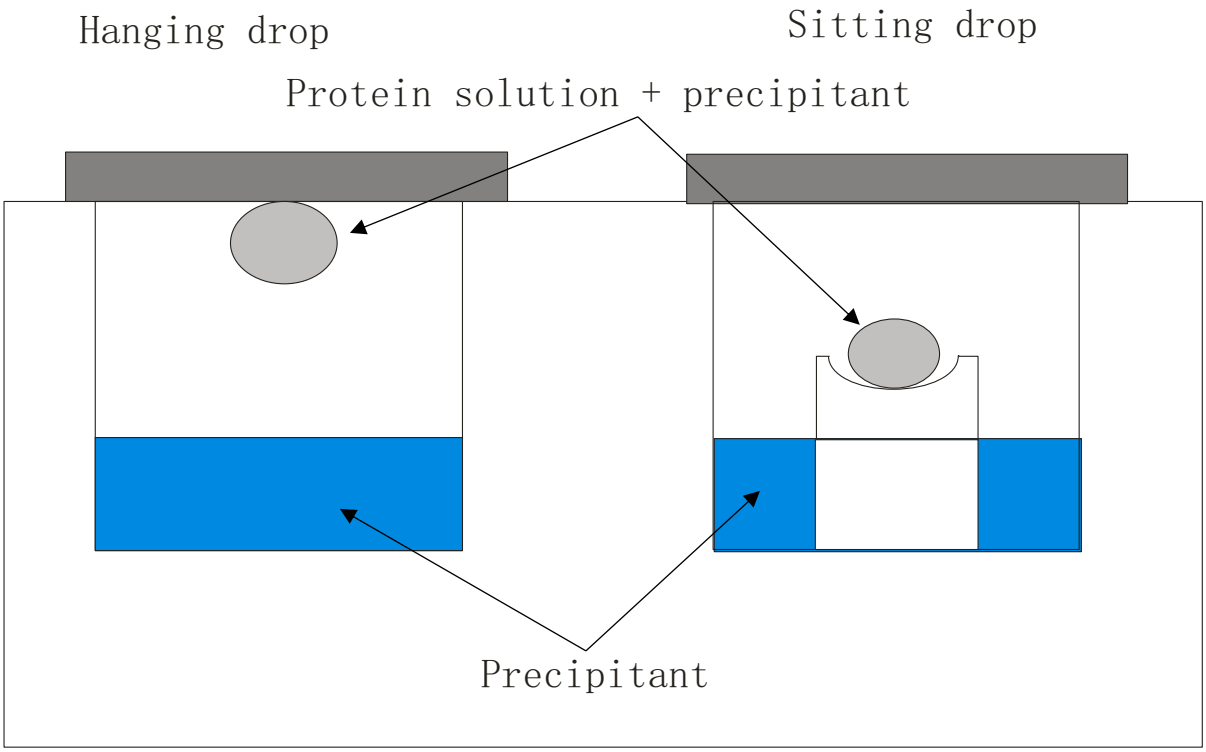


Figure 2.3. Hanging drop and sitting drop are included as the vapour-diffusion method. As theoretically lead water gradually moves through the vapour phase, out of the drop and into reservoir lead to reduce the volume of the drop, and it will increase the concentration of protein inside the drop to a point where protein molecules start to precipitate out of solution. Subsequently, protein molecules are starting concentrate, they interact with one another rather than interact with the water molecules.

2.5 Introduction of X-ray diffraction

In single and double slit experiments, visible light is used to produce a diffraction pattern on a screen. This is only possible because the width of the slit is on the order of wavelength of visible light (10^{-6} m) (**Figure 2.4**). Thus, if the slit width is much larger than wavelength of the wave, diffraction will be not observed. The difficulty in producing a diffraction pattern using X-rays lies in the fact that X-rays have a very small wavelength (10^{-10} m), which are much smaller than the size of the slits used in normal slit experiments. Further, if the X-rays are allowed to pass through opening, no diffraction pattern will be observed (**Figure 2.5**).

In 1912 Max von Laue suggested that a crystal lattice composed of atoms might have a spacing small enough to create a diffraction pattern using X-rays. In a crystal lattice, atoms are arranged as shown on **Figure 2.10**. Here, the separation distance is on the order of wavelength of the X-rays. Suppose X-rays are directed at the crystal lattice. Two incident X-rays are parallel to one another make an angle θ with respect to plane of atoms. Subsequently, when X-ray 1 and X-ray 2 reflect, they will interfere constructively when they travel a total distance that differs by a whole number multiple of their wavelength, which is when the two waves are fully in phase. Furthermore, Bragg's equation gives the angles for where these waves will constructively interfere (**Figure 2.10**).

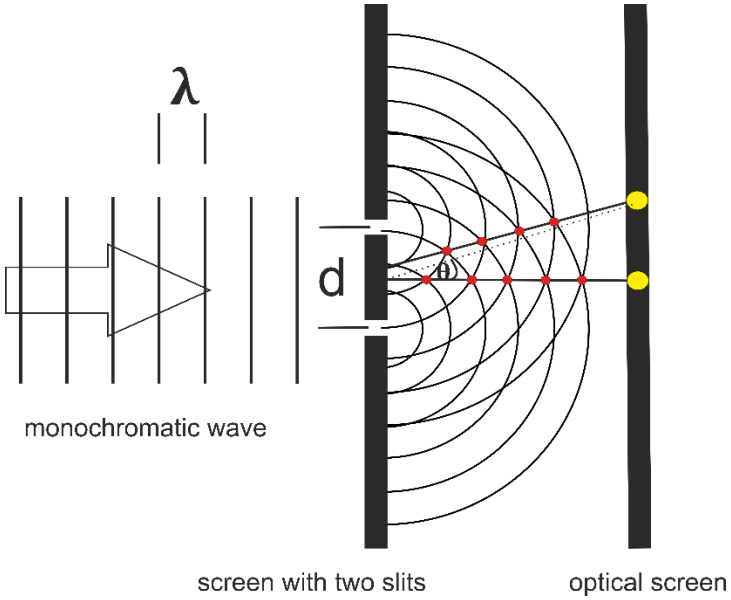


Figure 2.4. Young's double slit experiment used diffracted light from a single source passed into two more slits to be used as coherent sources. Yellow dots on optical screen represent the diffraction of light by slits.

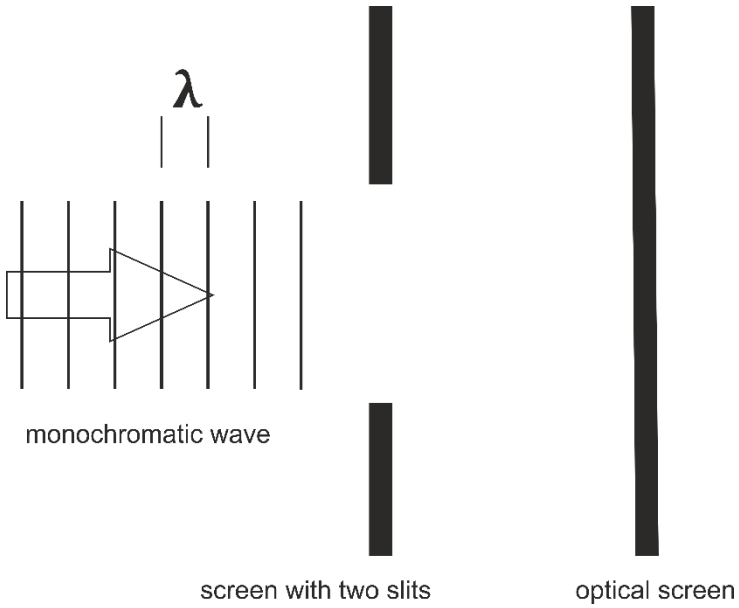


Figure 2.5. Model of X-rays are allowed to pass through the slit, hence there is no diffraction pattern will be observed.

2.6 Theory of X-ray diffraction

An X-ray is a form of electromagnetic radiation with a wavelength in the range 0.01-1.0 nm. Electromagnetism theory shows that X-rays are produced when an electron is accelerated or decelerated (De Graef and McHenry, 2007). If an X-ray beam is incident upon a collection of electrons, either bonded to atoms or in a conduction band, then the electric field associated with the X-rays will force those electrons into oscillation. Afterwards, because of the forced oscillation, they will emit their own X-rays, and this phenomenon is known as X-ray scattering (De Graef and McHenry, 2007). When an electron is treated as a particle, the term scattering is applied, but when an electron is treated as wave the term diffraction is applied. During elastic scattering (coherent scattering), also known as Thomson scattering, an X-ray photon interacts with a whole atom and causes it to become excited. This excitation causes the atom to emit an X-ray photon of equal wavelength but traveling in a different direction. Since, the wavelengths are equal there is no change in the energy level of the photon. This occurs when the photon has less than 10 keV of energy.

Another specific mechanism of the interaction between X-ray photons and matter is Compton scattering. Here, X-ray photons lose energy during scattering because the energy is transferred to an outer shell electron, and causes the atom to lose the electron, hence the process is known as an inelastic scattering event. During Compton scattering, the phase of the X-ray photon is changed in a random direction, so that the photon no longer carries phase sensitive (i.e., diffraction) information. Compton-modified radiation is thus not useful if, as in the case of X-ray

crystallography, systematic diffraction is required. Therefore, X-ray diffraction requires Thomson scattering, or coherent scattering, rather than inelastic scattering (De Graef and McHenry, 2007).

2.6.1 Electrons as an oscillation induction of the electrons

A proton is about 1800 times heavier than an electron. Most nuclei are made up of many nucleons that have a total mass that is greater than the mass of a proton. Because the scattered intensity is inversely proportional to the square of the mass of the particle emitting the X-ray photon, scattering of X rays from the nucleus is considered negligible compared to the scattering from the electrons of an atoms. Thus, X-ray scattering is considered to be due to the electron density of the atoms in a sample.

In an atomic level, electrons as an oscillations induction of the electrons are able to observed, the interaction of the oscillating electric field vector in the electromagnetic wave anatomy (**Figure 2.6.**) (Rupp, 2010). These accelerated, charged electrons emit electromagnetic waves of same frequency and is therefore coherent scattering or Thomson scattering. The phase difference between these emitted partial, scattered waves upon superposition gives rise to interference and diffraction phenomena. An electromagnetic wave comprises electronic and magnetic components. The electric vector **E** is perpendicular to the magnetic field vector **H**, and both oscillate perpendicular to the propagation vector $\mathbf{S}_0$ of the wave of wavelength λ. The vector $\mathbf{S}_0$ in the direction of wave propagation has magnitude $1/\lambda = n$. In physics,

the term wavenumber is common for *n* and the vector $\mathbf{S}_0$ is known as **K**. The position of any point of the wave in reference to the periodic origin node can be expressed in terms of phase shift $\Delta\varphi$ ranging from 0 to 2π (in units of radians or rad, 1 rad = $180/\pi$ degrees). The interaction of electric field vector **E** with dielectric matter is about six orders of magnitude larger than the interaction of the magnetic field vector **H,** hence the effect of **H** is neglected in the discussion of scattering and diffraction (Rupp, 2010).

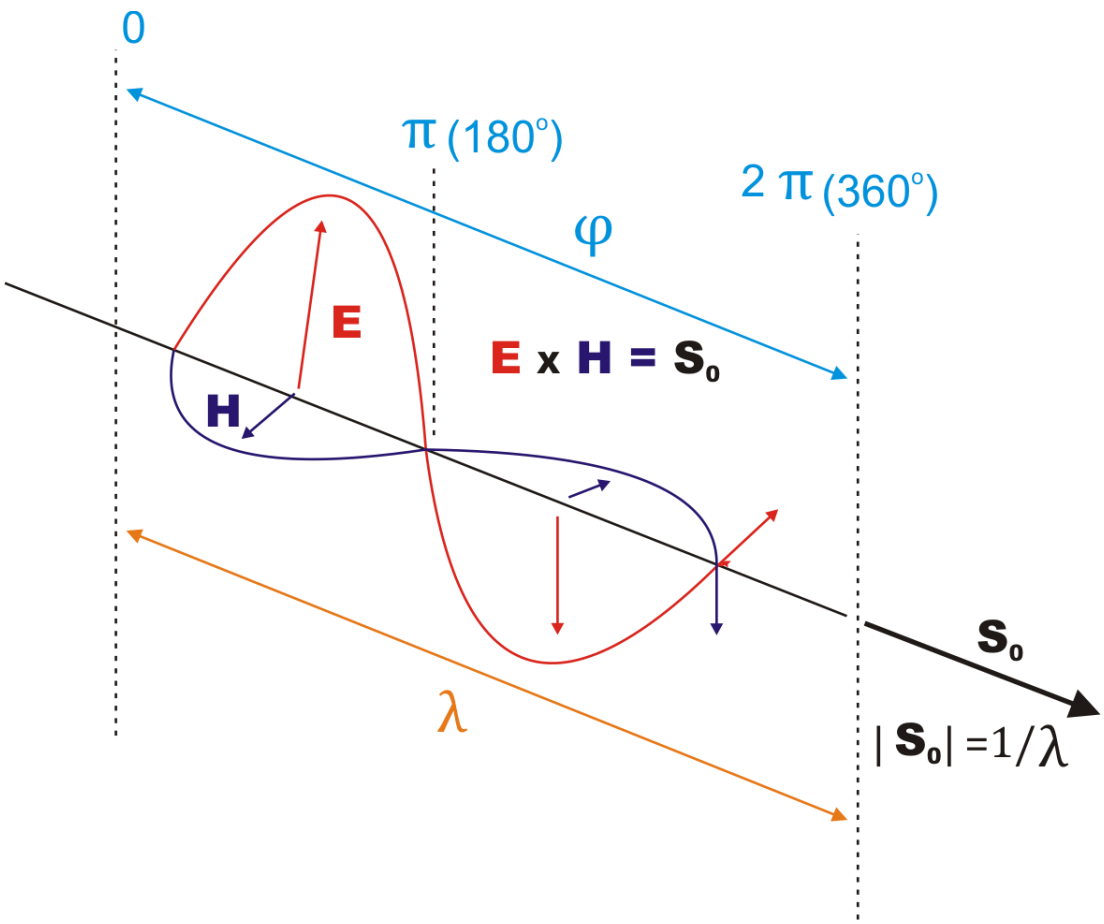


Figure 2.6. The interaction of the oscillating electric field vector in the anatomy of electromagnetic wave (Rupp, 2010). **H** is magnetic field vector, **E** is electric field vector, $\mathbf{S_0}$ is propagation vector, π is phase in radians with 1 rad = 180/π degrees. The vector $\mathbf{S}_0$ in the direction of wave propagation has magnitude $1/\lambda = n$.

2.6.2 Scattering by a single electron

When X-rays strike an electron coherent scattering occurs, which gives rise to interference. **Figure 2.7.** illustrates an X-ray hitting a single electron, and a section of the resultant spherical wave of scattered Thomson X-rays (**Figure 2.8)** (Kasai-Kakudo and Kakudo, 2005).

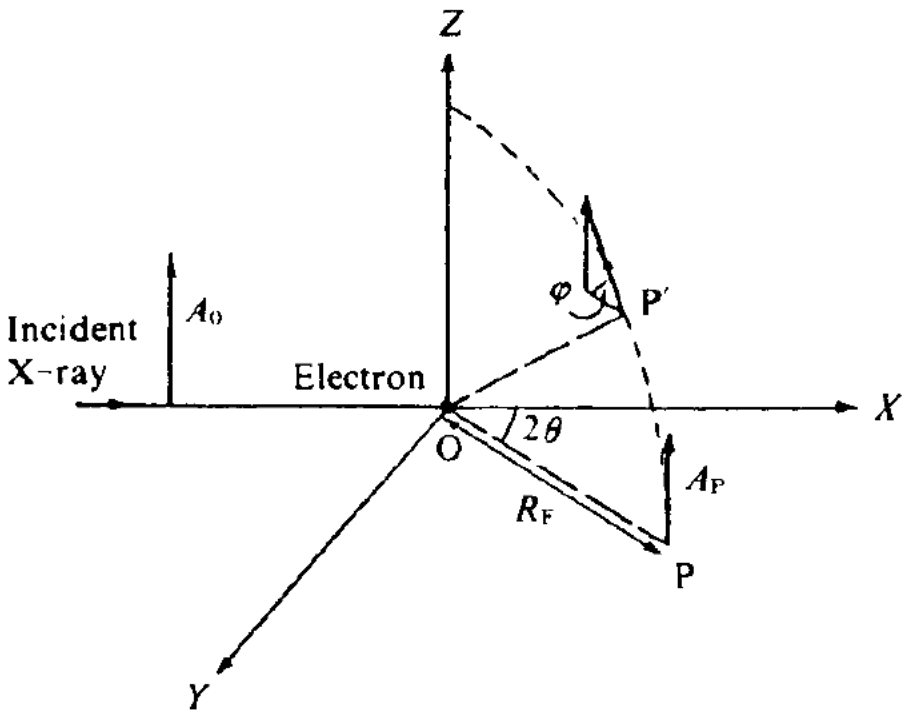


Figure 2.7. X-ray coherent (Thomson) scattering by a free electron (Kasai-Kakudo and Kakudo, 2005). **Ao** is an amplitude of the wave motion of the incident X-ray, plane **P** is an amplitude of the scattered spherical wave at point in XY plane, **RF** is a distance from the electron.

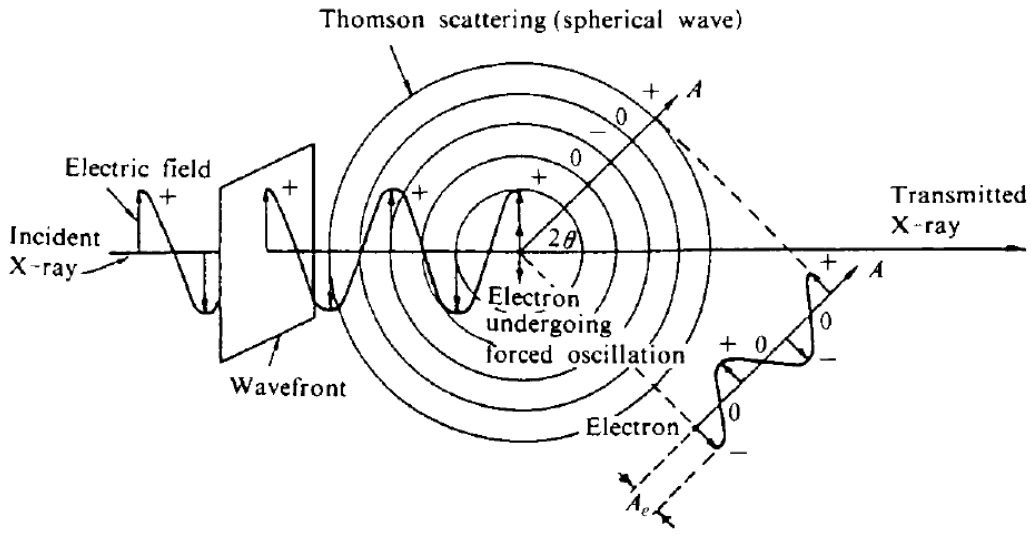


Figure 2.8. Propagation of a spherical wave with amplitude **Ae** in direction **A** (Kasai-Kakudo and Kakudo, 2005).

The electric field that accompanies the wave motion of the incident X-ray have an amplitude **Ao** and a direction parallel to **OZ**. The corresponding amplitude of the scattered spherical wave at a point in the **XY** plane **P**, at a distance $\mathbf{R_F}$ from the electron, is

$$A_p = A_0 \frac{1}{R_F} \frac{e^2}{mc^2}$$

Where **m** is the mass of the electron, **e** its charge, and **c** the velocity of light. The angle **2θ** shown between **OP** and **OX**.

The intensity of the wave is the energy passing through unit area per unit time, where the area is measured on the plane perpendicular to the direction of propagation of the energy. Hence, it is proportional to the square of the amplitude of the wave. The intensities $\mathbf{I_0}$ and $\mathbf{I_P}$ of the incident X-ray and the scattered wave at **P** will be

$$I_p = I_0 \frac{1}{R_F^2} \frac{e^4}{m^2 c^4}$$

2.6.3 Scattering by a single atom

X-rays are scattered by the electrons of the atomic shell. During the scattering process, the electron oscillates. It becomes a dipole and a spherical wave is emitted. The wavelength and energy of the scattered wave do not change (elastic scattering).

Scattering depends on the number and location of electrons in the atom. The atomic scattering factor (fs) equation describes the scattered wave of a single atom, with the formula:

$$f = \int_r \rho(r)\exp(2\pi i r.S)\delta r$$

Where, S is the difference between the incident X-ray vector and the radiation emitted and $\rho(r)$ is the electron density distance r from the centre of atom. As a result, integration of all electrons of the whole atom define the scattering of the whole atom, and its resultant electron density is considered spherical.

2.6.4 Scattering by number of atoms in a unit cell

A crystal unit cell is the smallest unit that can be repeated to form the whole crystal and is represented by a set of three vectors and angles that are a, b, c and α, β, γ, respectively (**Figure 2.9.**). The unit cell may consist of multiple atoms or molecules. Crystals are formed from unit cells structured a repeated manner in three dimensions and can be appreciated geometrically as an array of points on a lattice.

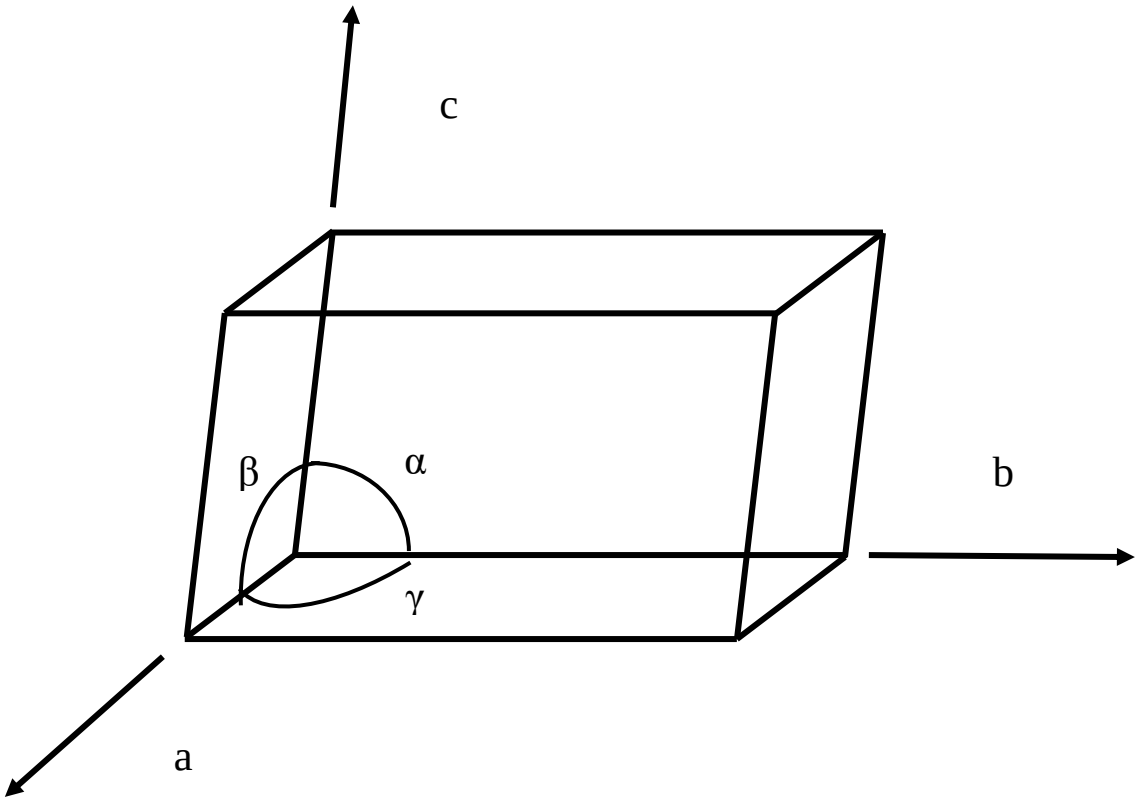


Figure 2.9. The three dimensions of unit cell are described as vectors a, b, c, with the angles α, β, γ.

For a single atom, the atoms scatter corresponding to their individual scattering factor. When the unit cell origin is employed instead if the atomic origin, there is a slight change in the phase angles by $2\pi i r_j$**.**S. Therefore, the atom group's scattering can now be described by:

$$F(S) = fj \exp(2\pi ir.S)$$

The sum of scattering from the group of atoms is known as a structure factor F(S), this factor is dependent on the atoms' three-dimensional arrangement.

2.6.5 Diffraction by a crystal

The geometric relationship between unit cells is represented by three direction translational vectors, a, b and c, which represent the x, y and z axes, respectively. In order to calculate the scattering by electrons within the crystal, hence the scattering by the entire unit cells, a single origin must be used. In the case of a single unit cell with origins at t.a + v.c, where t, u, v are whole numbers, the scattering is described as:

$$F(S) \times \exp(2\pi ita.S) \times \exp(2\pi iub.S) \times \exp(2\pi ivc.S)$$

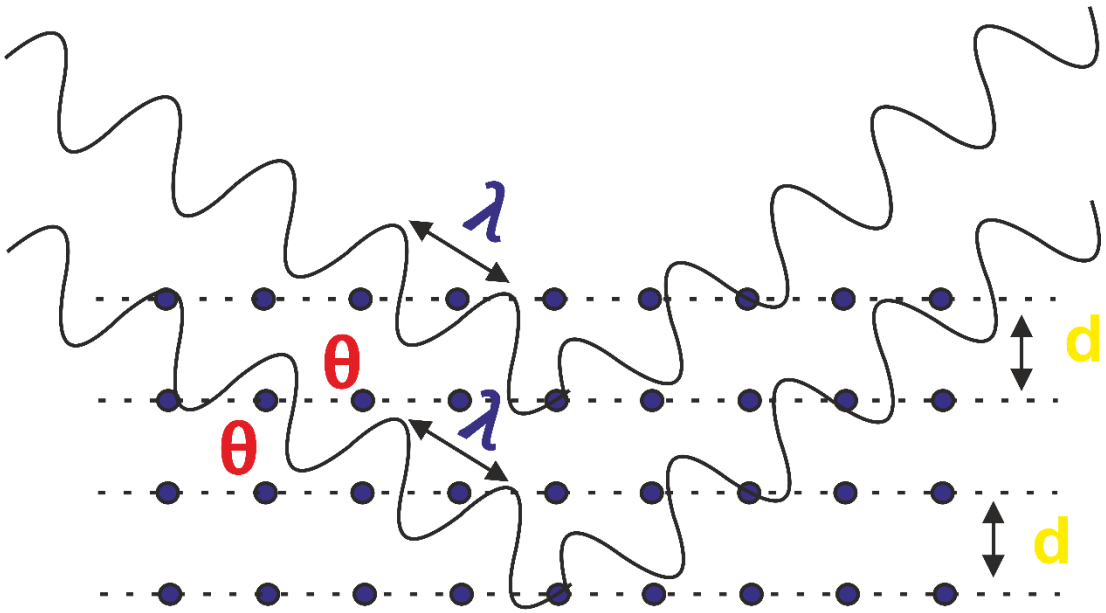
The total scattering of a crystal is obtained through a summation of scattering on individual unit cells; similar to obtaining the scattering of the unit cell through the summation of scattering of its constituent atoms.

$$K(S) = F(S) \times \sum_{t=0}^{n1} \exp(2\pi ita.S) \times \sum_{u=0}^{n2} \exp(2\pi iub.S) \times \sum_{v=0}^{n3} \exp(2\pi ivc.S)$$

The crystal itself comprises many unit cells and the scattering summation may frequently be 0. The exception to this case is if a.S, b.S and c.S are integers. These can also be represented by *h*, *k*, *l*; indices that are given to measured reflections or diffraction maximas.

2.6.6 Bragg's Law

Bragg's law describes the angles for coherent and incoherent scattering from a crystal lattice (**Figure 2.10**). As per Bragg's law, when X-rays are scattered from a crystal lattice, the peaks of scattered intensity correspond to the following conditions: 1) the angle of incidence is equal to the angle of scattering, 2) the difference in path length is an integral multiple of the number of wavelengths. Bragg's law gives the conditions for maximum intensity of the scattered waves, and the details about the crystal lattice. In conditions where the crystal structure is known, the wavelength of the X-rays incident on the crystal can be calculated using Bragg's law. Bragg diffraction was first proposed by William Lawrence Bragg and William Henry Bragg, in the year 1913, during their experiments on crystalline solids. Bragg diffraction occurs when electromagnetic radiation, or subatomic particles, have wavelengths that are comparable to the atomic spacing in a crystal lattice.



Bragg's Law:

$$n\lambda = 2d\sin(\theta)$$

where

λ is the wavelength of the rays

θ is the angle between the incident rays and the surface of the crystal

d is spacing between layers of atoms

and constructive interference occurs when n is an integer (whole number)

Figure 2.10. Bragg's law, it is a result of reflected waves **n** as integer (1, 2, 3 etc), from different layers that are perfectly in phase with each other and produce a bright point on a piece of photographic film.

Penetrating X-rays pass through the crystal and are reflected back. Each wave will be reflected by different planes of the crystal. The distance traversed by the wave is dependent on the distance between the planes of the lattice and the angle of incidence of the X-ray. Bragg's equation is given below:

$$2dsin\theta = n\lambda$$

Where n is the integer, λ is the wavelength, and θ is the angle of scattering.

2.6.7 The reciprocal lattice and Ewald sphere construction

The Ewald sphere is a geometric construction used in electron, neutron, and X-ray crystallography which demonstrates the relationship between: the wavevector of the incident and diffracted X-ray beams, the diffraction angle for a given reflection, and the reciprocal lattice of the crystal (**Figure 2.11**). With the help of Bragg's law and the Ewald construction, we can calculate the location of a reflection on the detector, provided we know the unit cell dimensions. Indeed, the position of a spot is determined alone by the metric symmetry of the unit cell. The intensity of a spot, however, depends on the contents of the unit cell (and, of course, on exposure time, crystal size, etc.).

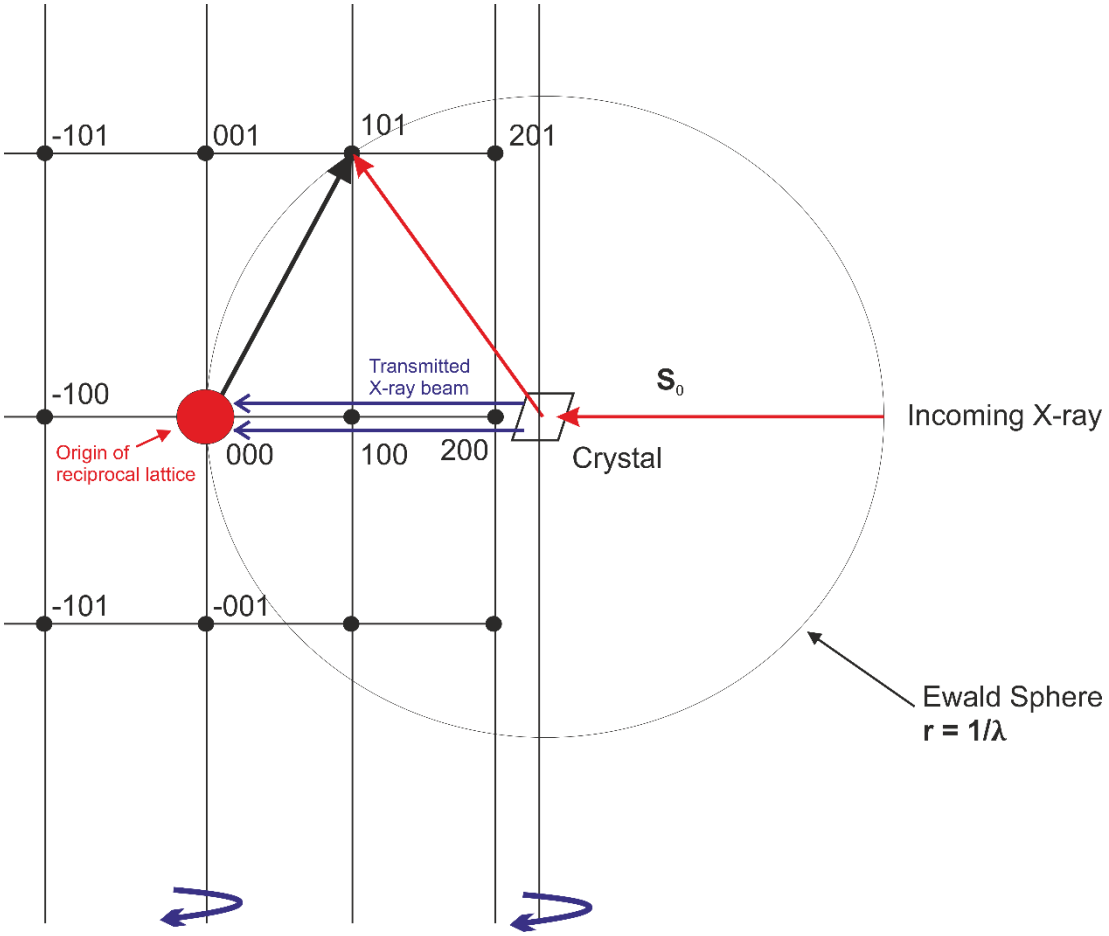


Figure 2.11. Ewald sphere, representation of the conditions necessary for an observed reflection. Shows the complicated rotations required to resolve all possible reflections in the unit cell when performing single crystal diffraction. Miller indices, group of three numbers that indicates the orientation of a plane or set of parallel planes of atoms in a crystal. If each atom in the crystal is represented by a point and these points are connected by lines, the resulting lattice may be divided into a number of identical blocks, or unit cells; the intersecting edges of one of the unit cells defines a set of crystallographic axes, and the Miller indices are determined by the intersection of the plane with these axes.

2.6.8 Data collection

When collecting X-ray diffraction data, the objective is to record, ultimately in numerical form, the diffracted intensities from every family of planes in the crystal that can possibly satisfy Bragg's law, such as the spacing $d > \lambda/2$. This process should be performed as efficiently as possible, as there are many reflections to record, and they must be measured as carefully and precisely as possible. Once the X-ray data have been recorded, the diffraction experiment is finished, leaving only manipulation of data in real or reciprocal space (Mcpherson, 2009).

In summary, monochromatic X-rays from a parallel source impinge on a crystal and are diffracted into a set of unique spots or *reflections.* The data collection process involves recording the intensity and location of the reflections. Rotation of the crystal and another round of observation leads to a different pattern of reflections. The intensity and location of each of the spots change. The process is continued until all possible reflections have been measured (Banaszak, 2000b).

2.7 Processing the data

Data processing may be divided into several stages: data reduction (indexing-bravais lattice, parameter refinement, and integration), checking symmetry (Laue group and space group), scaling and merging (merging partial reflections to form complete reflections, merging symmetry equivalents), truncation (analyse intensity distribution, convert $|F|^2$ to $|F|$.

The program used for data reduction include: Mosflm for indexing and integration, Pointless for checking symmetry, Scala/Aimless for scaling and merging, and Ctruncate or truncation. Frequently, however, it falls to the crystallographer to refine the choices and select among them in order to arrive at the correct unit cell, unit cell dimensions, space group of the crystal, and other properties essential for full three-dimensional structure determination (Mcpherson, 2009).

2.7.1 Indexing, parameter refinement, and integration

The indexing provides a description of the crystal unit-cell parameters and the orientation of the crystal relative to a laboratory frame. On the basis of the shape of the derived unit cell, it may be possible to propose (as an initial hypothesis) the Laue symmetry of the crystal (Powell et al., 2013).

Indexing provides an approximation of unit cell dimensions such as a, b, and c as well as crystal orientation. This information, in combination with known instrument parameters such as crystal to detector distance, wavelength of radiation, *etc.*, tell us where the diffraction spots occur on the detector for each image. Therefore, the entire indexing step comprises finding reflections on the images, converting two-dimensional co-ordinates to scattering vectors (corresponding to three-dimensional RL co-ordinates), indexing, cell reduction, apply Bravais lattice symmetry, pick a putative solution, estimate mosaic spread (Powell et al., 2013).

Indexing tends to be more robust when information from several images separated in phi are used, rather than from a single image. The two-dimensional co-ordinates can be mapped (using Ewald sphere construction) to scattering vectors that correspond to (approximate) three-dimensional reciprocal lattice co-ordinates. Unit cell dimensions are used in structure solution, refinement, model building, and analysis. Therefore, they need to be accurate values (Mcpherson, 2009).

The step after indexing or autoindexing that determines the unit-cell parameters and the orientation of the crystal. The unit-cell parameters may indicate the likely Laue group of the crystal. The second step is to refine the initial estimate of the unit-cell parameters and also the crystal mosaicity using a procedure known as post-refinement (Leslie, 2006). Refining the parameters optimises the fit of observed to predicted spot positions, so that measurement boxes can be placed accurately over the spots. Specifically, it involves improving estimates of both crystal parameters and instrument parameters. Accurate cell dimensions are important because they are used in all subsequent stages of structure determination, refinement and analysis. This may be performed by either positional refinement using spot co-ordinates and post-refinement using intensity measurements (Powell et al., 2013).

The third step is to integrate the images, which consists of predicting the positions of the Bragg reflections on each image and obtaining an estimate of the intensity of each reflection and its uncertainty. This is carried out while simultaneously refining various detector and crystal parameters. Basic features of the algorithms

employed for each of these three separate steps are described, principally with reference to the program MOSFLM (Leslie, 2006).

The starting point for data integration will therefore be a series of such diffraction images and the desired outcome is a data set consisting of the Miller indices (hkl) of all reflections recorded on these images together with an estimate of the diffracted intensities $I(hkl)$ and their standard uncertainties $\sigma I(hkl)$. This requires the prediction of which reflections occur on each image and also the precise position of each reflection on each image (Leslie, 2006). In MRC LMB Crystallography Course, Harry integration consists of two methods: summation integration and profile fitting. Profile fitting can be sub-divided into 2D fitting, which builds up reflections from single images, and 3D fitting, which builds up profiles across several adjacent images (Powell, 2013).

Integration is performed once the crystal and instrument parameters have been optimised by refinement. The first part of integration is to work out where the reflection occurs, and on what images it begins and ends. The assumption is made that, in the region of the reflection, the background is planar and may have a slope. The background plane and its slope are calculated from pixels in the neighbourhood of the reflection, once the reflection pixels have been determined (Mcpherson, 2009).

In summation integration, if the background intensity is negligible, the program does not even need to be very accurate in its placement of the integration boxes, provided they enclose the entire reflection. Profile fitting uses the assumption that full reflections in the same region of the detector (and on images nearby in phi) have similar profiles. Generally, before scaling the data, it is sensible to check that integration has not produced any errors. This can be achieved by examining any graphs that the integrating program has produced. They should all diverge smoothly from image to image, without any sharp discontinuities.

2.7.2 Scaling and merging

Scaling and merging the data are the next steps following integration. It is important because, it attempts to put all observations on a common scale and it provides the main diagnostics of data quality and indicates whether the data collection was satisfactory. Therefore, as diagnostic role, it is important that data are scaled as soon as possible after collection, or during collection, preferably while the crystal is still on the goniometer (Powell et al., 2013).

Scaling tries to make symmetry-related and duplicate measurements of a reflection equal by modelling the diffraction experiment, principally as a function of the incident and the diffracted beam directions in the crystal. Scaling attempts to make the data internally consistent, by minimising the differences between the individual observations, *I*, and the weighted mean of all the symmetry-related equivalents of

reflection *I*. However, systematic errors that are the same for symmetry-related reflections will remain review by Powell (2013).

Merging is the step after the observations are on a common scale, which is to merge the individual parts of partially recorded reflections into complete reflections, as well as to merge symmetry related reflections into unique observations. The symmetry related reflections that are merged together are those that are related by rotations characteristic of the Bravais lattice symmetry, not by reflections or inversions.

2.7.3 Truncation

While scaling tries to make the data internally consistent in order to put symmetry-related equivalents on to a common scale, truncation attempts to fit the overall distribution of intensities to what we expect for our crystal. The deviations from our expected model can be analysed to indicate the overall isotropic B-factor for our structure, and for crystal pathologies, such as twinning.

2.8 Phasing methods

A diffraction pattern tells us the intensity of diffracted waves at a particular angle. These intensities are determined largely by interference of diffracted waves. A

key factor in how waves interact with each other to produce interference is their phase angles.

Phase is a measure of how far through a cycle a wave is. The phases of waves that reach the detector are the missing links between the positions of the atoms in the protein and the interference pattern. The diffraction data do not contain the phases of diffracted waves.

Once waves are diffracted from a crystal, they give rise to diffraction spots. Each diffraction spot corresponds to a point in the reciprocal lattice and represents a wave with an amplitude and a relative phase. Theoretically, photons are reflected from the crystal in different directions with a probability proportional to the square of the amplitude of this wave. The photons may be counted, however, the information about the relative phases is lost. There are several methods to solve the phase problem, such as multiple isomorphous replacement, multiple anomalous dispersion, and Patterson function.

2.8.1 Multiple isomorphous replacement

The first method used to calculate these phases in protein crystals was multiple isomorphous replacement (MIR). Characteristically, in this method, the protein crystal is soaked in a solution containing heavy metal ions. The purpose of heavy metals is to bind to the protein at certain positions and become part of the crystal

structure. In order for this to work, the protein with the metal ions bound has to have a very similar conformation to the protein without the metal ions; termed isomorphous, as the crystal must be isomorphous.

Heavy metal atoms are large volumes of high electron density and therefore scatter more than light atoms. Diffraction patterns of the protein with and without the bound metal ions are compared, effectively 'zeroing' all diffraction except that of the metal ions. Hence, it is possible to separate their component of the diffraction data from that of the rest of the molecule and solve the sub-structure of the heavy atoms. Because there are usually few heavy atoms in the substructure, the solution of the phases can be obtained by direct methods. This is aided by the fact that when applying the Fourier transform, the resultant electron density can be constrained to be very large (from a heavy atom) or very small (no heavy atom). Moreover, if there are any major negative values for electron density, the solution can be rejected because negative electron density is impossible.

After the positions of the metals are located in the crystal structure, and their diffraction pattern (angles and intensities) is calculated, these data can be used to approximate the phase information for the rest of the structure.

2.8.2 Multiple anomalous dispersion

Multiple anomalous dispersion (MAD) is similar to MIR, the difference is that in MAD the X-ray wavelength chosen is determined by the metal atoms that are incorporated. Different metals absorb X-rays of different wavelengths. Therefore, by choosing a wavelength that the metal absorbs, the position of the metals can be determined by the 'holes' they leave in diffraction data. Afterwards, by observing the link between how the molecule structure changes and how diffraction data also changes so can be the way to work out the phases of the complex waves.

2.8.3 Molecular replacement

One solution for the phase problem is molecular replacement. The term of molecular replacement was introduced in 1972 by Michael G Rossman as the title of his book (Rossmann, 1972), previously molecular replacement concept known as concept of non-crystallographic symmetry (NCS) (Rossmann, 2001). NCS is a symmetry operation that is not compatible with the periodicity of a crystal pattern (Rossmann, 1990).

Molecular replacement can be used for obtaining approximate phasing of an unknown structure from a known related molecule and for phase improvement as well as extension in the presence of noncrystallographic symmetry (Rossmann, 1990). Original concept of the molecular replacement was stated by Rossmann and Blow (1962) was of a three-stage process: (i) determination of relative orientation (rotation)

of identical unknown structures in the same or different crystals. (ii) Use of information from first stage to determine the position of the local noncrystallographic operators relative to the crystallographic symmetry elements (translation). (iii) Phase determination by using a knowledge of the noncrystallographic operators derived in first and second stage (Rossmann, 1990).

The rotation function is the tool for determining relative orientation. The rotation or the determination of the relative orientation of unknown structures in the same crystal form might be of two or more molecules in one crystallographic asymmetric unit. Subsequently, this application can be used, for instance, in finding the relative orientation of a known molecular structure in an unknown unit cell. The purpose here is to use the known analogous molecule to solve the structure of the unknown crystal; that is, the known molecule is being used to search the unknown cell for a similar pattern. This is the most widely used application of the molecular replacement technique (Rossmann, 1990).

In translation function, after having determined the relative orientation in the first stage, one may now be able to place the molecule in space with respect to the crystallographic symmetry elements. Thus, for instance, if the orientation of a molecule has already been determined with a known search model, then it is necessary to define its position in the cell with respect to the selected origin. If there is no known or related structure but the molecule or macromolecular assembly has noncrystallographic symmetry, then it is necessary to define the position of a selected

origin of the molecule (*e.g*. the centre of the noncrystallographic point group, such as the intersection of the twofold axes in an object with 222 symmetry) relative to the chosen crystallographic (Rossmann, 1990).

Phaser is probably the newest and best molecular replacement program around at the moment. It uses maximum likelihood methods for its translation and rotation function searches. Phaser should be able to solve most structures with automated molecular replacement mode, and this is the first mode that should be tried. Automated molecular replacement combines the anisotropy correction, likelihood enhanced fast rotation and translation function, packing and refinement modes for multiple search models and a set of possible space groups to automatically solve a structure by molecular replacement. **Figure 2.12** shows flow diagram for automated molecular replacement.

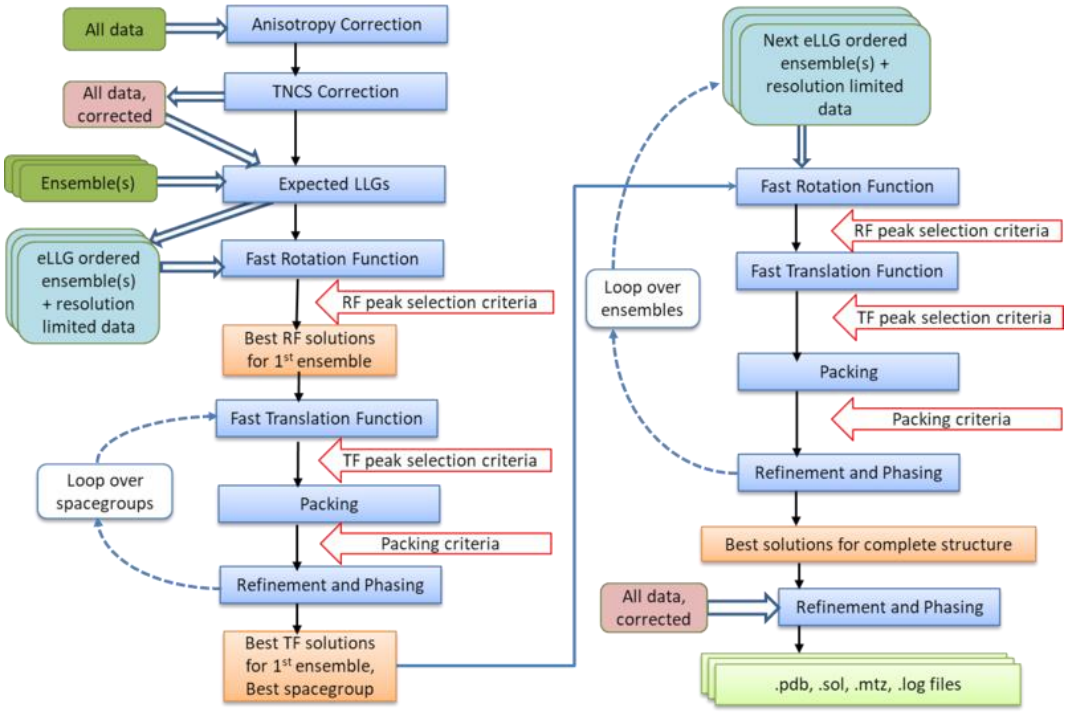


Figure 2.12. Flow diagram for automated molecular replacement (cite from http://www.phaser.cimr.cam.ac.uk/index.php/File:Phaser_MR_auto2.png). Showing seven discrete steps that are 1) Anisotropy correction, 2) translational non-crystallographic symmetry (tNCS) correction, 3) rotation function, 4) translation function, 5) packing analysis, 6) refinement and phasing, 7) log-likelihood gain calculation.

As can be seen on **Figure 2.12**, the automated molecular replacement method in phaser involves several discrete steps: 1) anisotropy correction that scales reflections as necessary to overcome anisotropy (weak data in particular direction). 2) translational non-crystallographic symmetry (tNCS) correction that checks for presence of tNCS. If present, parameters describing the translation and small orientation differences between copies are determined and used to compute correction factors. 3) rotation function (Carnoy et al.) that identifies possible orientations of the

model. 4) translation function (TF) that given the orientations from the RF, finds the absolute positions in the unit cell. 5) packing analysis that filters TF results based on number of clashes between atoms, given a certain cut-off. 6) refinement and phasing that performs simple rigid-body refinement of the placed molecules and calculates phases from final solution. 7) log-likelihood gain calculation that determines the final LLG, which can be used to evaluate the success of molecular replacement.

2.9 Model building, structure refinement and validation

The final stages of determining a macromolecule crystal structure are model building, structure refinement and validation, these steps are conducted in cycles with an overall aim to improve the phases of the structure factors. Firstly, structure building is initially performed by constructing a physical model into the electron density that was obtained from Fourier synthesis. The synthesis could be obtained by application of single or multiple isomorphous replacement, SAD or MAD, molecular replacement or other possible approaches to solving the phase problem.

An initial model built into an electron density map that calculated with experimental phases, or into a map poorly phased by molecular replacement, will usually contain many errors (Mcpherson, 2009). Subsequently, to produce an accurate model, crystallographic refinement as well as rebuilding using molecular visualisation tools is performed in a cyclical process of gradual improvement of the model (Kleywegt and Jones, 1997).

2.9.1 Model building

Once an electron-density map of sufficient quality has been generated by the phasing tools, atomic models can be built into an electron-density map. Model building requires fitting a polypeptide or nucleotide chain into the electron density in the map while maintaining chemical reality, and geometric and stereo-chemical properties (Mcpherson, 2009). The aim of model building and refinement is to construct a model that adequately explains the experimental observations, while making physical, chemical, and biological sense (Kleywegt and Jones, 1997). The primary program used for model building is COOT (Emsley and Cowtan, 2004) but O may also be used (Jones, 1978).

2.9.2 Model refinement

Crystallographic refinement has two purposes: first to fit a chemically and structurally sensible atomic model into observed X-ray crystallographic data. Second, to calculate best the possible electron density so that the atomic model can criticised (Murshudov et al., 1997). Brünger in 1992 introduced the free R value (R_{free}), a cross-validation method that uses a small fraction of the data that is not used in the refinement, but for which an R factor is nevertheless calculated. Comparing the values of the conventional R factor and free R factor tells something about the extent to which one has over fitted the data as well as about the quality of model and data. (Brünger, 1992, Kleywegt and Jones, 1997).

R_{free} and R factor is a calculation of the correlation of the measured structure factor amplitudes, F_{obs}, from the crystal, and the structure amplitudes, F_{calc}, calculated from the positions and scattering factors of the atoms making up the molecular model (Brünger, 1992, Mcpherson, 2009). The refinement process uses the agreement of the reciprocal space values F_{obs} and F_{calc} to indicate the extent of agreement of real space entities; the model and the real crystal structure. These two are linked to one another via the Fourier transform. Refinement is achieved by minimising the differences between F_{obs} and F_{calc} (Mcpherson, 2009).

As refinement is the iterative process of improving agreement between the molecular model and the crystallographic data. An important element in refinement is a computationally massive least-squares adjustment of the atomic positions in the model (x, y, z), occupancies (for multiple conformations), and temperature factors/B-factors (these can be for each individual atom or group of atoms). Changes on these factors in order to improve their agreement with the data (reflection intensities) and criteria of chemical reasonableness (structural parameters such as bond lengths and angles) (Rhodes, 2006).

In crystal structure refinement, there is an important distinction between a 'constraint' and a 'restraint'. A constraint is an exact mathematical condition which enables one or more least-squares variables to be expressed exactly in terms of other variables or constants, and hence eliminated. An example is the fixing of the x, y and z coordinates of an atom on an inversion center. A restraint takes the form of additional

information which is not exact but is subject to a probability distribution; for example, we could restrain two chemically but not crystallographically equivalent bonds to be approximately equal, with an effective standard deviation of (Sachdeva et al.) 0.01 Angstroms (Prince et al., 2004).

Restraints are a way of specifying prior knowledge. Standard restraints include bond lengths, angles, chirals, planes, some torsion angles as atoms are bonded to each other in specific ways. Subsequently, B-values as atoms close to one another cannot be dramatically different. In other word restraints stabilize refinement, reduce the chance of overfitting, and ensures that the final model is consistent with prior knowledge. Overfitting itself could be leaded by insufficient data (low resolution, partial occupancy), ignoring data (cutting by resolution), sub-optimal parameterisation, bad weights, excess of imagination. Cross-validation should be done in order to avoid overfitting.

Cross-validation itself has been explain on the first paragraph in this subsection, which is Rfree is an R-factor calculated from a set of reflections that is set aside and not used in refinement. Developed by Axel T. Brunger (Nature 1992). Since these reflections were never included in refinement, Rfree is unbiased. As Rfree is calculated from the test set (usually 5 % of reflections chosen randomly).

There are about eight available refinement programs such as SHELX, CNS, REFMAC5, TNT, BUSTER/TNT, Phenix.refine, RESTRAINT, and MOPRO. Meanwhile, REFMAC5 is the most popular recently. It has some features like Simple maximum likelihood restrained refinement, twin refinement, phased refinement (with Hendrickson-Lattmann coefficients), SAD/SIRAS refinement, structure idealisation, library for more than 10000 ligands, covalent links between ligands and ligand-protein, rigid body refinement, NCS local that restraints to external structures, TLS refinement, map sharpening, and occupancy refinement.

2.9.3 Validation of the model

Validation is the analysis of quality and completeness of reported information, and to make sure the structure is correct. To judge the quality of the model, the refinement program may assess stereochemistry, non-crystallographic symmetry (NCS), the Ramachandran plot, rotamer probability, peptide orientation, temperature factors, and residue real-space electron-density fit.

Stereochemistry is assessed by calculating the deviations from ideal bond lengths and bond angles, and determining violations of dihedral, flatness, and chirality restraints, which can be determined by programs such as X-PLOR and ProCheck (Laskowski et al., 1993, Kleywegt and Jones, 1997). Non-crystallographic symmetry (NCS) is the root mean square (Cheng et al.) distances, RMS ΔB values, $\Delta\phi$, $\Delta\psi$ plots (Kleywegt and Jones, 1995, Kleywegt, 1996, Korn and Rose, 1994), and multiple

model X_1, X_2 plots (Kleywegt, 1996) for NCS-related molecules are assessed if no constraints are used.

Preferred rotamer analysis, rotamer is a side-chain torsion (X-angle) combinations regarding to the local minima of potential energy (torsion terms and van-der-waals), produced by rotation about a single bond (Schrauber et al., 1993). Side-chain conformations are analysed with the RSC fit (rotamer sidechain) command in O (Jones et al., 1991, Zou and Mowbray, 1994, Kleywegt and Jones, 1997), which calculates the RMS distance between the side-chain atoms of a residue and those of the most similar preferred rotamer conformation; a value greater than 1.5 Å means that the side chain is not in a preferred rotamer conformation (Zou and Mowbray, 1994). Whereby, peptide orientation is the Pep_flip command in O (Jones et al., 1991), is used to superimpose the Cα atoms of a residue and its two nearest neighbours at both sides with similar fragments found in a database of well-refined structures. After the super positioning, the RMS distance between the carbonyl oxygen atom of the residue and the corresponding atom in the database fragments is calculated. A value greater than 2.5 Å implies that the peptide plane is flipped compared to the orientation most frequently observed in the database.

Chapter 3: Materials and Methods

3.1 Materials used

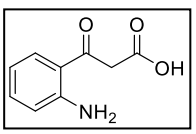
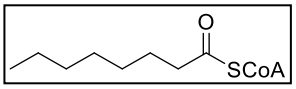
3.1.1 PqsBC enzyme

The PqsBC plasmids used in this study are pET28b::*pqsBC*-NHis$_{8,}$ pET28b::*pqsBC*^{C129A}-NHis$_{8,}$ and pET28b::*pqsBC*^{C129S}-NHis$_{8.}$ Those plasmids were prepared by the Fetzner Group (Westfälische Wilhelms-Universität Münster, Institut für Molekulare Mikrobiologie und Biotechnologie (IMMB)). The plasmid pET28b::*pqsBC*^{L229C}-NHis$_8$ was prepared at C84 center for biomolecular sciences. For PqsBC, PqsBC^{C129A}, PqsB^{C129S}, and PqsBC^{L229C} overproduction were prepared at C84, Center for biomolecular sciences in University of Nottingham. PqsBC, PqsBC^{C129A}, and PqsB^{C129S} were stored at -80° prior to crystallisation trials. Whilst PqsBC^{L229C} was produced for PqsBC oligomerisation study.

3.1.2 Subtrates (ligands)

The ligands of PqsBC enzymes used in this research are given in **table 3.1.**

Table 3.1. The ligands of PqsBC enzymes used in this research.

Compound	Supplier	Structure
2-ABA (2-Amino-benzoylacetate)	Fetzner Group	
Octanoyl-CoA	Sigma Aldrich	

3.1.3 Bacterial strains used

The *E. coli* strains used in this research were Novablue (DE3) (Novagen) and Rosetta2-(DE3).

3.1.4 Lysogeny Broth (LB) medium

LB medium (Lennox, Fischer Scientific, UK) contained tryptone 10 g/L, yeast extract 5 g/L, sodium chloride 10 g/L.

3.2 PCR

A 2X reaction mastermix contained 0.5 µl template (approx. 25-250 ng of DNA), 22.5 µl 5X HF buffer, 1.8 µl dNTPs (10 mM each nucleotide), 56.25 µl molecular grade H20. Each PCR reaction contained 36.1 µl mastermix, 2 µl 20 µM forward primer, 2 µl 20 µM reverse primer, 2 µl 50% DMSO, 7.4 µl molecular grade H20 and 0.5 µl PHUSION polymerase (Thermo Fisher Scientific). The PCR protocol is given in **Table 3.2.**

Table 3.2. PCR protocol.

Step	Temp (°C)		Time
Denaturation	95		5 minutes
	Denaturation	95	30 seconds
24 cycles	Annealing	55-65	30 seconds
	Elongation	72	1 minute/kb
Extension		72	10 minutes
Storage		4	∞

3.3 Expression and purification of His-TEV protease

Cells containing an expression vector for HisTEV protease were grown in Lysogeny Broth (LB) medium with 100 µg/ml ampicillin and 30 µg/ml chloramphenicol using 1000 ml narrow mouth erlenmeyer flasks at 37 °C until a cell density (OD_{600}) of 0.6. Then the temperature was decreased to 20 °C after induction of cells with 0.4 mM isopropyl-β-D-thiogalactopyranosid (IPTG, Melford, UK). After 16 to 18 hours, the cultures were centrifuged to collect the pellets/cells.

Harvested cells and then were resuspended in buffer A containing 50 mM Tris pH 8.0, 100 mM NaCl, 25 mM imidazole and 5% glycerol. Cells were lysed by

sonication using 60% amplitude whilst on ice for 6 minutes (20-second pulse with 20-second pause). Supernatants and cell debris were separated by centrifugation for 1 hour at 14,500 rpm at 4 ˚C and subsequently, the supernatant was filtered with the 0.45 µm filter. Immobilised metal affinity chromatography (IMAC) was performed using a 5 mL HisTrap column (GE Healthcare) that was preloaded with nickel sulphate and equilibrated in buffer A followed by loading of filtered supernatant.

The column was washed with 10 CV of buffer A before elution with a 10 CV gradient to 100% buffer B (50 mM Tris pH 8.0, 100 mM NaCl, 500 mM imidazole and 5% glycerol). The fractions that contained protein were pooled and DTT and EDTA were each added to a concentration of 1 mM. Afterwards, the fractions that contained His-TEV protease were further purified by size-exclusion chromatography (Akta PrimePlus GE Healthcare Life Sciences, USA) with a HiLoad Superdex 16/60 200 column. The size-exclusion column was equilibrated with 25 mM Tris pH 8.0, 200 mM NaCl, 2 mM EDTA, 10 mM DTT and 5% glycerol. His-TEV protease-containing fractions were centrifuged to remove precipitate/aggregate prior to injection on the size-exclusion column. Before storage at -80 ˚C, His-TEV protease was flash-frozen in liquid N_2. His-TEV protease concentration was measured using a UV spectrophotometer (Thermo Scientific Nanodrop, USA).

3.4 Expression and purification of PqsBC

The genes of *pqsB* and *pqsC* of *P. aeruginosa* PAO1 were cloned into plasmid pET28b using restriction-free (Carnoy et al.) cloning (van den Ent and Löwe, 2006). In the process, *pqsC* was fused with the sequences encoding a short linker (Ser-Ala-Gly), a recognition site for tobacco etch virus (Branda et al.) protease, and an N-terminal octahistidine tag. The vector-internal sequences for affinity tags were not used. The coding sequence of the resulting plasmid pET28b::*pqsBC*-NHis$_8$ was verified using commercial sequencing services. Site-specific mutations within the *pqsC* gene were also introduced using RF-cloning (van den Ent and Löwe, 2006).

PqsC was fused with Serine-Alanine-Glycine that are the sequences encoding a short linker. pET28b:*pqsBC*-NHis$_8$ was the resulting plasmid, whose sequence was subsequently confirmed using commercial sequencing services. Protein over-expression of pqsBC-NHis$_8$ was carried out in *E. coli* Rosetta2-(DE3)[pLysS] cells in TB medium (Carl Roth, Karlsruhe, Germany) with 150 µg/mL of kanamycin antibiotic (Applichem, Darmstadt, Germany).

Cells were grown in 2000 ml narrow mouth Erlenmeyer flasks at 37 °C until a cell density (OD_{600}) of 0.8 and and the temperature was decreased to 20 °C after induction with 0.2 mM isopropyl-β-D-thiogalactopyranosid (*IPTG, Thermo Scientific, Waltham, MA, USA*). After 8 to 12 hours of induction, the culture was centrifuged to harvest the cells. Harvested cells were resuspended in 20 mM Tris pH 8.0, 150 mM

NaCl, 5 mM EDTA, 10 mM imidazole, 0.5 mM β-mercaptoethanol and 0.1% Nonidet P40 (all Carl Roth, Karlsruhe, Germany). Cells were lysed by sonication (Hielscher UP200S Hielscher, Germany). Supernatants and cell debris were separated by centrifugation for 1 hour at 15,000 x *g* at 4 °C, and subsequently, the supernatant was filtered with a 0.45 µm filter (polyvinylidene fluoride membrane, Carl Roth, Karlsruhe, Germany).

PqsBC was purified using IMAC, size-exclusion chromatography and anion exchange chromatography, using either and Akta PrimePlus (GE Healthcare Life Sciences, Pittsburgh, PA, USA) or chromatography systems. For IMAC, a 5 ml Ni-NTA sepharose column (Qiagen, Hilden, Germany) was preloaded with nickel sulphate and equilibrated with buffer A containing 20 mM Tris, pH 8.0, 150 mM NaCl, and 10 mM imidazole prior to loading of the filtered supernatant.

The column was washed with 10 CV buffer A before elution with a 10 CV gradient to buffer B (20 mM Tris pH 8.0, 150 mM NaCl and 500 mM imidazole). In order to cleave the HisTag, 1 µg of TEV protease per 20 µg of total protein was added directly into a dialysis tube (Servapor, Serva Electrophoresis, Heidelberg, Germany) after 2 hours along with fresh buffer also containing 50 mM L-arginine as well as L-glutamate acid (Sigma-Aldrich, St. Louis, MO, USA). PqsBC^{129A}-HisTag was dialysed for overnight with gentle stirring. Particulate matter was pelleted by centrifugation at 15,000 x *g* for 20 minutes at 4 °C.

Furthermore, PqsBC was separated from the cleaved His-Tag peptides by passing the solution through a 1 ml HisTrap column (GE Healthcare Life Sciences) which was equilibrated with 20 mM Tris, pH 8. The flow through was applied to a 6 ml Resource Q column (GE Healthcare Life Sciences) equilibrated with 15 mM MOPS buffer pH 8.1 (Carl Roth, Karlsruhe, Germany) and 1 mM DTT. Then, 20 CV wash buffer was applied before a linear 20 CV gradient against 15 mM MOPS pH 8.0, 400 mM NaCl, 1 mM DTT.

The cleared lysate was loaded onto the column after being equilibrated in 25 CV of buffer A using a peristaltic pump. The column was washed with 30 ml buffer A to clear the lysate and remove any non-specifically bound proteins. Typically, a 20 CV, linear concentration gradient of buffer B was used to elute the protein.

Afterwards, the flow through was eluted gradiently into another 1 ml HisTrap column equilibrated with 15 mM MOPS buffer, pH 8.0, 150 mM NaCl, to clear the lysate and remove any non-specifically bound proteins. The fractions containing protein were collected and purified further by size-exclusion chromatography (Akta PrimePlus GE Healthcare Life Sciences, USA) with a HiLoad Superdex 16/60 200 column. The column was pre-equilibrated with 40 mM MOPS buffer, pH 8.1 and 150 mM NaCl. The protein sample was centrifuged to remove precipitate/aggregate prior to injection onto the Superdex 16/60 200 column. The fractions containing PqsBC were collected, pooled and DTT was added. Subsequently, the PqsBC solution was loaded onto a 5 ml HiTrap buffer exchange columns (GE Healthcare Life Sciences)

equilibrated with the 40 mM MOPS buffer, pH 8.1, and 50 mM NaCl. Eluted protein fractions were pooled, aliquoted, flash-frozen, and stored at −80 °C until required for further use. Protein concentration was determined by UV spectroscopy (Thermo Scientific™ NanoDrop™) using a calculated extinction coefficient of 72,880 M^{-1} cm^{-1}. Purification of PqsBC protein variants followed the same protocol. PqsBC protein was stored at -80 °C after flash-freezing it in liquid N_2.

3.5 Crystallisation and structure determination of PqsBC

Protein samples of wild-type PqsBC and the active site protein variant $PqsBC^{C129A}$, $PqsBC^{C129S}$, $PqsBC^{C129A}$ with the substrates such as 2-ABA and Oct-CoA with additive screen HR2-428 (Hampton Research) in 40 mM MOPS buffer, pH 8.1, 100 mM NaCl, 0.3 mM DTT at protein concentrations of 31.5 and 36.5 mg ml^{-1}, respectively, were diluted with 100 mM NaCl to give 3 mg/ml. These samples were subjected to screens, including Pi-PEG, Procomplex, classics lite, Mbclass, Index, PACT, Morpheus, JCSG+, and MIDAS, using the sitting drop vapor diffusion method (Mosquito robot, TTP Labtech, Melbourne, UK).

Crystals of $PqsBC^{C129A}$, $PqsBC^{C129A}$-Fe^{3+}, and $PqsBC^{C129A}$-Fe^{3+}-2ABA resulted from the conditions of 0.2 M NaCl, 0.1 M Tris, pH 8.5, 25% PEG 3350 within 24 h, whereas octanoylated or apo-forms of wild-type PqsBC and active site protein variant $PqsBC^{C129S}$ did not form crystals. Optimisation was performed using 24-well sitting drop plates varying PEG in 1% increments, 23–27%, as well as Tris, pH 8.3–

8.7. The final optimized crystallization condition was 25% PEG 3350, 0.1 M Tris, pH 8.3, and 0.2 M NaCl with 3 mg ml^{-1} protein concentration and a total volume of 4 µl. $PqsBC^{C129A}$ crystals were cryoprotected in a solution of 27% PEG 3350, 0.1 M Tris, pH 8.3, 0.2 M NaCl, 25% glycerol, and flash-cooled in liquid nitrogen prior to data collection at the Diamond Light Source synchrotron facility beamline I02 to 2.0 Å . Likewise, $PqsBC^{129A}$-iron (III) chloride hexahydrate crystals were exposed at beamline I03 at Diamond by using a wavelength of 1.1401 Å, and data were collected to 2.3 Å

Datasets were collected using the strategy provided by íMosflm and FastDP. Further, the processed datas were continue with Truncate, Matthews coeff. Molecular replacement was performed with PHASER using a variety of templates generated using MrBUMP from PDB codes 3h76, 3h77, and 3h78 of the PqsD structure. The model was completed manually using COOT and refined with REFMAC5. Values for surface area buried were calculated using PISA.

3.6 SDS-Polyacrylamide gel electrophoresis (PAGE)

Sodium dodecyl sulphate polyacrylamide gel electrophoresis (SDS-PAGE) was used to separate proteins to assess purity, it uses a discontinuous polyacrylamide gel as a support medium and SDS to denature the proteins. 15% polyacrylamide resolving gels were prepared as shown in **Table 3.3**.

Table 3.3. Constituents used for making four of 15% SDS-PAGE gels.

	Resolving gel	Stacking gel
Acrylamide (30%)	8 mL	2 mL
1.5 M TRIS-HCl pH 8.8	4 ml	-
0.5 M TRIS-HCl pH 6.8	-	2.5 ml
10% SDS	160 µl	100 µl
Distilled water	3.7 mL	5.3 mL
TEMED	16 µl	10 µL
10% APS	160 µl	100 µl

Prior to loading into the gel, PqsBC and the marker were heated for 5 minutes in 10% w/v SDS, 20% glycerol, 10 mM DTT, 0.2 M Tris pH 6.8, and 0.05% w/v bromophenol blue. Example for SDS-PAGE gel that was used can be seen in **Figure 3.1.**

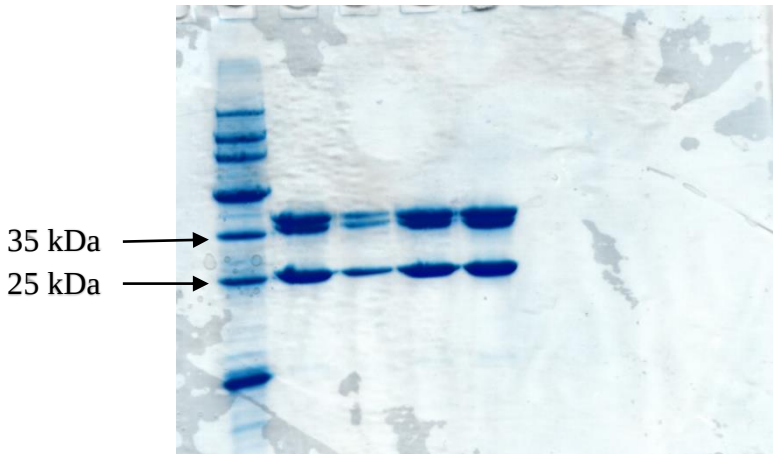


Figure 3.1. example of SDS-PAGE result showing cleaved PqsBC^{C129S} on 15% SDS-PAGE gel.

3.7 Analysing protein concentration

A Nanodrop 1000 (Thermo Scientific) was used to analyse the concentration of purified proteins. For samples from the nickel column, pooled fractions were analysed using a blank at the average % B concentration over the pooled peak. This was essential as imidazole has fluorescence at 280 nm so using either buffer A or buffer B would over- or underestimate the protein concentrations, respectively. Extinction coefficients were calculated by inputing the primary sequence into Protparam (Wilkins et al., 1999). The value obtained from the Nanodrop 1000 was divided by the correction factor from Protparam to obtain the true concentration.

Chapter 4: Expression, purification, and crystallisation of PqsBC

4.1 Introduction

The protein sample for crystallisation must have a purity of >95%, be homogenous, stable, and active. The presence of any impurity (as assessed by SDS-PAGE) may impede the crystallisation process. Meanwhile, protein source for crystallography is recombinant protein expression, which is started with a gene cloned into a suitable vector for bacterial expression. Subsequently, the vector is transformed into bacteria and the cells are picked by using selectable markers, such as antibiotics. Furthermore, these cells are then cultivated in cultures where induction of gene transcription is carried out. In the end, the cells are harvested after a specific time of period and lysed to release the contents of cell before it will be purified.

PqsBC is a subset of the PqsABCDEH enzymes, where PqsABCDEH is an autoinducer synthase of PQS in *P. aeruginosa* QS. Protein expression systems should preferably be easy to culture, fast growing, and able to produce large yields of protein. Therefore, instead of using *P. aeruginosa* as an expression organism for PqsBC, *E. coli*, was used as it fullfils the above criteria.

After PqsBC is expressed by *E. coli*, purification of the PqsBC enzyme complex is performed. In crystallography, protein purification also holds a vital role for characterisation of function, structure, and interactions of the protein interest. In general, obtaining protein in its active conformation is preferable, where characteristics such as size, solubility, specific binding affinity, and charge are

assessed (Berg et al., 2002). Available techniques for the protein purification are salting out, dialysis, gel-filtration chromatography, ion-exchange chromatography, affinity chromatography, and high-pressure liquid chromatography (Berg et al., 2002).

4.2 Expression and purification of PqsBC

The genes of *pqsB* and *pqsC* of *P. aeruginosa* PAO1 were cloned into plasmid pET28b using restriction-free (Carnoy et al.) cloning (van den Ent and Löwe, 2006). Protein overexpression of pqsBC-NHis$_8$ was carried out in *E. coli* Rosetta2-(DE3)[pLysS] cells in TB medium with 150 µg/mL of kanamycin antibiotic.

PqsBC^{C129A} was purified using immobilised metal affinity chromatography (IMAC) (**Figure 4.1.)**, and gel filtration chromatography (**Figure 4.2.)** using either Akta PrimePlus (GE Healthcare Life Sciences, Pittsburgh, PA, USA) or BioLogic (BioRad, Hercules, CA, USA) chromatography systems. PqsBC^{C129A} based on gel filtration data indicating that PqsB and PqsC form a tight complex with an apparent molecular mass of 51 kDa.

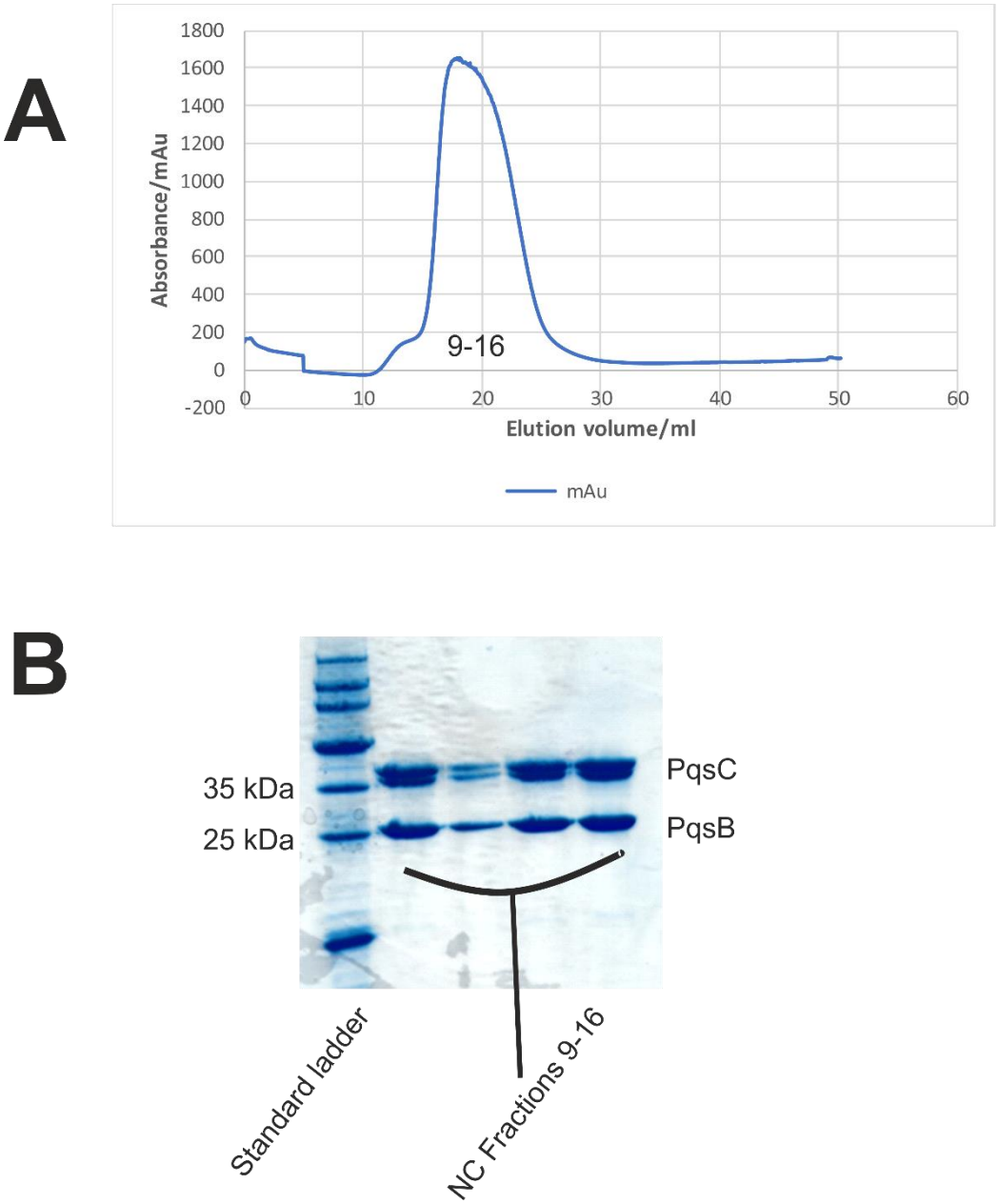


Figure 4.1. Purification of PqsBC^{C129A} **(A)** Nickel column chromatogram. Curve of UV absorbance and the concentration of buffer B are shown. (**B**). SDS-PAGE of Nickel column fractions 9-16 shows that the protein is relatively pure.

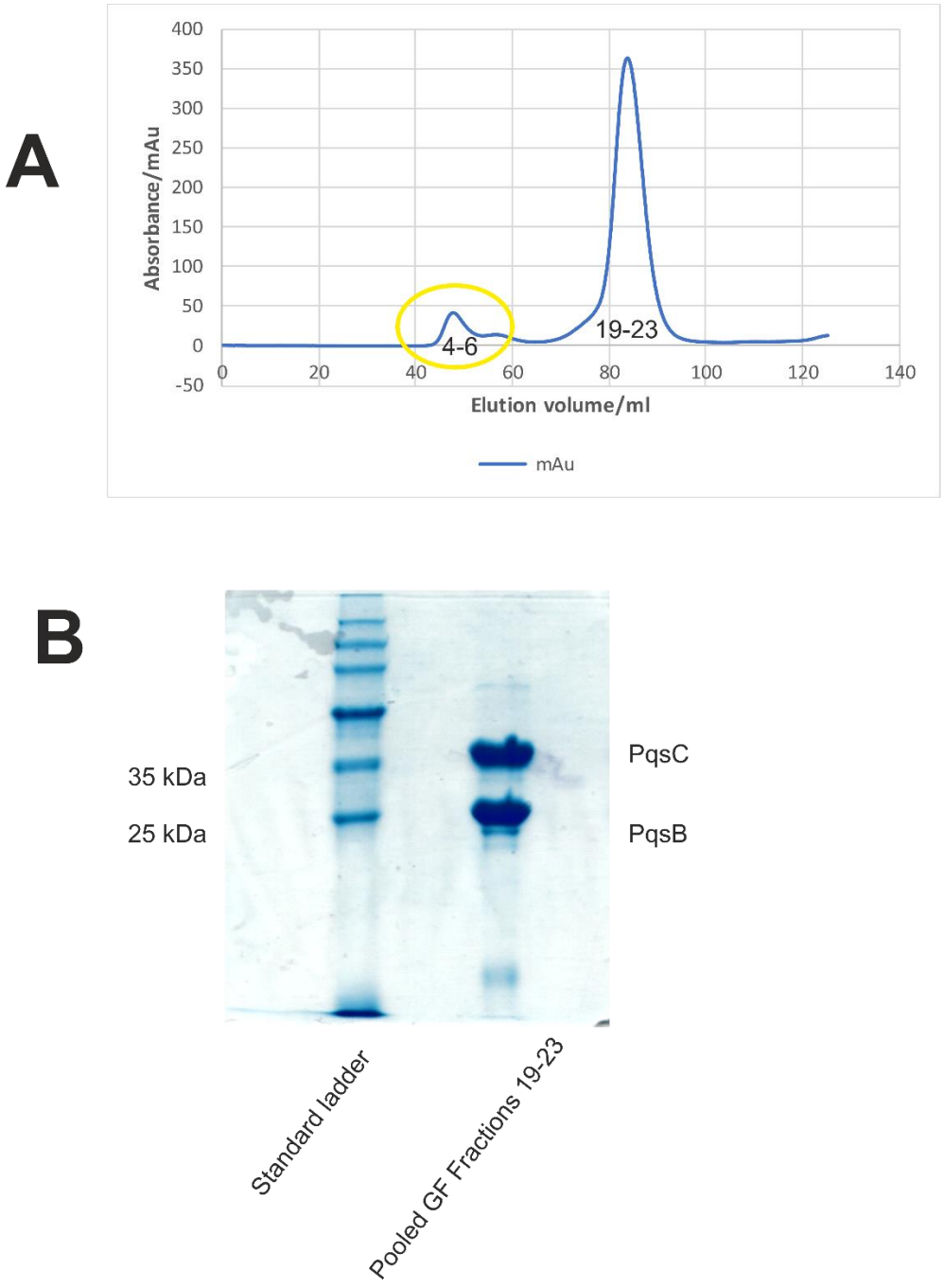


Figure 4.2. Purification of PqsBC^{C129A} by Superdex 200 16/60 column (**A)** Gel filtration chromatogram showing a small peak at elution volume 50-60 ml (in yellow circle) which is an oligomer of PqsBC (explanation on chapter 8), and the heterodimer PqsBC^{C129A} peak at 80-90 ml elution volume (61 kDa). (**B**) SDS-PAGE of pooled gel filtration fractions 19-23 shows that the protein is relatively pure.

4.3 Crystallisation of PqsBC

Principally, the process of protein crystallisation is to supersaturate a protein solution. Therefore, protein concentration, pH, ionic strength, salts, ligands, temperature, precipitant, and crystallisation method have a major impact on the success rate of crystallisation. Further, there are two steps to the crystallisation process, which are screening conditions in which the protein will crystallise, and subsequent optimisation of physical and chemical parameters to produce diffraction quality crystals.

Protein samples of wild-type PqsBC and the active site protein variant $PqsBC^{C129A}$, $PqsBC^{C129S}$, $PqsBC^{C129A}$ with the substrates such as 2-ABA and Oct-CoA with additive screen HR2-428 (Hampton Research) in 40 mM MOPS buffer, pH 8.1, 100 mM NaCl, 0.3 mM DTT at protein concentrations of 31.5 and 36.5 mg ml^{-1}, respectively, were diluted with 100 mM NaCl to give 3 mg/ml. These samples were subjected to screens, including Pi-PEG, Procomplex, classics lite, Mbclass, Index, PACT, Morpheus, JCSG+, and MIDAS, using the sitting drop vapor diffusion method (Mosquito robot, TTP Labtech, Melbourne, UK). The plates consisted of 96 different conditions for crystal growth.

The screening plates were made using a Mosquito HTS micro-dispensing system (TTP Labtech). The concentration of protein used for crystallisation was 3 mg/ml. The volume of the sitting drop plate was 0.6 µl total (0.3 µl protein and 0.3 µl reservoir solution). The initial crystal hits were obtained in Index-HR2-144 (**Figure 4.3**) condition 73: of 0.2 M Sodium chloride, 0.1 M Tris pH 8.5, 25% w/v Polyethylene glycol 3350. Crystals appeared within 24 hours.

In this precipitant solution, sodium chloride consists of charged ions capable of affecting protein solubility through interaction with the protein's surface-exposed, charged residues (Rupp, 2009). Whereas PEG is an organic precipitant that decreases the protein's solubility. The decrease in protein solubility can be explained by competition of this polyalcohol for water molecules around the protein, thus forcing the protein molecules to interact with each other rather than the polar solvent (Tardieu et al., 2002). In some cases, ordered PEG molecules are occasionally visible as electron density in the space between protein molecules, where they may participate in crystal contacts, although this is not their main functional role in crystallisation (Rupp, 2009). Tris provides the buffer to maintain the pH (and hence a specific local charge distribution) of the protein independent of the other components and the original protein stock solution's pH, thereby allowing a systematic variation of the pH during crystallisation screening (Rupp, 2009).

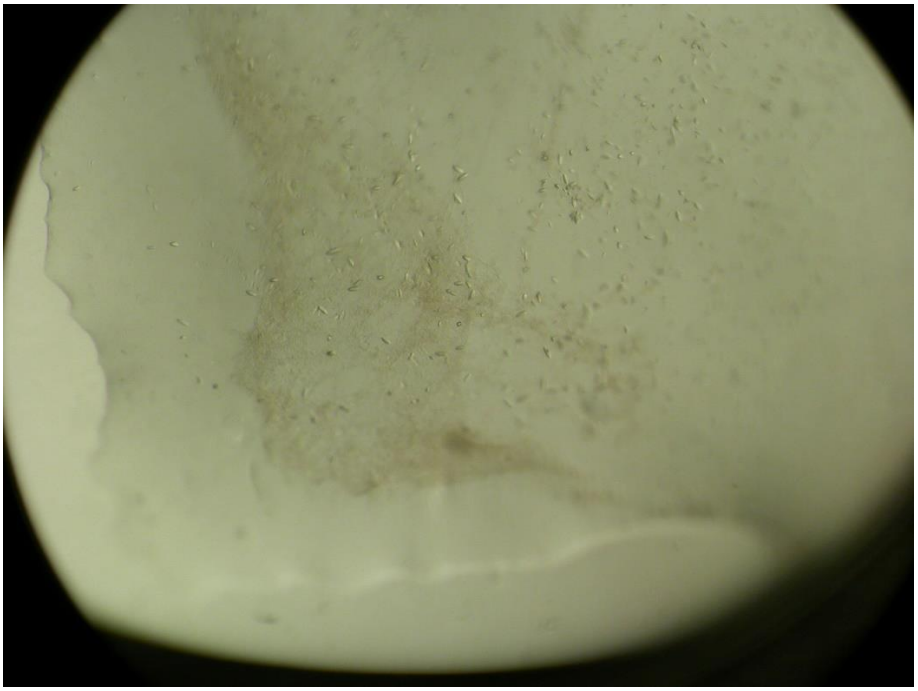


Figure 4.3. The initial hit of PqsBC^{C129A} crystals from a solution containing 0.2 M sodium chloride, 0.1 M Tris pH 8.5, 25% w/v polyethylene glycol 3,350.

4.4 Optimisation of PqsBC crystallisation

The initial screening condition that produced crystals was optimised to improve the quality of the crystals. The PqsBC^{C129A} and PqsBC^{C129A}-Fe^{3+} optimisations were performed using a 24 well sitting drop plate instead 96 well by altering variables such as buffer and salt concentration, pH and protein concentration. The PEG concentration was varied in 1% increments: 23-27%, and three pHs were used: 8.3, 8.5, and 8.7. The concentration of protein used for optimisation was 3 mg/ml. The volume of the sitting drop plate was 4 µl total (2 µL protein and 2 µL reservoir solution). PqsBC^{C129A} also appeared after 24 hours. The size of the crystals on 24 well optimisation plate at pH 8.3 were larger than at pH 8.5 (**Figure 4.4**). The

final optimised crystal condition comprised 25% PEG 3350, 0.1 M Tris pH 8.3, and 0.2 M NaCl.

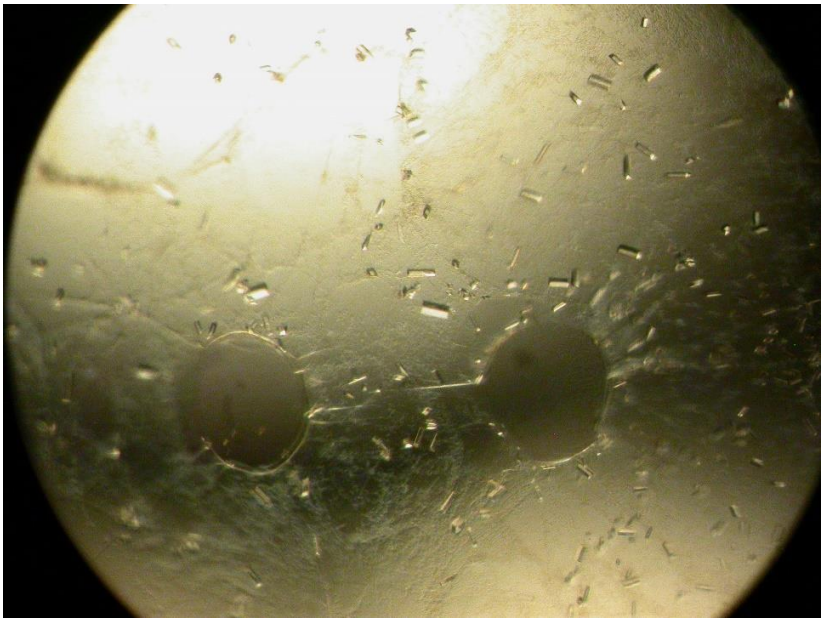


Figure 4.4. The optimisation of PqsBC^{C129A} crystals produced in a precipitant solution of 0.2 M sodium chloride, 0.1 M Tris pH 8.3, 25% w/v polyethylene glycol 3350.

Chapter 5: Crystal structure of PqsBC^{C129A}-Fe^{3+}

5.1 Co-crystallisation of PqsBC with additives

Each atom in the unit cell contributes to every reflection in reciprocal space. The contribution of an atom's scattering is greatest when the *h,k,l* indices correspond to lattice planes that intersect that atom. Therefore, a specific atom contributes to some reflections strongly and weakly to others. Also, one atom could contribute much more strongly than others if it has a higher atomic number; a so-called heavy atom. In this study an additive screen was used, and successfully generated crystals with different morphologies. Specifically, 0.1 M iron (III) chloride hexahydrate and 0.1 M spermidine gave different crystals, which have an octahedral shape. Moreover, not only did the crystal have a different morphology, the space group and unit cell of these PqsBC crystals was different. Here, PqsBC co-crystallised with iron in space group P 4_12_12 with unit cell indices a=166.27, b=166.27, c=63.2, α=90, β=90 and γ=90. The space group and unit cell indices from PqsBC without the heavy atom were $P2_12_12_1$, a=78.486, b=114.96, c=289.67, α=90, β=90 and γ=90.

5.2 Crystallisation of PqsBC^{C129A}-Fe^{3+}

Initial crystallisation experiments were carried out with a protein concentration 3 mg/ml and 0.6 µl total drop size (0.3 µl protein and 0.3 µl precipitant solution). The PqsBC^{C129A}-Fe^{3+}crystal was obtained in Index-HR2-144 (**Figure 5.1**) condition 73; 0.2 M sodium chloride, 0.1 M Tris pH 8.5, 25% w/v polyethylene glycol 3350 with 0.01 M iron (III) chloride hexahydrate. Crystals appeared within approximately 24 hours.

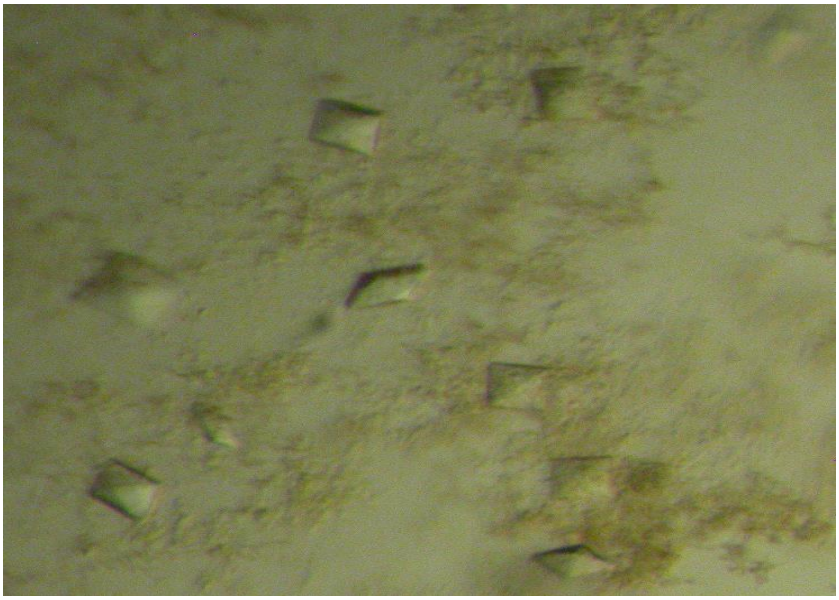


Figure 5.1. PqsBC^{C129A} crystals on 96 well within solution of 0.2 M Sodium chloride, 0.1 M Tris pH 8.5, 25% w/v Polyethylene glycol 3,350 that added 0.01 M iron (III) chloride hexahydrate.

5.3 Data collection the PqsBC^{C129A}-Fe^{3+} crystal form

PqsBC^{C129A}-Fe^{3+} crystals were cryoprotected in a solution of 27% PEG 3350, 0.1 M Tris pH 8.3, 0.2 M NaCl, 25% glycerol, and flash-cooled in liquid nitrogen prior data collection at the Diamond Light Source synchrotron facility beamline I02. The wavelength used for its data collection was 1.1401 Å and data collected to 2.30Å. Details of PqsBC^{C129A} data collection crystal as shown in **Table 5.1.**

Table 5.1. Data collection of $PqsBC^{C129A}$-Fe^{3+}

	$PqsBC^{C129A}$ Iron
Data collection	
Space group	$P4_12_12$
Cell dimensions	
a, *b*, *c* (Å)	166.27, 166.27, 63.2
α, β, γ (°)	90, 90, 90
wavelength	1.14014
Resolution (Å)	2.346
*R*merge[a] *	0.083
$I / \sigma I$	14.5 (2.8)
Completeness (%)	99.6 (95.7)
Redundancy	6.5 (3.4)
CC 1/2[b]	0.997 (0.808)
Unique reflections	244497

*Values in parenthesis correspond to the highest resolution shell. [a]R_{merge}= Σh Σi |*I*i(h) - <*I*(h)> / | Σh Σi *I*i(h), where *I* is the observed intensity and <*I*> is the average intensity of multiple observations from symmetry-related reflections calculated with XDS. [b]Correlation coefficient value calculated using XDS to determine the resolution cut-off.

5.4 $PqsBC^{C129A}$-Fe^{3+} crystal structure refinement and validation

Datasets were collected using the strategy provided by FastDP and íMosflm. Further, the processed data were continuing with Truncate, Matthews coeff. Molecular replacement was performed with PHASER using a variety of templates generated using MrBUMP (D. Winn et al., 2006) from pdb codes 3h76, 3h77, 3h78 of the PqsD structure (McCoy et al., 2007). Using different resolution cut-offs resulted in an incomplete solution from which a partial model was built using BUCCANEER (Cowtan, 2006) and electron density maps were subsequently improved using 2-fold non-

crystallographic symmetry. The model was completed manually using COOT and refined with REFMAC5 (**Figure 5.2**) (A Vagin et al., 2005) giving 631 residues in total.

Details of $PqsBC^{C129A}$-Fe^{3+} data refinement statistics and Ramachandran plot are shown in **Table 5.2** and **Figure 5.3**, which show that $PqsBC^{C129A}$-Fe^{3+} residues are within the preferred and allowed regions, as is known in a polypeptide the main chain N-C_α and C_α-C bonds relatively are free to rotate. These rotations are represented by the torsion angles phi and psi, respectively. Ramachandran used computer models of small polypeptides to systematically vary phi and psi with the objective of finding stable conformations. For each conformation, the structure was examined for close contacts between atoms. Atoms were treated as hard spheres with dimensions corresponding to their van der Waals radii. Therefore, phi and psi angles which cause spheres to collide correspond to sterically disallowed conformations of the polypeptide backbone. The pink regions correspond to conformations where there are no steric clashes, i.e. these are the allowed regions namely the α-helical and β-sheet conformations. The yellow areas show the allowed regions if slightly shorter van der Waals radii are used in the calculation, ie the atoms are allowed to come a little closer together. This brings out an additional region which corresponds to the left-handed alpha-helix.

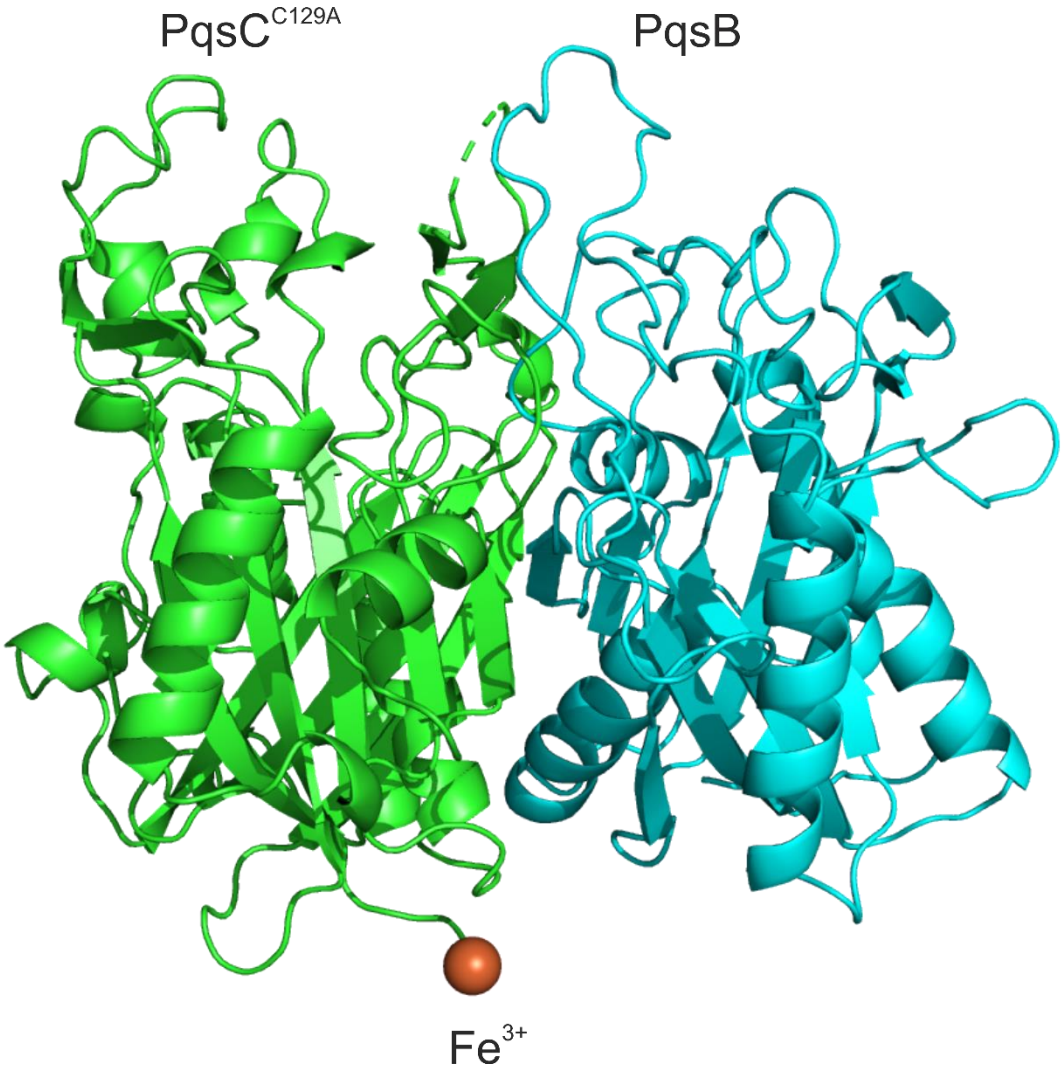


Figure 5.2. Cartoon diagram of refined PqsBC^{C129A}-Fe^{3+} crystal structure. PqsC^{C129A} (green), PqsB (cyan) and Fe^{3+} are shown (red sphere).

Table 5.2. Refinement statistics of PqsBC^{C129A}-Fe^{3+}

Refinement [c]	
R_{work}	0.157 (0.2363)
R_{free}	0.211 (0.2630)
Overall B factor (A^2)	41.9
Stereochemical r.m.s. deviations	
Bond lengths (Å)	0.0186
Bond angles (°)	2.19
Ramachandran plot	
Most Favoured	97.44
Allowed	2.56
Outliers	0

*Values in parenthesis correspond to the highest resolution shell. [c]All values calculated using REFMAC. R_{work} = Σh ||Fo|h - |Fc|h| / Σh|Fo|h, where Fo and Fc are the observed and calculated structure factors, respectively. R_{free} computed as in R_{work}, but only for (5%) randomly selected reflections, which were omitted in refinement.

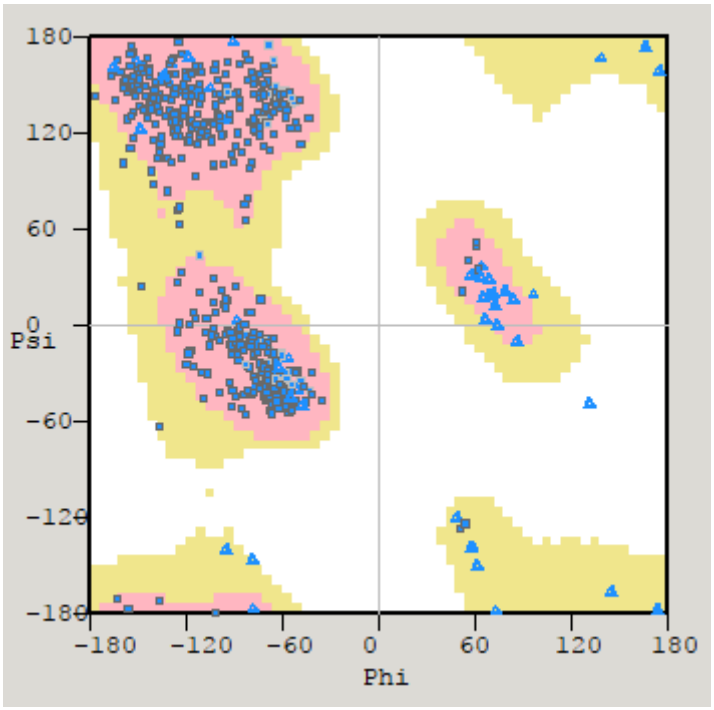


Figure 5.3. Ramachandran plot of PqsBC^{C129A}-Fe^{3+} crystal structure showing residues in the most favoured regions (pink) 97.44% and additional allowed regions (yellow) 2.56% regions, generated using Coot (Emsley and Cowtan, 2004). The squares denote non-glycine residues, whereas glycine residues are denoted by triangles.

5.5 PqsBC^{C129A}-Fe^{3+} crystal structure shows iron binding to PqsB and PqsC

In addition to the interactions through PqsC residues 88–102 (termed loop B), PqsB and PqsC are also linked by iron (**Figure 5.4**). However, unlike catalytic site that located only on PqsC, the iron is bound to both PqsB and PqsC^{C129A} (**Figure 5.4**).

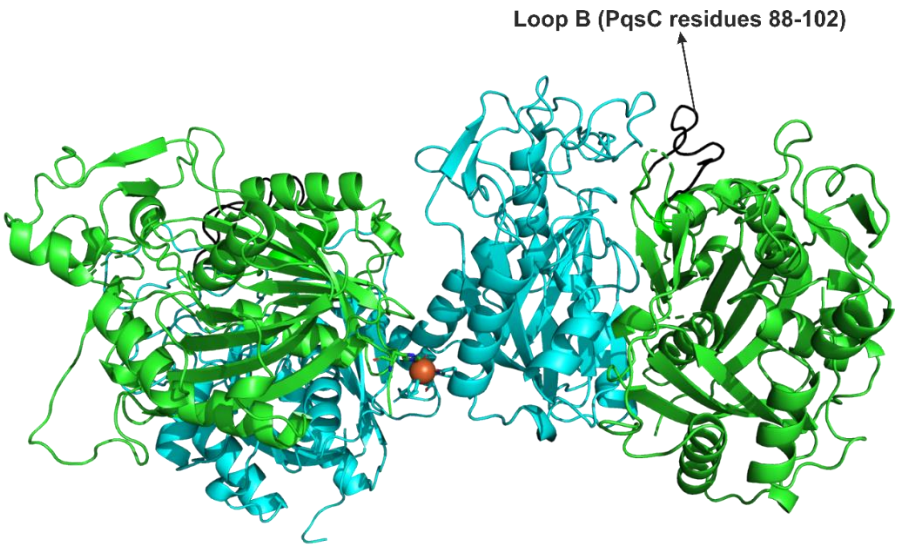


Figure 5.4. Cartoon diagram of refined PqsBC^{C129A}-Fe^{3+} crystal structure with space group $P4_12_12$. PqsC^{C129A} (green), PqsB (cyan) and Fe^{3+} (red sphere). Residues that involved on binding to Fe^{3+} shown by stick diagram.

Furthermore, as can be seen on **Figure 5.5**, iron is bound to His2, Glu48, Glu280, and His282. Whereas, His2 is located at the N-terminus of PqsC and Glu280 with His282 located toward the C-terminus of PqsB.

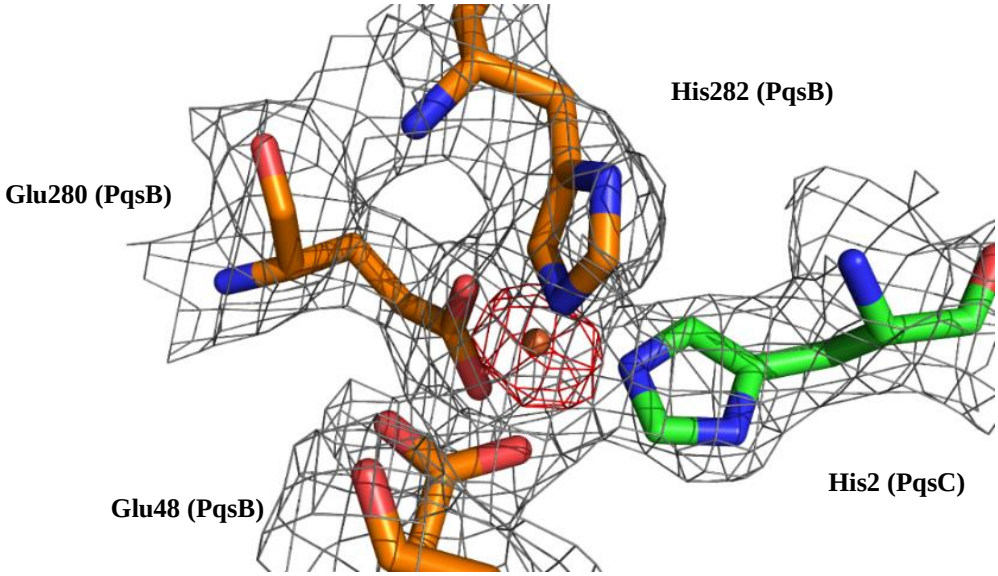


Figure 5.5. Stick diagram of the binding site of PqsB and PqsC, a 2.3 Å electron density map is shown (grey), and the anomalous map is shown (red), rendered with Pymol showing the PqsC residue His2 as a stick in green, the PqsB residues Glu48, Glu280, and His282 as sticks in orange.

5.6 PqsBC^{C129A}-Fe^{3+} and PqsBC^{C129A} crystal structure alignment

There is no significant difference of PqsBC^{C129A}-Fe^{3+} and PqsBC^{C129A} crystal structures (**Figure 5.6**). As it can be seen on **Figure 5.6** only some loops are having slightly different conformation.

However, the prominent difference would only be seen on quaternary structure, whereas PqsBC^{C129A}-Fe^{3+} conformed as hetero dimer that linked by Fe^{3+} whilst PqsBC^{C129A} conformation as hetero tetramer (**Figure 5.7**).

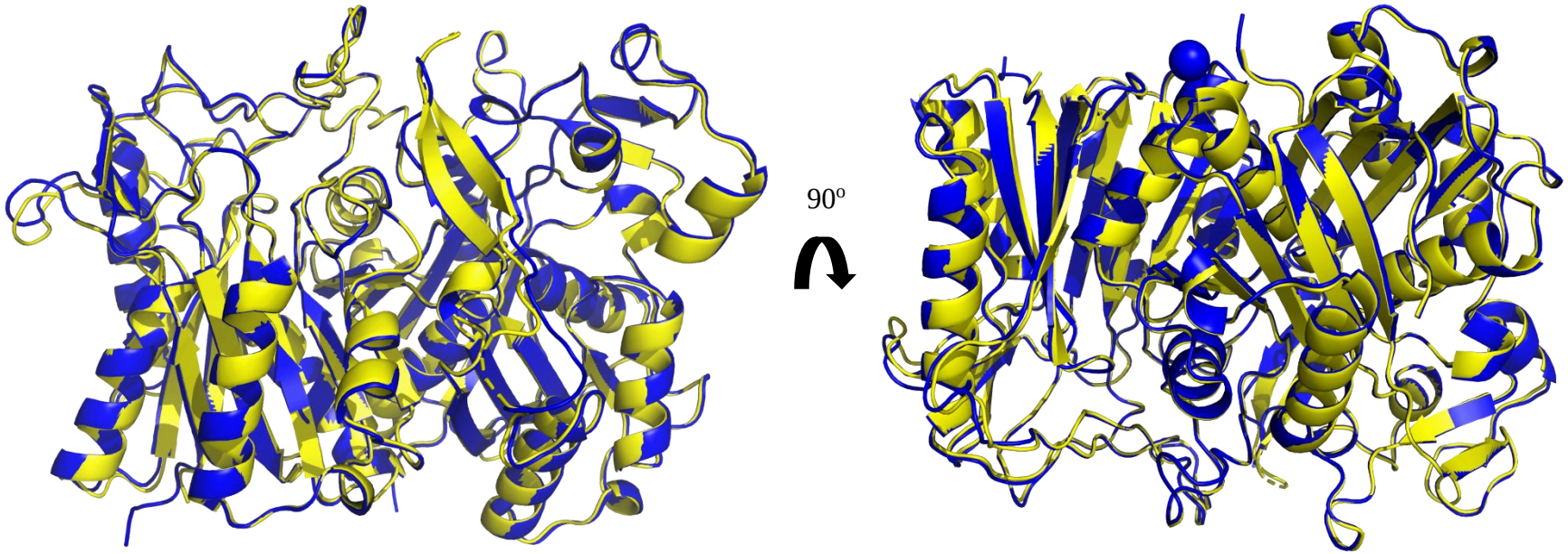


Figure 5.6. Cartoon diagram of structure superposition of PqsBC^{C129A}-Fe^{3+} (blue) and PqsBC^{C129A}(yellow) crystal structures. RMSD value is 1.021 aligned and calculated with PyMOL.

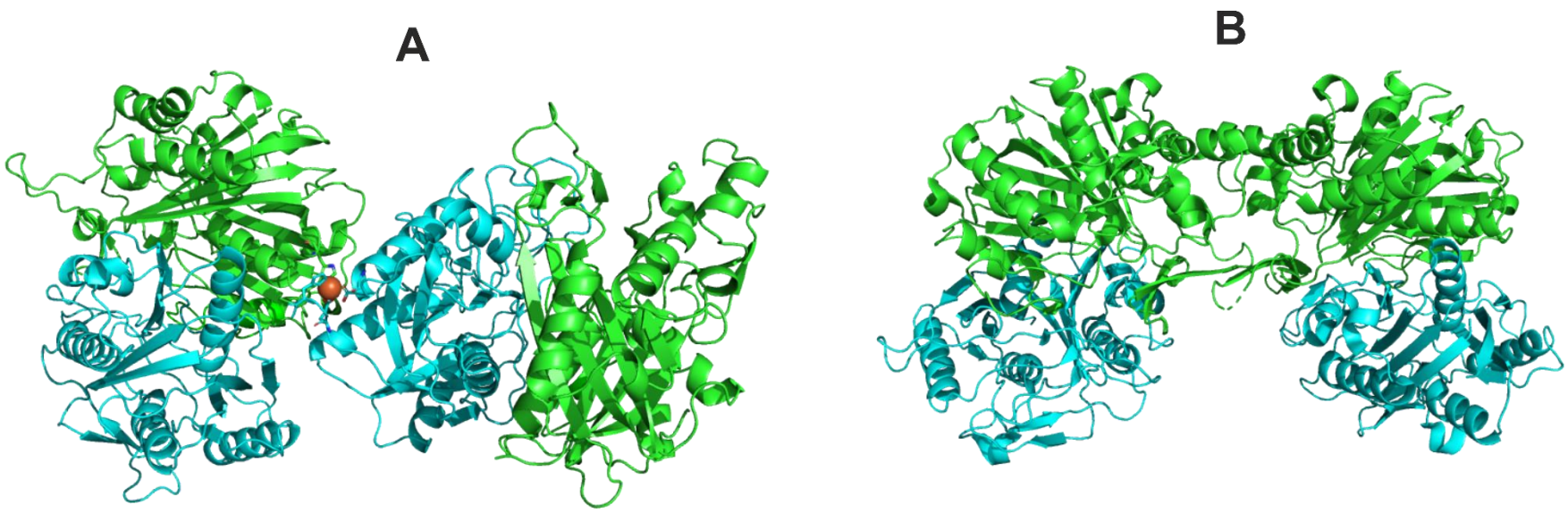


Figure 5.7. Cartoon diagram of $PqsBC^{C129A}$-Fe^{3+} (**A**) and $PqsBC^{C129A}$ (**B**) quaternary crystal structures-conformation comparison. $PqsC^{C129A}$ (green), PqsB (cyan) and Fe^{3+} (red sphere). Residues are involved on binding to Fe^{3+} shown by stick diagram.

5.7 PqsBC^{C129A}-Fe^{3+} crystal interfaces and packing analysis

The crystal structure of PqsBC^{C129A}-Fe^{3+} was predicted to have one PqsB and one PqsC molecule in the asymmetric unit. PISA (Krissinel and Henrick, 2007) was employed to study the interfacial contacts and calculate the surface area involved in the interaction. It was observed that PqsBC^{C129A}-Fe^{3+} has three relevant crystal contact surfaces, with contact areas 2204.1 Å^2 (SC1-BC), 986.5 Å^2 (SC2-CC), 93.6 Å^2(SC3-FeBC) (**Table 5.3**); stabilised through a combination of hydrophobic and hydrophilic interactions.

Table 5.3. PISA interfaces list. Interfaces in PqsBC^{C129A}-Fe^{3+} crystal.

Contact surface of PqsB	**Number of amino acids involved in interface contact**	**Symmetry operators**	**Contact surface area, Å^2**
Surface contact 1 (SC1-BC)	116	x,y,z	2204.1 Å^2
Surface contact 2 (SC2-CC)	66	y,x,-z	986.5 Å^2
Surface contact 3 (SC3-FeBC)	10	-y-1/2,x+1/2,z+1/4 x,y,z	93.6 Å^2

The largest interface area (SC1-BC) comprises 61 PqsB residues and 55 PqsC^{C129A} residues with a surface area of 2240.2 Å^2 (**Figure 5.8**). This interface comprises thirty-eight hydrogen bonds and two salt bridges (**Table 5.4)** (**Figure 5.8 and 5.9**). This largest interface area is likely the mediator for complex formation, as the interface scored 0.831 for the complex formation significance score (CSS), where the CSS can range from 0 to 1 as the interface relevance increases with respect to

complex formation. Twenty-four residues of PqsB form hydrogen bonds in the SC1-BC interface, including residues from α helix-2 (Gln85, Lys86), helix-2-adjacent loop residues (Ala63, Pro66, Asp74, Met76, Ala77, Pro78), β strand-5 (Arg92, Ala93, Val95, Asp97, Thr99, Asp100), α helix-3 (Arg105, Thr112, Ser115, Asp116, Gln117, Tyr119), β strand-9 (Gly156, Arg162), and loops between β strand-9 with β strand-10 (Ile178, leu180) (**Figure 5.9**).

In addition, there are twenty-two residues hydrogen bonding residues from PqsC in the SC1-BC interface. They include β strand-9 (Gly101, Leu103, Tyr104), α helix-3 (Asn109), β strand-6 (Pro122, Asp124, Gln126), α helix-4 (Arg137, Ser141, Lys147), β strand-9 (Ser195, Glu197, His 198, Ser 199), three residues after β strand-9 (Ala201, Thr202, Tyr204), β strand-10 (Gly209, Trp211), α helix-5 (Lys255) (**Figure 5.9**). It is also clearly seen that the charge distribution of the SC1-BC interface is fairly homogeneous (**Figure 5.10**). Subsequently, the second largest interface area within $PqsBC^{C129A}$-Fe^{3+} is Surface contact 2 (SC2-CC), with an interface area 986.5 $Å^2$, and is composed of 33 residues from $PqsB^{C129A}$ and 33 residues from $PqsC^{C129A}$ (**Figure 5.11**). The interface is stabilised via 16 hydrogen bonds (**Table 5.5**). This interface scored 0.100 for CSS, hence, this interface plays an auxiliary role in complex formation. Furthermore, the third interface SC3-FeBC is engaged between PqsB, PqsC and the Fe^{3+} ion, The SC3-FeBC interface scored 0.169 for CSS, hence, it implies that interface also plays an auxiliary role in complex formation. In this interface, iron binds to two nitrogen atoms of His282 (PqsB) and His2 (PqsC) along with two oxygen atoms on Glu48 (PqsB) and Glu280 (PqsB) (**Figure 5.5**) (**Figure 5.12**).

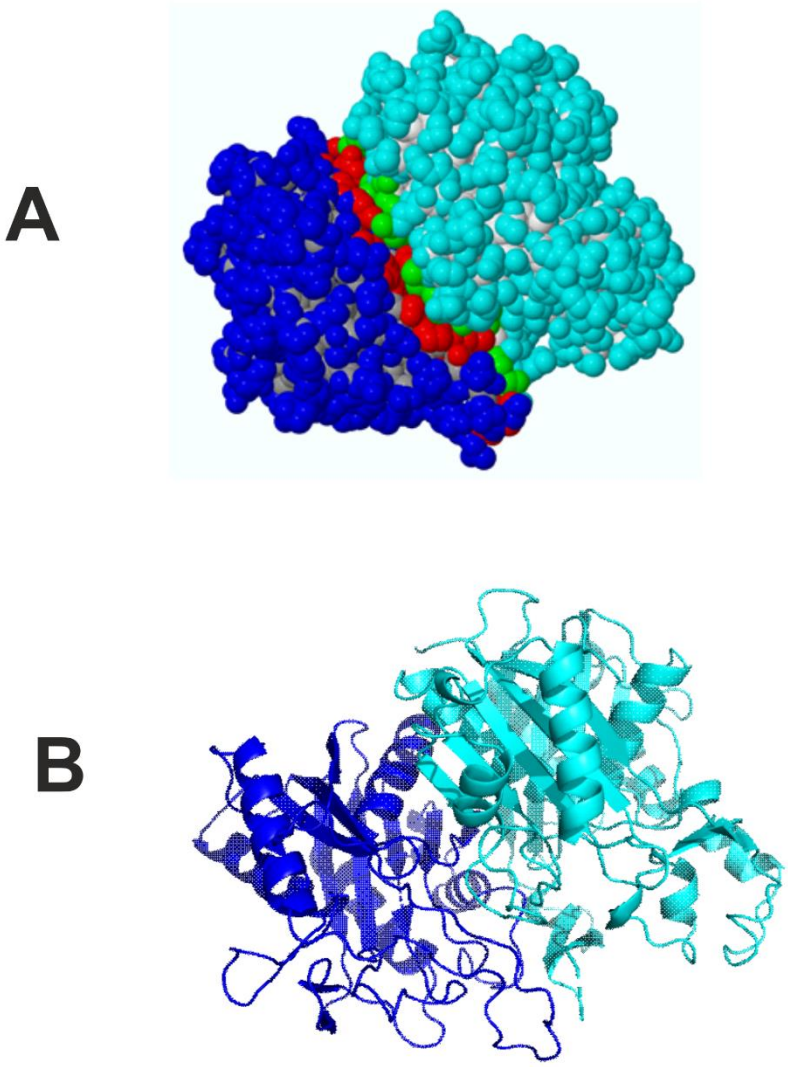


Figure 5.8. Sphere (A) rendered with JyMOL and Cartoon (B) rendered with PyMOL diagram of SC1-BC interface. **A)** PqsB (blue), $PqsC^{C129A}$ (cyan), interface area (red and green). **B)** PqsB (blue) and $PqsC^{C129A}$ (cyan).

Table 5.4. Hydrogen bonds and salt bridges of interfacial contact 1 (SC1-BC)

No.	PqsB	Dist. Å^2	PqsC^{C129A}
1	B:LEU 180[N]	2.91	C:GLY 101[O]
2	B:LYS 79[NZ]	3.90	C:TYR 104[OH]
3	B:ILE 178[N]	2.85	C:TYR 104[O]
4	B:ARG 162[NH2]	2.99	C:ASN 109[OD1]
5	B:ARG 105[NE]	3.19	C:PRO 122[O]
6	B:THR 99[OG1]	2.69	C:ASP 124[O]
7	B:ASP 97[N]	3.20	C:GLN 126[O]
8	B:GLN 117[NE2]	3.05	C:SER 195[OG]
9	B:GLN 117[NE2]	3.67	C:SER 195[O]
10	B:TYR 119[OH]	3.69	C:GLU 197[OE1]
11	B:GLN 117[NE2]	2.65	C:GLU 197[OE1]
12	B:VAL 95[N]	2.84	C:SER 199[OG]
13	B:GLN 85[NE2]	2.98	C:SER 199[O]
14	B:LYS 86[NZ]	3.84	C:ALA 201[O]
15	B:MET 76[N]	2.76	C:GLY 209[O]
16	B:ALA 77[N]	3.33	C:GLY 209[O]
17	B:ALA 63[O]	3.86	C:TYR 104[OH]
18	B:PRO 66[O]	2.87	C:TRP 211[NE1]
19	B:ASP 74[O]	3.13	C:TRP 211[N]
20	B:ALA 77[O]	2.86	C:GLY 209[N]
21	B:PRO 78[O]	2.80	C:TYR 204[OH]
22	B:GLN 85[OE1]	3.50	C:ALA 201[N]
23	B:ARG 92[O]	3.85	C:HIS 198[ND1]
24	B:ALA 93[O]	3.64	C:HIS 198[ND1]
25	B:ALA 93[O]	3.02	C:SER 199[N]
26	B:VAL 95[O]	3.86	C:SER 199[OG]
27	B:ASP 97[O]	2.90	C:GLN 126[N]
28	B:ASP 100[OD2]	2.98	C:ARG 106[N]
29	B:THR 112[OG1]	3.18	C:LYS 147[NZ]
30	B:THR 112[O]	3.77	C:GLN 145[NE2]
31	B:SER 115[OG]	3.17	C:GLN 145[NE2]
32	B:ASP 116[OD2]	3.00	C:SER 141[OG]
33	B:ASP 116[OD2]	2.74	C:ARG 137[NH2]
34	B:GLN 117[OE1]	3.51	C:LYS 255[NZ]
35	B:GLN 117[OE1]	3.69	C:ARG 137[NH2]
36	B:GLY 156[O]	2.95	C:LYS 147[NZ]
37	B:ILE 178[O]	2.88	C:LEU 103[N]
38	B:ILE 178[O]	3.62	C:TYR 104[N]
Salt bridges			
No.	**PqsB**	**Dist. Å^2**	**PqsC^{C129A}**
1	B:ASP 116[OD2]	3.40	C:ARG 137[NH1]
2	B:ASP 116[OD2]	2.74	C:ARG 137[NH2]

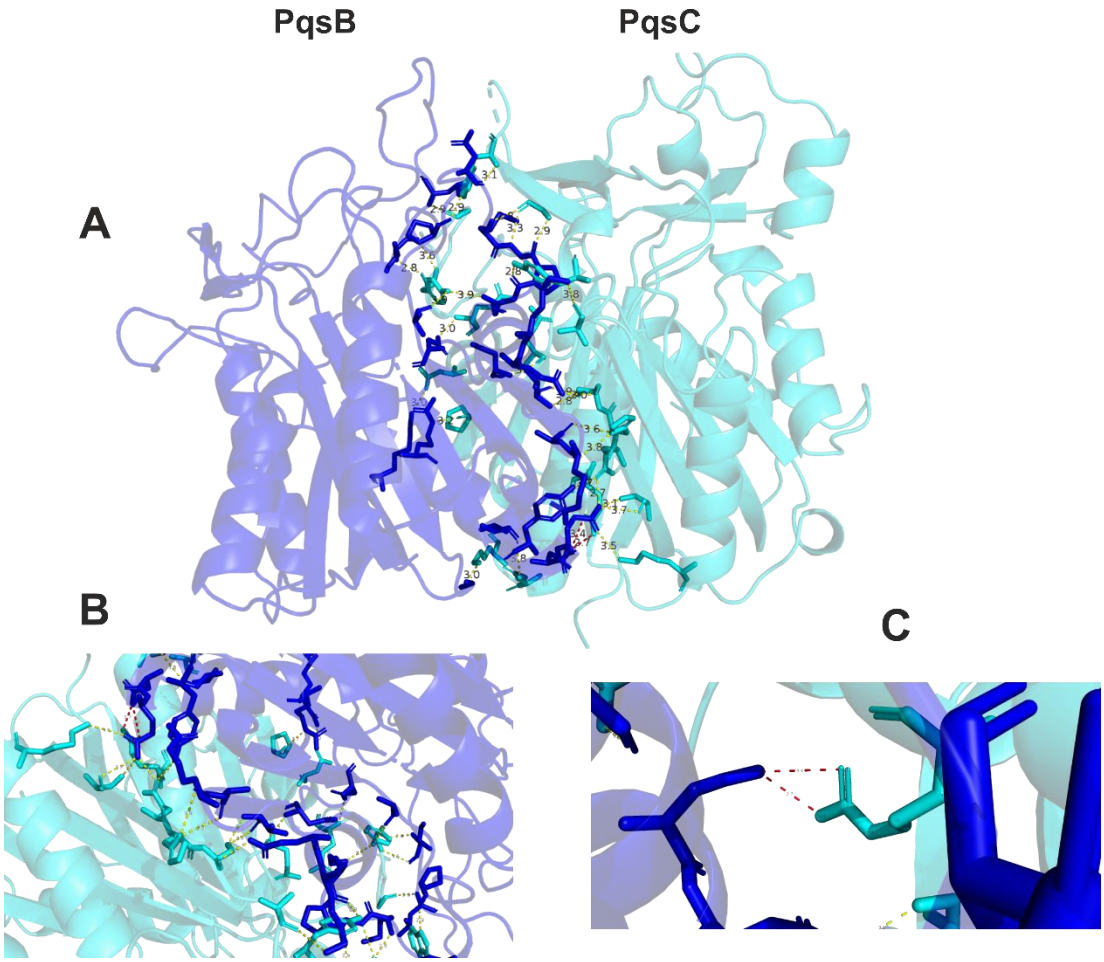


Figure 5.9. Part of PqsBC residues involved in stabilising the surface contact 1 (SC1-BC) through hydrogen interactions. **A**. Cartoon and stick diagram of SC1-BC residues that build the interface between PqsB (blue) and PqsC (cyan). **B**. Different angle of SC1-BC interface. **C**. Salt bridges on SC1-BC (dash in red), PqsB Asp116[O] – PqsC Arg137[NH].

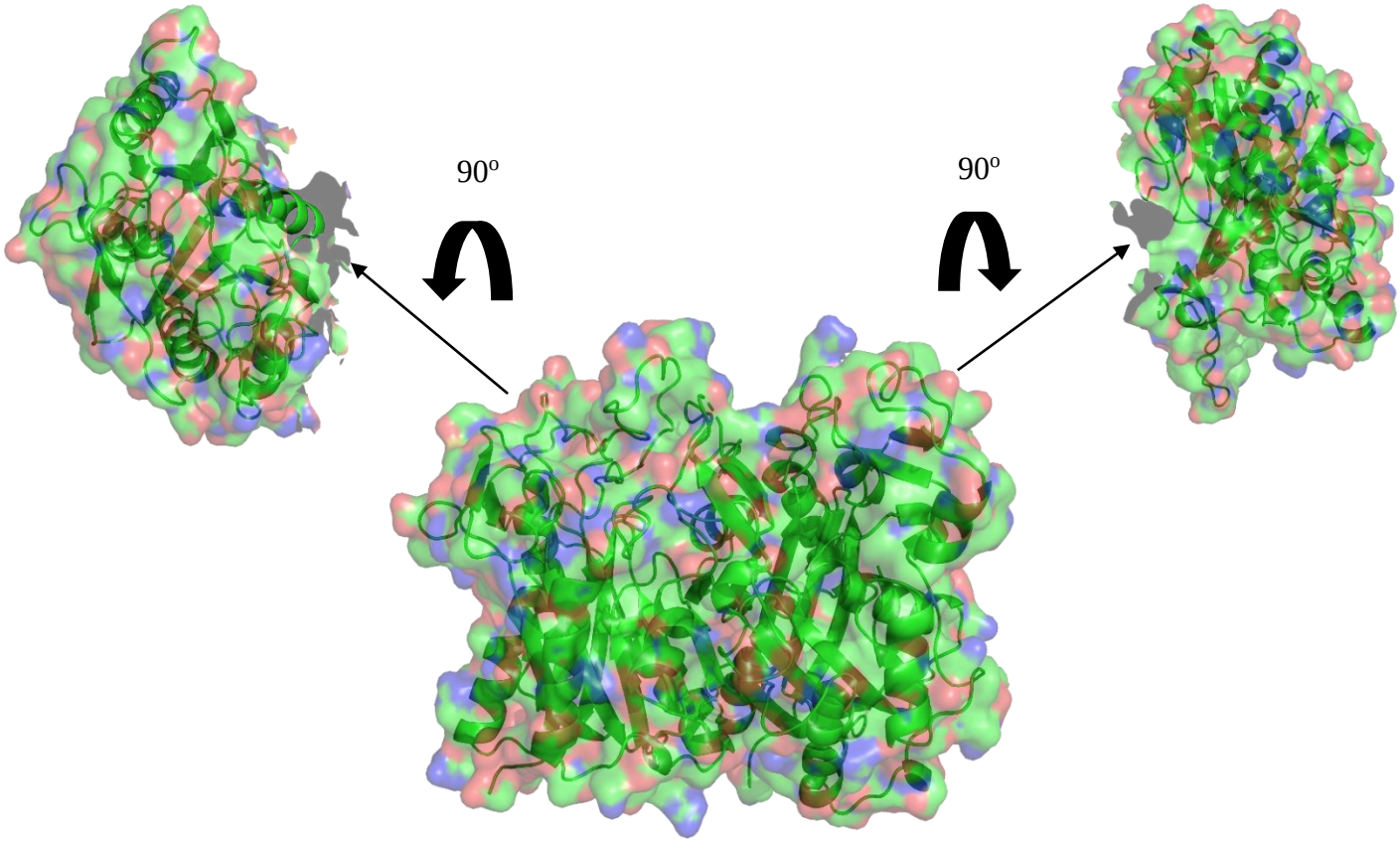


Figure 5.10. The surface contact 1 (SC1-BC) within PqsB and PqsC^{C129A}. The Molecules were rotated 90º along X axis to show the contact surface of each monomer. The electrostatic surface representation clearly shows the charge distribution on the contact surface. The blue colour represents the positive charge and red represents the negative charge. This also clearly, show the surface is equally through hydrophobic and hydrophilic interactions.

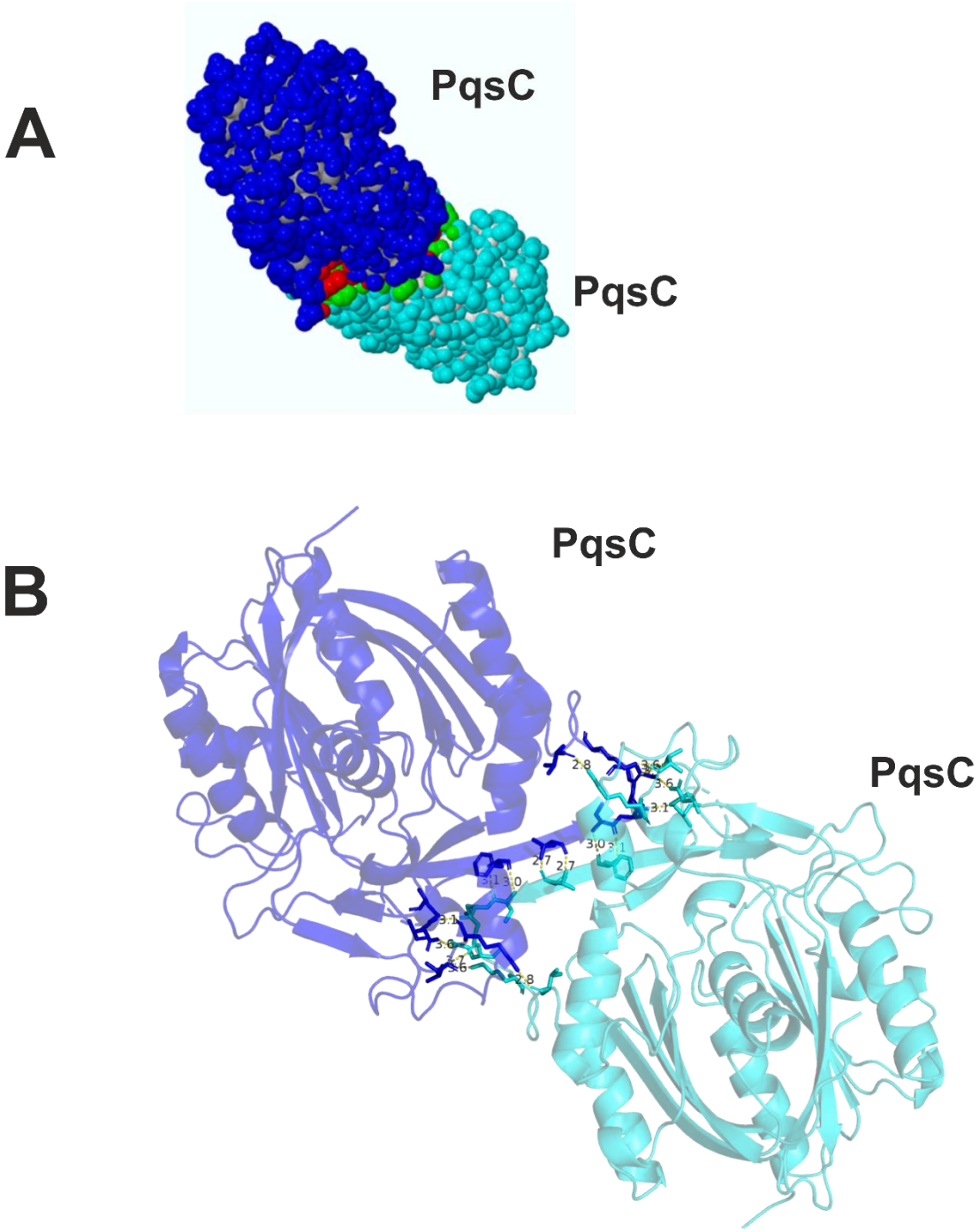


Figure 5.11. Sphere (A) rendered with JyMOL and Cartoon (B) rendered with PyMOL diagram of SC2-BC interface. **A)** $PqsC^{C129A}$ (blue), $PqsC^{C129A}$ (cyan), interface area (red and green). **B)** $PqsC^{C129A}$ (blue), $PqsC^{C129A}$ (cyan), interface area is shown in stick diagram.

Table 5.5. Hydrogen bonds of surface contact 2 (SC2-CC)

No.	PqsC^{C129A}	Dist. Å^2	PqsC^{C129A}
1	C:THR 166[OG1]	3.67	C:GLY 233[O]
2	C:ARG 168[NH2]	2.84	C:VAL 241[O]
3	C:ARG 212[NH1]	3.14	C:ASP 232[O]
4	C:PHE 227[N]	3.08	C:SER 231[O]
5	C:LEU 229[N]	2.74	C:LEU 229[O]
6	C:SER 231[N]	2.98	C:PHE 227[O]
7	C:GLN 234[NE2]	3.56	C:ASP 164[OD2]
8	C:LYS 236[NZ]	3.56	C:THR 166[OG1]
9	C:ASP 164[OD2]	3.56	C:GLN 234[NE2]
10	C:THR 166[OG1]	3.56	C:LYS 236[NZ]
11	C:PHE 227[O]	2.98	C:SER 231[N]
12	C:LEU 229[O]	2.74	C:LEU 229[N]
13	C:SER 231[O]	3.08	C:PHE 227[N]
14	C:ASP 232[O]	3.14	C:ARG 212[NH1]
15	C:GLY 233[O]	3.67	C:THR 166[OG1]
16	C:VAL 241[O]	2.84	C:ARG 168[NH2]

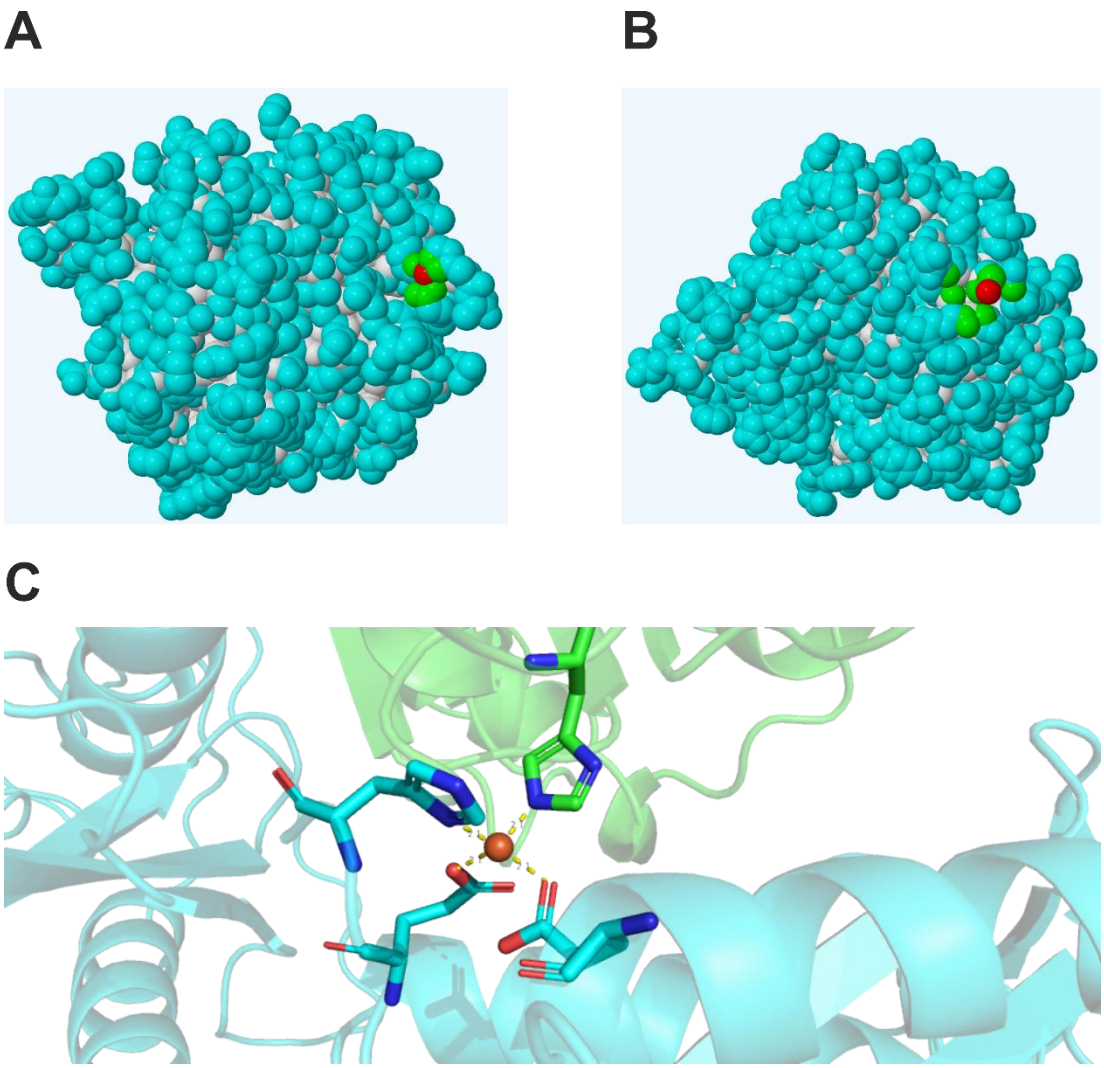


Figure 5.12. Sphere (**A**) and (**B**) rendered with JyMOL, Stick and cartoon diagram (**B**) rendered with PyMOL diagram of SC3-FeBC interface. (**A**) Interface of Fe^{3+} (red, green) with PqsB (cyan). (**B**) Interface of Fe^{3+} (red, green) with $PqsC^{C129A}$ (cyan). (**C**) Interface that is formed by Fe^{3+} (red sphere) that binds to two nitrogen atoms of His282 (PqsB) and His2 (PqsC) along with two oxygen atoms on Glu48 (PqsB) and Glu280 (PqsB), PqsB stick and cartoon diagram in cyan and PqsC stick and cartoon diagram in green.

5.8 Packing analysis of PqsBC^{C129A}-Fe^{3+} and PqsBC^{C129A}

PqsBC^{C129A}-Fe^{3+} crystals belong to the tetragonal space group $P4_12_12$ and contain a single heterodimer of PqsBC^{C129A}-Fe^{3+} in the asymmetric unit. **Figure 5.13** and **Figure 5.14** show the tetragonal crystal structure (in projection). In fact, the Fe^{3+} that binds to PqsBC^{C129A} has altered the crystal packing in comparison with PqsBC^{C129A}. **Figure 5.15** shows the orthorhombic crystal structure with space group $P2_12_12_1$ for PqsBC^{C129A} without Fe^{3+}. The asymmetric unit of PqsBC^{C129A} contains four copies of PqsB and four copies of PqsC. Analysis reveals a large 2,238 Å^2 surface area interface between the PqsB and PqsC subunits that is also present in the PqsBC^{C129A}-Fe^{3+} structure, as shown in **Figure 5.16.**

This differentiation of crystal packing between PqsBC^{C129A}-Fe^{3+} with PqsBC^{C129A} may happen due to PqsBC^{C129A}-Fe^{3+} has three interfaces that have achieved Complex Formation Significance Score (CSS) which are 0.831 for SC1-BC, 0.100 for SC2-CC, 0.169 for SC3-FeBC (**Figure 5.8**, **Figure 5.11**, **Figure 5.12**) (**Table 5.3**). To explain CSS for SC1-BC implies that the interface plays an essential role in complex formation. Meanwhile, CSS of SC1-CC and SC1-FeBC suggest that the interfaces play an auxiliary role in complex formation. On the other hand, PqsC^{C129A} without Fe^{3+} has only one almost identical type of interface that achieved Complex Formation Significance Score (CSS), which is the interface between PqsB and PqsC^{C129A} with the surface area buried by interactions is 2204.1 Å^2 (**Figure 5.15** and **5.16**). This interface scored 1.000 in Complex Formation Significance Score (CSS).

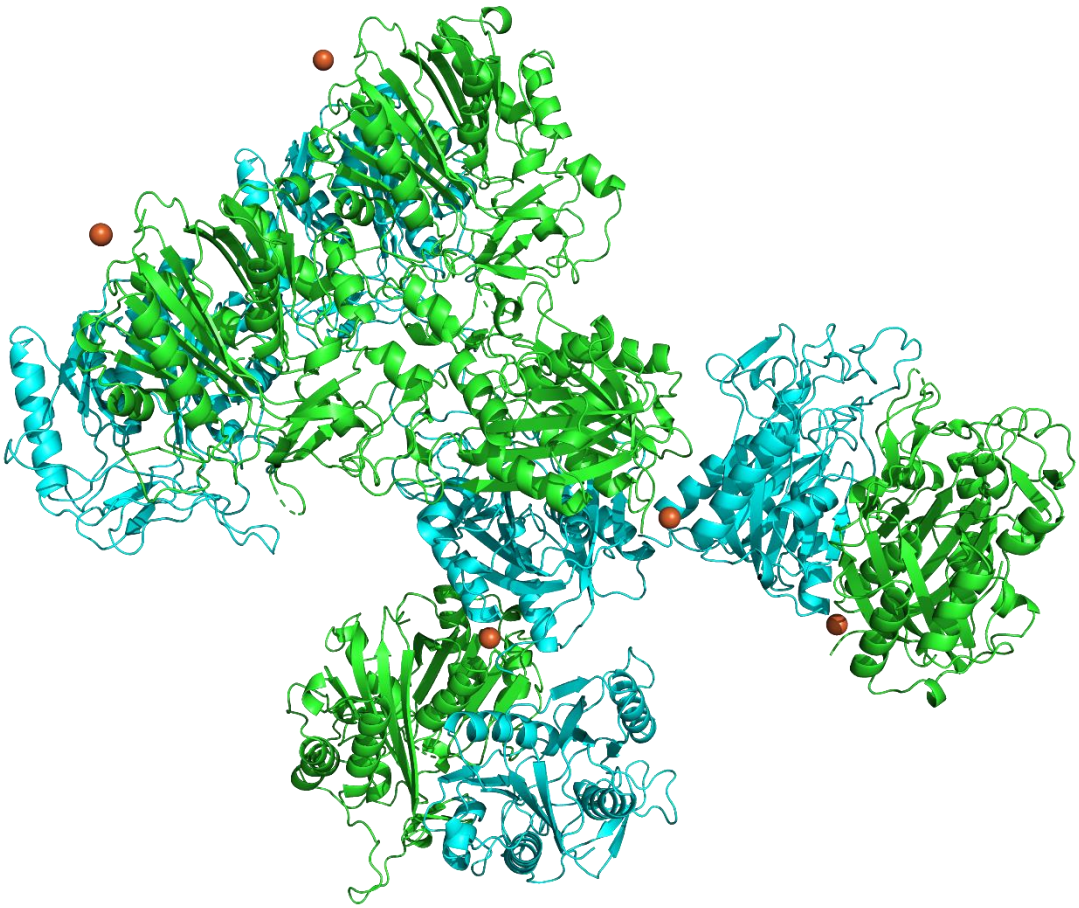


Figure 5.13. Cartoon diagram of PqsBC^{C129A}-Fe^{3+} (PqsB in cyan, PqsC in green, iron in red) symmetry generated within 4 Å**,** tetragonal crystal form (space group $P4_12_12$).

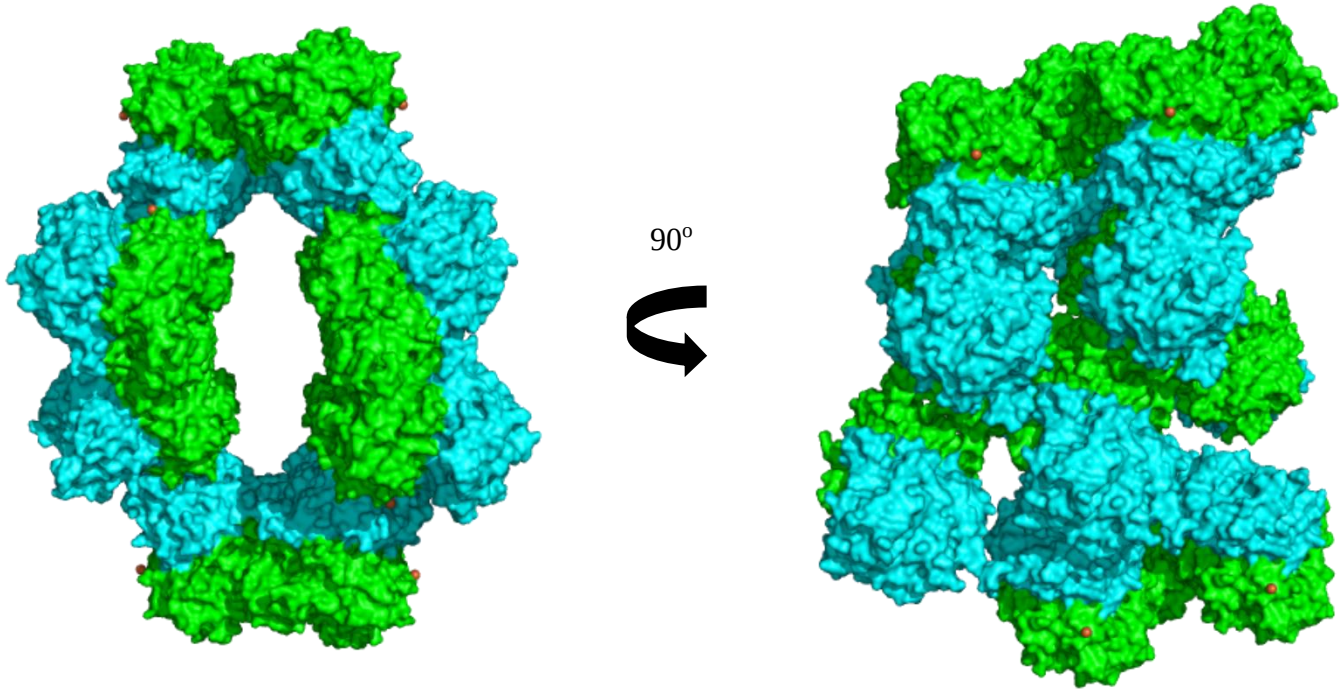


Figure 5.14. Surface representation of $PqsBC^{C129A}$-Fe^{3+} (PqsB in cyan, PqsC in green) crystallographic packing symmetry generated within 12 Å**,** tetragonal crystal form (space group $P4_12_12$). The Molecules were rotated 90º along X axis to show the different views.

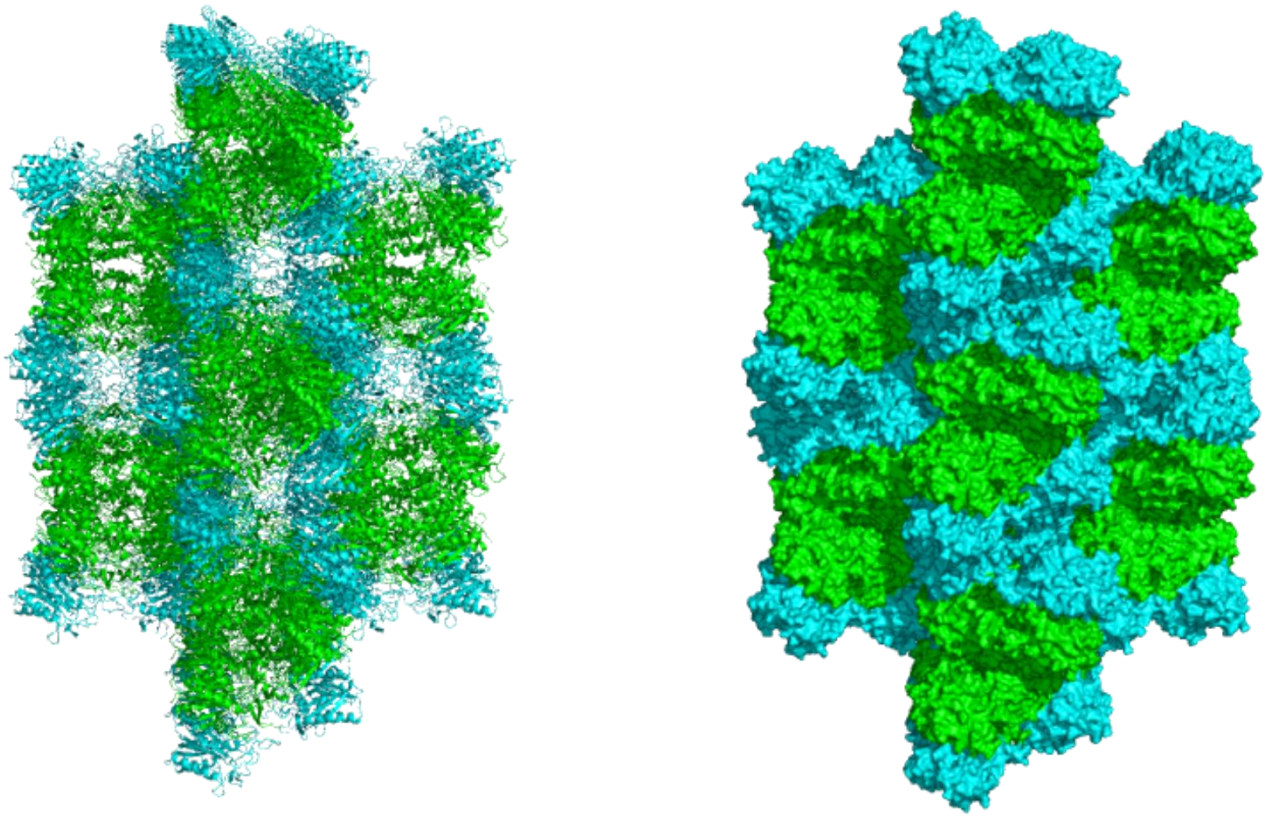


Figure 5.15. Cartoon and surface representation of PqsBC^{C129A} (PqsB in cyan, PqsC in green) crystallographic packing symmetry generated within 4 Å, orthorhombic crystal form (space group $P2_12_12_1$).

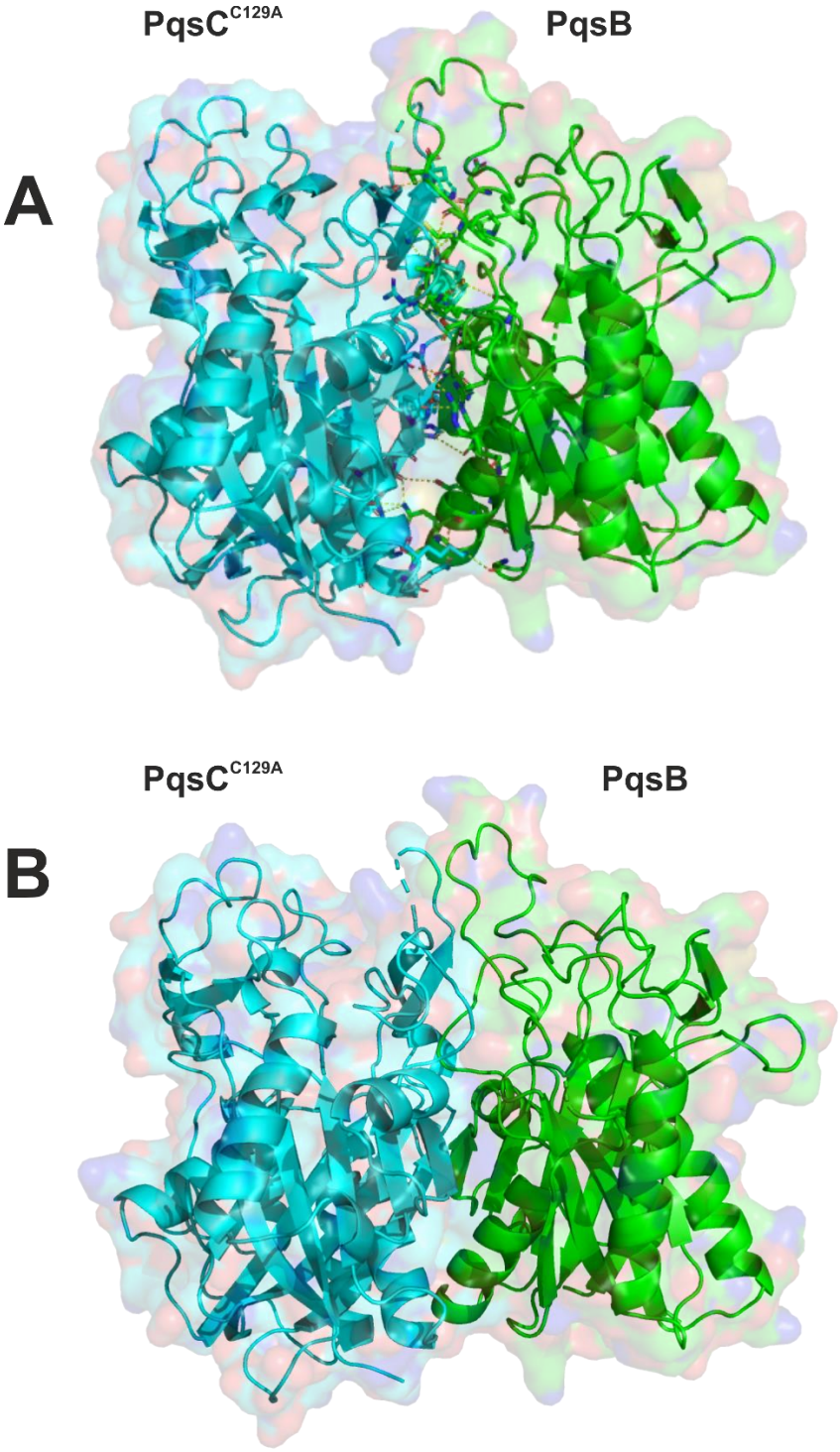


Figure 5.16. Cartoon diagram of (**A**) PqsBC^{C129A}-Fe^{3+} crystal structure with residues formed interface in stick diagram and (**B**) PqsBC^{C129A} heterodimer is shown with PqsB (green) and PqsC (cyan) covered with a transparent molecular surface illustrating the interface, interfaces reveals a large 2204.1 $Å^2$ surface area.

5.9 Analysis of Fe^{3+} bond length in $PqsBC^{C129A}$-Fe^{3+} structure

$PqsBC^{C129A}$-Fe^{3+} crystal structure shows that Fe^{3+} binds to two nitrogen atoms of His282 (PqsB) and His2 (PqsC) along with two oxygen atoms on Glu48 (PqsB) and Glu280 (PqsB) (**Figure 5.5**) (**Figure 5.12**) (**Figure 5.17**). The bond lengths are 2.1 Å on Fe-N (His282, PqsB), 2.1 Å on Fe-N (His2, $PqsC^{C129A}$), 2.1 Å on Fe-O (Glu280, PqsB), and 2.1 Å on Fe-O (Glu48, PqsB). It means, there are four bonds interaction between Fe^{3+} to $PqsBC^{C129A}$. In term of bond lengths that are observed, those are very similar to bond lengths of Azurin mutant M121E with iron ((Liu et al., 2014) and structure of FutA1 with Iron (II) (Koropatkin et al., 2007).

Iron bond lengths based on Azurin mutant M121E with iron (PDB code: 4QLW) (**Figure 5.17**) is consisted of 1.9 Å, 2.1 Å, and 2.4 Å. Meanwhile, structure of FutA1 with Iron (II) (PDB code: 2PT2) (**Figure 5.17**) is comprised of 2.0 Å and 2.6 Å. Another specific determination of iron−ligand bond length to nitrogen suggested that Fe−N bond lengths of 1.98−1.99 Å for both oxidation states of cyt *c* (Cheng et al., 1999). Furthermore, Fe-O bond distances varying from 1.90 to 2.31 Å (Acton, 2012). In conclusion, regarding all those data related iron bond lengths especially to nitrogen and oxygen, hence, Fe^{3+} bond lengths in $PqsBC^{C129A}$-Fe^{3+} crystal structure is legitimate.

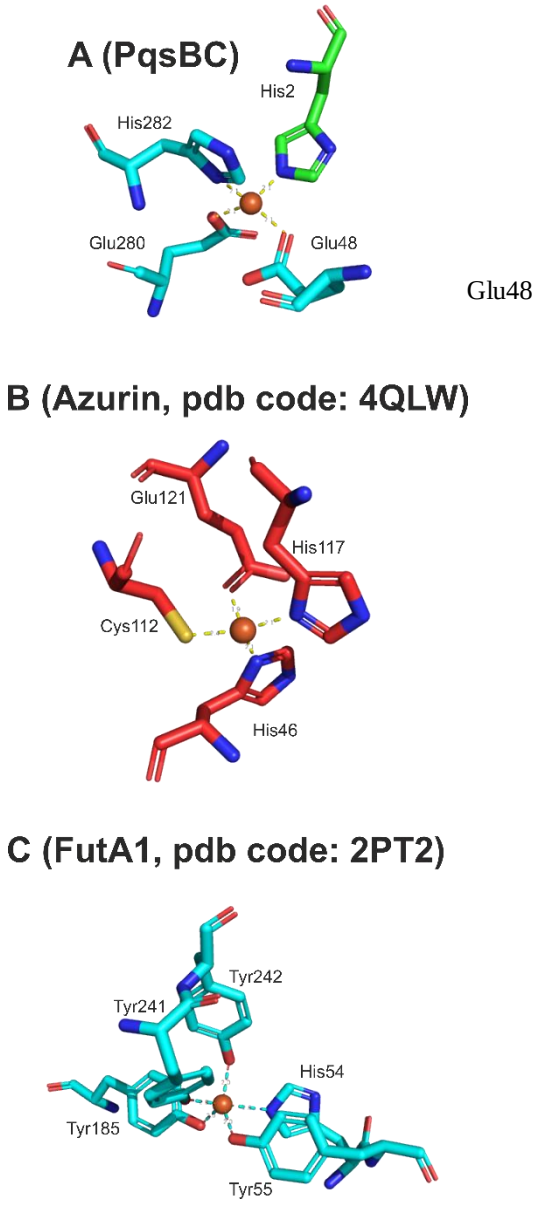


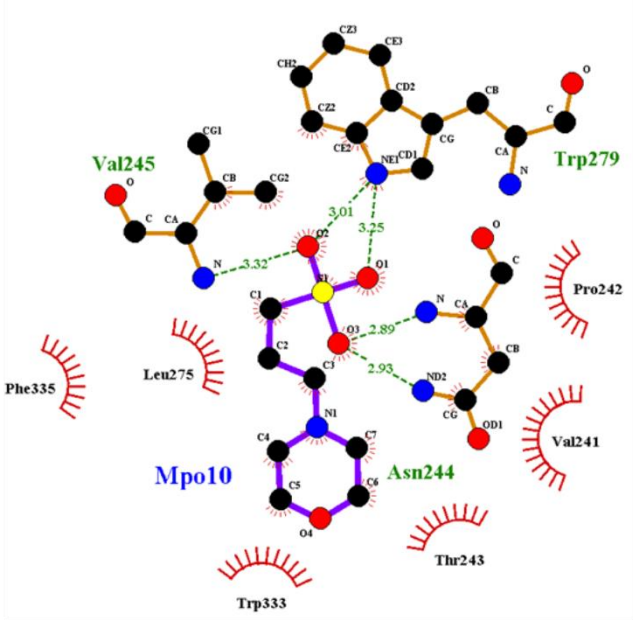
Figure 5.17. Sticks diagram of Fe^{3+} Interface that is formed by Fe^{3+} (red) that binds to **A**. Two nitrogen atoms of His282 (PqsB) and His2 (PqsC) along with two oxygen atoms on Glu48 (PqsB) and Glu280 (PqsB). **B**. One sulphur atom as one disulphide bond on Cys112 (2.4 Å), two nitrogen atoms of His117 (2.1 Å) and His46 (2.1 Å) along with one oxygen atoms on Glu121 (1.9 Å). **C**. Four oxygen atoms of Tyr55 (2.0 Å), Tyr185 (2.0 Å), Tyr241 (2.0 Å), Tyr242 (2.0 Å), one nitrogen atom of His54 (2.6 Å).

5.10 Ligands in PqsBC^{C129A}-Fe^{3+} structure

Two types of ligands that can be found on PqsBC^{C129A}-Fe^{3+} crystal structure, which are 3-(N-morpholino) propane-sulfonic acid (MOPS) and phosphates. MOPS is a buffer solution, whereas, phosphate is obtained from *E. coli* as the bacteria for protein overproduction. As can be seen on **Figure 5.18**, MOPS interactions generated using Ligplot (Wallace et al., 1995) and MOPS interactions generated using Pymol with a 2.3 Å electron density surrounded by Asn244, Val245, and Trp279 of PqsC^{C129A}.

Another interesting phenomenon in the crystal structure is that the phosphate ions line up along active site pocket of PqsBC^{C129A} (**Figure 5.19**). Furthermore, right at the end of the active site pocket of PqsBC^{C129A}, one of oxygen atoms of a phosphate moiety interact with a nitrogen atom of the imidazole side chain of His269 (**Figure 5.20**), a residue of the catalytic dyad of PqsBC^{C129A}. The bond length is 3.10 Å, which is similar to the bond of the catalytic triad residue His244 from *E. coli* FabH. This residue interacts with the thioester oxygen group of malonyl-ACP during enolisation to facilitate the formation of the carbanion at C2 (Davies et al., 2000, Heath and Rock, 2002).

A



B

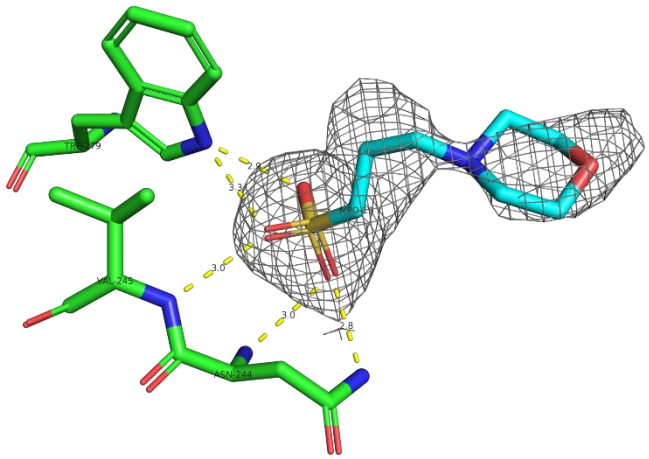


Figure 5.18. Ligplot (Wallace et al., 1995) show interactions between 3-(N-morpholino) propane-sulfonic acid (MOPS) to Asn244, Val245, and Trp279 of $PqsC^{C129A}$. **B.** Stick diagram of MOPS (cyan) covered by a 2.3 Å electron density map is shown (grey), rendered with Pymol showing MOPS are surrounded by $PqsC^{C129A}$ residues Asn244, Val245, and Trp279 as sticks in green.

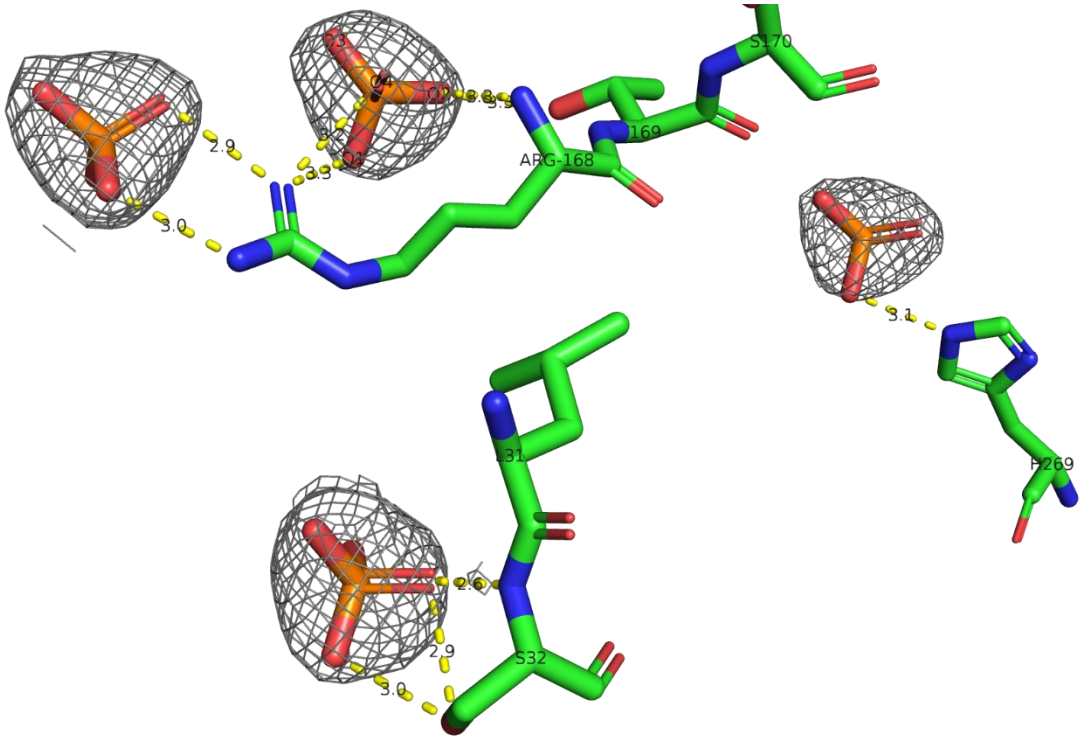


Figure 5.19. Stick diagram of four phosphate molecules (red) that inside the active site cleft covered by a 2.3 Å electron density map is shown (grey), rendered with Pymol showing phosphates molecules that interact to by PqsC residues Ser32, Arg168, Thr169, and His269 as sticks in green.

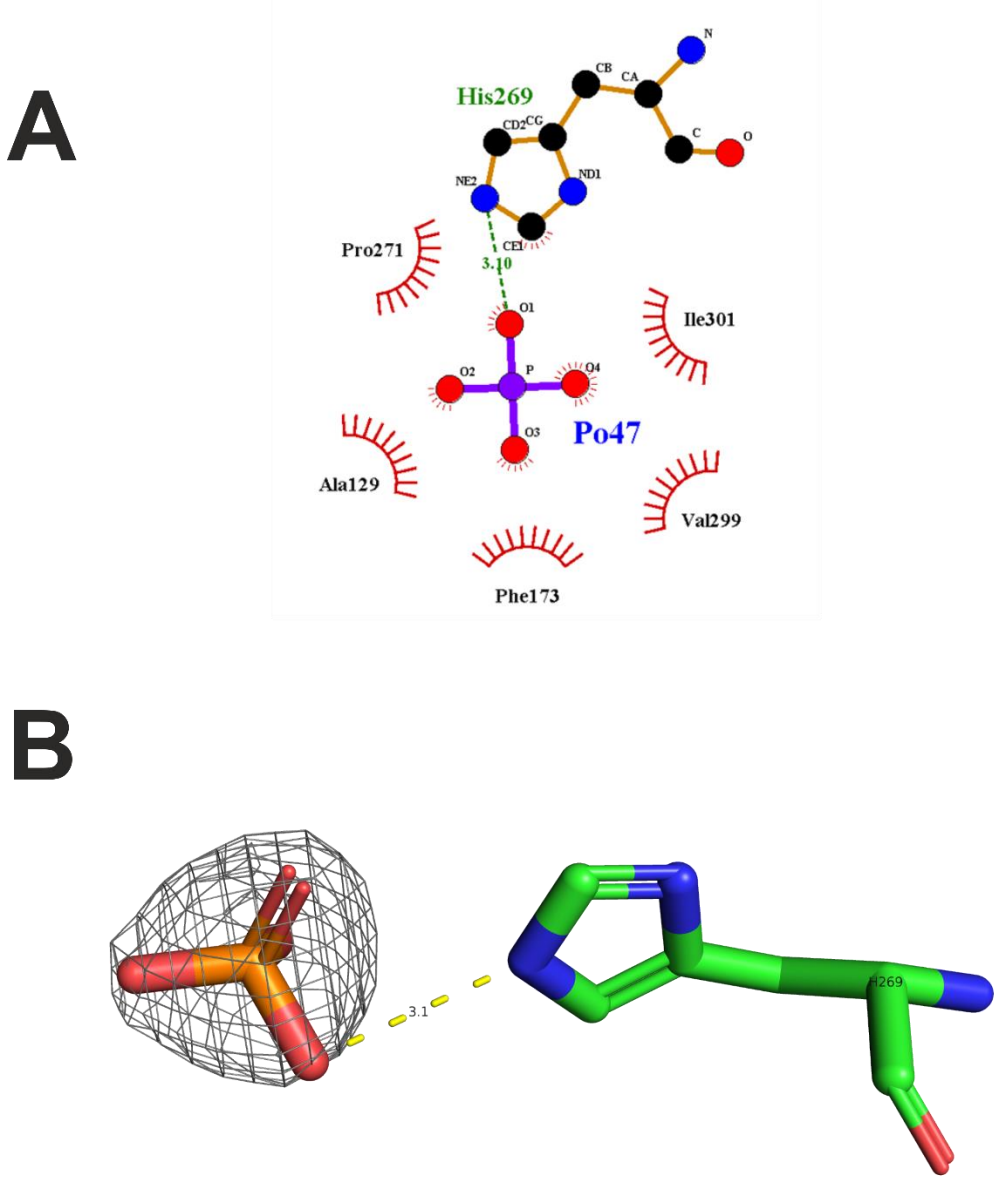


Figure 5.20. **A**. Ligplot (Wallace et al., 1995) show interactions between one of phospate ions inside PqsBC active site cleft to His269 of PqsC^{C129A}. **B**. Stick diagram of a phosphate molecule (red) covered by a 2.3 Å electron density map is shown (grey), rendered with Pymol showing the interaction one of PqsBC^{C129A} enzyme catalytic residue His269 with one of phosphate molecules that are lining up within active site pocket. With the bond length is 3.10 ÅChapter 6: Structure determination and characterisation of PqsBC^{C129A}

Chapter 6: Structure determination and characterisation of PqsBC^{C129A}

6.1 Data collection of PqsBC^{C129A} crystal

PqsBC^{C129A} crystals were cryoprotected in a solution of 27% PEG 3350, 0.1 M Tris pH 8.3, 0.2 M NaCl, 25% glycerol, and flash-cooled in liquid nitrogen prior to data collection at the Diamond Light Source synchrotron facility beamline I02. The wavelength used for its data collection was 0.97949 Å and data were collected to 2.0Å. Details of PqsBC^{C129A} data collection are shown in **Table 6.1.**

Table 6.1. Data collection of PqsBC^{C129A}

	PqsBC^{C129A}
Data collection	
Space group	$P2_12_12_1$
Cell dimensions	
a, *b*, *c* (Å)	78.5, 115.0, 289.7
α, β, γ (°)	90, 90, 90
wavelength	0.97949
Resolution (Å)	2.04
*R*merge[a] *	0.069
$I / \sigma I$	12.5 (1.9)
Completeness (%)	99.2 (96.7)
Redundancy	4.5 (4.6)
CC 1/2[b]	0.998 (0.661)
Unique reflections	166566

*Values in parenthesis correspond to the highest resolution shell. [a]R_{merge}= Σh Σi |*I*i(h) - <*I*(h)> / | Σh Σi *I*i(h), where *I* is the observed intensity and <*I*> is the average intensity of multiple observations from symmetry-related reflections calculated with XDS. [b]Correlation coefficient value calculated using XDS to determine the resolution cut-off.

6.2 PqsBC^{C129A} crystal structure refinement and validation

Molecular replacement was performed with PHASER using a variety of templates generated using MrBUMP (D. Winn et al., 2006) from PqsBC-Fe^{3+} model. Using different resolution cut-offs resulted in an incomplete solution from which a partial model was built using BUCCANEER (Cowtan, 2006) and electron density maps were subsequently improved using 4-fold non-crystallographic symmetry and solvent flattening with the CCP4 programs PARROT (Carter and Sweet, 1997). The resulting density-modified 2.0Å electron density map was of high quality allowing 95% of the model to be built by BUCCANEER. The model was completed manually using COOT and refined with REFMAC5 (**Figure 6.1**) (A Vagin et al., 2005) comprising 2474 residues in total. Details of PqsBC^{C129A} data refinement statistics and Ramachandran plot by PROCHECK (Laskowski et al., 1993) within PDBsum (Laskowski, 2001) are shown in **Table 6.2** and **Figure 6.2**. In polypeptide chains, main chain N-Cα and Cα-C bonds are relatively free to rotate. These rotations are represented by the torsion angles phi and psi, respectively. The Ramachandran plot shows PqsBC^{C129A} residues are in the preferred and allowed regions.

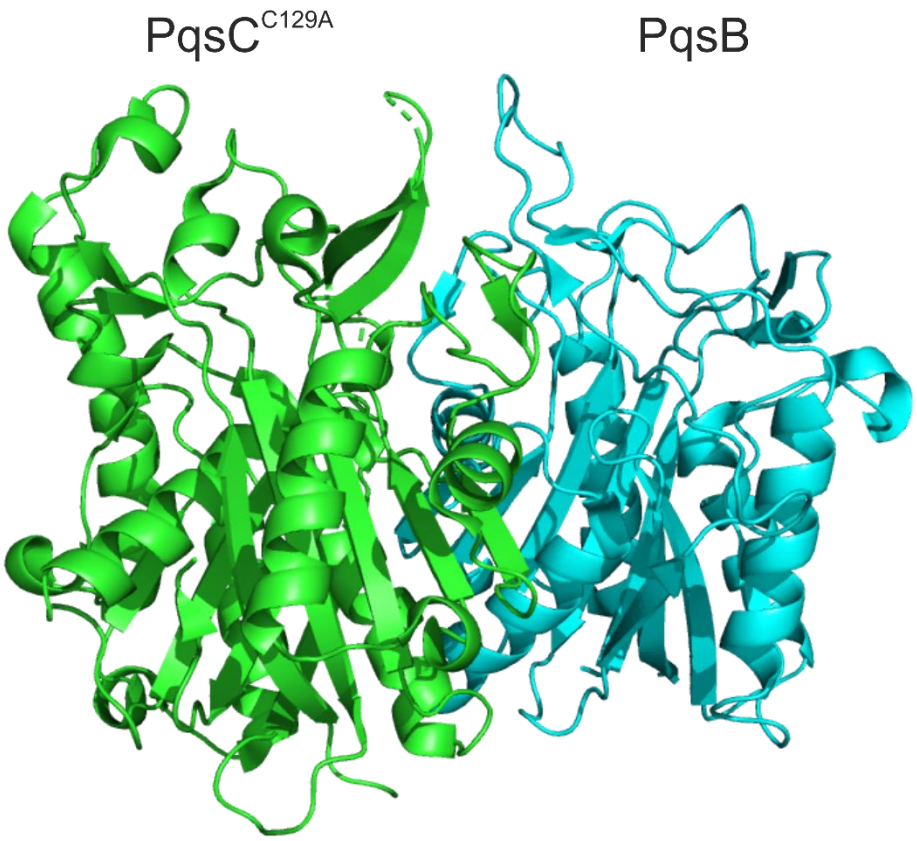


Figure 6.1. Refined PqsBC^{C129A} crystal structure with space group $P2_12_12_1$. PqsC^{C129A} (green) and PqsB (cyan).

Table 6.2. Refinement statistics of PqsBC^{C129A}

Refinement [c]	
R_{work}	0.190 (0.291)
R_{free}	0.237 (0.321)
Overall B factor (A^2)	38.1
Stereochemical r.m.s. deviations	
Bond lengths (Å)	0.016
Bond angles (°)	1.81
Ramachandran plot	
Most Favoured	97.7
Allowed	2.3
Outliers	0

*Values in parenthesis correspond to the highest resolution shell. [c]All values calculated using REFMAC. R_{work} = Σh ||Fo|h - |Fc|h| / Σh|Fo|h, where Fo and Fc are the observed and calculated structure factors, respectively. R_{free} computed as in R_{work}, but only for (5%) randomly selected reflections, which were omitted in refinement.

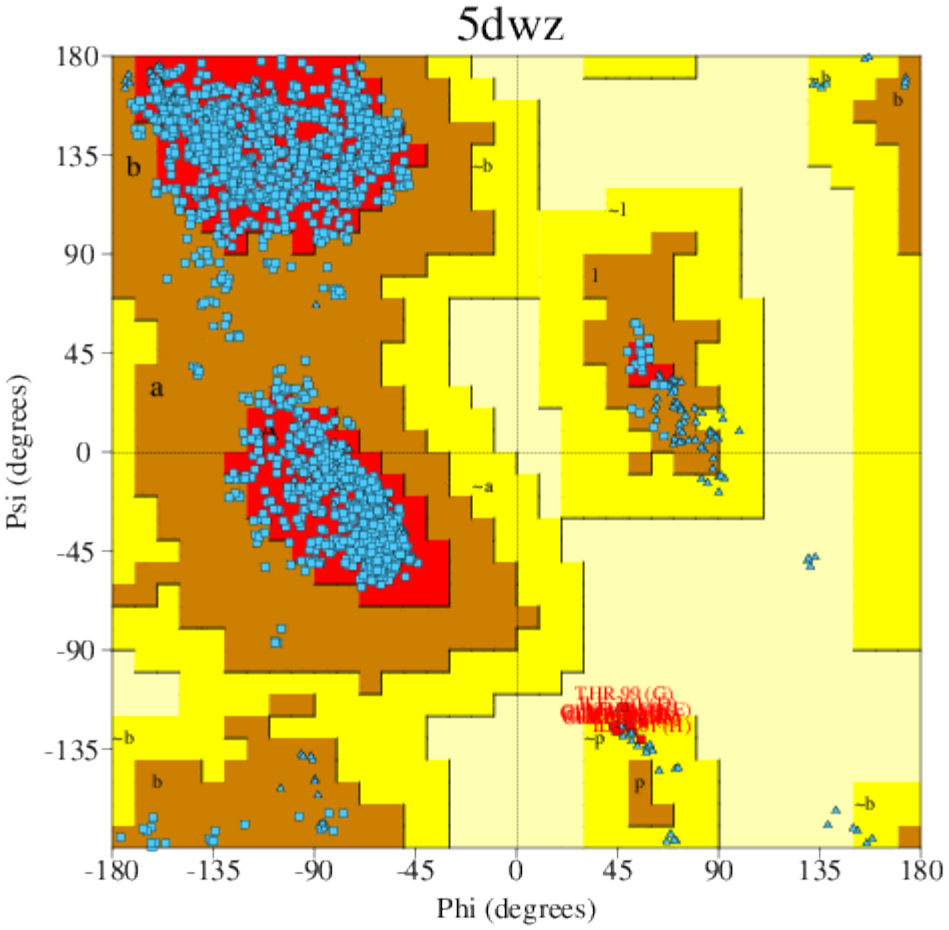


Figure 6.2. Ramachandran plot of PqsBC^{C129A} crystal structure showing residues in the most favoured regions (red) 90.9%, additional allowed regions (yellow) 8.6%, generously allowed regions 0.5% (pale yellow), processed using PROCHECK (Laskowski et al., 1993). The squares denote non-glycine residues, whereas glycine residues are denoted by triangles.

6.3 Structure comparisons of PqsBC^{C129A}

It is useful in structural biology to compare protein structures to other proteins, especially the active site as it can be used to investigate mechanisms of catalysis and substrate selectivity. In favourable cases, comparing 3D structures may reveal biologically interesting similarities that are not detectable by comparing sequences. Within this study, the similarity between the PqsBC^{C129A} structure and structurally homologous proteins was found using the program Dali (Holm and Rosenström, 2010).

6.4 PqsBC^{C129A} crystal structure shows the similarity to FabH-like enzyme

The comparison revealed that FabH (*Aquifex aeolicus*) has the highest similarity (Z-score 38.7), followed by FabH (*Burkholderia xenovorans*; Z-score 37.4), FabH (*Neisseria meningitides*; Z-score 37.3), FabH (*Thermus Thermophilus*; Z-score 36.4) and FabH (*P. aeruginosa*/PqsD; Z-score 35.7). As can be seen in **Table 6.3** the range of Z-scores was 36.8 to 38.7, where a score of 2 or greater is considered significant. Indeed, this was not surprising as PqsBC catalyses the condensation of octanoyl-coenzyme A and 2-ABA to form HHQ, and FabH participates in fatty acid biosynthesis. **Table 6.3** below shows the proteins that Dali identified with the highest Z-score and percentage similarity to PqsBC. Following **Table 6.3** shown the result from Dali server which having highest percentage of similarity with PqsC (pdb file).

Table 6.3. Conservation mapping of PqsBC^{C129A} crystal structure

No.	Chain	Z	Rmsd	Nres	% ID	Description
1	2ebd-B	38.7	1.8	308	25	3-oxoacyl-(acyl-carrier-protein) synthase III of *Aquifex aeolicus VF5*
2	4dfe-A	37.4	2.1	322	27	3-oxoacyl-(acyl-carrier-protein) synthase III of *Burkholderia xenovorans*
3	4ryb-B	37.3	2.0	319	26	Beta-ketoacyl (acyl-carrier-protein) synthase III of *Neisseria meningitidis*
4	1ub7-B	36.4	2.2	321	28	Beta-ketoacyl (acyl-carrier-protein) synthase III of *Thermus Thermophilus*
5	3h78-A	35.7	2.3	329	25	3-oxoacyl-(acyl-carrier-protein) synthase III of *Pseudomonas aeruginosa* (PqsD)
6	1hnj-A	36.5	2.1	317	21	Beta-ketoacyl (acyl-carrier-protein) synthase III of *Escherichia coli*
7	3gwa-A	36.2	2.4	337	25	3-oxoacyl-(acyl-carrier-protein) synthase III of *Burkholderia pseudomallei*
8	1u6s-B	36.0	2.1	334	26	Beta-ketoacyl (acyl-carrier-protein) synthase III of *Mycobacterium Tuberculosis*
9	1u6e-B	36.0	2.2	334	26	Beta-ketoacyl (acyl-carrier-protein) synthase III of Mutant of *Mycobacterium Tuberculosis*
10	1zow-A	37.4	2.0	312	24	Beta-ketoacyl (acyl-carrier-protein) synthase III of *Staphylococcus aureus*
11	2x3e-A	36.8	2.2	325	25	3-oxoacyl-(acyl-carrier-protein) synthase III of *Pseudomonas aeruginosa* PAO1

6.5 PqsBC^{C129A} crystal structure is a heterodimer

Unlike other members of the FabH family of proteins, which form homodimers, PqsB and PqsC form a pseudo 2-fold symmetric heterodimer that imitates the FabH homodimer, as shown **in Figure 6.3**. The structure reveals that PqsB and PqsC assemble as a dimer with the N-termini close to the pseudo 2-fold axis, and C-termini are located away from the axis (**Figure 6.4**). The PqsB and PqsC folds are similar to PqsD and FabH enzymes, which contain two subdomains

each consisting of a four-strand β-sheet surrounded by α-helices. Structural superposition of PqsB and PqsC (**Figure 6.5**) shows that the N-terminal subdomains show high similarity (**Figure 6.6**). Furthermore, the main differences that occur in the C-terminal subdomains with PqsB having a shorter sequence (124 amino acids) with only two α-helices and PqsC (160 amino acids) having four α-helices (**Figure 6.7**).

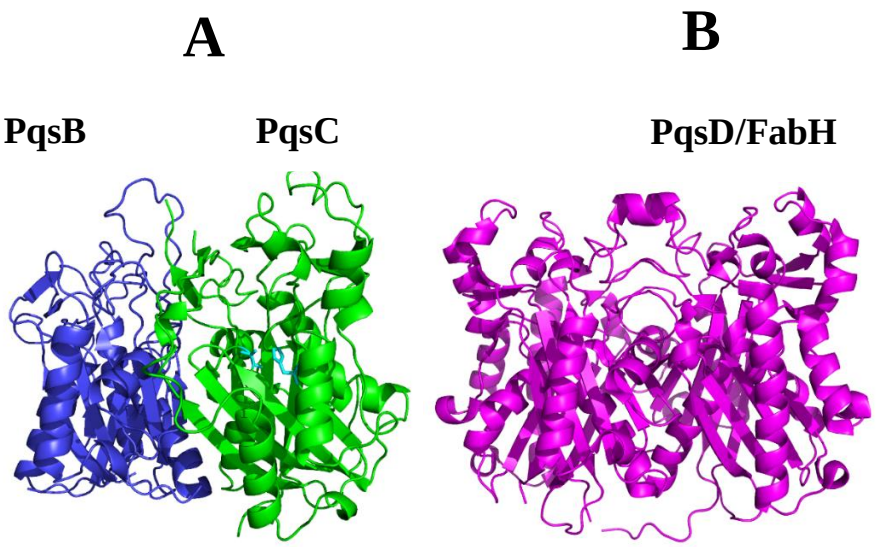


Figure 6.3. A, Cartoon diagram of the PqsBC^{C129A} structure as a heterodimer is shown with PqsB (blue) and PqsC (green), Cys/Ala129 and His269 in cyan are catalytic dyad. B. Cartoon diagram of PqsD which is a homodimer in magenta.

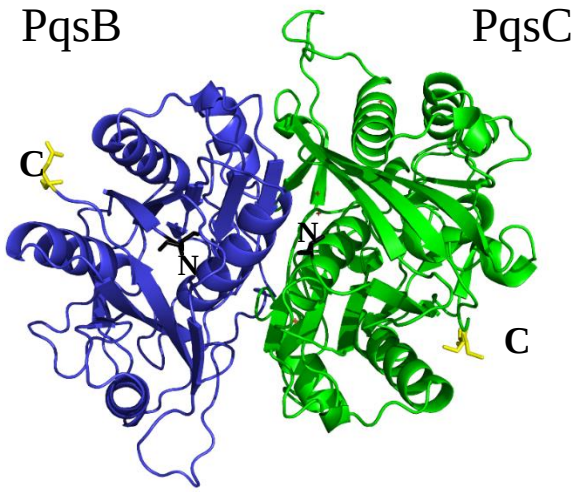


Figure 6.4. Cartoon diagram of the PqsBC^{C129A} structure as a heterodimer are shown with N-termini (black) and C-termini (yellow), PqsB in blue and PqsC in green.

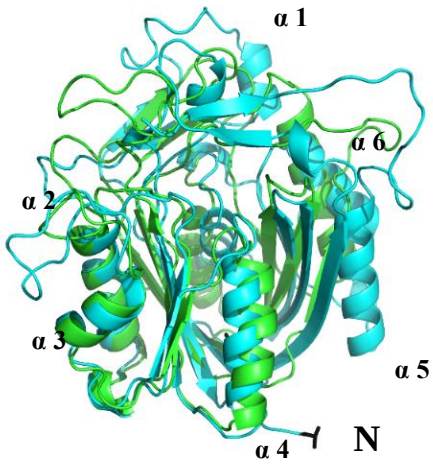


Figure 6.5. Cartoon diagram of a superposition of PqsB (green) and PqsC^{C129A} (cyan).

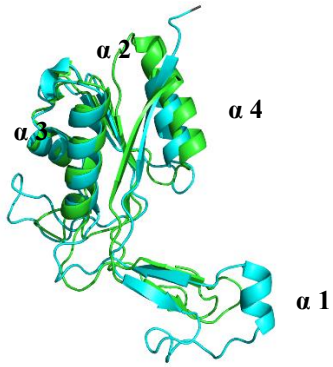


Figure 6.6. Cartoon diagram of a superposition of PqsB (green) and PqsC^{C129A} (cyan), in the N-terminal subdomain.

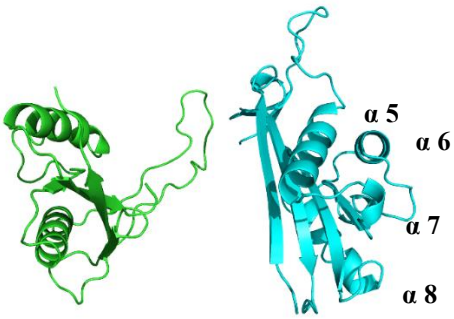


Figure 6.7. Cartoon diagram of C-terminal subdomains of PqsB (155-279) in green and PqsC (188-348) in cyan, showing PqsB has a shorter sequence.

6.6 PqsC^{129A} structure reveals a catalytic diad

The active site residues His269 and the mutated Ala129 (replacing Cys129) are clearly defined in the electron density (**Figure 6.8**). In contrast to the FabH enzyme family, PqsBC forms a catalytic diad, not triad. Typically, an asparagine would be found in close location to the catalytic histidine and cysteine. In PqsBC this is not observed, and a valine (Val299) is present where the asparagine would normally be found.

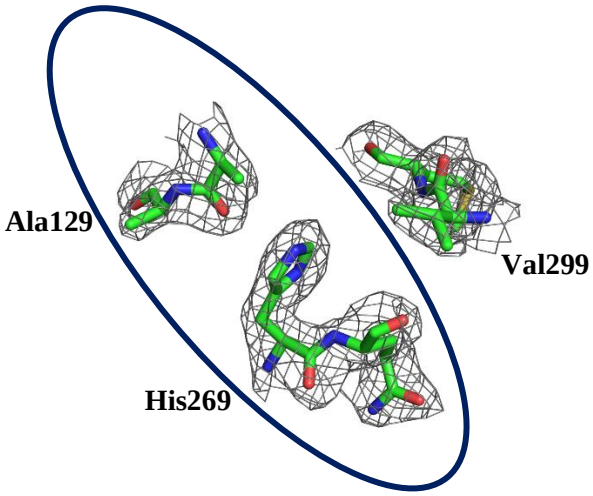


Figure 6.8. Stick diagrams of the catalytic site of PqsBC^{C129A} catalytic dyad, a 2.3 Å 2Fo-Fc electron density map is shown (grey) calculated using FFT, rendered with Pymol showing PqsC residues Ala129, Ala130, His 269, Gln270, Val 299, Met300 as sticks in green.

Figure 6.9 shows the superposition of PqsC with the PqsD catalytic triad. To ensure that the protein was active with only the diad, activity assays with a desamino-substrate analogue benzoylacetate (BA) were performed (Drees et al., 2016). The wild-type protein showed 300-fold lower activity with BA as a substrate compared to 2-ABA. A PqsBC^{V299N} variant, which theoretically restores a full catalytic triad, was significantly more active with BA than 2-ABA (Drees et al., 2016).

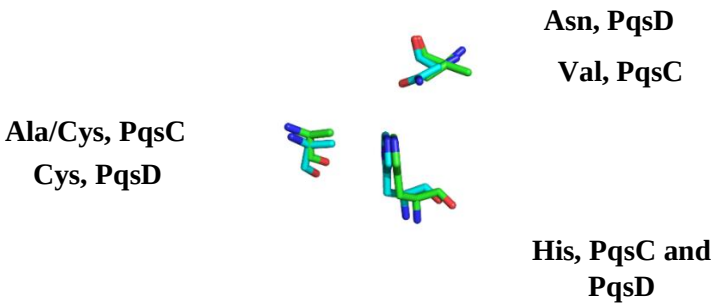


Figure 6.9. Stick diagrams of a superposition of PqsBC^{C129A} catalytic dyad (green) and PqsD catalytic triad (cyan).

6.7 Active site volume comparison of PqsBC^{C129A} with FabH and PqsD

The PqsC^{C129A} active site volume is twice as large as those of other FabH/PqsD proteins, with a calculated volume of 761Å^3 compared to 389Å^3 for PqsD (pdb:3H76) and 367Å^3 for FabH (pdb:2QNZ) (calculated using 3vee (Voss and Gerstein, 2010)) (**Figure 6.10**). This increased volume within the active site may be a requirement to accommodate the aromatic substrate 2-ABA. 2-ABA has an aromatic ring, which makes the molecule much larger than other common FabH ligands, such as malonyl-ACP.

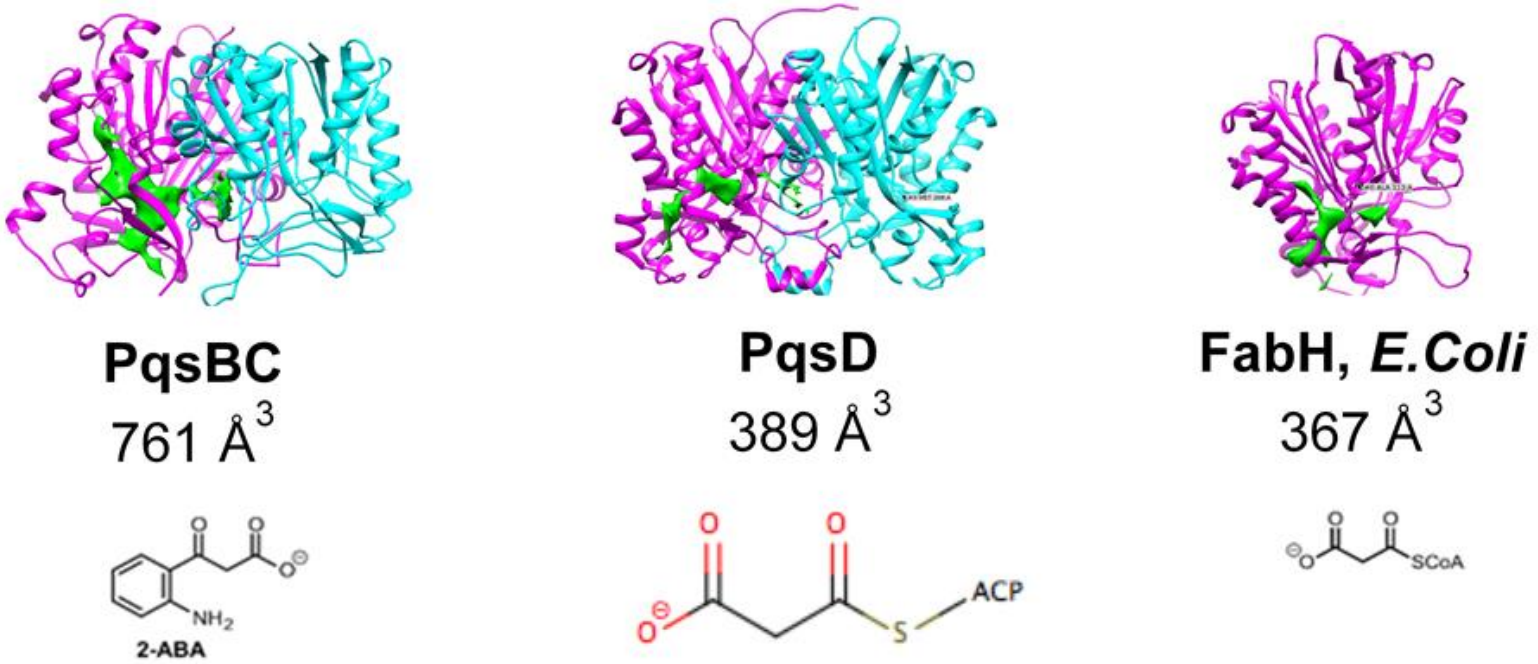


Figure 6.10. Cartoon diagrams of active site volume calculated by using 3Vee (Voss and Gerstein, 2010). Calculated volume of PqsC^{C129A} active site approximately twice the volume of related FabH enzymes which may be a requirement to accommodate the aromatic substrate 2-ABA instead malonyl-ACP in case of FabH, malonyl-CoA or malonyl-ACP in PqsD.

6.8 Active site pocket of PqsBC^{C129A} is formed by PqsB and PqsC

Although the catalytic residues are only provided by PqsC, the active site pocket is fomed by residues from PqsB and PqsC (**Figure 6.11**). There are thirty-two residues that form the active site pocket of PqsBC^{C129A}. Five of thirty-two pocket residues consist of PqsB residues Met76, Lys79, Leu69, Ile80, and Ala63..

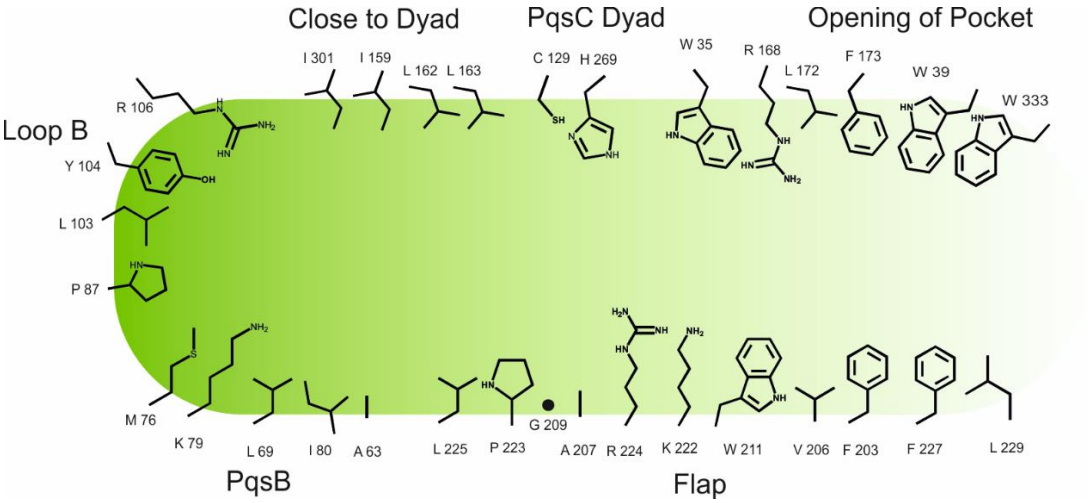


Figure 6.11. Graphical representation of the PqsBC active site cleft created by using corel draw. Residues conserved with CoA binding sites of FabH/PqsD enzymes are W35 and R168.

6.9 Central cavity of PqsBC^{C129A}

In the asymmetric unit of the crystal also is found a large active site cavity, PqsBC^{C129A} also has a central cavity within PqsBC^{C129A} heterotetramer conformation.

The volume is 5034 $Å^3$, calculated by using 3Vee (Voss and Gerstein, 2010). Graphical representation of $PqsBC^{C129A}$ central cavity is shown on **Figure 6.12** and **Figure 6.13**. As can be seen on the **Figure 6.12** and **Figure 6.13**, the $PqsBC^{C129A}$ central cavity is arranged up by only $PqsC^{C129A}$ that also exactly in the point where the two of catalytic sites lining up face to face.

Furthermore, PISA (Krissinel and Henrick, 2007) was employed to study the interfacial contacts and calculate the surface area involved in the interaction between two $PqsC^{C129A}$ where two active site located side by side. It was observed that the interface area between two PqsC is 902.5 $Å^2$ and composed of 31 residues from one $PqsC^{C129A}$ and 32 residues from another $PqsC^{C129A}$ (**Figure 6.14**). The interface is stabilised via 16 hydrogen bonds and 2 salt bridges (**Table 6.4**). This interface scored 0.114 for CSS, hence, this interface plays an auxiliary role in complex formation.

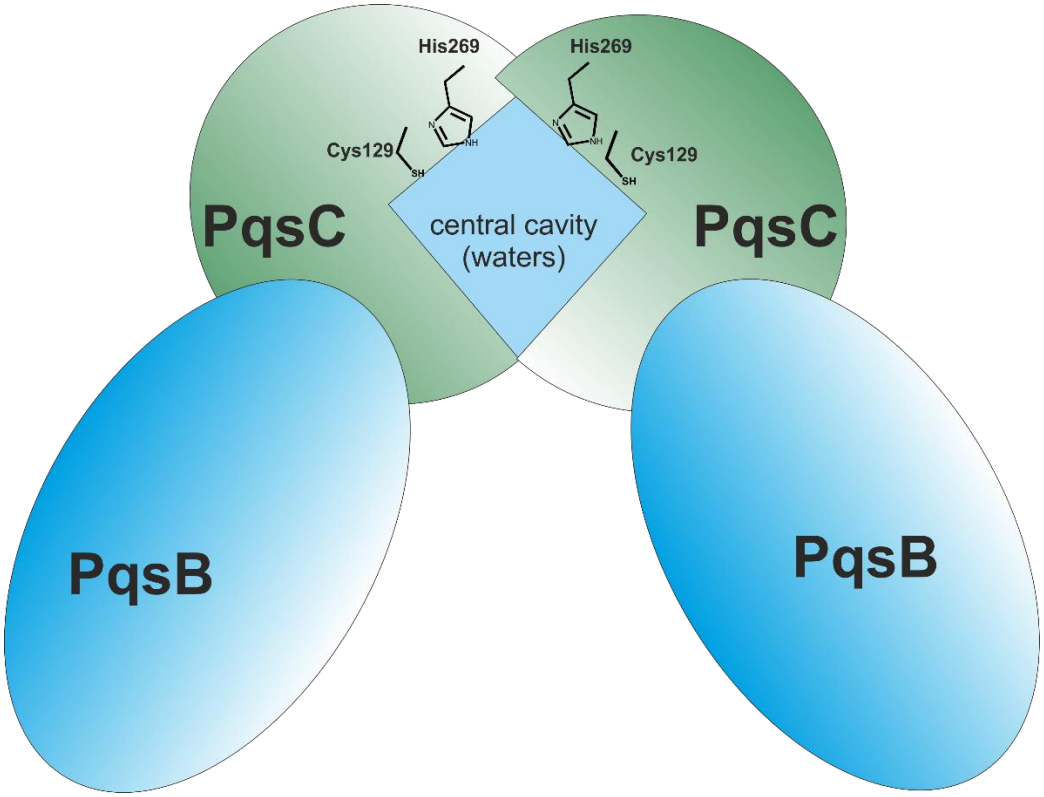


Figure 6.12. Graphical representation of PqsBC^{C129A} central cavity with volume is 5034 Å^3, calculated by using 3Vee (Voss and Gerstein, 2010).

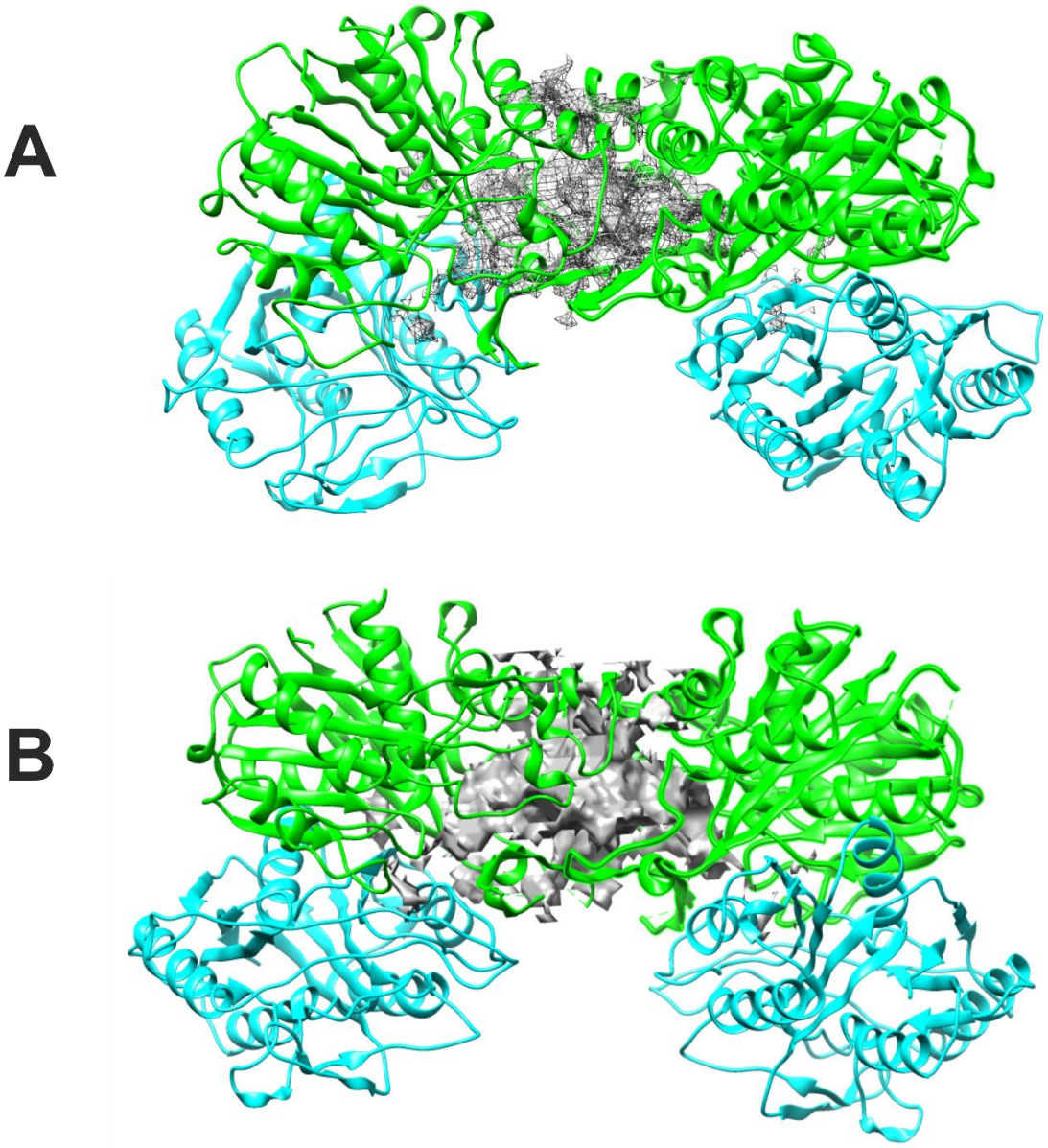


Figure 6.13. Cartoon diagram of PqsBC^{C129A} central cavity with volume is 5043 Å^3, **A.** Central cavity volume shown in mesh. **B.** Central cavity shown in surface. Both diagram rendered using UCSF Chimera (Pettersen et al., 2004). Central cavity volume calculated by using 3Vee (Voss and Gerstein, 2010). PqsB (cyan) and PqsC (green).

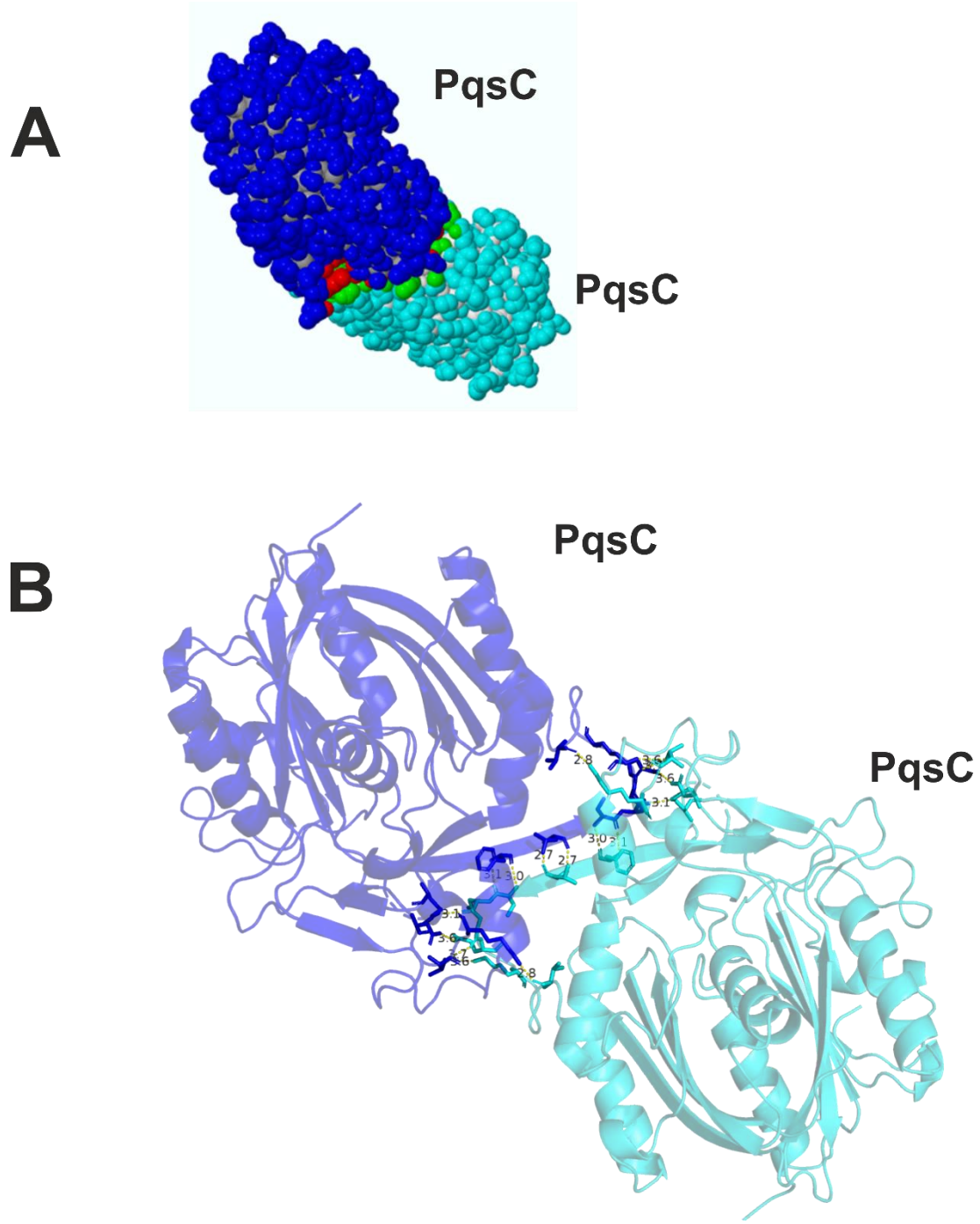


Figure 6.14. Sphere (A) rendered with JyMOL and Cartoon (B) rendered with PyMOL diagram of interface area between two PqsC is 902.5 Å^2. **A)** PqsC^{C129A} (blue), PqsC^{C129A} (cyan), interface area (red and green). **B)** PqsC^{C129A} (blue), PqsC^{C129A} (cyan), interface area is shown in stick diagram.

Table 6.4. Hydrogen bonds and salt bridges of surface contact between two PqsC.

No.	**PqsC^{C129A}**	**Dist. Å^2**	**PqsC^{C129A}**
1	H:LYS 236[NZ]	3.84	D:THR 166[OG1]
2	H:LYS 236[NZ]	2.98	D:SER 167[OG]
3	H:GLN 234[NE2]	3.54	D:LEU 213[O]
4	H:SER 231[N]	2.83	D:PHE 227[O]
5	H:LEU 229[N]	2.92	D:LEU 229[O]
6	H:PHE 227[N]	2.93	D:ASP 231[OD2]
7	H:ARG 168[NH2]	3.07	D:VAL 241[O]
8	H:THR 166[OG1]	3.76	D:LYS 236[NZ]
9	H:THR 166[O]	2.77	D:LYS 236[NZ]
10	H:PHE 227[O]	3.87	D:ASP 231[N]
11	H:LEU 229[O]	2.74	D:LEU 229[N]
12	H:SER 231[O]	2.71	D:PHE 227[N]
13	H:ASP 232[OD2]	3.09	D:ARG 212[NH1]
14	H:GLY 233[O]	3.49	D:SER 167[OG]
15	H:GLN 234[OE1]	3.34	D:ASN 215[N]
16	H:VAL 241[O]	2.84	D:ARG 168[NH2]
	Salt bridges		
1	H:ASP 232[OD2]	3.09	D:ARG 212[NH1]
2	H:ASP 232[OD2]	3.87	D:ARG 212[NE]

6.10 Alignment of the PqsC with PqsD and FabH *E.coli* enzymes

PqsC, PqsD and *E. coli* FabH were aligned in order to compare their primary sequences (aligned using ESPript 3 (Robert and Gouet, 2014)) (**Figure 6.15)**. A significant difference between PqsC and FabH/PqsD structures is an insertion of 14 amino acids in PqsC between strand β4 and helix α3 (PqsC residues 88-102). This insertion is termed loop B and forms a network of interactions with the PqsC flap and contributes to the dimer interface with PqsB.

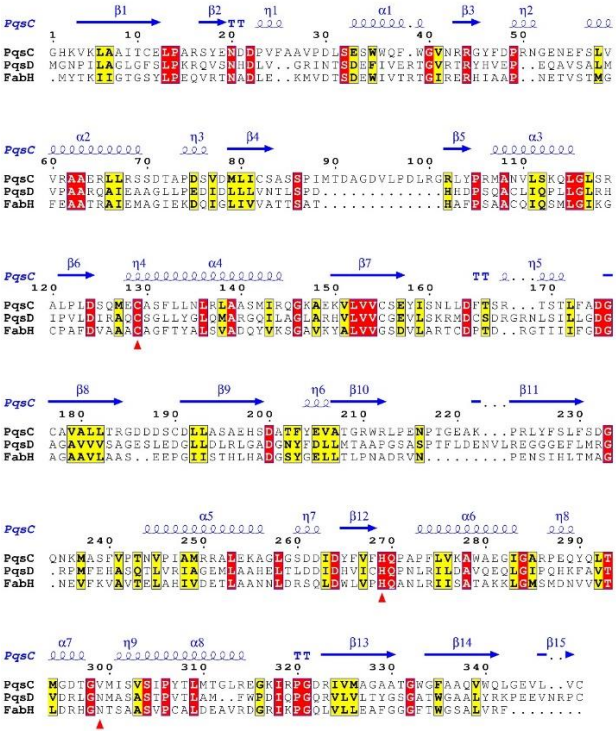


Figure 6.15. Alignment of the PqsC amino acid sequence with related enzymes showing the assignments of the PqsC^{C129A} structure at the top (*blue*). The catalytic residues are marked by *red triangles*. The sequences shown are PqsD (*P. aeruginosa*) and FabH (*E. coli*).

6.11 PqsBC^{C129A}, PqsD, and FabH *E.coli* crystal structure superposition

Comparison of the PqsC^{C129A} and PqsD crystal structures (PDB code 3h78), show that there are significant structural differences in the region of the active site cleft (**Figure 6.16**). The region known as the flap in FabH enzymes (Sachdeva et al., 2008) is conserved as a short α-helix in PqsD, whereas in PqsC it is formed by a short antiparallel sheet (β9-β10). Directly C-terminal to this, further differences are apparent as the PqsC helix α5 is shorter than the equivalent α-helix in PqsD/FabH. Pro-242 breaks the helix α5 in PqsC and directs an alternate path for the polypeptide compared with FabH/PqsD, forming an irregular loop structure, termed loop A, which effectively opens up the active site cleft.

Figure 6.17 shows the PqsBC^{C129A} heterodimer crystal structure compared with PqsD homodimer. It shows the flap region lying close to the PqsD dimer axis (**Figure 6.18**) exhibits two orientations of a C-α trace of PqsBC polypeptide backbone superposed on the PqsD homodimer. The superposition is driven largely by the similarity between PqsC and PqsD and shows the close relative positioning of the PqsBC subunits compared with the PqsD homodimer. The PqsB β-sheets are displaced by 2–3 Å when overlaid with PqsD (**Figure 6.19**). The PqsBC active site cavity is elongated in the direction of the heterodimer interface where it narrows and extends into PqsB. The gap in the interface is not observed in FabH/PqsD and in part accounts for the smaller, ~2,240 Å^2, surface area buried in PqsBC heterodimer interface compared with the larger value of 3,000 Å^2 for the FabH/PqsD homodimer.

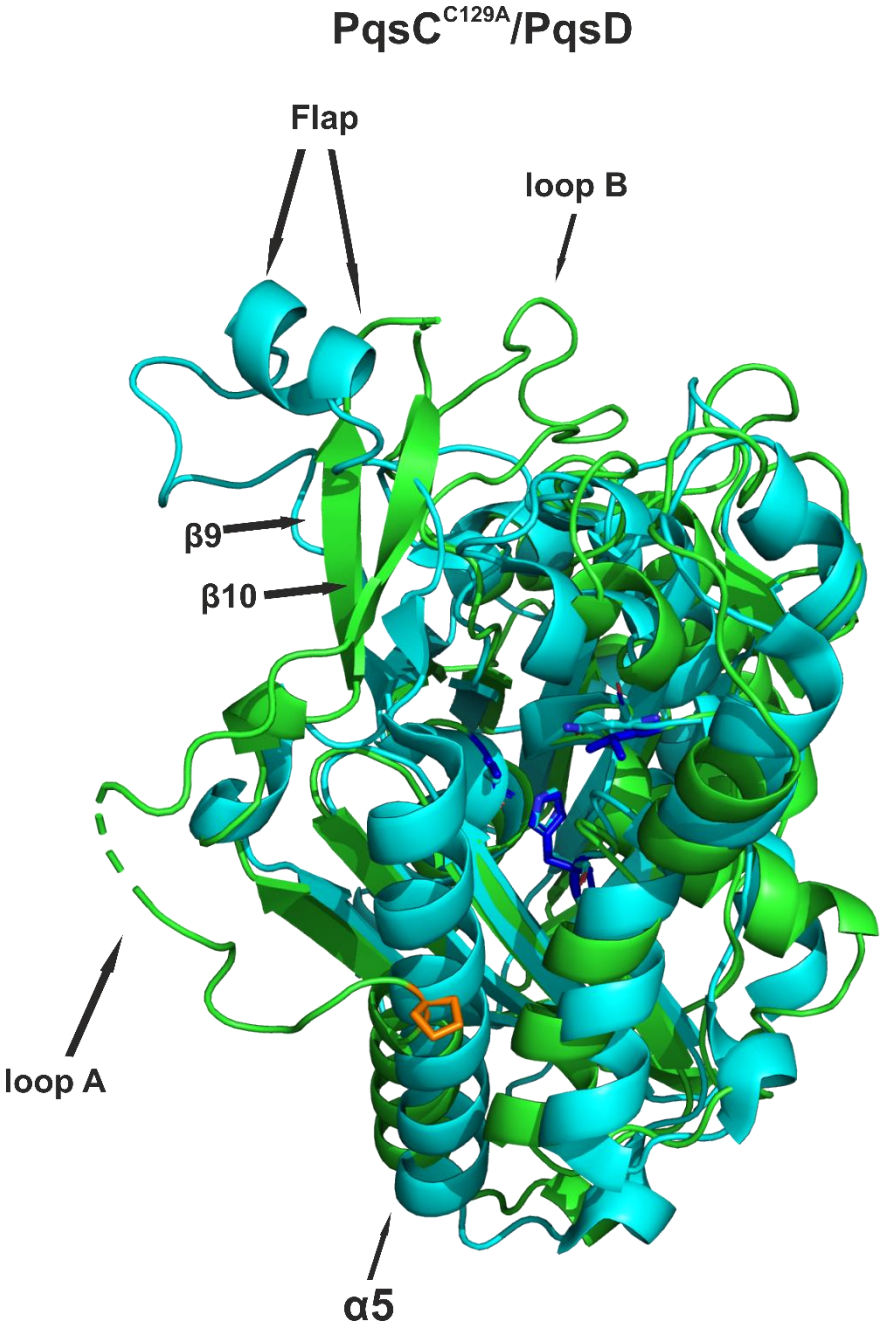


Figure 6.16. Cartoon diagram of the PqsC^{C129A} structure is shown (*green*) superposed onto PqsD (*cyan*). Residues from PqsC shown as *sticks* in *blue* are Ala-129, His-269, Val-299, and Pro-242 (*orange*). PqsD residues Ala-112, His-257, and Asn-287 are shown as sticks (*cyan*). Showing the comparison of the PqsC^{C129A} and PqsD crystal structures (PDB code 3h78), show that there are significant structural differences in the region of the active site cleft.

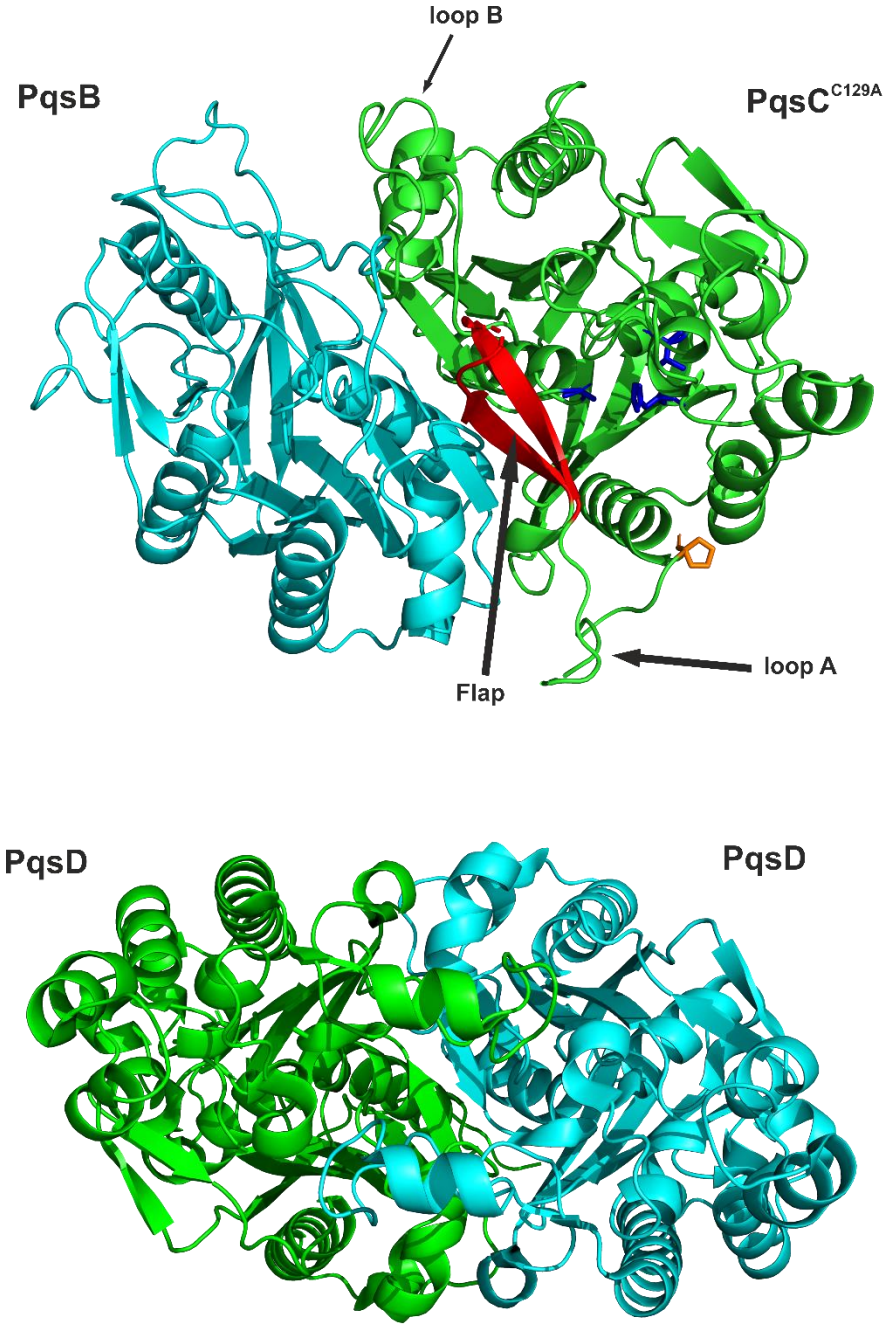


Figure 6.17. Schematic diagram of PqsBC (*cyan*, *green*) with the flap (PqsC residues 207–227) in *red* shown in the same orientation as the PqsD homodimer below (*green*, *cyan*).

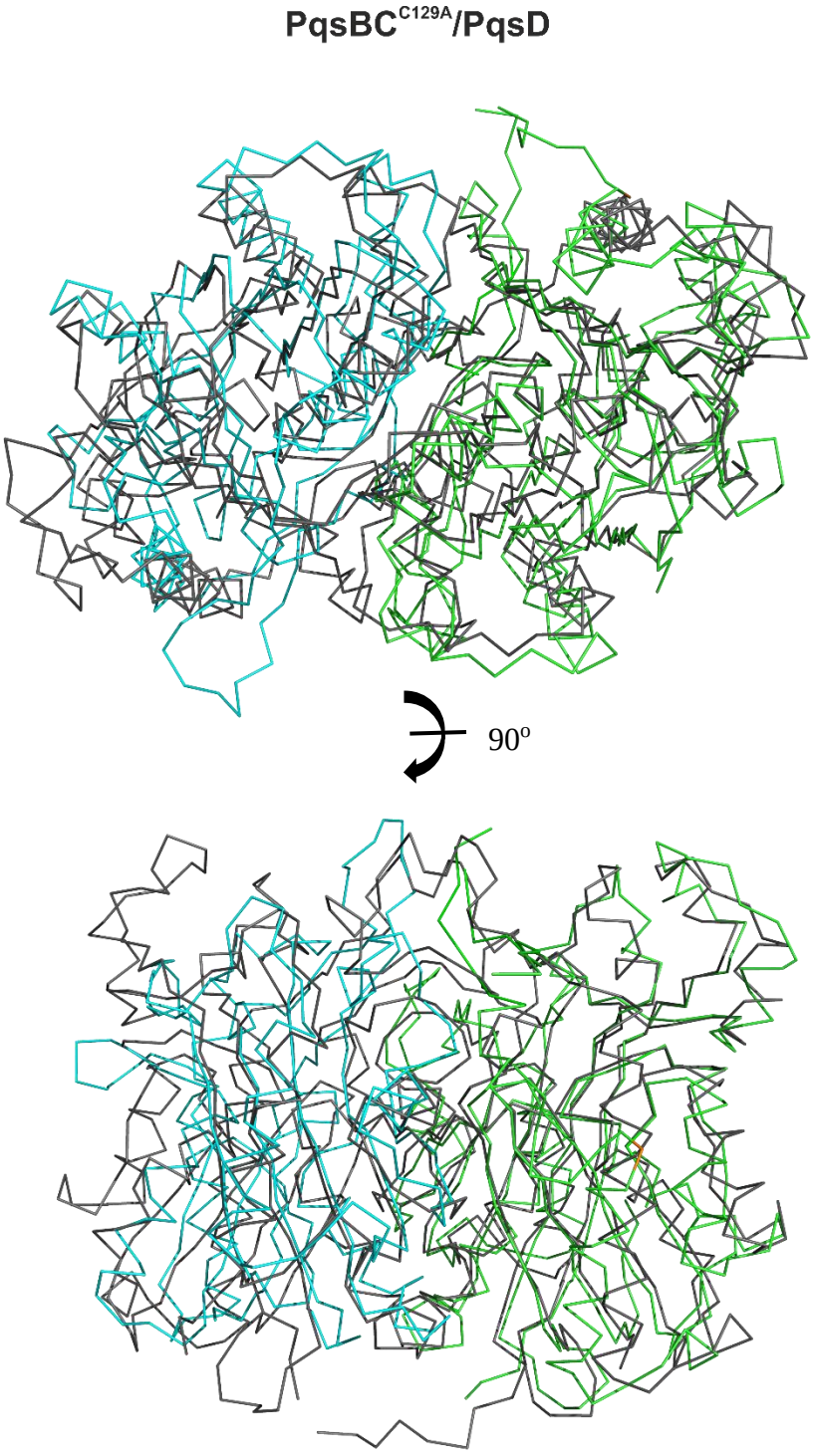


Figure 6.18. Superposition of the PqsBC structure (*cyan*, *green*) with the PqsD homodimer (*grey*) illustrated as Cα-backbone representations with two views shown.

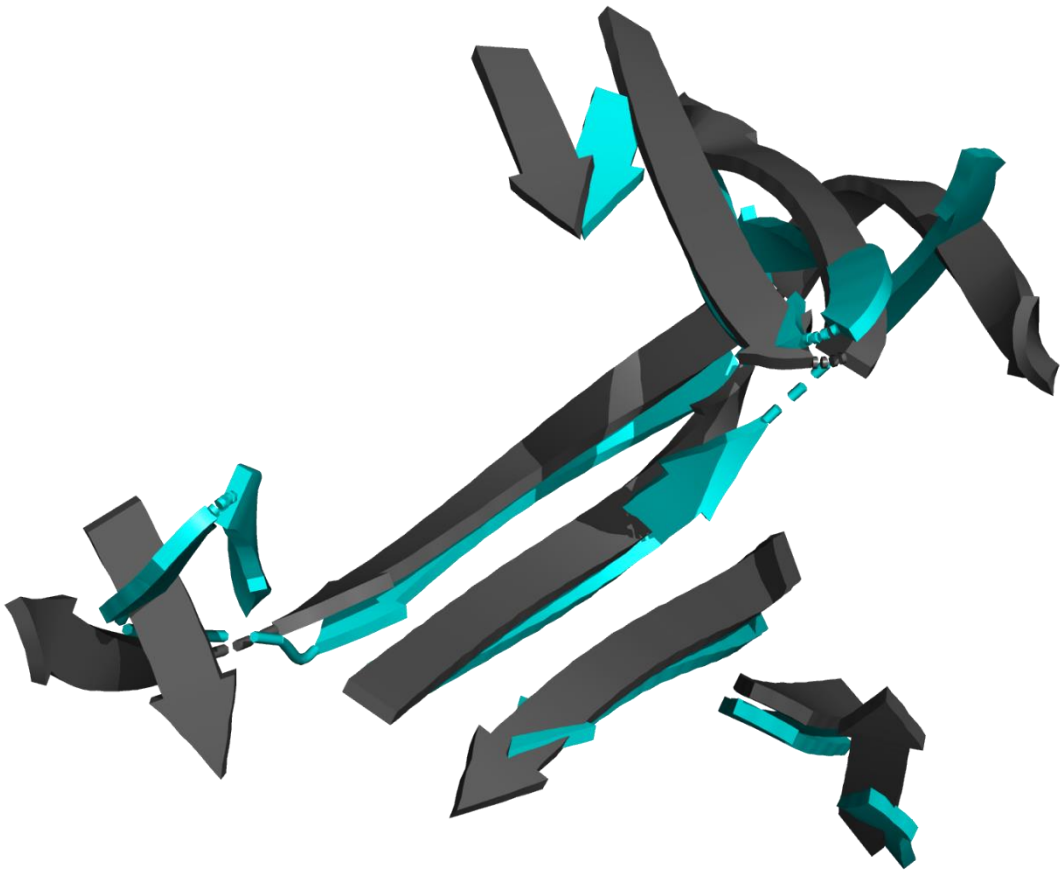


Figure 6.19. Superposition of β-strands for PqsB (*cyan*) and PqsD (*gray*) are shown as schematics.

Chapter 7: Comparison of PqsBC with FabH

7.1 PqsBC, a condensing enzyme in the biosynthesis of PQS

PqsB and PqsC are member of the β-ketoacyl-ACP-synthase III family also known as FabH, which are condensing enzymes involved in fatty acid metabolism and thus in the elongation of the acyl side chains of the quinolones (Diggle et al., 2003, Deziel et al., 2004, Drees et al., 2016). PqsC and PqsB form a tight heterodimer complex (Dulcey et al., 2013, Drees and Fetzner, 2015, Drees et al., 2016).

The FabH-like proteins PqsBC are involved in HHQ biosynthesis. PqsBC-catalysed reactions proceed in a similar manner to that of the model enzyme FabH: in the initial step, the acyl moiety of an activated carboxylic acid is transferred to a strictly conserved active-site cysteine residue. Subsequently, a β-ketoalkanoic acid (malonyl-ACP in the case of FabH, malonyl-CoA, 2-ABA in PqsBC) is decarboxylated, and the resulting reactive enolate intermediate attacks the thioester bond of the acyl-enzyme to form the reaction product. Intermediates and products of the alkyl quinolone biosynthetic pathway which is HHQ a precursor of PQS.

7.2 FabH (β-ketoacyl-ACP-synthase III) crystal structures

β-ketoacyl-ACP-synthase III family in enzymology also known as FabH, catalyse the reaction of Acetyl-CoA with malonyl-[acyl-carrier-protein] to acetoacetyl-[acyl-carier-protein] along with CoA as well as CO_2. This enzyme specifically uses CoA thioesters rather than acyl-ACP as the primer. FabH engages in fatty acid biosynthesis.

FabH crystal structures have been solved from *E. coli* (Qiu et al., 1999) (**Figure 7.1**), *Mycobacterium tuberculosis* (Scarsdale et al., 2001) (**Figure 7.2**), *Staphylococcus aureus* (Qiu et al., 2005) (**Figure 7.3**), *Thermus thermophilus* (Inagaki et al., 2007) (**Figure 7.4**), and *Neisseria meningitidis*. All of these crystal structures are homodimers.

Another characteristic of FabH proteins is the presence of a catalytic triad. In *E. coli* and *M. tuberculosis* FabH the catalytic site is composed of Cys112, His244, and Asn274 (**Figure 7.5**); and in *S. aureus* FabH the catalytic triad consists of Cys112, His238, and Asn268.

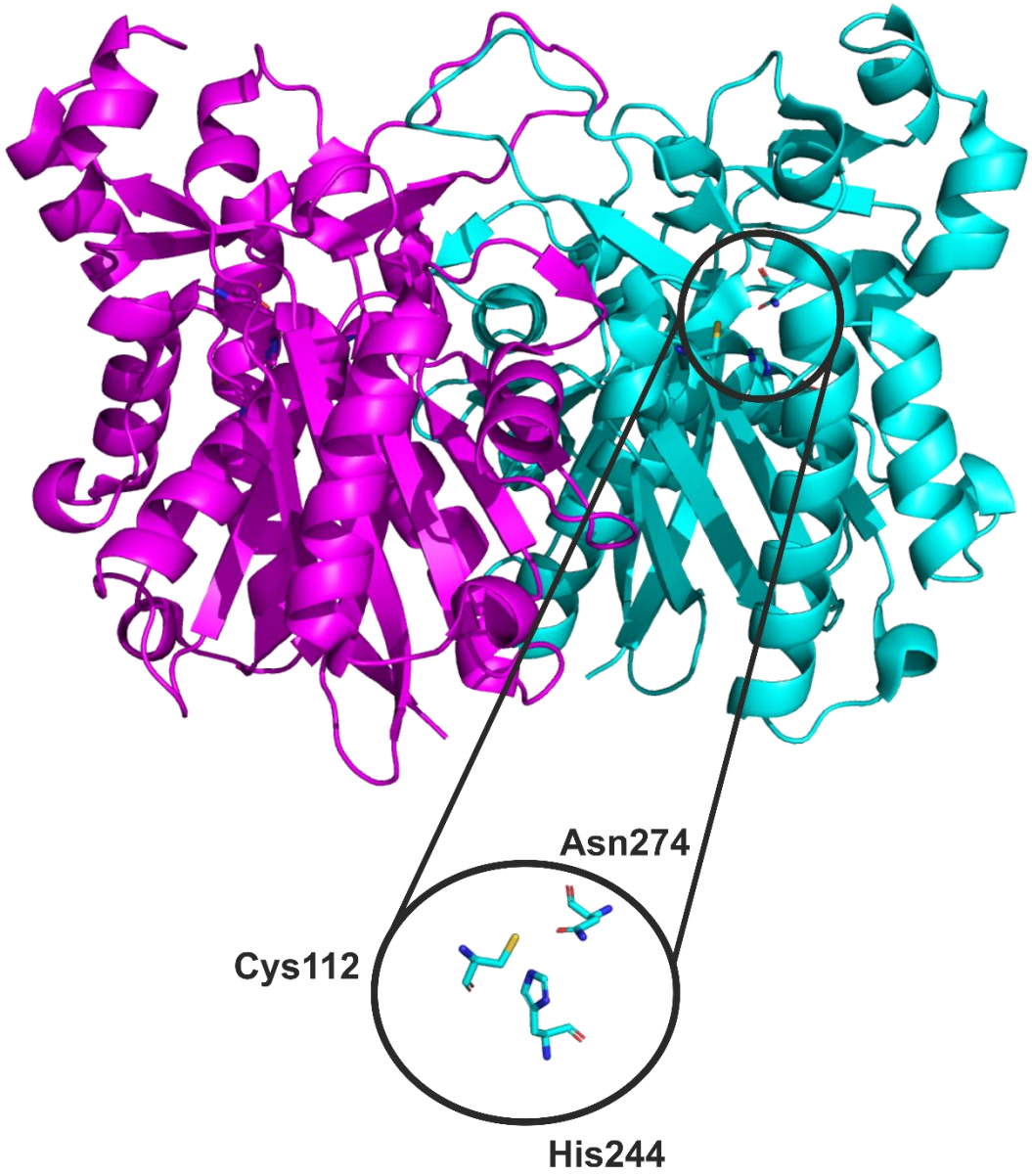


Figure 7.1. Cartoon diagram of FabH *Escherichia coli* (magenta, cyan) (PDB code, 1hn9) as homodimeric subunit composition with the catalytic triad that is composed of Cys112, His244, and Asn274 (Qiu et al., 1999).

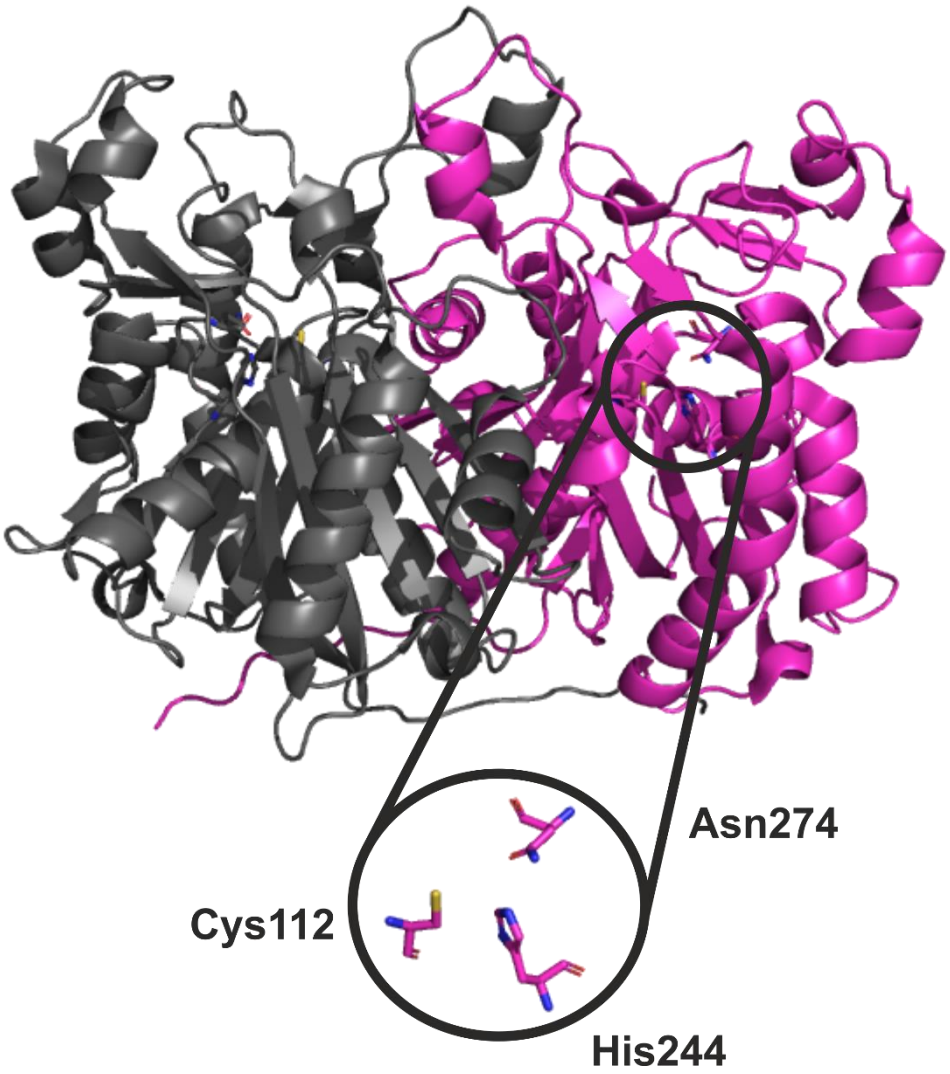


Figure 7.2. Cartoon diagram of FabH *Mycobacterium tuberculosis* (grey, magenta) (PDB code: 1hzp) as homodimeric subunit composition with the catalytic triad that is composed of Cys112, His244, and Asn274 (Scarsdale et al., 2001).

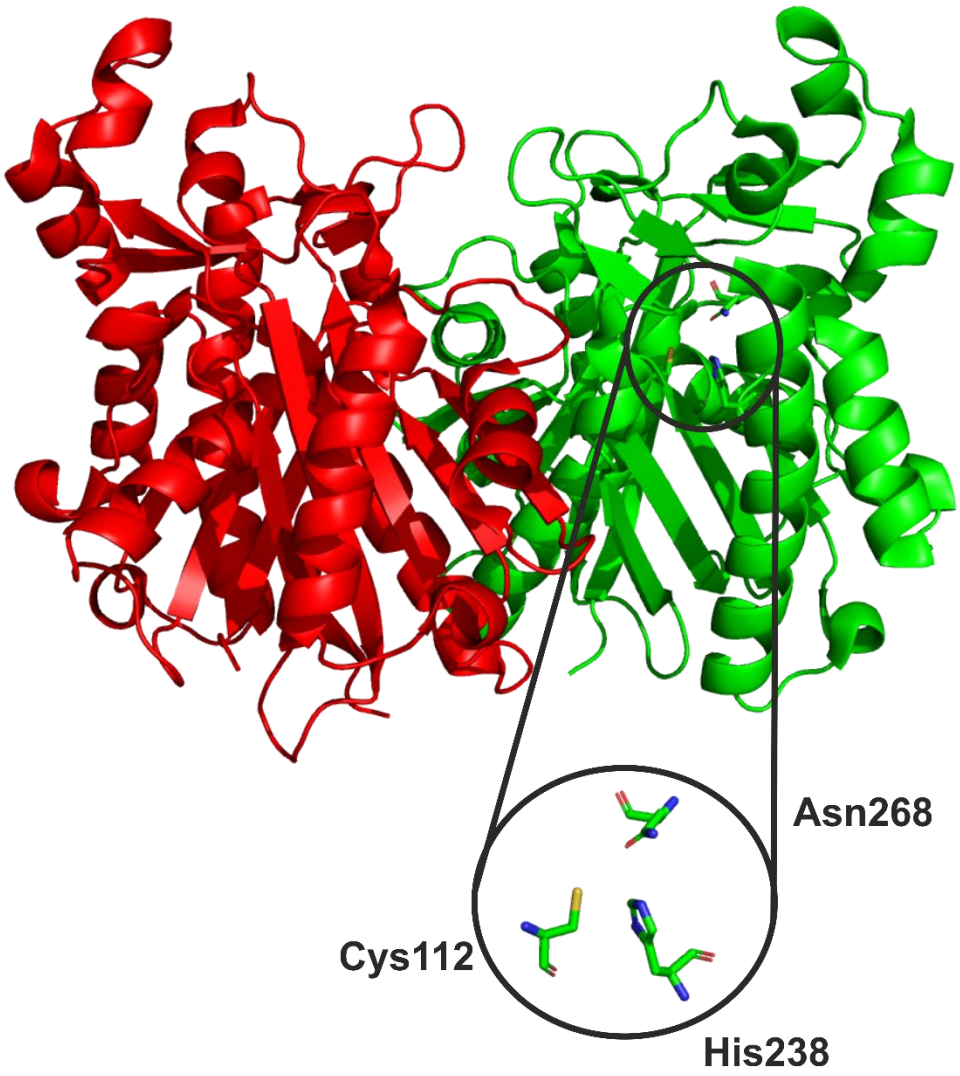


Figure 7.3. Cartoon diagram of FabH *Staphylococcus aureus* (red, green) a(PDB code: 1zow) as homodimeric subunit composition with the catalytic triad that is composed of Cys112, His238, and Asn268 (Qiu et al., 2005).

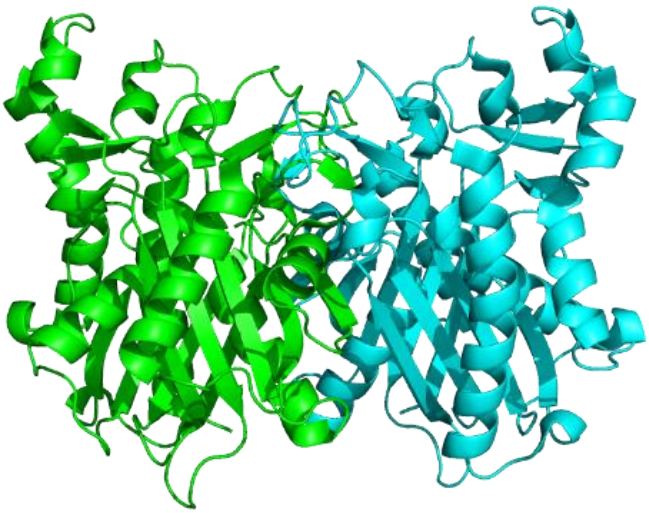


Figure 7.4. Cartoon diagram of FabH *Thermus thermophilus* (green, cyan) as homodimer (PDB code: 1ub7) (Inagaki et al., 2007).

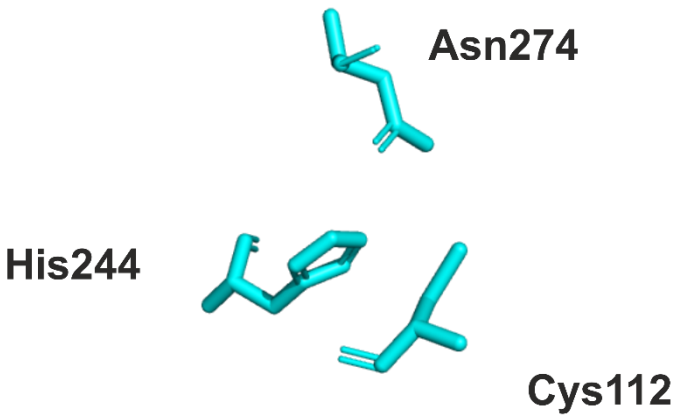


Figure 7.5. Cartoon diagram of FabH *Escherichia coli* (cyan) catalytic triad that is composed of Cys112, His244, and Asn274 (Qiu et al., 1999).

The reaction catalysed by FabH begins with the acetyl transfer from acetyl-CoA to a catalytic cysteine, which in *E. coli* FabH is Cys112 (**Figure 7.6**) (Qiu et al., 1999). His244 extracts a proton from Cys112, which can then attack the carbonyl of acetyl-CoA (Siggaard-Andersen, 1993). Furthermore, Asn274 interacts with the carbonyl group (Siggaard-Andersen, 1993), the decarboxylation produces a carbanion, which resonates with an enol intermediate that is stabilised by Asn274. The nucleophilic attack from the carbanion to the enzyme-bound acetyl group leads to a tetrahedral intermediate and finally the acetoacetyl-ACP product.

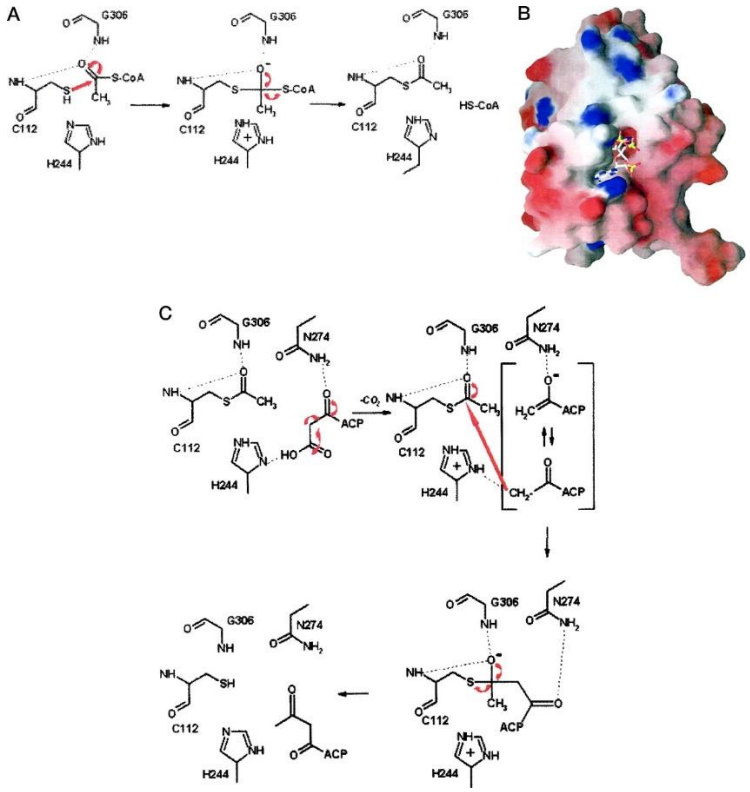


Figure 7.6. Cartoon Proposed mechanism of the FabH reactions. **A**, schematic diagram of the acetylation reaction mechanism. Dotted lines indicate hydrogen bonds ; thick arrows indicate attack or electron transfer directions. His244 extracts a proton from Cys112, which may then attack the carbonyl of acetyl-CoA. The tetrahedral intermediate is stabilized by backbone nitrogen of Gly306 and Cys112. His244 may donate a proton at the end of acetylation to form a neutral CoA. **B**, FabH surface charge distribution viewed toward the active site cavity. The figure was calculated with the acetyl-CoA complex structure after removing the bound CoA. Red indicates negative potential, and blue indicates positive potential. The CoA molecule is shown to occupy the active site, with white for carbon atoms, blue for nitrogen, red for oxygens, yellow for phosphors, and green for the sulfur. **C**, the carboxylic acid moiety probably binds His244, whereas the carbonyl group interacts with Asn274. The decarboxylation produces a carbanion, which resonates with an enol intermediate that is stabilized by Asn274. The nucleophilic attack from the carbanion to the enzyme-bound acetyl group leads to a tetrahedral intermediate and finally yields the product acetoacetyl-ACP (Qiu et al., 1999).

7.3 PqsBC as a heterodimer FabH with catalytic diad

As a member of the β-ketoacyl-ACP-synthase III family which also known as FabH, PqsBC catalyse the elongation of the acyl side chains of the quinolones (Diggle et al., 2003, Deziel et al., 2004, Drees et al., 2016). PqsBC catalyses the condensation of octanoyl-coenzyme A and 2-aminobenzoylacetate (2-ABA) to form the signal molecule 2-heptyl-4(1*H*)-quinolone HHQ which is a precursor of PQS (Drees et al., 2016).

However, as a FabH, the PqsBC crystal structure shows clear differences to the typical FabH enzymes, specifically with regards to their homodimeric form and presence of a catalytic triad. PqsBC forms a heterodimeric complex and lacks the canonical active-site asparagine (**Figure 7.7**).

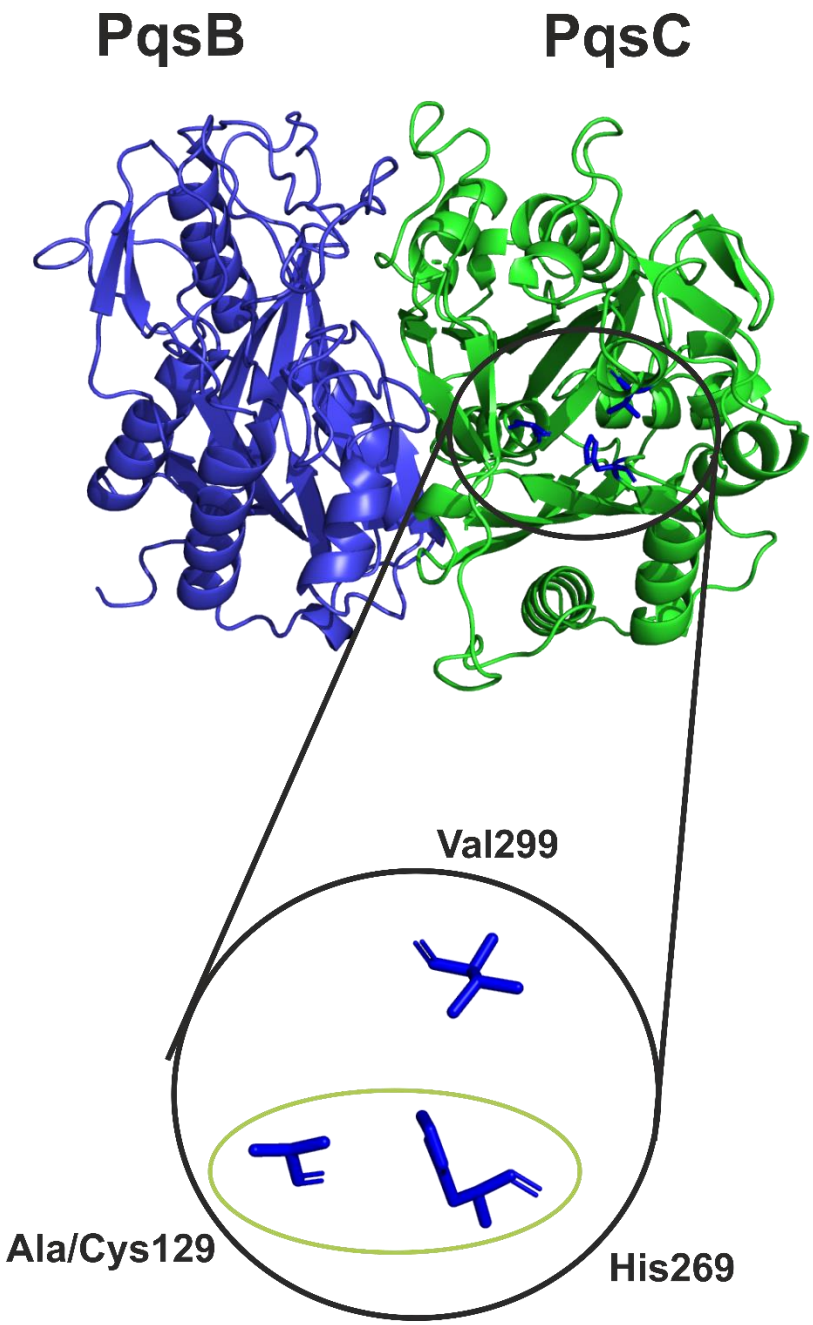


Figure 7.7. Cartoon diagram of PqsBC^{C129A} (blue, green) as a heterodimeric subunit composition with the active site residues Ala/Cys129 along with His269 which lack of the canonical active-site asparagine (here Val299) in stick diagram (blue).

It is known that the histidine and asparagine in the FabH active site interact with the thioester oxygen group of malonyl-ACP during enolisation to facilitate the formation of the carbanion at C2 (Davies et al., 2000, Heath and Rock, 2002). Furthermore, the carbanion is formed, then a nucleophile attacks the acetyl group attached to cysteine in the catalytic site (Davies et al., 2000, Heath and Rock, 2002) (**Figure 7.8**).

With PqsBC, it has been proposed that the amino group of 2-ABA functionally replaces the canonical catalytic asparagine (**Figure 7.9**) (Dulcey et al., 2013, Drees and Fetzner, 2015, Drees et al., 2016). In *E. coli* FabH, both His244 and Asn274 are required for decarboxylation activity (Davies et al., 2000, Heath and Rock, 2002). Interestingly, replacement of His269 to alanine in PqsBC nearly abolishes catalytic activity, this is in contrast with the mutation of His244 to alanine, which does not affect the transacylation reaction. This indicates histidine in *E. coli* FabH has only a minor influence on the nucleophilicity of Cys112 (Davies et al., 2000, Heath and Rock, 2002). Therefore, in PqsBC, His269 is clearly necessary and does not depend on participation of asparagine residues. The amino group of 2-ABA functionally replaces the amide group of the missing active-site asparagine (Drees et al., 2016), which has been proven by conversion of BA by PqsBC. Using octanoyl-CoA consumption to determine the rate of the reaction, a greatly diminished reaction velocity of 0.02 s^{-1} was observed (Drees et al., 2016).

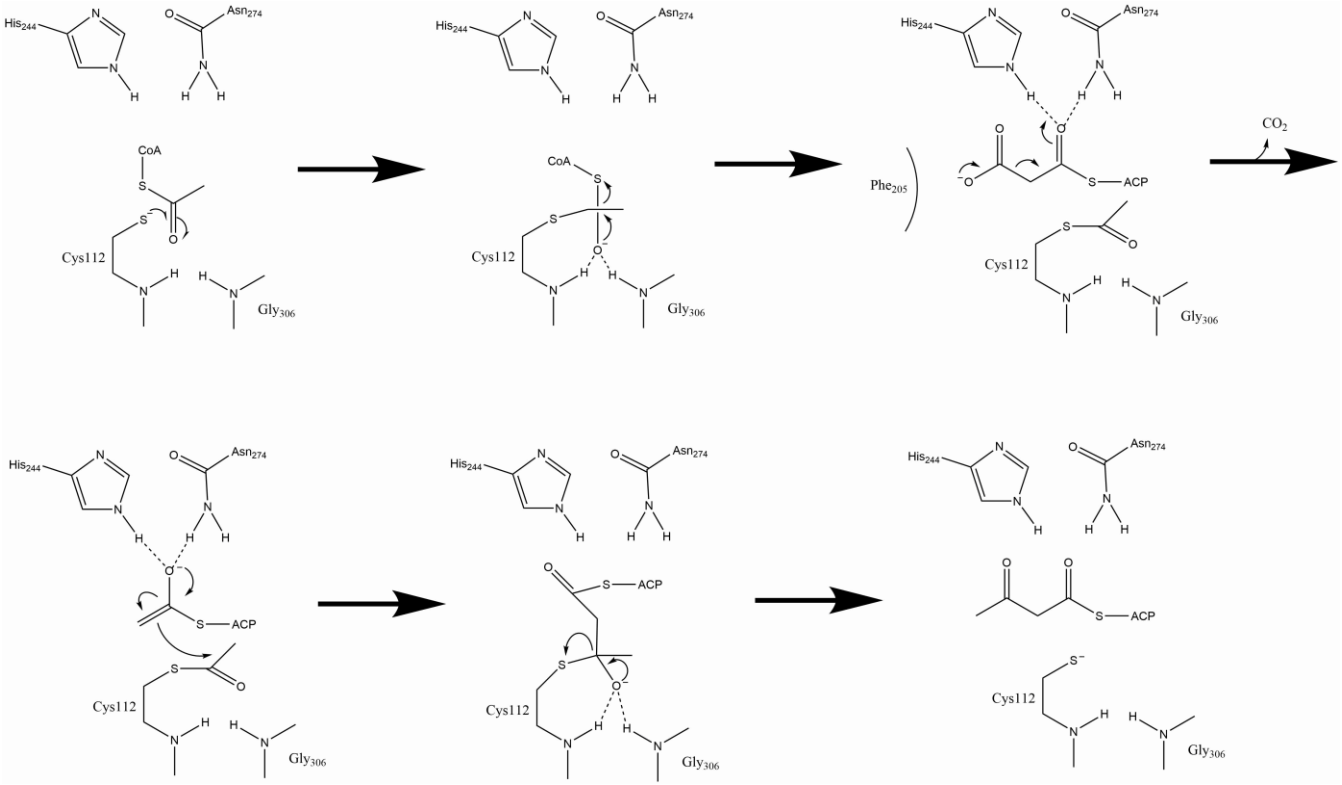


Figure 7.8. FabH mechanism the thiol of Cys112 is activated by the α-helix dipole effect. The acetyl-CoA forms a tetrahedral intermediate during loading onto the Cys. Decarboxylation of malonyl-ACP is assisted by the electron pushing of Phe205, and the charge formed on the thioester carbonyl is stabilized by Nε of His244 and Nδ of Asn274. A carbanion then forms on C2 of the substrate, and the nucleophile attacks the C1 of the acetate on the Cys. A tetrahedral intermediate is stabilized by the oxyanion hole formed by the backbone amides of Cys112 and Gly306. Breakdown of the intermediate releases product, acetoacetyl-ACP, from the enzyme (Heath and Rock, 2002).

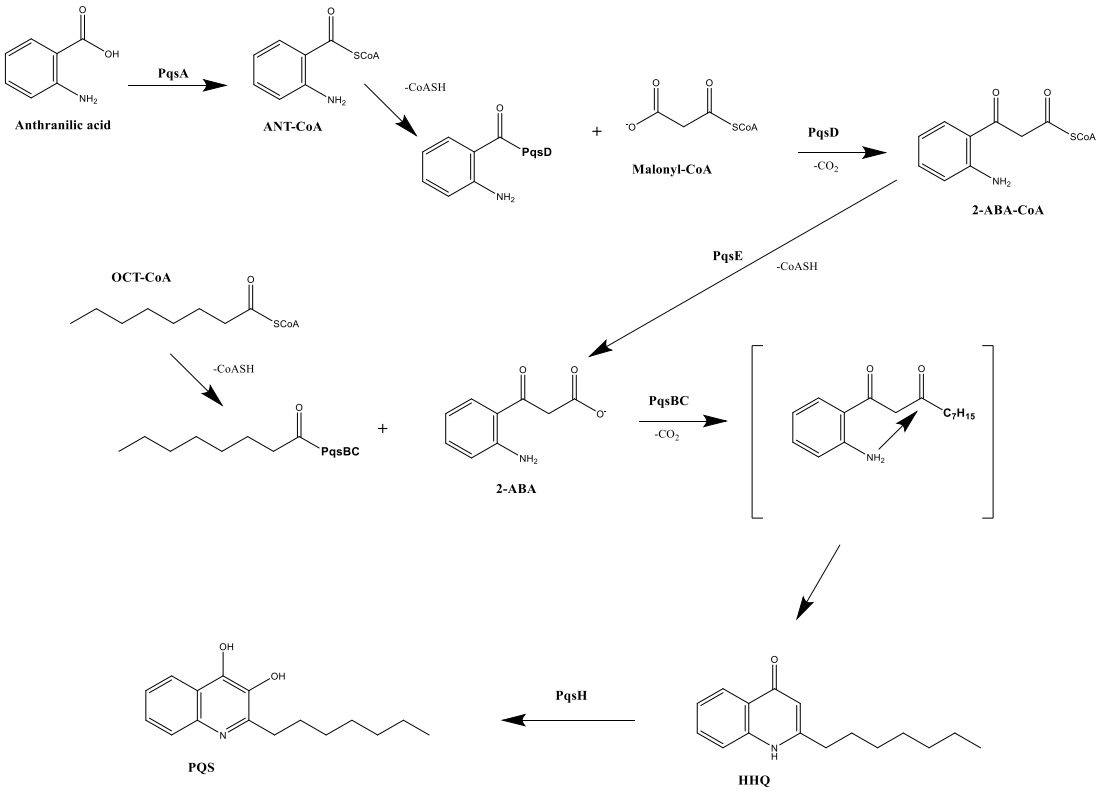


Figure 7.9. The Biosynthetic pathway of PQS by PqsABCDEH operon. In the initial step, the acyl moiety of an activated carboxylic acid is transferred to a strictly conserved active-site cysteine residue. Subsequently, a β-ketoalkanoic acid (malonyl-ACP in the case of FabH, malonyl-CoA or malonyl-ACP in PqsD, 2-ABA in PqsBC) is decarboxylated. Intermediates and products of the alkyl quinolone biosynthetic pathway: Ant-CoA − anthranilate-coenzyme A, 2-ABA-CoA − 2-aminobenzoylacetyl-CoA, 2-ABA – 2-aminobenzoylacetate, HHQ –2-heptyl-4-hydroxyquinoline, PQS – *Pseudomonas* quinolone signal.

Additional data that strongly support a model in which 2-ABA itself supplies the asparagine-equivalent function to assists in catalysis of decarboxylation step is that PqsBC^{V299N} has a very low activity toward 2-ABA (*k*cat = 0.013 s^{-1}) (Drees et al., 2016). Furthermore, that PqsBC is functional without the catalytic asparagine was addressed with the desamino-substrate analogue benzoylacetate (BA), and by reintroducing the asparagine into the protein. Whereas for the wild-type protein the activity toward BA was about 300-fold lower than toward 2-ABA, the PqsBC^{V299N} variant performed significantly better with BA than with 2-ABA (Drees et al., 2016).

In order to get a clear picture about how 2-ABA interact with PqsBC, hence co-crystallisation of PqsBC^{C129A} with 2-ABA (**Figure 7.10**) and PqsBC^{C129A}-Fe^{3+} with 2-ABA (**Figure 7.11**) by using ratio 1:1 were set up. Both co-crystallisation with and without Fe^{3+} resulting crystal. However, only PqsBC^{C129A}-Fe^{3+} with 2-ABA dataset that collected to 2.6 Å showing possibility of 2-ABA on active site pocket, as it can be seen that the 2-ABA possible electron density inside the active site pocket that is connected with Ala129 residue. This is fit with the cysteine to act as a nucleophile in the initial acylation step. However, it is hard to confirm whether that electron density belong to 2-ABA, as the resolution is too low (**Figure 7.12**). The co-crystallisation was set up with the same way as PqsBC^{C129A}-Fe^{3+} in 24 well plate for optimisation, only this time it has been added 2-ABA. Crystals also appeared within approximately 24 hours.

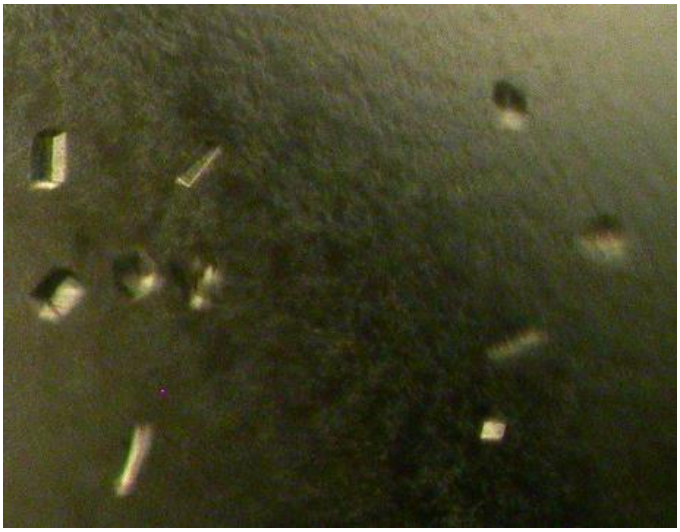


Figure 7.10. PqsBC^{C129A}-2ABA (1:1) crystals on 24-well sitting drop within solution of 0.2 M Sodium chloride, 0.1 M Tris pH 8.5, 25% w/v Polyethylene glycol 3,350.



Figure 7.11. PqsBC^{C129A}-Fe^{3+}-2ABA (1:1) crystals on 24-well sitting drop within solution of 0.2 M Sodium chloride, 0.1 M Tris pH 8.5, 25% w/v Polyethylene glycol 3,350 that added 0.1 M iron (III) chloride hexahydrate.

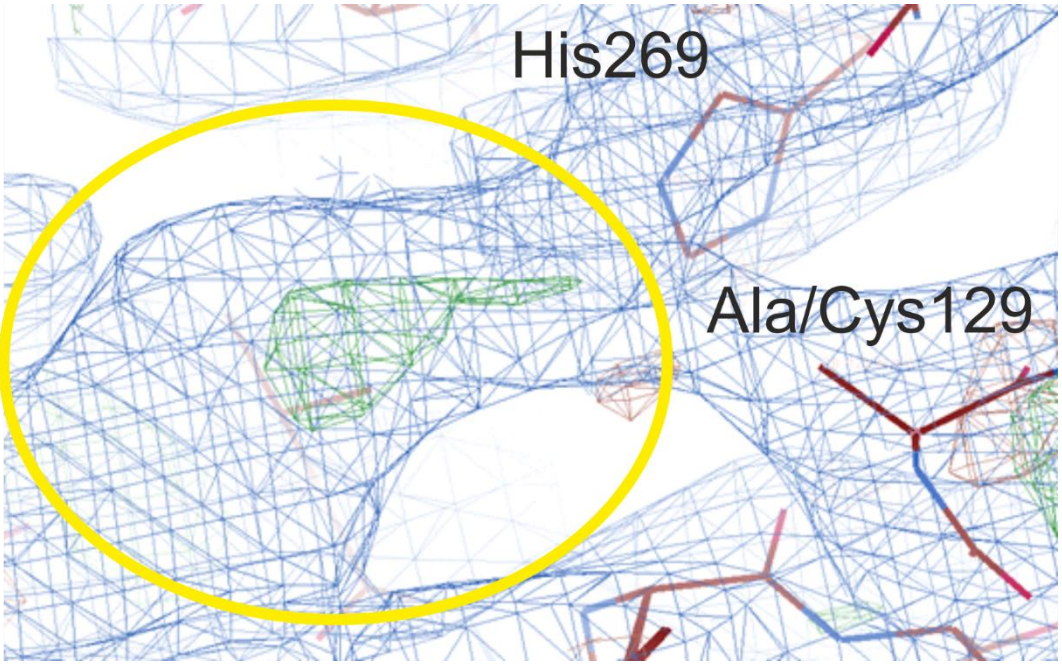


Figure 7.12. Part of PqsBC^{C129A} showing the possibility 2-ABA electron density site, showing catalytic diad residues which are His269 and Cys129. Yellow oval circle showing the 2-ABA possibility site (opened on WinCoot displays maps and models).

In addition, octanoylation of PqsBC Cys129 is also similar to FabH. In FabH, the cysteine's role as a nucleophile in the initial acylation step is independent of the histidine because of its location. The cysteine is located at the N-terminus of an α-helix (**Figure 7.13**) (Heath and Rock, 2002), which can account for a reduction in the *pKa* by 1.6 units (Kortemme and Creighton, 1995). Mutagenic studies do suggest that a H244A mutant was relatively less active in the acyltransferase reaction at pH 6.0 than was the wild type compared to their relative activities at pH 7.0 (Davies et al., 2000).

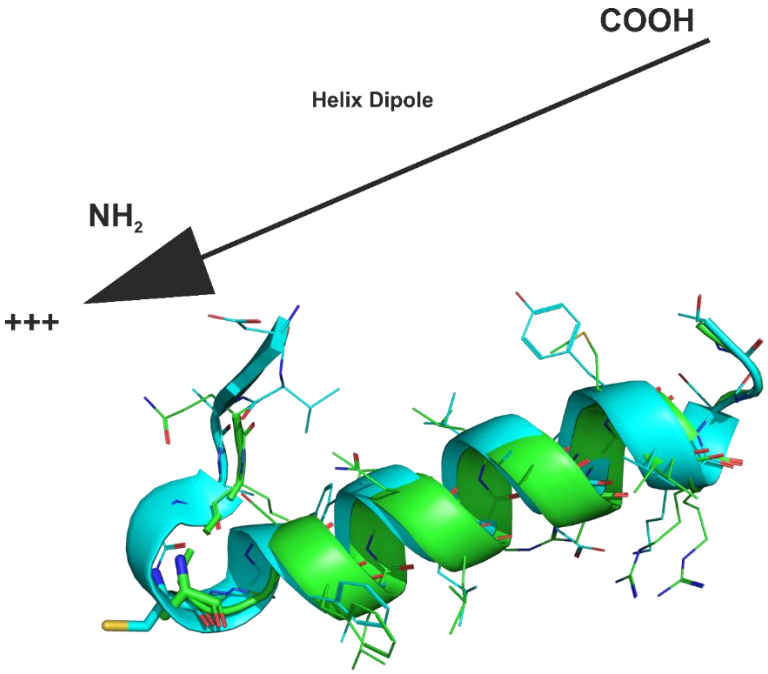


Figure 7.13. Alignment of cartoon and line diagram of Cys112 (*cyan* stick diagram) on FabH *Escherichia coli* and Cys/Ala129 (*green* stick diagram) on PqsBC^{C129A} and α-helix dipole effect cysteine which is positioned at the amino terminal end helix Cα, where the microenvironment of the pH is affected by the α-helix dipole effect to reduce the pKa of the Cys112 by 1.6 pH units (Kortemme and Creighton, 1995, Heath and Rock, 2002).

7.4 Active site volume comparison of PqsBC^{C129A} with FabH

The PqsC^{C129A} active site volume is twice the volume of FabH, with a calculated volume of 761Å^3 compared to 367Å^3 for *E. coli* FabH (pdb:2QNZ) (calculated using 3vee (Voss and Gerstein, 2010)) (**Figure 7.14**). This may be a

requirement to accommodate the bulky aromatic ring of 2-ABA, which is not present in malonyl-ACP (common substrates of FabH).

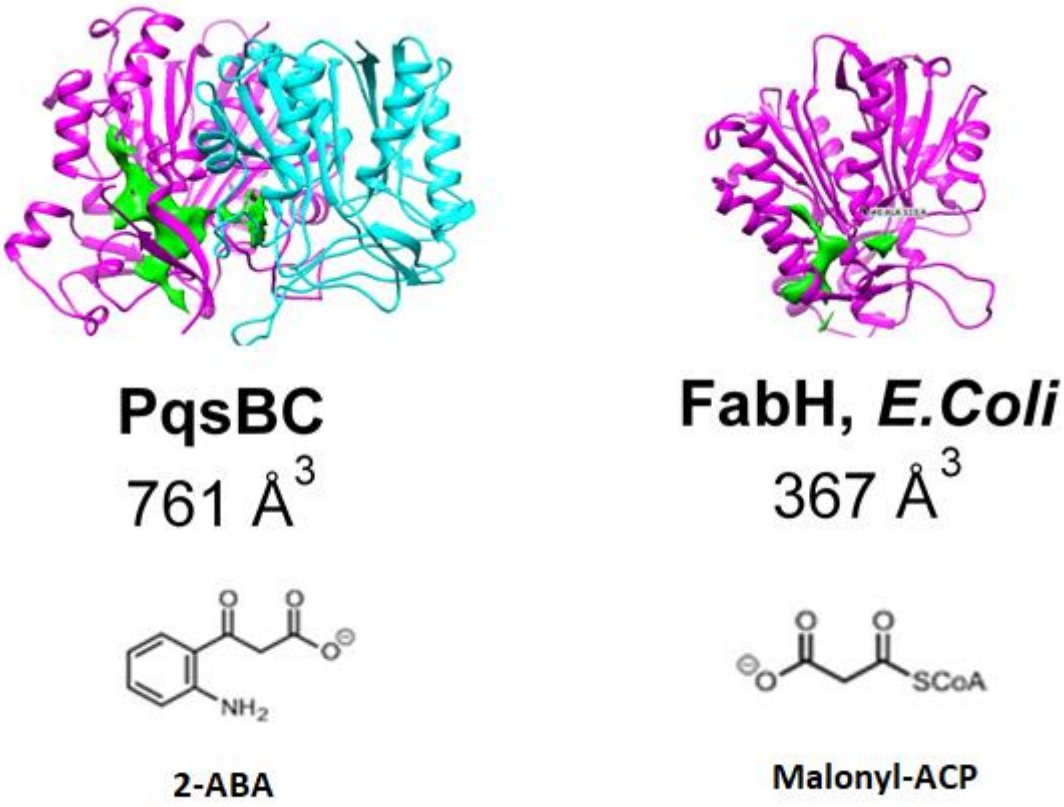


Figure 7.14. Cartoon diagrams of active site volume calculated by using 3Vee (Voss and Gerstein, 2010). Calculated volume of PqsC^{C129A} active site approximately twice the volume of related FabH enzymes which may be a requirement to accommodate the aromatic substrate 2-ABA instead malonyl-ACP in case of FabH.

7.5 Active site pocket residues comparison of PqsBC^{C129A} with FabH

The active site pockets of *E. coli* FabH and *S. aureus* FabH are mostly composed of only one monomer consisting of 30 residues for *E. coli* FabH and 34 residues for *S. aureus* FabH. Only one residue from the other monomer, which is Phe87 aids in forming the pockets (**Figure 7.15** and **Figure 7.16**). However, the *M. tuberculosis* FabH pockets are formed from 34 residues within the monomer, and 3 residues from the other monomer; Gln86, Thr87, and Ile196 (**Figure 7.17**).

Unlike *E. coli* FabH and *S. aureus* FabH, PqsBC's active site pocket seems to be shared more equally between both PqsB and PqsC. It is deeper and larger in volume (**Figure 7.18**). In fact, there are 18 residues of PqsB and 62 residues from PqsC (**Figure 7.18**). In total 80 residues compose the active site pocket of PqsBC, which is more than double the residues that build the active site pocket of the other FabH enzymes.

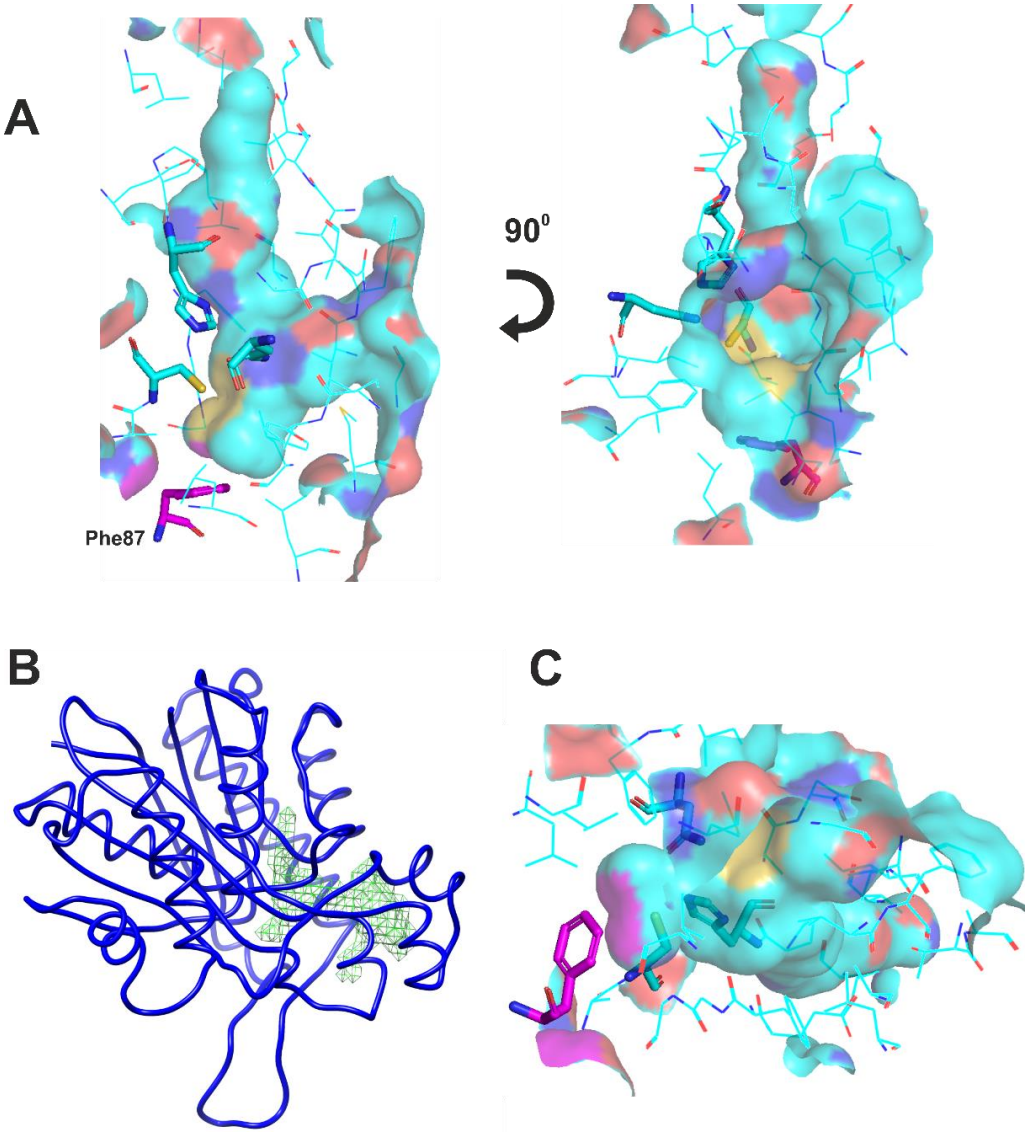


Figure 7.15. Line and surface diagram of FabH *E. coli* active site pocket (*cyan*) (PDB code, 1hn9), stick diagram of catalytic triad residues (*cyan*) Cys112, His244, and Asn274, with Phe87 (*magenta*) residue from another monomer. **A.** a whole FabH *E. coli* active site pocket (*cyan*) with different angle. **B**. active site pocket of FabH *E. coli* shows in green mesh rendered by using 3Vee (Voss and Gerstein, 2010). **C**. focus on Phe87 (*magenta*) residue from another monomer which involved on active site pocket construction.

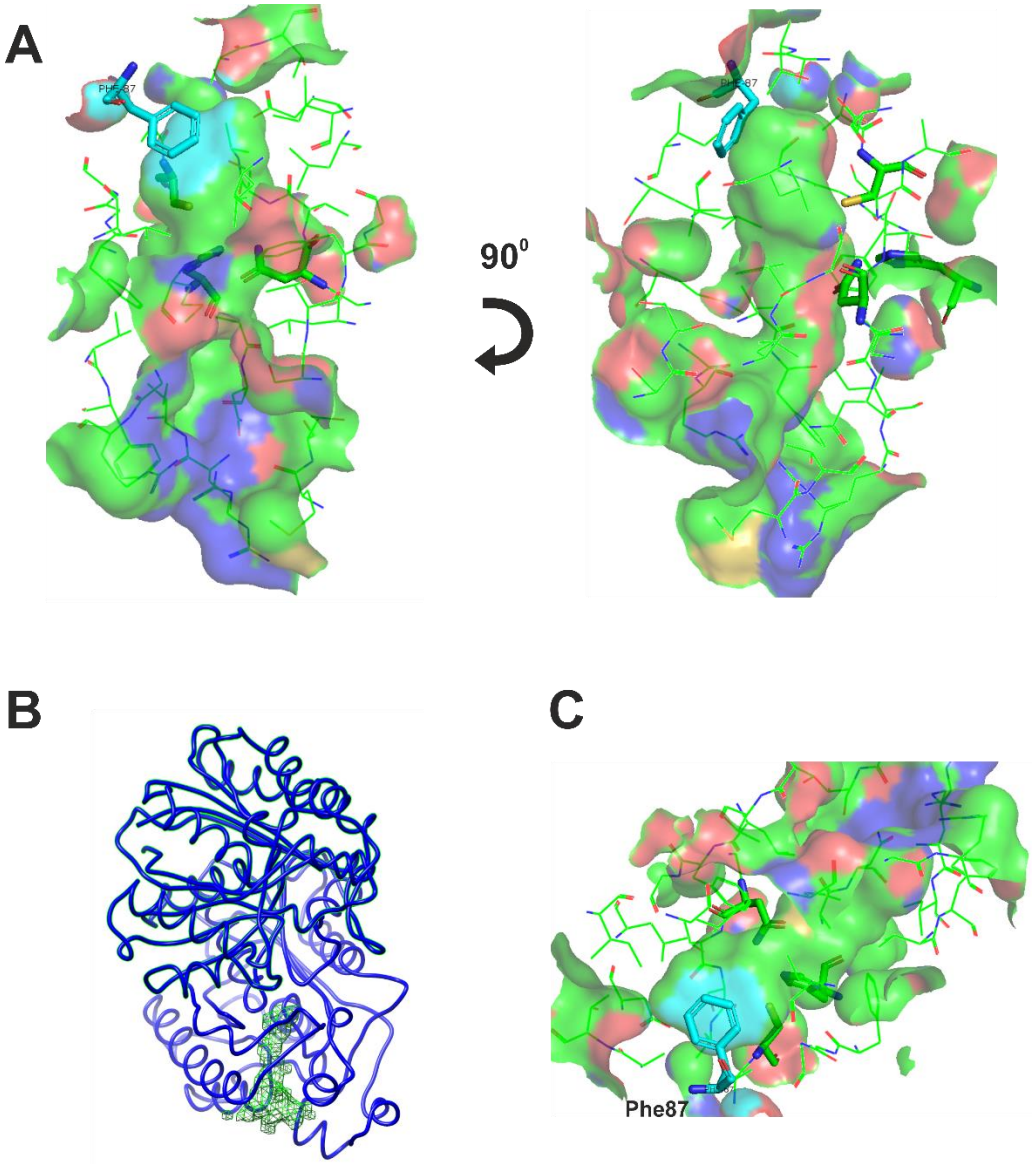


Figure 7.16. Line and surface diagram of FabH *Staphylococcus aureus* active site pocket (*green*) (PDB code: 1zow), stick diagram of catalytic triad residues (*green*) Cys112, His244, and Asn274, with Phe87 (*cyan*) residue from another monomer. **A**. a whole FabH *Escherichia coli* active site pocket (*green*) with different angle. **B**. active site pocket of FabH *S. aureus* shows in green mesh rendered by using 3Vee (Voss and Gerstein, 2010). **C**. focus on Phe87 (*cyan*) residue from another monomer which involved on active site pocket construction.

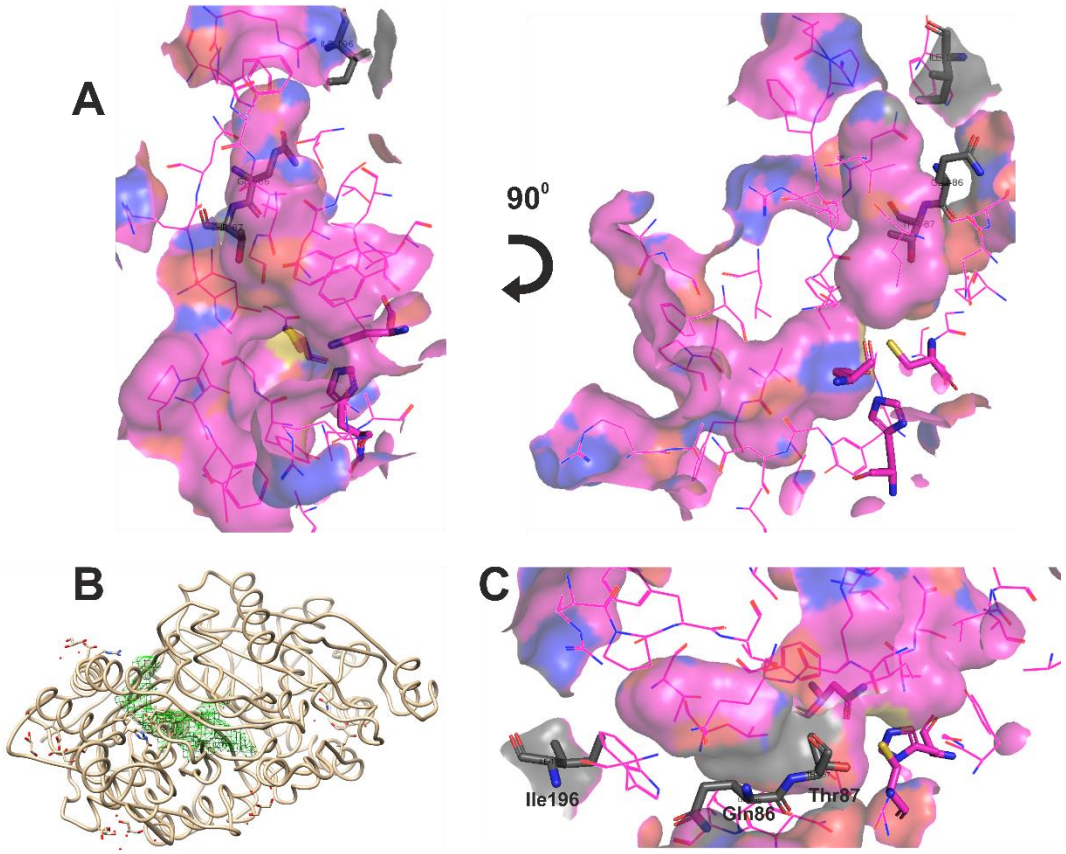


Figure 7.17. Line and surface diagram of FabH *Mycobacterium tuberculosis* active site pocket (*magenta*) (PDB code: 1hzp), stick diagram of catalytic triad residues (*magenta*) Cys112, His244, and Asn274, with Gln86, Thr87, Ile196 (*grey*) residues from another monomer. A) a whole FabH *Escherichia coli* active site pocket (*magenta*) with different angle. B) focus on Gln86, Thr87, Ile196 (*grey*) residue from another monomer which involved on active site pocket construction.

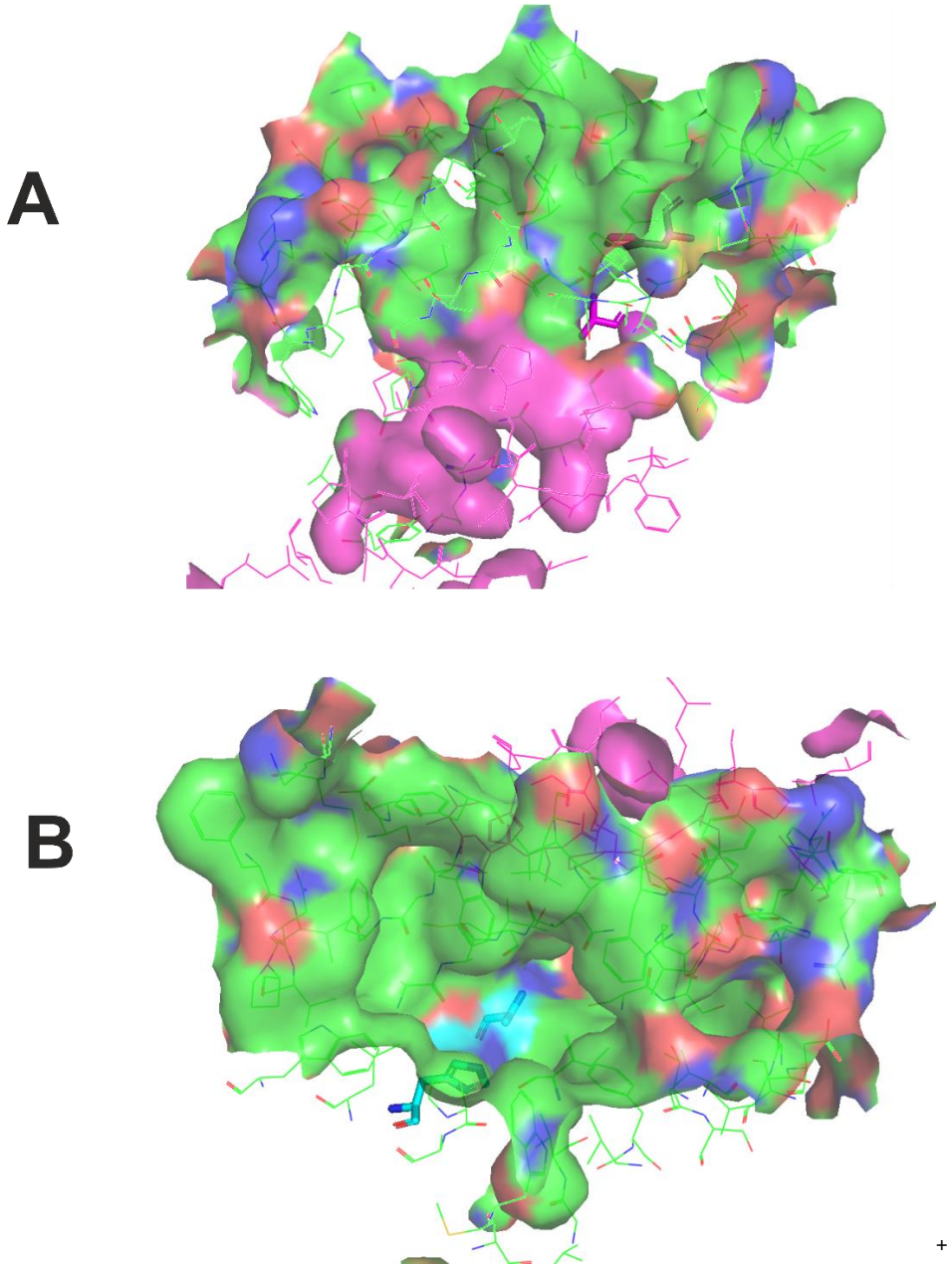


Figure 7.18. Line and surface diagram of PqsBC^{C129A} active site pocket (*green*, *magenta*), stick diagram of catalytic diad residues (*cyan*) Ala/Cys129, His269. A) angle that shows PqsB (*magenta*) and PqsC (*green*) sharing the active site pocket construction. B) opening of active site pocket which is located on PqsC.

7.6 Substrates processing by PqsBC

Based on *E. coli* FabH (**Figure 7.15**) and *S. aureus* FabH (**Figure 7.16**) active site pockets extended to form an L-shaped channel with only a single solvent access portal.

Whereas, based on the crystal structure of $PqsBC^{C129A}$ and $PqsBC^{C129A}$-Fe^{3+}, it is clearly observed that the active site pocket of PqsBC has branching channels (**Figure 7.19**), where it is possible that these are entrance and exit portals. Furthermore, it is also observed that the two different channels are also similar in size also in shape. However, the first channel is a little bit smaller than the second channel, especially at the opening active site pocket (**Figure 7.20**). Therefore, maybe there is different way in and out for substrates that have been catalysed by PqsBC. As it can be seen on **Figure 7.8**, the initial step, the acyl moiety of an activated carboxylic acid is transferred to a strictly conserved active-site cysteine residue, which may occur at the first, smaller channel (**Figure 7.20**). Subsequently, a β-ketoalkanoic acid, 2-ABA in PqsBC is decarboxylated at the second/bigger channel (**Figure 7.20**).

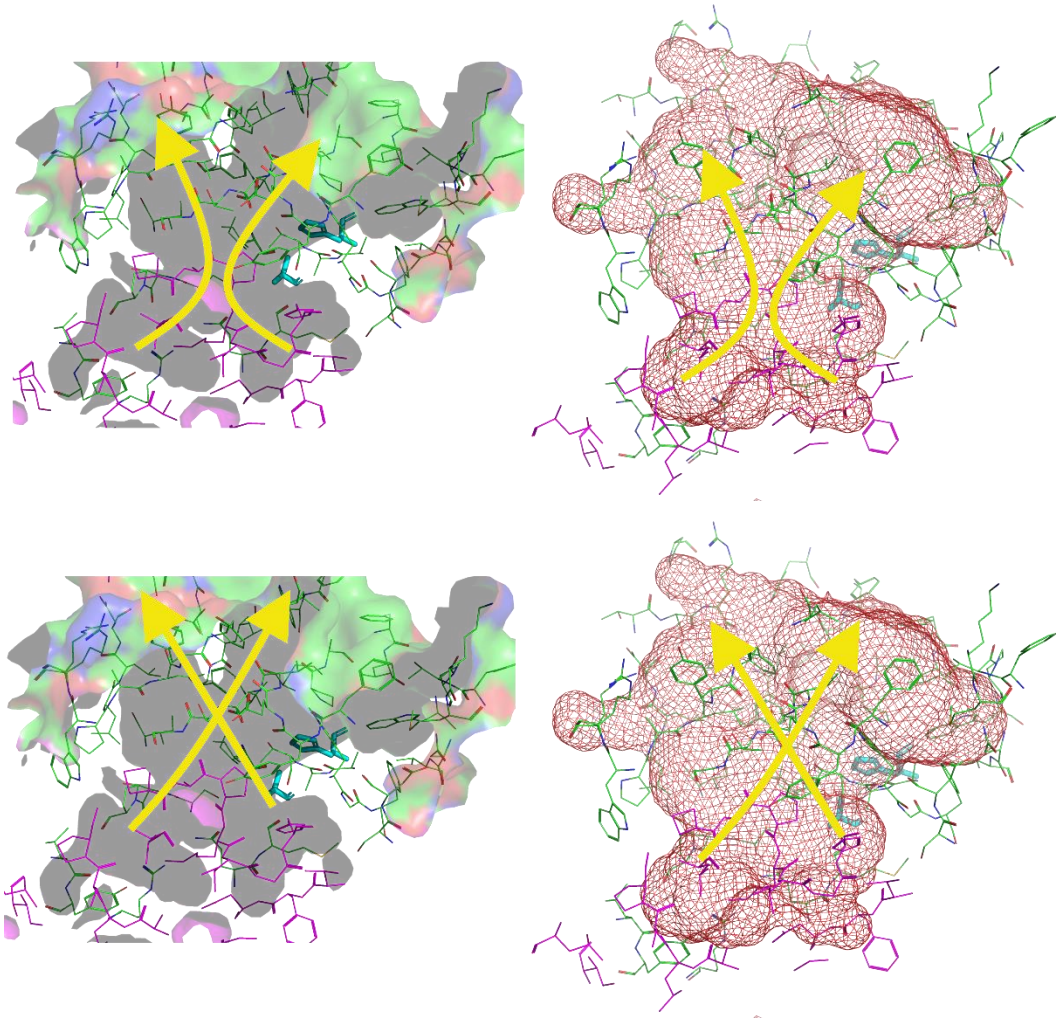


Figure 7.19. Line, surface and mesh diagrams of PqsBC active site pocket (PqsB in *magenta*, PqsC in *green*, Ala/Cys129 and His269 in *cyan* stick diagram). The figure shows two branching-channel of PqsBC active site pocket as well as the possibilities direction way in and way out (*yellow arrow*). Mesh diagram of active site pocket rendered using MetaPocket (Huang, 2009).

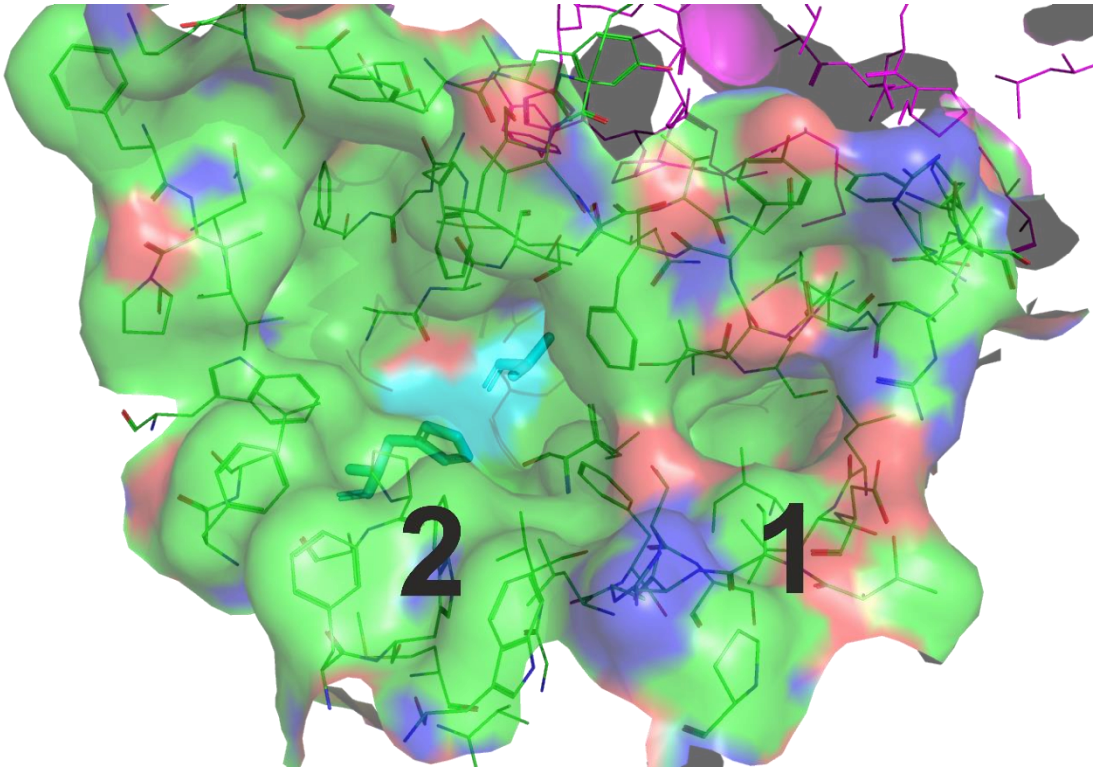


Figure 7.20. Line and surface diagram of PqsBC active site pocket (PqsB in *magenta*, PqsC in *green*, Ala/Cys129 and His269 in *cyan* stick diagram). The first/smaller (**1**) channel seems may a place for the initial step, the acyl moiety of an activated carboxylic acid is transferred to a strictly conserved active-site cysteine residue. Subsequently, the second/bigger (**2**) channel is the place for β-ketoalkanoic acid, 2-ABA in PqsBC is decarboxylated due to it will need bigger space for aromatic substrate 2-ABA.

Chapter 8: Oligomerisation of PqsBC

8.1 Mutagenesis stabilising tetramer PqsBC^{L229C}

As can be seen on **Figure 8.1**, **the** PqsBC^{C129A} crystal structure shows a heterotetrametric conformation, this heterotetrameric conformation reveals that there are four interfaces between PqsC (**Figure 8.1**). However, based on gel filtration chromatography, PqsBC^{C129A} is a dimer in solution. The calculated molecular weight of PqsBC^{C129A} is 61 kDa. To assess whether this was the molecular weight of the complex in solution, the elution volume was compared to protein standards run on a S200 16/60 gel filtration column. The protein eluted at 85 ml, which suggests that the dimeric configuration of 61 kDa is correct rather than a tetrameric protein of 122 kDa (**Figure 4.2 and Figure 8.7**).

There is observed there is a prominent 879.2 Å^2 interface area between two PqsC proteins (**Figure 8.2**). The interface is stabilised by fourteen hydrogen bond interactions and four salt bridges (**Table 8.1**). It is also observed that Leu229 in PqsC is involved to form the tetramer (**Table 8.1**) (**Figure 8.3**). Therefore, with the aim to stabilising the tetramer, Leu229 was mutated to Cys229, so that a covalent bond derived from two thiol groups would form. With this covalent bond present, then the tetrameric complex should be stable in solution provided the cysteines are oxidised to form a disulphide bond (**Figure 8.4**).

Site directed mutagenesis was used to mutate the DNA sequence of PqsBC plasmid to produce PqsBC^{L229C}. The methods for restriction-free cloning is shown in **Table 8.1**. The coding sequence of the resulting plasmid pET28b::*pqsBC*^{L229C}-NHis$_8$ was verified using commercial sequencing services.

PqsBC^{L229C} overproduction was carried out in *E. coli* Rosetta2-(DE3)-[pLysS] cells that were carrying the respective expression plasmid using TB medium (Carl Roth, Karlsruhe, Germany) with 150 µg/ml of kanamycin antibiotic (Applichem, Darmstadt, Germany).

PqsBC^{L229C} was purified using immobilised metal affinity chromatography (IMAC) (**Figure 8.5)**, and gel filtration chromatography with S200 16/60 column (**Figure 8.6)**. PqsBC^{L229C} based on gel filtration data indicating that PqsBC^{L229C} as a dimer with an apparent molecular mass of 61 kDa and PqsBC^{L229C} as oligomer with an apparent molecular mass of 490 kDa.

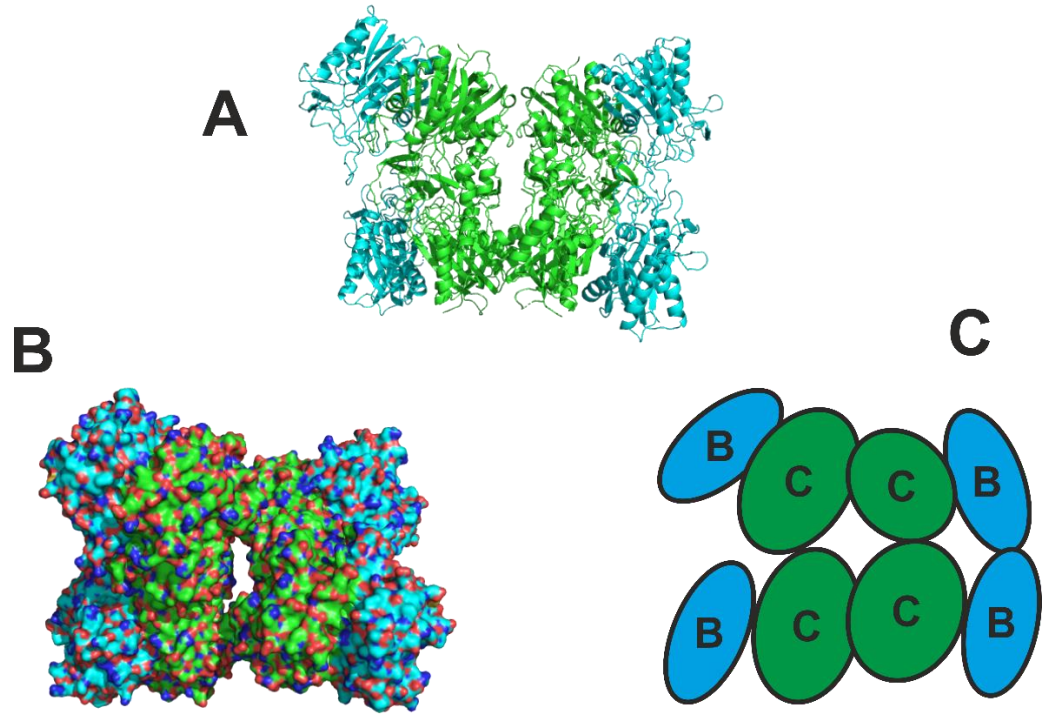


Figure 8.1. (**A**)**.** Cartoon diagram of PqsBC^{C129A} (**A**), surface diagram (**B**), and schematic (**C**) crystal structure as heterotetrameric conformation. PqsC^{C129A} (green) and PqsB (cyan). It can be seen that four of PqsC assembling on the centre that also forming four interfaces between them.

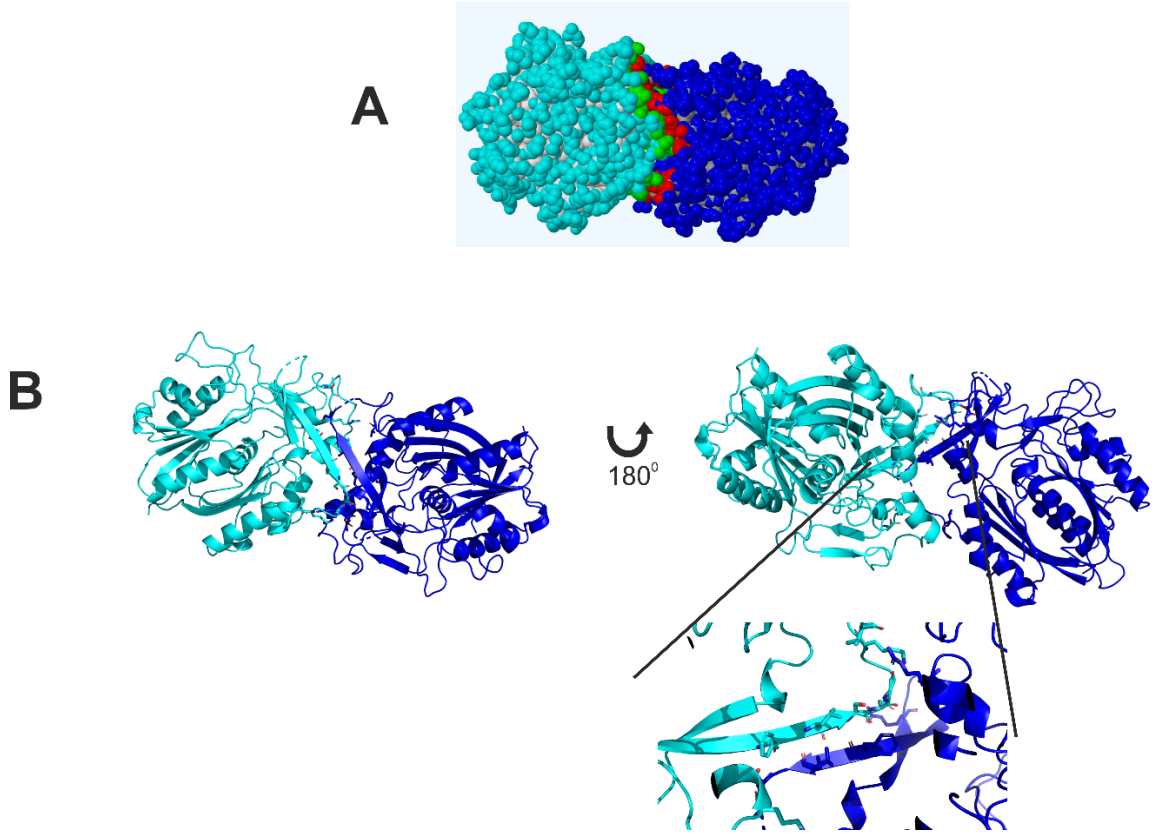


Figure 8.2. Sphere (**A**) rendered with JyMOL and Cartoon (**B**) rendered with PyMOL. Diagram of two of pqsC interface. **A)** Sphere diagram of PqsC (blue), PqsC (cyan), interface area (red and green). **B)** Cartoon diagram **of** PqsC (blue) and PqsC (cyan) rotate 180^0, residues that involved making interface are in sticks.

Table 8.1. Hydrogen bonds and salt bridges of PqsC interface

No.	PqsC	Dist. Å^2	PqsC
1	F:ARG 168[NH2]	2.93	C:VAL 241[O]
2	F:PHE 227[N]	2.79	C:SER 231[OG]
3	F:LEU 229[N]	3.03	C:LEU 229[O]
4	F:SER 231[N]	2.96	C:PHE 227[O]
5	F:LYS 236[NZ]	3.06	C:SER 167[OG]
6	F:THR 166[O]	2.84	C:LYS 236[NZ]
7	F:PHE 227[O]	3.61	C:SER 231[OG]
8	F:PHE 227[O]	2.93	C:SER 231[N]
9	F:LEU 229[O]	2.91	C:LEU 229[N]
10	F:SER 231[O]	2.95	C:PHE 227[N]
11	F:ASP 232[OD2]	2.71	C:ARG 212[NE]
12	F:ASP 232[OD2]	2.86	C:ARG 212[NH2]
13	F:GLY 233[O]	3.75	C:SER 167[OG]
14	F:VAL 241[O]	2.94	C:ARG 168[NH2]
Salt bridges			
No.	**PqsC**	**Dist. Å^2**	**PqsC**
1	F:ASP 232[OD1]	3.66	C:ARG 224[NE]
2	F:ASP 232[OD1]	3.53	C:ARG 212[NE]
3	F:ASP 232[OD2]	2.71	C:ARG 212[NE]
4	F:ASP 232[OD2]	2.86	C:ARG 212[NH2]

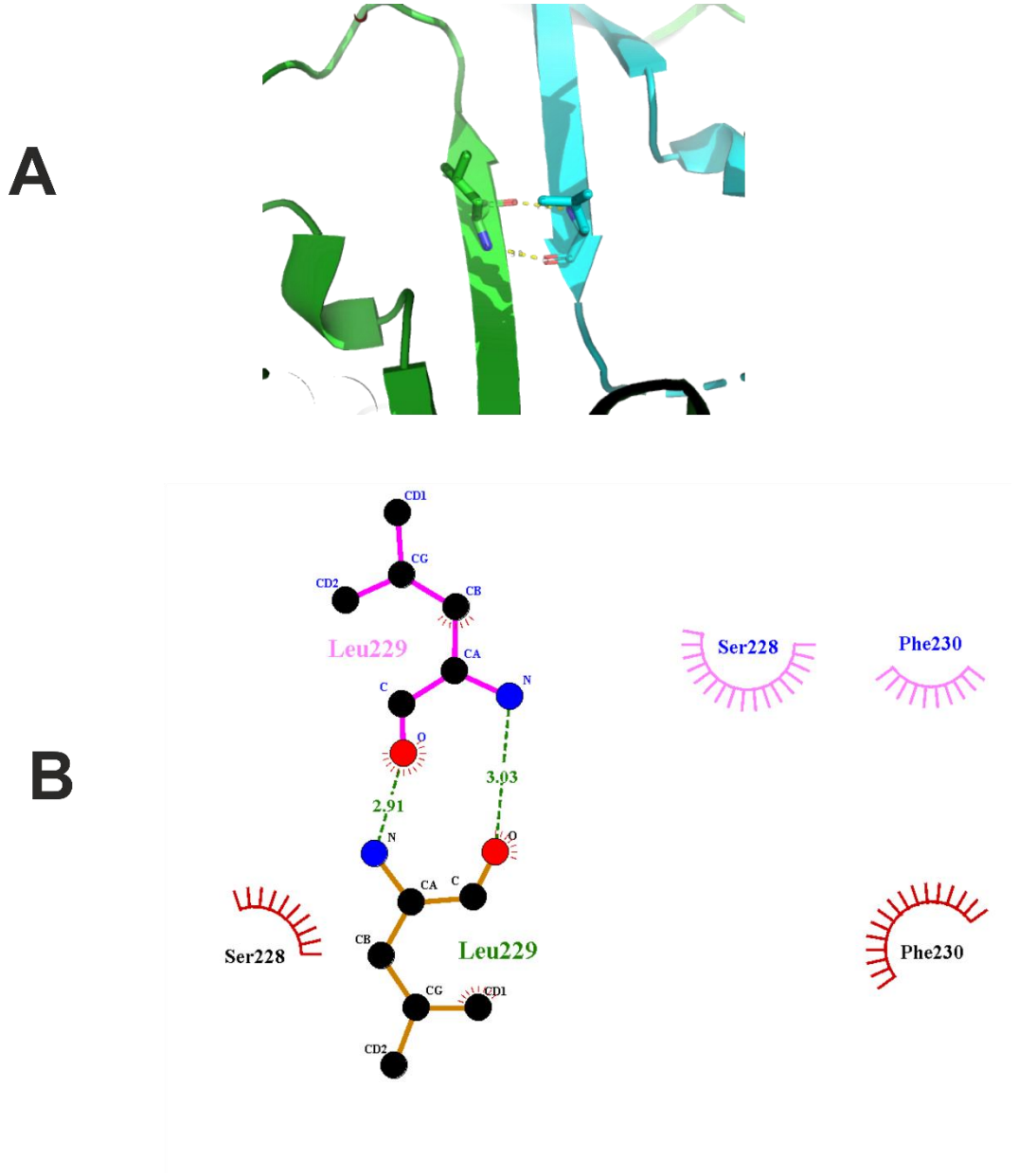


Figure 8.3. **A.** Cartoon diagram of two Leu229 (green and cyan stick) interaction within two subunit PqsC **B.** Ligplot (Wallace et al., 1995) show interactions between two Leu229 within different subunit PqsBC^{C129A}.

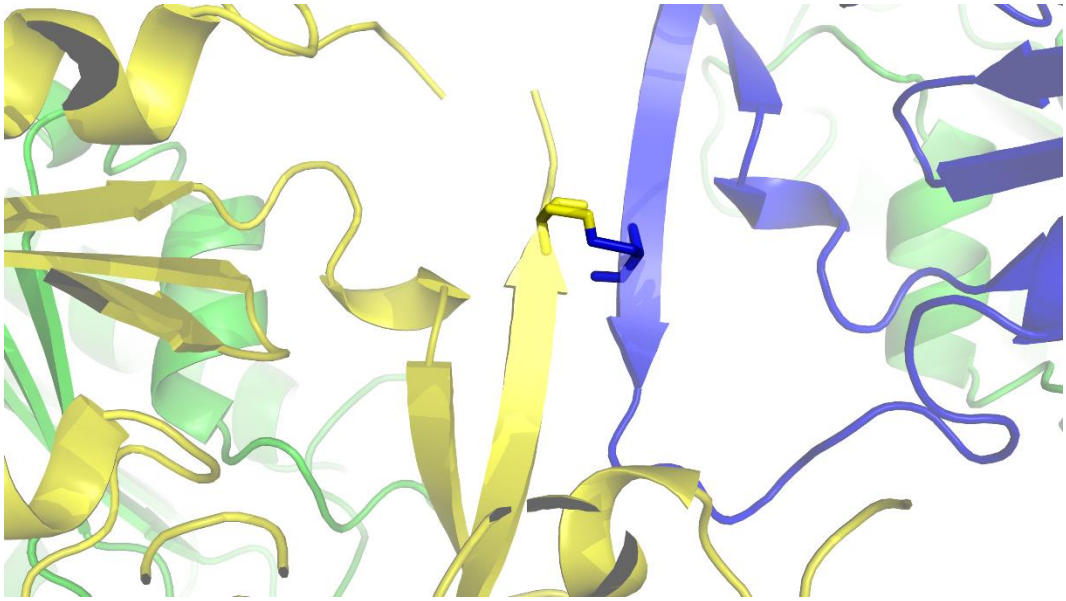


Figure 8.4. Model of cartoon diagram of two Cys229 (yellow and blue sticks) interaction within two subunit PqsBC^{L229C} to form disulphide bond.

Table 8.2. Cloning of PqsBC^{L229C} *Eschericia coli* expression constructs.

Insertion plasmid	Method	Template	Forward primer	Reverse primer
pET28b+N-His-tev2	Restriction-free cloning	PqsBC^{C129A}	ccgcggctttatttctcgtgcttcagcgacggccagaac	gttctggccgtcgctgaagcacgagaaataaagccgcgg

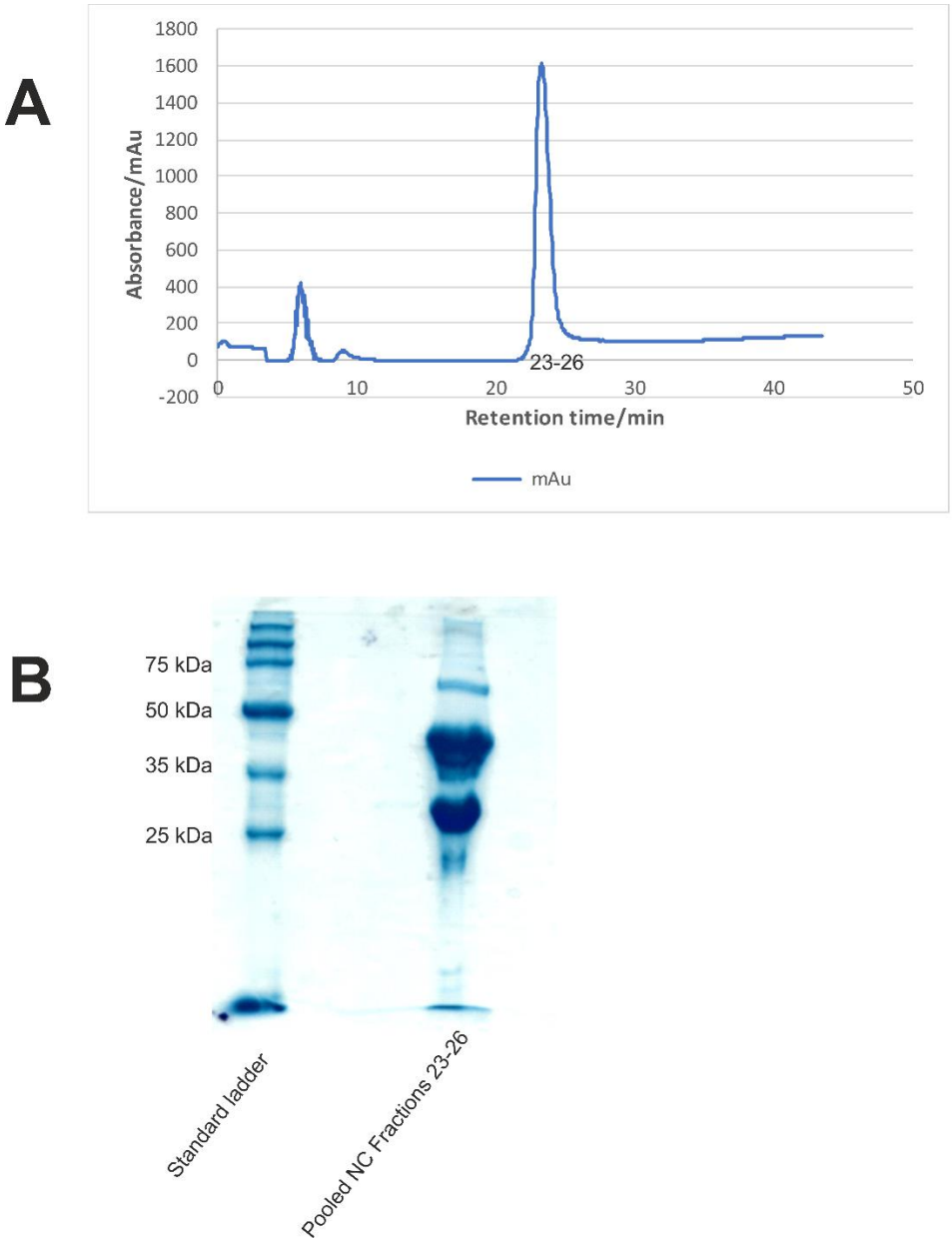


Figure 8.5. Purification of PqsBC^{L229C} (**A)** Nickel column chromatogram. Curve of UV absorbance and the concentration of buffer B contains 500 mM imidazole which gradiently increase are shown. (**B**). SDS-PAGE of pooled Nickel column fractions 60-75 shows that the protein is relatively pure.

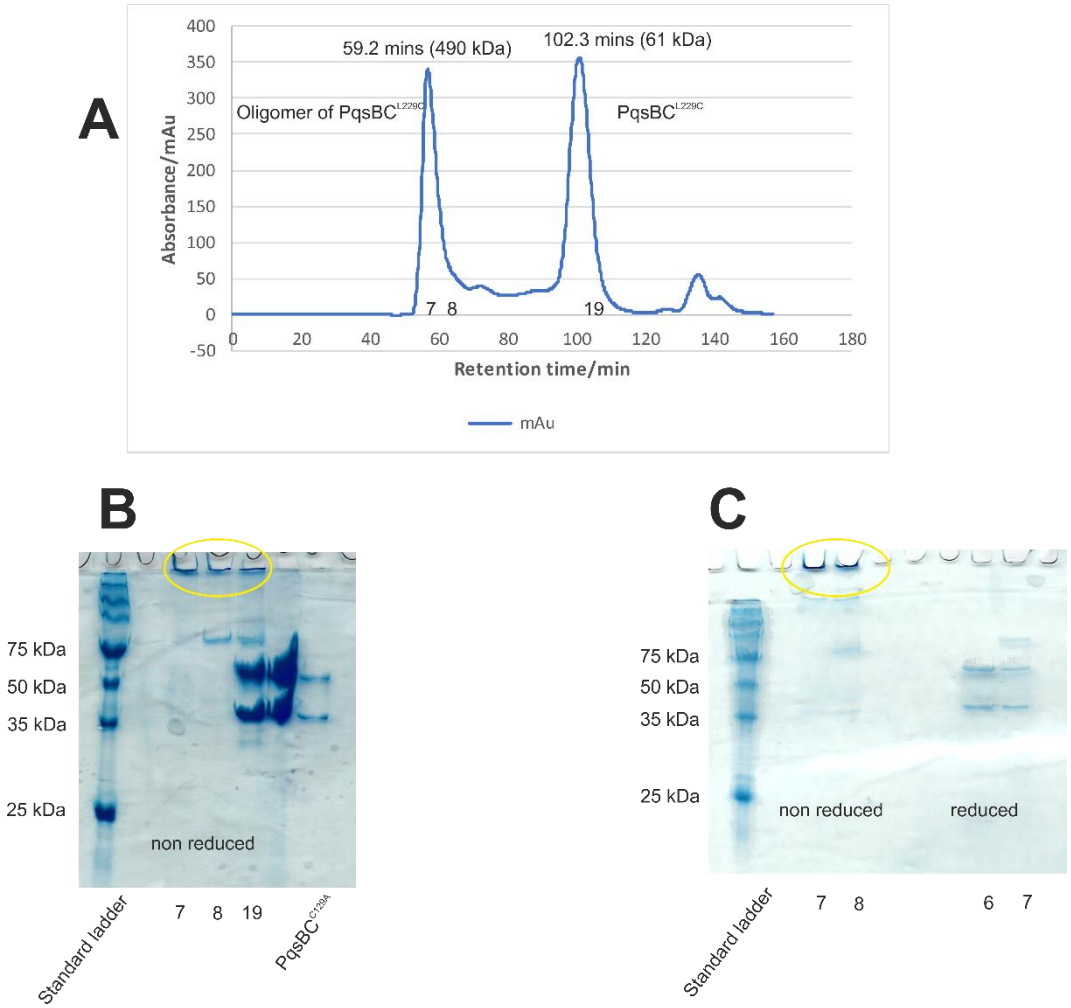


Figure 8.6. Purification of PqsBC^{L229C} (**A)** Gel filtration chromatogram showing another peak at retention time 59.2 minutes or elution volume 51.79 ml (490 kDa), beside the normal peak that used to appear at retention time 102.3 minutes or 80.81 ml elution volume (61 kDa) for a normal heterodimer PqsBC. (**B**) SDS-PAGE of Gel filtration fractions number 7 and 8 from the first peak and number 19 from the second peak. The yellow oval circle indicates the PqsBC^{L229C} oligomer that is too big to pass through 15% SDS-PAGE gel. Bands from fraction no 7 and 8 only visible in the presence of a reducing agent on (**C**).

Unlike a nickel column chromatogram on Purification of $PqsBC^{C129A}$ (**Figure 4.1**), which is only appear one peak. Meanwhile, there are two peaks observed on a nickel column chromatogram of $PqsBC^{L229C}$. Furthermore, on gel filtration chromatogram the first new peak presence at retention time 59.2 minutes or elution volume 51.79 ml (490 kDa) (**Figure 8.5**) and second peak at retention time 102.3 minutes or 80.81 ml elution volume (61 kDa) for a normal heterodimer PqsBC as this peak. Therefore, the first peak that presence at retention time 59.2 minutes or elution volume 51.79 ml (490 kDa) is the peak as a result of Leu229 was mutated to Cys229. It seems mutation on Leu229 to Cys229 worked, however the size of molecule that suggested by retention time is too big for a tetramer. The retention time 59.2 minutes or elution volume 51.79 ml (490 kDa) suggested the peak is represent of oligomer PqsBC instead a PqsBC tetramer. This PqsBC oligomer was observed on gel filtration chromatography and SDS-PAGE (**Figure 8.6C**).

A peak at a retention time 59.2 minutes or an elution volume of 51.79 ml indicates a protein size of 490 kDa. However, is too big to pass into the gel when it was analysed by non-reducing SDS-PAGE. That was likely due to the disulphide bond that formed by Cys229. This protein that stuck at the top of the resolving gel (inside the yellow oval circle on **Figure 8.6B** and **8.6C)** was confirmed to be $PqsBC^{L229C}$ as it started migrating in the presence of a reducing agent. Moreover, the protein that migrated showed bands of the same molecular weight as PqsB and PqsC.

8.2 Four of PqsC interfaces on PqsBC^{C129A} crystal structure

As was described in the previous paragraph within this chapter, the prominent PqsC interface on between four of PqsC has 879.2 Å^2 interface area between two of PqsC (**Figure 8.2**). The interface is stabilised by fourteen hydrogen bond interactions and four salt bridges (**Table 8.1**). Apart from the interface that has been explained, there are three more interfaces that hold four of PqsC assembled together. First interface (ICC-1) has 917.5 Å^2 interface area (**Figure 8.7**) that is composed of 16 hydrogen bonds and 2 salt bridges (**Table 8.3**). Subsequently, second interface (ICC-2) has 214.3 Å^2 (**Figure 8.8**) interface area that is formed by 1 hydrogen bond and 3 salt bridges (**Table 8.4**). Whereas, the third interface (ICC-3) has 202.5 Å^2 (**Figure 8.9**), arranged by 2 hydrogen bonds and 2 salt bridges (**Table 8.5**).

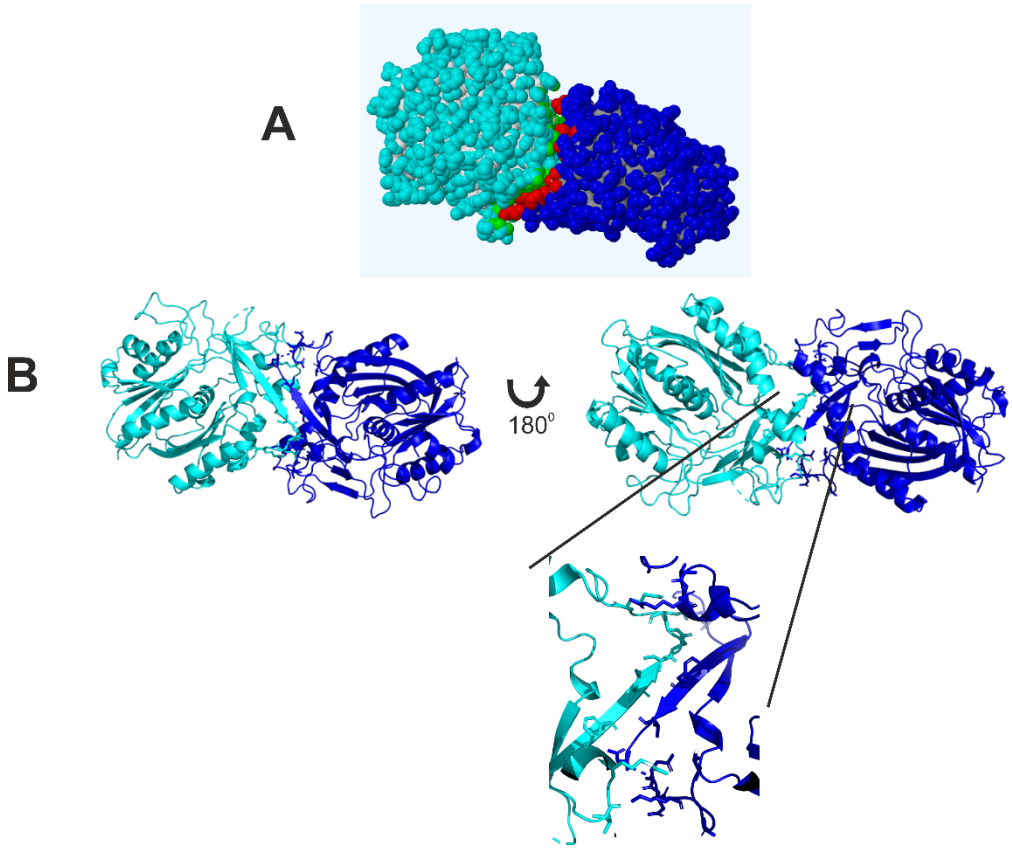


Figure 8.7. ICC-1 interface, sphere (**A**) rendered with JyMOL and cartoon (**B**) rendered with PyMOL. Diagram of two of pqsC interface. **A)** Sphere diagram of PqsC (blue), PqsC (cyan), interface area (red and green). **B)** Cartoon diagram **of** PqsC (blue) and PqsC (cyan) rotate 180^0, residues that involved making interface are in sticks.

Table 8.3. Hydrogen bonds and salt bridges of PqsC ICC-1 interface

No.	PqsC	Dist. Å^2	PqsC
1	H:LYS 236[NZ]	3.84	D:THR 166[OG1]
2	H:LYS 236[NZ]	2.98	D:SER 167[OG]
3	H:GLN 234[NE2]	3.54	D:LEU 213[O]
4	H:SER 231[N]	2.83	D:PHE 227[O]
5	H:LEU 229[N]	2.92	D:LEU 229[O]
6	H:PHE 227[N]	2.93	D:ASP 231[OD2]
7	H:ARG 168[NH2]	3.07	D:VAL 241[O]
8	H:THR 166[OG1]	3.76	D:LYS 236[NZ]
9	H:THR 166[O]	2.77	D:LYS 236[NZ]
10	H:PHE 227[O]	3.87	D:ASP 231[N]
11	H:LEU 229[O]	2.74	D:LEU 229[N]
12	H:SER 231[O]	2.71	D:PHE 227[N]
13	H:ASP 232[OD2]	3.09	D:ARG 212[NH1]
14	H:GLY 233[O]	3.49	D:SER 167[OG]
15	H:GLN 234[OE1]	3.34	D:ASN 215[N]
16	H:VAL 241[O]	2.84	D:ARG 168[NH2]
Salt bridges			
No.	**PqsC**	**Dist. Å^2**	**PqsC**
1	H:ASP 232[OD2]	3.09	D:ARG 212[NH1]
2	H:ASP 232[OD2]	3.87	D:ARG 212[NE]

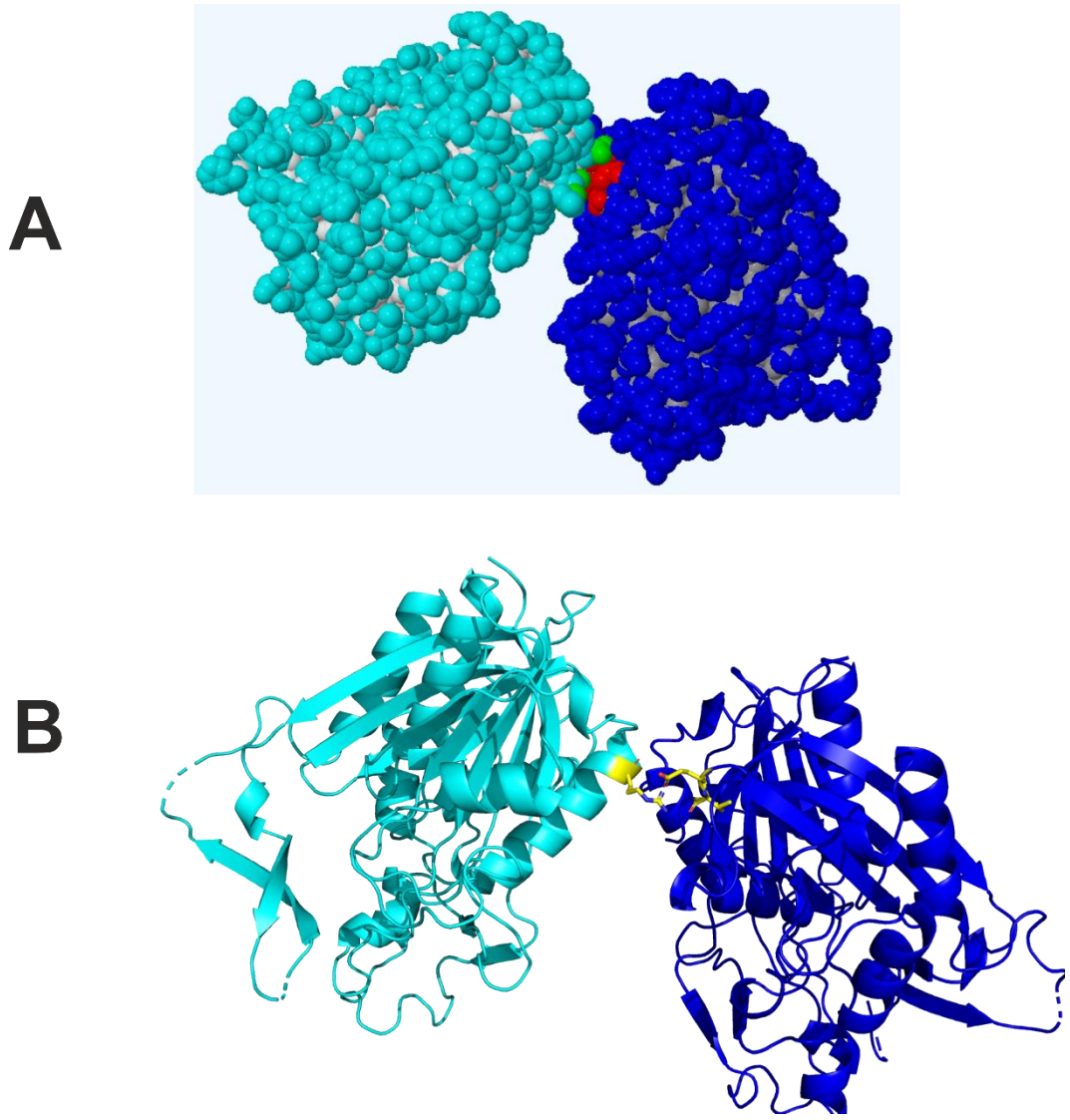


Figure 8.8. ICC-2 interface, sphere (**A**) rendered with JyMOL and cartoon (**B**) rendered with PyMOL. Diagram of two of pqsC interface. **A)** Sphere diagram of PqsC (blue), PqsC (cyan), interface area (red and green). **B)** Cartoon diagram **of** PqsC (blue) and PqsC (cyan), residues that involved making interface are in yellow sticks.

Table 8.4. Hydrogen bonds and salt bridges of PqsC ICC-2 interface

No.	PqsC	Dist. Å^2	PqsC
1	C:ARG 68[NH2]	2.97	D:VAL 345[O]
Salt bridges			
No.	**PqsC**	**Dist. Å^2**	**PqsC**
1	C:ARG 68[NE]	3.19	D:GLU 344[OE1]
2	C:ARG 68[NH1]	3.62	D:GLU 344[OE1]
3	C:ARG 68[NH2]	3.48	D:GLU 344[OE1]

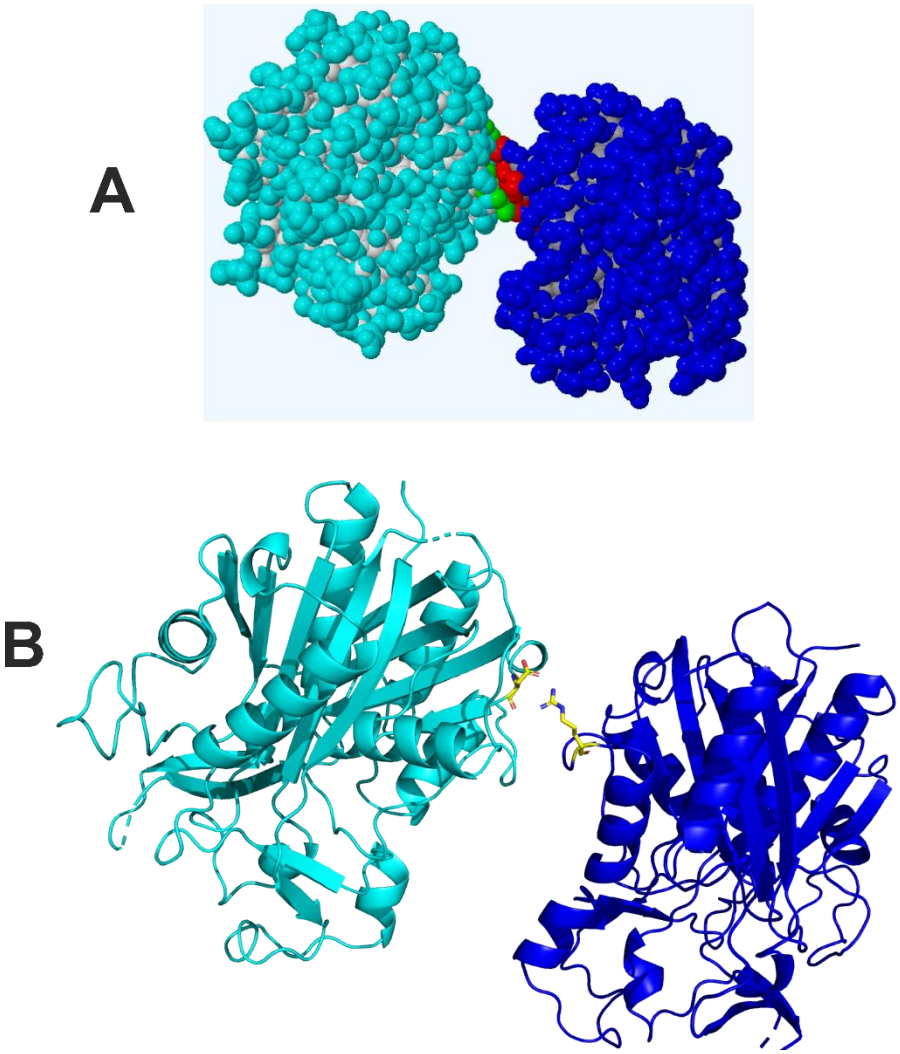


Figure 8.9. ICC-3 interface, sphere (**A**) rendered with JyMOL and cartoon (**B**) rendered with PyMOL. Diagram of two of pqsC interface. **A)** Sphere diagram of PqsC (blue), PqsC (cyan), interface area (red and green). **B)** Cartoon diagram **of** PqsC (blue) and PqsC (cyan), residues that involved making interface are in yellow sticks.

Table 8.5. Hydrogen bonds and salt bridges of PqsC ICC-3 interface

No.	**PqsC**	**Dist. Å²**	**PqsC**
1	H:ARG 286[NH1]	3.25	F:ASP 264[O]
2	H:ARG 286[NH2]	2.50	F:ASP 264[OD1]
Salt bridges			
No.	**PqsC**	**Dist. Å²**	**PqsC**
1	H:ARG 286[NH1]	3.61	F:ASP 264[OD1]
2	H:ARG 286[NH2]	2.50	F:ASP 264[OD1]

Chapter 9: Conclusion and future work

9.1 Conclusion and future work

As QS in *P. aeruginosa* controls the secretion of virulence factors and biofilm formation, hence, the nature of *P. aeruginosa* and its high level of antibiotic resistance means there is an urgency to understand structural, physical and chemical properties of the PqsABCDEH enzymes. This project will focus on PqsBC, as PqsBC is the enzyme that catalyses condensation of 2-aminobenzoylacetate (2-ABA) and octanoyl-coenzyme A to form HHQ (Drees et al., 2016). HHQ itself was discovered to function as an autoinducer molecule per se (Diggle et al., 2007). Moreover, HHQ is the precursor of PQS which is an extracellular messenger that involves in QS systems in *P. aeruginosa*.

Protein samples of wild-type PqsBC and the active site protein variant $PqsBC^{C129A}$, $PqsBC^{C129S}$, $PqsBC^{C129A}$ with the substrates such as 2-ABA and Oct-CoA with additive screen HR2-428 (Hampton Research) have been attempted to crystallise. These samples were subjected to screens, including Pi-PEG, Procomplex, classics lite, Mbclass, Index, PACT, Morpheus, JCSG+, and MIDAS, using the sitting drop vapor diffusion method (Mosquito robot, TTP Labtech, Melbourne, UK)

The first PqsBC crystal was $PqsBC^{C129A}$ then followed by $PqsBC^{C129A}$-Fe^{3+} and $PqsBC^{C129A}$-Fe^{3+}-2ABA (1:1), resulted from the conditions of 0.2 M NaCl, 0.1 M Tris, pH 8.5, 25% PEG 3350 within 24 h, whereas octanoylated or apo-forms

of wild-type PqsBC, active site protein variant PqsBC^{C129S}, and PqsBC-OctCoA did not form crystals. Datasets were collected using the strategy provided by íMosflm and FastDP. Further, the processed datas were continue with Truncate, Matthews coeff. Molecular replacement was performed with PHASER using a variety of templates generated using MrBUMP from PDB codes 3h76, 3h77, and 3h78 of the PqsD structure. The model was completed manually using COOT and refined with REFMAC5. Values for surface area buried were calculated using PISA

PqsBC crystal structure is unlike any other member of the FabH family of proteins. Other members of this group form homodimers, whereas PqsB and PqsC form a pseudo 2-fold symmetric heterodimer that imitates the FabH homodimer. The PqsB and PqsC folds are similar to PqsD and FabH enzymes, which contain two subdomains each consisting of a four stranded β-sheet surrounded by α-helices. The structural superimposition of PqsB and PqsC shows that similarities are primarily in the N-terminal subdomain. Larger differences occur in the C-terminal subdomains, with PqsB having a shorter sequence (124 amino acids) and only two α-helices, and PqsC (160 amino acids) having four α-helices.

In contrast to the FabH enzyme family, PqsBC forms a catalytic diad, rather than the typical triad. An asparagine amino acid, the third amino acid in the triad and typical of FabH enzymes, does not form a catalytic triad with His269, Cys129. In PqsBC, a valine (Val299) is present where the asparagine residue is

normally located. To confirm that PqsBC is functional without the catalytic asparagine, the activity was assessed with the desamino-substrate analogue benzoylacetate (BA) and by reintroducing the asparagine into the protein (Drees et al., 2016). For wild-type PqsBC the activity toward BA was about 300-fold lower than toward 2-ABA. The $PqsBC^{V299N}$ variant performed significantly better with BA than with 2-ABA (Drees et al., 2016). Octanoylation of Cys129 of PqsBC was also similar with that obtained for FabH, as the nucleophile in the initial acylation step is independent from histidine. This is because FabH Cys112 is located at the NH_2-terminus of an α-helix (Heath and Rock, 2002), which can account for a reduction in the *pKa* by 1.6 units (Kortemme and Creighton, 1995).

The $PqsBC^{C129A}$ active site volume is twice as large as those of FabH/PqsD, with a calculated volume of 761$Å^3$ compared to 389$Å^3$ for PqsD (pdb:3H76) and 367$Å^3$ for FabH (pdb:2QNZ) (calculated using 3vee (Voss and Gerstein, 2010)). The PqsBC pocket volume is approximately twice the volume of related FabH enzymes, which may be a requirement to accommodate the aromatic ring of 2-ABA, which malonyl-ACP (common substrates of FabH) does not have.

Although the catalytic residues are only formed by PqsC residues, the active site pocket is formed by both PqsB and PqsC. Beside the active site cavity, $PqsBC^{C129A}$ also has a central cavity formed by the heterotetramer conformation.

This volume is 5034 Å^3 and is formed only by PqsC^{C129A} surfaces that orient so the catalytic sites line up face-to-face.

In addition to connection through PqsC residues 88–102 (termed loop B), PqsB and PqsC are also linked by iron. The iron ion is bound to both PqsB and PqsC^{C129A}. Furthermore, it is coordinated by His2, Glu48, Glu280, and His282. His2 is located N-terminally of PqsC, and Glu280 and His282 are found within the C-terminus of PqsB.

The PqsBC^{C129A}-Fe^{3+} crystal structure shows that Fe^{3+} binds to the side chain nitrogens of His282 (PqsB) and His2 (PqsC) along with side chain oxygen atoms from Glu48 (PqsB) and Glu280 (PqsB). The bond lengths are 2.06 Å for Fe-N (His282, PqsB), 2.07 Å for Fe-N (His2, PqsC^{C129A}), 2.12 Å for Fe-O (Glu280, PqsB), and 2.13 Å for Fe-O (Glu48, PqsB). The bond lengths that are observed are very similar to those in the Azurin-iron complex crystal structure ((Liu et al., 2014) and structure of FutA1 with Iron(II) (Koropatkin et al., 2007).

Binding of Fe^{3+} at the C-terminus of an α-helix could inactivate the dipole effect of the helix. As the dipole is thought to promote deprotonation of Cys129 (Kortemme and Creighton, 1995), binding of the iron ion could lower the activity of the enzyme. Therefore, enzyme kinetic studies of PqsBC- Fe^{3+} could improve our understanding of the effect of Fe^{3+} binding on PqsBC activity. Moreover, the

PqsBC^{C129A} crystal structure has revealed many characteristics of this important enzyme, especially with regards to the active site and how it can accommodate the small molecules involved in QS. Therefore, this information will enable the design inhibitors of PqsBC in order to antagonise *P. aeruginosa* QS.

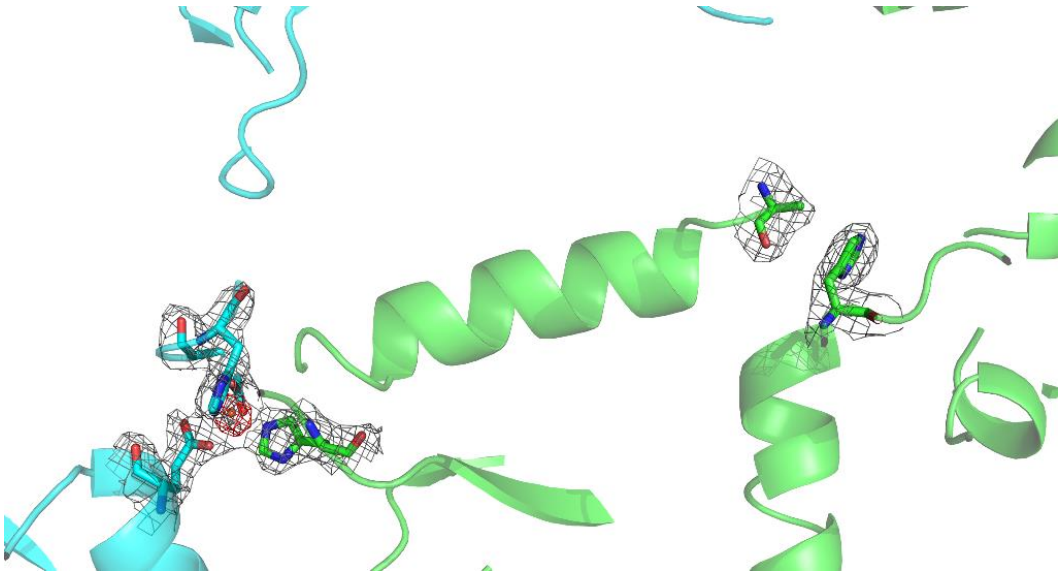


Figure 9.1. Cartoons and sticks diagram of the PqsBC^{C129A}-Fe^{3+} structure shows part of PqsB (cyan) and pqsC^{C129A} (green) that binding with iron which is seen may affect cysteine role as a nucleophile in the initial acylation step, a 2.3 Å electron density map is shown (grey).

References

References

A VAGIN, A., STEINER, R. A., LEBEDEV, A., POTTERTON, L., MCNICHOLAS, S., LONG, F. & MURSHUDOV, G. 2005. *REFMAC5 dictionary: organization of prior chemical knowledge and guidelines for its use*.

ACTON, Q. A. 2012. *Advances in Hydrofluoric Acid Research and Application: 2012 Edition: ScholarlyBrief*, ScholarlyEditions.

ALHAZMI, A. 2015. Pseudomonas aeruginosa – Pathogenesis and Pathogenic Mechanisms. *International Journal of Biology,* Vol. 7, No. 2; 2015.

ARAI, H. 2011. Regulation and Function of Versatile Aerobic and Anaerobic Respiratory Metabolism in Pseudomonas aeruginosa. *Frontiers in Microbiology,* 2**,** 103.

ARORA, S. K., RITCHINGS, B. W., ALMIRA, E. C., LORY, S. & RAMPHAL, R. 1998. The Pseudomonas aeruginosa flagellar cap protein, FliD, is responsible for mucin adhesion. *Infect Immun,* 66**,** 1000-7.

BANASZAK, L. J. 2000a. CHAPTER 1 - Introduction to Protein Structure. *Foundations of Structural Biology.* San Diego: Academic Press.

BANASZAK, L. J. 2000b. *Foundations of Structural Biology*, Elsevier Science.

BARKEN, K. B., PAMP, S. J., YANG, L., GJERMANSEN, M., BERTRAND, J. J., KLAUSEN, M., GIVSKOV, M., WHITCHURCH, C. B., ENGEL, J. N. & TOLKER-NIELSEN, T. 2008. Roles of type IV pili, flagellum-mediated motility and extracellular DNA in the formation of mature multicellular structures in Pseudomonas aeruginosa biofilms. *Environ Microbiol,* 10**,** 2331-43.

BEN HAJ KHALIFA, A., MOISSENET, D., VU THIEN, H. & KHEDHER, M. 2011. [Virulence factors in Pseudomonas aeruginosa: mechanisms and modes of regulation]. *Ann Biol Clin (Paris),* 69**,** 393-403.

BERG, J. M., TYMOCZKO, J. L. & STRYER, L. 2002. *Biochemistry, Fifth Edition*, W.H. Freeman.

BRADLEY, D. E. 1980. A function of Pseudomonas aeruginosa PAO polar pili: twitching motility. *Can J Microbiol,* 26**,** 146-54.

BRANDA, S. S., VIK, Å., FRIEDMAN, L. & KOLTER, R. 2005. Biofilms: the matrix revisited. *Trends in microbiology,* 13**,** 20-26.

BRANDEL, J., HUMBERT, N., ELHABIRI, M., SCHALK, I. J., MISLIN, G. L. & ALBRECHT-GARY, A. M. 2012. Pyochelin, a siderophore of Pseudomonas aeruginosa: physicochemical characterization of the iron(III), copper(II) and zinc(II) complexes. *Dalton Trans,* 41**,** 2820-34.

BRAUN, V. & KILLMANN, H. 1999. Bacterial solutions to the iron-supply problem. *Trends Biochem Sci,* 24**,** 104-9.

BREDENBRUCH, F., GEFFERS, R., NIMTZ, M., BUER, J. & HÄUSSLER, S. 2006. The Pseudomonas aeruginosa quinolone signal (PQS) has an iron-chelating activity. *Environmental Microbiology,* 8**,** 1318-1329.

BRINT, J. M. & OHMAN, D. E. 1995. Synthesis of multiple exoproducts in Pseudomonas aeruginosa is under the control of RhlR-RhlI, another set of

regulators in strain PAO1 with homology to the autoinducer-responsive LuxR-LuxI family. *J Bacteriol,* 177**,** 7155-63.
BRÜNGER, A. T. 1992. Free R value: a novel statistical quantity for assessing the accuracy of crystal structures. *Nature,* 355**,** 472.
CALFEE, M. W., COLEMAN, J. P. & PESCI, E. C. 2001. Interference with Pseudomonas quinolone signal synthesis inhibits virulence factor expression by Pseudomonas aeruginosa. *Proc Natl Acad Sci U S A,* 98**,** 11633-7.
CAO, H., KRISHNAN, G., GOUMNEROV, B., TSONGALIS, J., TOMPKINS, R. & RAHME, L. G. 2001. A quorum sensing-associated virulence gene of Pseudomonas aeruginosa encodes a LysR-like transcription regulator with a unique self-regulatory mechanism. *Proceedings of the National Academy of Sciences,* 98**,** 14613-14618.
CARNOY, C., SCHARFMAN, A., VAN BRUSSEL, E., LAMBLIN, G., RAMPHAL, R. & ROUSSEL, P. 1994. Pseudomonas aeruginosa outer membrane adhesins for human respiratory mucus glycoproteins. *Infect Immun,* 62**,** 1896-900.
CARTER, C. W. & SWEET, R. M. 1997. *Macromolecular crystallography. Part B Part B,* San Diego, Academic Press.
CHENG, M.-C., RICH, A. M., ARMSTRONG, R. S., ELLIS, P. J. & LAY, P. A. 1999. Determination of Iron−Ligand Bond Lengths in Ferric and Ferrous Horse Heart Cytochrome c Using Multiple-Scattering Analyses of XAFS Data. *Inorganic Chemistry,* 38**,** 5703-5708.
CHIRGADZE, D. 2001. *Protein Crystallisation in Action* [Online]. Available: http://www.xray.bioc.cam.ac.uk/xray_resources/whitepapers/xtal-in-action/node3.html [Accessed 2017].
COLEMAN, J. P., HUDSON, L. L., MCKNIGHT, S. L., FARROW, J. M., 3RD, CALFEE, M. W., LINDSEY, C. A. & PESCI, E. C. 2008. Pseudomonas aeruginosa PqsA is an anthranilate-coenzyme A ligase. *J Bacteriol,* 190**,** 1247-55.
COMOLLI, J. C., WAITE, L. L., MOSTOV, K. E. & ENGEL, J. N. 1999. Pili binding to asialo-GM1 on epithelial cells can mediate cytotoxicity or bacterial internalization by Pseudomonas aeruginosa. *Infect Immun,* 67**,** 3207-14.
CORNELIS, P. & DINGEMANS, J. 2013. Pseudomonas aeruginosa adapts its iron uptake strategies in function of the type of infections. *Frontiers in Cellular and Infection Microbiology,* 3**,** 75.
CORNFORTH, J. W. & JAMES, A. T. 1956. Structure of a naturally occurring antagonist of dihydrostreptomycin. *Biochem J,* 63**,** 124-30.
COWTAN, K. D. 2006. *The Buccaneer software for automated model building*.
COX, C. D., RINEHART, K. L., JR., MOORE, M. L. & COOK, J. C., JR. 1981. Pyochelin: novel structure of an iron-chelating growth promoter for Pseudomonas aeruginosa. *Proc Natl Acad Sci U S A,* 78**,** 4256-60.
D. WINN, M., KEEGAN, R. & D. STEIN, N. 2006. *MrBUMP: automated search model discovery and preparation for structure solution by molecular replacement*.

DAVIES, C., HEATH, R. J., WHITE, S. W. & ROCK, C. O. 2000. The 1.8 Å crystal structure and active-site architecture of β-ketoacyl-acyl carrier protein synthase III (FabH) from Escherichia coli. *Structure,* 8**,** 185-195.

DE GRAEF, M. & MCHENRY, M. E. 2007. *Structure of Materials: An Introduction to Crystallography, Diffraction and Symmetry*, Cambridge University Press.

DEKIMPE, V. & DEZIEL, E. 2009. Revisiting the quorum-sensing hierarchy in Pseudomonas aeruginosa: the transcriptional regulator RhlR regulates LasR-specific factors. *Microbiology,* 155**,** 712-23.

DENNING, G. M., RAILSBACK, M. A., RASMUSSEN, G. T., COX, C. D. & BRITIGAN, B. E. 1998. Pseudomonas pyocyanine alters calcium signaling in human airway epithelial cells. *Am J Physiol,* 274**,** L893-900.

DEZIEL, E., GOPALAN, S., TAMPAKAKI, A. P., LEPINE, F., PADFIELD, K. E., SAUCIER, M., XIAO, G. & RAHME, L. G. 2005. The contribution of MvfR to Pseudomonas aeruginosa pathogenesis and quorum sensing circuitry regulation: multiple quorum sensing-regulated genes are modulated without affecting lasRI, rhlRI or the production of N-acyl-L-homoserine lactones. *Mol Microbiol,* 55**,** 998-1014.

DEZIEL, E., LEPINE, F., MILOT, S., HE, J., MINDRINOS, M. N., TOMPKINS, R. G. & RAHME, L. G. 2004. Analysis of Pseudomonas aeruginosa 4-hydroxy-2-alkylquinolines (HAQs) reveals a role for 4-hydroxy-2-heptylquinoline in cell-to-cell communication. *Proc Natl Acad Sci U S A,* 101**,** 1339-44.

DICKERSON, R. E., KENDREW, J. C. & STRANDBERG, B. E. 1961. The crystal structure of myoglobin: Phase determination to a resolution of 2 A by the method of isomorphous replacement. *Acta Crystallographica,* 14**,** 1188-1195.

DIGGLE, S. P., MATTHIJS, S., WRIGHT, V. J., FLETCHER, M. P., CHHABRA, S. R., LAMONT, I. L., KONG, X., HIDER, R. C., CORNELIS, P., CAMARA, M. & WILLIAMS, P. 2007. The Pseudomonas aeruginosa 4-quinolone signal molecules HHQ and PQS play multifunctional roles in quorum sensing and iron entrapment. *Chem Biol,* 14**,** 87-96.

DIGGLE, S. P., WINZER, K., CHHABRA, S. R., WORRALL, K. E., CÁMARA, M. & WILLIAMS, P. 2003. The Pseudomonas aeruginosa quinolone signal molecule overcomes the cell density-dependency of the quorum sensing hierarchy, regulates rhl-dependent genes at the onset of stationary phase and can be produced in the absence of LasR. *Molecular Microbiology,* 50**,** 29-43.

DOIG, P., SMITH, N. R., TODD, T. & IRVIN, R. T. 1987. Characterization of the binding of Pseudomonas aeruginosa alginate to human epithelial cells. *Infect Immun,* 55**,** 1517-22.

DOIG, P., TODD, T., SASTRY, P. A., LEE, K. K., HODGES, R. S., PARANCHYCH, W. & IRVIN, R. T. 1988. Role of pili in adhesion of Pseudomonas aeruginosa to human respiratory epithelial cells. *Infect Immun,* 56**,** 1641-6.

DOYLE, S. A. 2008. *High Throughput Protein Expression and Purification: Methods and Protocols*, Humana Press.
DREES, S. L. & FETZNER, S. 2015. PqsE of Pseudomonas aeruginosa Acts as Pathway-Specific Thioesterase in the Biosynthesis of Alkylquinolone Signaling Molecules. *Chem Biol,* 22**,** 611-8.
DREES, S. L., LI, C., PRASETYA, F., SALEEM, M., DREVENY, I., WILLIAMS, P., HENNECKE, U., EMSLEY, J. & FETZNER, S. 2016. PqsBC, a Condensing Enzyme in the Biosynthesis of the Pseudomonas aeruginosa Quinolone Signal: CRYSTAL STRUCTURE, INHIBITION, AND REACTION MECHANISM. *Journal of Biological Chemistry,* 291**,** 6610-6624.
DULCEY, C. E., DEKIMPE, V., FAUVELLE, D. A., MILOT, S., GROLEAU, M. C., DOUCET, N., RAHME, L. G., LEPINE, F. & DEZIEL, E. 2013. The end of an old hypothesis: the pseudomonas signaling molecules 4-hydroxy-2-alkylquinolines derive from fatty acids, not 3-ketofatty acids. *Chem Biol,* 20**,** 1481-91.
EDWIN E. HAYS, I. C. W., PHILIP A. KATZMAN, C. K. CAIN, FRANCIS A. JACOBS, SIDNEY A. THAYER, EDWARD A. DOISY, W. L. GABY, E. C. ROBERTS, R. D. MUIR, C. J. CARROLL, L. R. JONES, AND NELSON J. WADE 1945. ANTIBIOTIC SUBSTANCES PRODUCED BY PSEUDOMONAS AERUGINOSA *J. Biol. Chem.* , J. Biol. Chem. 1945 159: 725-. **,** J. Biol. Chem. 1945 159: 725-. .
EMSLEY, P. & COWTAN, K. 2004. Coot: model-building tools for molecular graphics. *Acta Crystallogr D Biol Crystallogr,* 60**,** 2126-32.
FLEMMING, H.-C. & WINGENDER, J. 2010. The biofilm matrix. *Nature Reviews Microbiology,* 8**,** 623-633.
FUQUA, C., PARSEK, M. R. & GREENBERG, E. P. 2001. Regulation of gene expression by cell-to-cell communication: acyl-homoserine lactone quorum sensing. *Annu Rev Genet,* 35**,** 439-68.
FUQUA, W. C., WINANS, S. C. & GREENBERG, E. P. 1994. Quorum sensing in bacteria: the LuxR-LuxI family of cell density-responsive transcriptional regulators. *J Bacteriol,* 176**,** 269-75.
GACESA, P. & WUSTEMAN, F. S. 1990. Plate assay for simultaneous detection of alginate lyases and determination of substrate specificity. *Appl Environ Microbiol,* 56**,** 2265-7.
GALLAGHER, L. A. & MANOIL, C. 2001. Pseudomonas aeruginosa PAO1 kills Caenorhabditis elegans by cyanide poisoning. *J Bacteriol,* 183**,** 6207-14.
GALLAGHER, L. A., MCKNIGHT, S. L., KUZNETSOVA, M. S., PESCI, E. C. & MANOIL, C. 2002. Functions required for extracellular quinolone signaling by Pseudomonas aeruginosa. *J Bacteriol,* 184**,** 6472-80.
GAMBELLO, M. J. & IGLEWSKI, B. H. 1991. Cloning and characterization of the Pseudomonas aeruginosa lasR gene, a transcriptional activator of elastase expression. *J Bacteriol,* 173**,** 3000-9.
GHANNOUM, M. A. & O'TOOLE, G. A. 2004. Microbial Biofilms. Washington, DC: ASM Press.

GLICK, B. R. & PATTEN, C. L. 2017. *Molecular Biotechnology: Principles and Applications of Recombinant DNA*, ASM Press.
GUINA, T., PURVINE, S. O., YI, E. C., ENG, J., GOODLETT, D. R., AEBERSOLD, R. & MILLER, S. I. 2003. Quantitative proteomic analysis indicates increased synthesis of a quinolone by Pseudomonas aeruginosa isolates from cystic fibrosis airways. *Proc Natl Acad Sci U S A,* 100**,** 2771-6.
HEATH, R. J. & ROCK, C. O. 2002. The Claisen condensation in biology. *Nat Prod Rep,* 19**,** 581-96.
HOIBY, N., FLENSBORG, E. W., BECK, B., FRIIS, B., JACOBSEN, S. V. & JACOBSEN, L. 1977. Pseudomonas aeruginosa infection in cystic fibrosis. Diagnostic and prognostic significance of Pseudomonas aeruginosa precipitins determined by means of crossed immunoelectrophoresis. *Scand J Respir Dis,* 58**,** 65-79.
HOLM, L. & ROSENSTRÖM, P. 2010. Dali server: conservation mapping in 3D. *Nucleic Acids Research,* 38**,** W545-W549.
HUANG, B. 2009. MetaPocket: A Meta Approach to Improve Protein Ligand Binding Site Prediction. *OMICS: A Journal of Integrative Biology,* 13**,** 325-330.
INAGAKI, E., KURAMITSU, S., YOKOYAMA, S., MIYANO, M. & TAHIROV, T. H. 2007. The Crystal Structure of Beta-Ketoacyl-[Acyl Carrier Protein] Synthase III (Fabh) from Thermus Thermophilus. http://www.rcsb.org/structure/1UB7.
JENSEN, V., LONS, D., ZAOUI, C., BREDENBRUCH, F., MEISSNER, A., DIETERICH, G., MUNCH, R. & HAUSSLER, S. 2006. RhlR expression in Pseudomonas aeruginosa is modulated by the Pseudomonas quinolone signal via PhoB-dependent and -independent pathways. *J Bacteriol,* 188**,** 8601-6.
JONES, T. 1978. A graphics model building and refinement system for macromolecules. *Journal of Applied Crystallography,* 11**,** 268-272.
JONES, T. A., ZOU, J.-Y., COWAN, S. W. & KJELDGAARD, M. 1991. Improved methods for building protein models in electron density maps and the location of errors in these models. *Acta Crystallographica Section A,* 47**,** 110-119.
KARATAN, E. & WATNICK, P. 2009. Signals, Regulatory Networks, and Materials That Build and Break Bacterial Biofilms. *Microbiology and Molecular Biology Reviews,* 73**,** 310-347.
KASAI-KAKUDO & KAKUDO, M. 2005. *X-ray Diffraction by Macromolecules*, Kodansha.
KENDREW, J. C., BODO, G., DINTZIS, H. M., PARRISH, R. G., WYCKOFF, H. & PHILLIPS, D. C. 1958. A Three-Dimensional Model of the Myoglobin Molecule Obtained by X-Ray Analysis. *Nature,* 181**,** 662.
KENNETH TODAR 2012. Todar's Online Textbook of Bacteriology. University of Wisconsin, Department of Bacteriology

KIIL, K., BINNEWIES, T. T., WILLENBROCK, H., HANSEN, S. K., YANG, L., JELSBAK, L., USSERY, D. W. & FRIIS, C. 2008. Comparative Genomics of Pseudomonas. Wiley-VCH Verlag GmbH & Co. KGaA.
KIM, E. J., SABRA, W. & ZENG, A. P. 2003. Iron deficiency leads to inhibition of oxygen transfer and enhanced formation of virulence factors in cultures of Pseudomonas aeruginosa PAO1. *Microbiology,* 149**,** 2627-34.
KJELLEBERG, S. & GIVSKOV, M. 2007. The

Biofilm Mode of Life: Mechanisms and Adaptations (eds. S. Kjelleberg and M. Givskov). Wymondham: Horizon Bioscience.
KLEYWEGT, G. J. 1996. Use of non-crystallographic symmetry in protein structure refinement. *Acta Crystallographica Section D: Biological Crystallography,* 52**,** 842-857.
KLEYWEGT, G. J. & JONES, T. A. 1995. Where freedom is given, liberties are taken. *Structure,* 3**,** 535-540.
KLEYWEGT, G. J. & JONES, T. A. 1997. Model building and refinement practice. *Methods Enzymol,* 277**,** 208-30.
KOCH, C. & HOIBY, N. 1993. Pathogenesis of cystic fibrosis. *Lancet,* 341**,** 1065-9.
KOHLER, T., CURTY, L. K., BARJA, F., VAN DELDEN, C. & PECHERE, J. C. 2000. Swarming of Pseudomonas aeruginosa is dependent on cell-to-cell signaling and requires flagella and pili. *J Bacteriol,* 182**,** 5990-6.
KORN, A. P. & ROSE, D. R. 1994. Torsion angle differences as a means of pinpointing local polypeptide chain trajectory changes for identical proteins in different conformational states. *Protein Engineering, Design and Selection,* 7**,** 961-967.
KOROPATKIN, N., RANDICH, A. M., BHATTACHARYYA-PAKRASI, M., PAKRASI, H. B. & SMITH, T. J. 2007. The Structure of the Iron-binding Protein, FutA1, from Synechocystis 6803. *Journal of Biological Chemistry,* 282**,** 27468-27477.
KORTEMME, T. & CREIGHTON, T. E. 1995. Ionisation of Cysteine Residues at the Termini of Model α-Helical Peptides. Relevance to Unusual Thiol pKaValues in Proteins of the Thioredoxin Family. *Journal of Molecular Biology,* 253**,** 799-812.
KRISSINEL, E. & HENRICK, K. 2007. Inference of Macromolecular Assemblies from Crystalline State. *Journal of Molecular Biology,* 372**,** 774-797.
LAM, J., CHAN, R., LAM, K. & COSTERTON, J. W. 1980. Production of mucoid microcolonies by Pseudomonas aeruginosa within infected lungs in cystic fibrosis. *Infect Immun,* 28**,** 546-56.
LASKOWSKI, R. A. 2001. PDBsum: summaries and analyses of PDB structures. *Nucleic Acids Research,* 29**,** 221-222.
LASKOWSKI, R. A., MACARTHUR, M. W., MOSS, D. S. & THORNTON, J. M. 1993. PROCHECK: a program to check the stereochemical quality of protein structures. *Journal of Applied Crystallography,* 26**,** 283-291.
LATIFI, A., WINSON, M. K., FOGLINO, M., BYCROFT, B. W., STEWART, G. S., LAZDUNSKI, A. & WILLIAMS, P. 1995. Multiple homologues of LuxR and LuxI control expression of virulence determinants and

secondary metabolites through quorum sensing in Pseudomonas aeruginosa PAO1. *Mol Microbiol,* 17**,** 333-43.
LAU, G. W., HASSETT, D. J., RAN, H. & KONG, F. 2004. The role of pyocyanin in Pseudomonas aeruginosa infection. *Trends in Molecular Medicine,* 10**,** 599-606.
LEE, J., WU, J., DENG, Y., WANG, J., WANG, C., WANG, J., CHANG, C., DONG, Y., WILLIAMS, P. & ZHANG, L.-H. 2013. A cell-cell communication signal integrates quorum sensing and stress response. *Nat Chem Biol,* 9**,** 339-343.
LEE, J. & ZHANG, L. 2015. The hierarchy quorum sensing network in Pseudomonas aeruginosa. *Protein & Cell,* 6**,** 26-41.
LESLIE, A. 2006. The integration of macromolecular diffraction data. *Acta Crystallographica Section D,* 62**,** 48-57.
LI, Y. H. & TIAN, X. 2012. Quorum sensing and bacterial social interactions in biofilms. *Sensors (Basel),* 12**,** 2519-38.
LILLEHOJ, E. P., KIM, B. T. & KIM, K. C. 2002. Identification of Pseudomonas aeruginosa flagellin as an adhesin for Muc1 mucin. *Am J Physiol Lung Cell Mol Physiol,* 282**,** L751-6.
LIMA-DE-FARIA, J. 1990. *Historical Atlas of Crystallography,* Springer Netherlands.
LIU, J., MEIER, K. K., TIAN, S., ZHANG, J.-L., GUO, H., SCHULZ, C. E., ROBINSON, H., NILGES, M. J., MÜNCK, E. & LU, Y. 2014. Redesigning the Blue Copper Azurin into a Redox-Active Mononuclear Nonheme Iron Protein: Preparation and Study of Fe(II)-M121E Azurin. *Journal of the American Chemical Society,* 136**,** 12337-12344.
LUFT, J. R., NEWMAN, J. & SNELL, E. H. 2014. Crystallization screening: the influence of history on current practice. *Acta Crystallographica. Section F, Structural Biology Communications,* 70**,** 835-853.
LYCZAK, J. B., CANNON, C. L. & PIER, G. B. 2000. Establishment of Pseudomonas aeruginosa infection: lessons from a versatile opportunist. *Microbes Infect,* 2**,** 1051-60.
MACHAN, Z. A., TAYLOR, G. W., PITT, T. L., COLE, P. J. & WILSON, R. 1992. 2-Heptyl-4-hydroxyquinoline N-oxide, an antistaphylococcal agent produced by Pseudomonas aeruginosa. *J Antimicrob Chemother,* 30**,** 615-23.
MAH, T. F., PITTS, B., PELLOCK, B., WALKER, G. C., STEWART, P. S. & O'TOOLE, G. A. 2003. A genetic basis for Pseudomonas aeruginosa biofilm antibiotic resistance. *Nature,* 426**,** 306-10.
MAHENTHIRALINGAM, E. & SPEERT, D. P. 1995. Nonopsonic phagocytosis of Pseudomonas aeruginosa by macrophages and polymorphonuclear leukocytes requires the presence of the bacterial flagellum. *Infect Immun,* 63**,** 4519-23.
MCCOY, A. J., GROSSE-KUNSTLEVE, R. W., ADAMS, P. D., WINN, M. D., STORONI, L. C. & READ, R. J. 2007. Phaser crystallographic software. *Journal of Applied Crystallography,* 40**,** 658-674.

MCDOUGALD, D., KLEBENSBERGER, J., TOLKER-NIELSEN, T., WEBB, J. S., CONIBEAR, T., RICE, S. A., KIROV, S. M., MATZ, C. & KJELLEBERG, S. 2008. Pseudomonas aeruginosa: A Model for Biofilm Formation, in Pseudomonas: Model Organism, Pathogen, Cell Factory (ed B. H. A. Rehm). *Pseudomonas aeruginosa: A Model for Biofilm Formation, in Pseudomonas: Model Organism, Pathogen, Cell Factory (ed B. H. A. Rehm).* Germany: Wiley-VCH Verlag GmbH & Co. KGaA, Weinheim, Germany.

MCPHERSON, A. 2009. *Introduction to Macromolecular Crystallography, 2nd Edition,* John Wiley & Sons, Inc.

MCPHERSON, A., MALKIN, A. J. & KUZNETSOV, Y. G. The science of macromolecular crystallization. *Structure,* 3**,** 759-768.

MEYER, J. M. 2000. Pyoverdines: pigments, siderophores and potential taxonomic markers of fluorescent Pseudomonas species. *Arch Microbiol,* 174**,** 135-42.

MIDDLETON, B., RODGERS, H. C., CAMARA, M., KNOX, A. J., WILLIAMS, P. & HARDMAN, A. 2002. Direct detection of N-acylhomoserine lactones in cystic fibrosis sputum. *FEMS Microbiol Lett,* 207**,** 1-7.

MILLER, M. B. & BASSLER, B. L. 2001. Quorum sensing in bacteria. *Annu Rev Microbiol,* 55**,** 165-99.

MONTIE, T. C., DOYLE-HUNTZINGER, D., CRAVEN, R. C. & HOLDER, I. A. 1982. Loss of virulence associated with absence of flagellum in an isogenic mutant of Pseudomonas aeruginosa in the burned-mouse model. *Infect Immun,* 38**,** 1296-8.

MURSHUDOV, G. N., VAGIN, A. A. & DODSON, E. J. 1997. Refinement of macromolecular structures by the maximum-likelihood method. *Acta Crystallogr D Biol Crystallogr,* 53**,** 240-55.

NEALSON, K. H. & HASTINGS, J. W. 1979. Bacterial bioluminescence: its control and ecological significance. *Microbiol Rev,* 43**,** 496-518.

NEALSON, K. H., PLATT, T. & HASTINGS, J. W. 1970. Cellular control of the synthesis and activity of the bacterial luminescent system. *J Bacteriol,* 104**,** 313-22.

NG, W.-L. & BASSLER, B. L. 2009. Bacterial Quorum-Sensing Network Architectures. *Annual review of genetics,* 43**,** 197-222.

NIKOLAEV, Y. A. & PLAKUNOV, V. 2007. Biofilm—"City of microbes" or an analogue of multicellular organisms? *Microbiology,* 76**,** 125-138.

OBRITSCH, M. D., FISH, D. N., MACLAREN, R. & JUNG, R. 2004. National Surveillance of Antimicrobial Resistance in Pseudomonas aeruginosa Isolates Obtained from Intensive Care Unit Patients from 1993 to 2002. *Antimicrobial Agents and Chemotherapy,* 48**,** 4606-4610.

OCHSNER, U. A., KOCH, A. K., FIECHTER, A. & REISER, J. 1994. Isolation and characterization of a regulatory gene affecting rhamnolipid biosurfactant synthesis in Pseudomonas aeruginosa. *J Bacteriol,* 176**,** 2044-54.

OCHSNER, U. A., WILDERMAN, P. J., VASIL, A. I. & VASIL, M. L. 2002. GeneChip® expression analysis of the iron starvation response in Pseudomonas aeruginosa: identification of novel pyoverdine biosynthesis genes. *Molecular Microbiology,* 45**,** 1277-1287.

PAPENFORT, K. & BASSLER, B. L. 2016a. Quorum sensing signal-response systems in Gram-negative bacteria. *Nat Rev Micro,* 14**,** 576-588.

PAPENFORT, K. & BASSLER, B. L. 2016b. Quorum sensing signal–response systems in Gram-negative bacteria. *Nature Reviews Microbiology,* 14**,** 576.

PARAD, R. B., GERARD, C. J., ZURAKOWSKI, D., NICHOLS, D. P. & PIER, G. B. 1999. Pulmonary outcome in cystic fibrosis is influenced primarily by mucoid Pseudomonas aeruginosa infection and immune status and only modestly by genotype. *Infect Immun,* 67**,** 4744-50.

PEARSON, J. P., PESCI, E. C. & IGLEWSKI, B. H. 1997. Roles of Pseudomonas aeruginosa las and rhl quorum-sensing systems in control of elastase and rhamnolipid biosynthesis genes. *J Bacteriol,* 179**,** 5756-67.

PESCI, E. C., MILBANK, J. B., PEARSON, J. P., MCKNIGHT, S., KENDE, A. S., GREENBERG, E. P. & IGLEWSKI, B. H. 1999. Quinolone signaling in the cell-to-cell communication system of Pseudomonas aeruginosa. *Proc Natl Acad Sci U S A,* 96**,** 11229-34.

PESCI, E. C., PEARSON, J. P., SEED, P. C. & IGLEWSKI, B. H. 1997. Regulation of las and rhl quorum sensing in Pseudomonas aeruginosa. *J Bacteriol,* 179**,** 3127-32.

PETTERSEN, E. F., GODDARD, T. D., HUANG, C. C., COUCH, G. S., GREENBLATT, D. M., MENG, E. C. & FERRIN, T. E. 2004. UCSF Chimera--a visualization system for exploratory research and analysis. *J Comput Chem,* 25**,** 1605-12.

PIER, G. B., COLEMAN, F., GROUT, M., FRANKLIN, M. & OHMAN, D. E. 2001. Role of alginate O acetylation in resistance of mucoid Pseudomonas aeruginosa to opsonic phagocytosis. *Infect Immun,* 69**,** 1895-901.

POWELL, H. 2013. Integration and scaling

POWELL, H. R., JOHNSON, O. & LESLIE, A. G. W. 2013. Autoindexing diffraction images with iMosflm. *Acta Crystallographica Section D,* 69**,** 1195-1203.

PRINCE, E., FINGER, L. W. & KONNERT, J. H. 2004. Constraints and restraints in refinement. *In:* PRINCE, E. (ed.) *International Tables for Crystallography Volume C: Mathematical, physical and chemical tables.* Dordrecht: Springer Netherlands.

PUNSALANG, A. P., JR. & SAWYER, W. D. 1973. Role of pili in the virulence of Neisseria gonorrhoeae. *Infect Immun,* 8**,** 255-63.

QIU, X., CHOUDHRY, A. E., JANSON, C. A., GROOMS, M., DAINES, R. A., LONSDALE, J. T. & KHANDEKAR, S. S. 2005. Crystal structure and substrate specificity of the β-ketoacyl-acyl carrier protein synthase III (FabH) from Staphylococcus aureus. *Protein Science,* 14**,** 2087-2094.

QIU, X., JANSON, C. A., KONSTANTINIDIS, A. K., NWAGWU, S., SILVERMAN, C., SMITH, W. W., KHANDEKAR, S., LONSDALE, J.

& ABDEL-MEGUID, S. S. 1999. Crystal Structure of β-Ketoacyl-Acyl Carrier Protein Synthase III: A KEY CONDENSING ENZYME IN BACTERIAL FATTY ACID BIOSYNTHESIS. *Journal of Biological Chemistry,* 274**,** 36465-36471.
RASAMIRAVAKA, T., LABTANI, Q., DUEZ, P. & EL JAZIRI, M. 2015. The Formation of Biofilms by Pseudomonas aeruginosa: A Review of the Natural and Synthetic Compounds Interfering with Control Mechanisms. *BioMed Research International,* 2015**,** 17.
RASHID, M. H. & KORNBERG, A. 2000. Inorganic polyphosphate is needed for swimming, swarming, and twitching motilities of Pseudomonas aeruginosa. *Proc Natl Acad Sci U S A,* 97**,** 4885-90.
RAVEL, J. & CORNELIS, P. 2003. Genomics of pyoverdine-mediated iron uptake in pseudomonads. *Trends Microbiol,* 11**,** 195-200.
REHM, B. H. A. 2008. *Pseudomonas: Model Organism, Pathogen, Cell Factory*, Wiley.
RHODES, G. 2006. Chapter 5 - From Diffraction Data to Electron Density. *In:* RHODES, G. (ed.) *Crystallography Made Crystal Clear (Third Edition).* Burlington: Academic Press.
ROBERT, X. & GOUET, P. 2014. Deciphering key features in protein structures with the new ENDscript server. *Nucleic Acids Research,* 42**,** W320-W324.
RODNEY, M. D. 2002. Biofilms: Microbial Life on Surfaces. *Emerging Infectious Disease journal,* 8**,** 881.
ROSSMANN, M. G. 1972. *The Molecular Replacement Method*, New York: Gordon & Breach.
ROSSMANN, M. G. 1990. The molecular replacement method. *Acta Crystallogr A,* 46 (Pt 2)**,** 73-82.
ROSSMANN, M. G. 2001. Molecular replacement – historical background. *Acta Crystallographica Section D,* 57**,** 1360-1366.
RUPP, B. 2009. *Biomolecular Crystallography: Principles, Practice, and Application to Structural Biology*, Taylor & Francis Group.
RUPP, B. 2010. *Biomolecular Crystallography: Principles, Practice, and Application to Structural Biology*, Garland Science.
SACHDEVA, S., MUSAYEV, F. N., ALHAMADSHEH, M. M., SCARSDALE, J. N., WRIGHT, H. T. & REYNOLDS, K. A. 2008. Separate entrance and exit portals for ligand traffic in Mycobacterium tuberculosis FabH. *Chem Biol,* 15**,** 402-12.
SCARSDALE, J. N., KAZANINA, G., HE, X., REYNOLDS, K. A. & WRIGHT, H. T. 2001. Crystal Structure of the Mycobacterium tuberculosisβ-Ketoacyl-Acyl Carrier Protein Synthase III. *Journal of Biological Chemistry,* 276**,** 20516-20522.
SCHAADT, N. S., STEINBACH, A., HARTMANN, R. W. & HELMS, V. 2013. Rule-based regulatory and metabolic model for Quorum sensing in P. aeruginosa. *BMC Syst Biol,* 7**,** 81.
SCHALK, I. J., MISLIN, G. L. & BRILLET, K. 2012. Structure, function and binding selectivity and stereoselectivity of siderophore-iron outer membrane transporters. *Curr Top Membr,* 69**,** 37-66.

SCHRAUBER, H., EISENHABER, F. & ARGOS, P. 1993. Rotamers: To be or not to be?: An Analysis of Amino Acid Side-chain Conformations in Globular Proteins. *Journal of Molecular Biology,* 230**,** 592-612.
SCHUSTER, M., URBANOWSKI, M. L. & GREENBERG, E. P. 2004. Promoter specificity in Pseudomonas aeruginosa quorum sensing revealed by DNA binding of purified LasR. *Proceedings of the National Academy of Sciences of the United States of America,* 101**,** 15833-15839.
SIFRI, C. D. 2008. Quorum Sensing: Bacteria Talk Sense. *Clinical Infectious Diseases,* 47**,** 1070.
SIGGAARD-ANDERSEN, M. 1993. Conserved residues in condensing enzyme domains of fatty acid synthases and felated sequences. *Protein sequences & data analysis,* 5.
SILHAVY, J. 2010. *Pseudomonas aeruginosa* [Online]. Available: http://web.mst.edu/~microbio/BIO221_2010/P_aeruginosa.html [Accessed].
SINGH, P. K., SCHAEFER, A. L., PARSEK, M. R., MONINGER, T. O., WELSH, M. J. & GREENBERG, E. P. 2000. Quorum-sensing signals indicate that cystic fibrosis lungs are infected with bacterial biofilms. *Nature,* 407**,** 762-4.
SORENSEN, R. U. & KLINGER, J. D. 1987. Biological effects of Pseudomonas aeruginosa phenazine pigments. *Antibiot Chemother (1971),* 39**,** 113-24.
STOVER, C. K., PHAM, X. Q., ERWIN, A. L., MIZOGUCHI, S. D., WARRENER, P., HICKEY, M. J., BRINKMAN, F. S., HUFNAGLE, W. O., KOWALIK, D. J., LAGROU, M., GARBER, R. L., GOLTRY, L., TOLENTINO, E., WESTBROCK-WADMAN, S., YUAN, Y., BRODY, L. L., COULTER, S. N., FOLGER, K. R., KAS, A., LARBIG, K., LIM, R., SMITH, K., SPENCER, D., WONG, G. K., WU, Z., PAULSEN, I. T., REIZER, J., SAIER, M. H., HANCOCK, R. E., LORY, S. & OLSON, M. V. 2000. Complete genome sequence of Pseudomonas aeruginosa PAO1, an opportunistic pathogen. *Nature,* 406**,** 959-64.
SUTHERLAND, I. W. 2001. The biofilm matrix–an immobilized but dynamic microbial environment. *Trends in microbiology,* 9**,** 222-227.
TANG, H. B., DIMANGO, E., BRYAN, R., GAMBELLO, M., IGLEWSKI, B. H., GOLDBERG, J. B. & PRINCE, A. 1996. Contribution of specific Pseudomonas aeruginosa virulence factors to pathogenesis of pneumonia in a neonatal mouse model of infection. *Infect Immun,* 64**,** 37-43.
TARDIEU, A., BONNETE, F., FINET, S. & VIVARES, D. 2002. Understanding salt or PEG induced attractive interactions to crystallize biological macromolecules. *Acta Crystallogr D Biol Crystallogr,* 58**,** 1549-53.
TODAR, K. 2012. *Pseudomonas aeruginosa* [Online]. Available: http://textbookofbacteriology.net/pseudomonas.html [Accessed 15 May 2016].
USHER, L. R., LAWSON, R. A., GEARY, I., TAYLOR, C. J., BINGLE, C. D., TAYLOR, G. W. & WHYTE, M. K. 2002. Induction of neutrophil apoptosis by the Pseudomonas aeruginosa exotoxin pyocyanin: a potential mechanism of persistent infection. *J Immunol,* 168**,** 1861-8.

VAN ‘T WOUT, E. F. A., VAN SCHADEWIJK, A., VAN BOXTEL, R., DALTON, L. E., CLARKE, H. J., TOMMASSEN, J., MARCINIAK, S. J. & HIEMSTRA, P. S. 2015. Virulence Factors of Pseudomonas aeruginosa Induce Both the Unfolded Protein and Integrated Stress Responses in Airway Epithelial Cells. *PLOS Pathogens,* 11**,** e1004946.

VAN DELDEN, C. 2004. *Virulence factors in Pseudomonas aeruginosa,* New York: Kluwer Academic lPlenum Pubishers.

VAN DELDEN, C. & IGLEWSKI, B. H. 1998. Cell-to-cell signaling and Pseudomonas aeruginosa infections. *Emerg Infect Dis,* 4**,** 551-60.

VAN DEN ENT, F. & LÖWE, J. 2006. RF cloning: A restriction-free method for inserting target genes into plasmids. *Journal of Biochemical and Biophysical Methods,* 67**,** 67-74.

VENTURI, V. 2006. Regulation of quorum sensing in Pseudomonas. *FEMS Microbiol Rev,* 30**,** 274-91.

VOSS, N. R. & GERSTEIN, M. 2010. 3V: cavity, channel and cleft volume calculator and extractor. *Nucleic Acids Research,* 38**,** W555-W562.

WAGNER, V. E. & IGLEWSKI, B. H. 2008. P. aeruginosa Biofilms in CF Infection. *Clin Rev Allergy Immunol,* 35**,** 124-34.

WALLACE, A. C., LASKOWSKI, R. A. & THORNTON, J. M. 1995. LIGPLOT: a program to generate schematic diagrams of protein-ligand interactions. *Protein Eng,* 8**,** 127-34.

WATERS, C. M. & BASSLER, B. L. 2005. Quorum sensing: cell-to-cell communication in bacteria. *Annu Rev Cell Dev Biol,* 21**,** 319-46.

WATNICK, P. & KOLTER, R. 2000. Biofilm, City of Microbes. *Journal of Bacteriology,* 182**,** 2675-2679.

WHITELEY, M., LEE, K. M. & GREENBERG, E. P. 1999. Identification of genes controlled by quorum sensing in Pseudomonas aeruginosa. *Proc Natl Acad Sci U S A,* 96**,** 13904-9.

WILKINS, M. R., GASTEIGER, E., BAIROCH, A., SANCHEZ, J. C., WILLIAMS, K. L., APPEL, R. D. & HOCHSTRASSER, D. F. 1999. Protein identification and analysis tools in the ExPASy server. *Methods Mol Biol,* 112**,** 531-52.

WILLENBROCK, H., FRIIS, C., JUNCKER, A. S. & USSERY, D. W. 2006. An environmental signature for 323 microbial genomes based on codon adaptation indices. *Genome Biol,* 7**,** R114.

WILLENBROCK, H. & USSERY, D. W. 2007. Prediction of highly expressed genes in microbes based on chromatin accessibility. *BMC Mol Biol,* 8**,** 11.

WILLIAMS, P. & CAMARA, M. 2009. Quorum sensing and environmental adaptation in Pseudomonas aeruginosa: a tale of regulatory networks and multifunctional signal molecules. *Curr Opin Microbiol,* 12**,** 182-91.

WINN, M. D., BALLARD, C. C., COWTAN, K. D., DODSON, E. J., EMSLEY, P., EVANS, P. R., KEEGAN, R. M., KRISSINEL, E. B., LESLIE, A. G. W., MCCOY, A., MCNICHOLAS, S. J., MURSHUDOV, G. N., PANNU, N. S., POTTERTON, E. A., POWELL, H. R., READ, R. J., VAGIN, A. & WILSON, K. S. 2011. Overview of the CCP4 suite and current developments. *Acta Crystallographica Section D,* 67**,** 235-242.

WINZER, K., FALCONER, C., GARBER, N. C., DIGGLE, S. P., CAMARA, M. & WILLIAMS, P. 2000. The Pseudomonas aeruginosa Lectins PA-IL and PA-IIL Are Controlled by Quorum Sensing and by RpoS. *Journal of Bacteriology,* 182**,** 6401-6411.

WOODS, D. E., STRAUS, D. C., JOHANSON, W. G., JR., BERRY, V. K. & BASS, J. A. 1980. Role of pili in adherence of Pseudomonas aeruginosa to mammalian buccal epithelial cells. *Infect Immun,* 29**,** 1146-51.

ZHANG, Y.-M., FRANK, M. W., ZHU, K., MAYASUNDARI, A. & ROCK, C. O. 2008. PqsD Is Responsible for the Synthesis of 2,4-Dihydroxyquinoline, an Extracellular Metabolite Produced by Pseudomonas aeruginosa. *Journal of Biological Chemistry,* 283**,** 28788-28794.

ZOU, J. & MOWBRAY, S. L. 1994. An evaluation of the use of databases in protein structure refinement. *Acta Crystallographica Section D,* 50**,** 237-249.

ZUMFT, W. G. 1997. Cell biology and molecular basis of denitrification. *Microbiology and Molecular Biology Reviews,* 61**,** 533-616.

Appendices

Amino Acid Abreviations:

Amino acid	Three letter code	One letter code
alanine	ala	A
arginine	arg	R
asparagine	asn	N
aspartic acid	asp	D
asparagine or aspartic acid	asx	B
cysteine	cys	C
glutamic acid	glu	E
glutamine	gln	Q
glutamine or glutamic acid	glx	Z
glycine	gly	G
histidine	his	H
isoleucine	ile	I
leucine	leu	L
lysine	lys	K
methionine	met	M
phenylalanine	phe	F
proline	pro	P
serine	ser	S
threonine	thr	T
tryptophan	trp	W
tyrosine	tyr	Y
valine	val	V